Study of the metabolic reprogramming associated to metastasis in colon cancer

Josep Tarragó Celada

Study of the metabolic reprogramming associated to metastasis in colon cancer

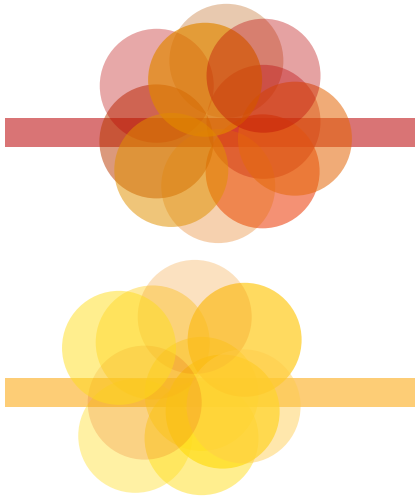

Josep Tarragó Celada

PhD Thesis

2020

UNIVERSITAT DE BARCELONA

PROGRAMA DE DOCTORAT EN BIOTECNOLOGIA

Departament de Bioquímica i Biomedicina Molecular

Facultat de Biologia

Study of the metabolic reprogramming associated to metastasis in colon cancer

Memòria presentada per Josep Tarragó Celada per
optar al grau de doctor per la Universitat de Barcelona

Josep Tarragó Celada
Doctorand

Dra. Marta Cascante Serratosa
Directora i tutora

A la meva família

"Tot art i tota investigació,
igual que tota acció i tota elecció,
tendeixen, sembla, cap algun bé"
ARISTÒTIL

"Non temete i momenti difficili,
il meglio viene da lì"
RITA LEVI-MONTALCINI

ABSTRACT

Metastasis is the main cause of cancer-related deaths and it is of great biomedical importance to develop new therapeutic strategies that specifically target metastatic cells. Therefore, a better comprehension of the process of how the disseminated tumour cells manage to survive the circulation and initiate new tumours is crucial. Genetic alterations are established to be the main driving force of tumorigenesis, while when it comes to metastasis, fewer genetic changes are identified and the metabolic adaptation emerges as an important hallmark. With the aim to elucidate the metabolic reprogramming supporting metastasis in colorectal cancer, we performed a thorough metabolic characterisation *in vitro* and *in vivo* of a primary colon cancer cell line (SW480), a cell line derived from the lymph node metastasis of the same patient (SW620) and a metastatically enriched derivative of the latter (LiM2). We revealed that the metastatic cell lines present enhanced glucose, glutamine and mitochondrial metabolism, and present higher metabolic flexibility. Additionally, from a systems biology approach, the metabolic dependencies of the metastatic cell lines were identified and validated *in vitro*, using a healthy colon cell line (NCM460). Specifically, we determined that the metastatic cell lines are selectively vulnerable to the inhibition of cysteine import and folate metabolism, among other targets. Together, the thesis presented here contributes to the knowledge of the mechanisms underlying metastasis as well as the development of new therapies capable of selectively blocking the metastatic spread of colorectal cancer.

INDEX

1 LIST OF ABBREVIATIONS 3

2 INTRODUCTION 11

2.1 BIOLOGY OF CANCER AND METASTASIS 11
2.1.1 GENERALITIES ON CANCER 11
2.1.1.1 The genetic background of cancer 11
2.1.1.2 Types and subtypes of cancer 11
2.1.1.3 Cancer incidence, mortality and risk factors 12
2.1.1.4 The hallmarks of cancer 13
2.1.2 MECHANISMS OF METASTASIS 13
2.1.2.1 The metastatic cascade 13
2.1.2.2 Cancer stem cells in the origin of metastasis 14
2.1.2.3 Epithelial-mesenchymal transition, intravasation, and circulation 15
2.1.2.4 Extravasation and organ-specific metastasis 16
2.1.3 BIOLOGY OF COLORECTAL CANCER AND METASTASIS 18
2.1.3.1 Colorectal cancer epidemiology 18
2.1.3.2 Genetic alterations in hereditary syndromes 18
2.1.3.3 Carcinogenic cascade in colorectal cancer 20
2.1.3.4 Signalling pathways altered in colorectal cancer 21
2.1.3.5 Diagnosis and staging of colorectal cancer 23
2.1.3.6 Colorectal cancer metastasis 26
2.2 METABOLIC REPROGRAMMING IN CANCER AND METASTASIS 27
2.2.1 METABOLIC PATHWAYS ALTERED IN TUMOUR CELLS 27
2.2.1.1 Otto Warburg and the first contributions to cancer metabolism 27
2.2.1.2 Beyond Warburg effect: Mitochondrial activity 29
2.2.1.3 Glutamine addiction and other amino acid addictions 30
2.2.1.4 One-carbon metabolism and redox balance 31
2.2.1.5 Lipid metabolism 32
2.2.2 THE CANCER METABOLIC REPROGRAMMING IN ITS CONTEXT 33
2.2.2.1 Signalling pathways and cancer metabolism 33
2.2.2.2 ROS signalling and homeostasis 36
2.2.3 METABOLIC REPROGRAMMING UNDERLYING METASTASIS 37
2.2.3.1 Glucose metabolism and EMT 37
2.2.3.2 Mitochondrial metabolism and EMT 39

2.2.3.3 Other pathways supporting EMT 40
2.2.3.4 Antioxidant metabolism in CTCs 40
2.2.3.5 Metabolic flexibility in the metastatic site 41
2.2.4 METABOLIC REPROGRAMMING IN COLORECTAL CANCER AND METASTASIS 43
2.2.4.1 Metabolic alterations in the primary stages of colorectal cancer 43
2.2.4.2 Metabolic alterations in metastatic colorectal cancer 44
2.3 CANCER THERAPY AND METABOLIC-BASED STRATEGIES 45
2.3.1 CURRENT AND NEW THERAPIES OF CANCER 45
2.3.1.1 Generalities on cancer treatment 45
2.3.1.2 Pharmacological treatment of cancer 46
2.3.1.3 Current therapies of colorectal cancer 48
2.3.2 METABOLISM IN CANCER TREATMENT 50
2.3.2.1 Metabolic-based cancer diagnosis 50
2.3.2.2 Metabolic-based therapeutic strategies 52
2.3.2.3 Metabolic-based therapeutic strategies in colorectal cancer 55
2.3.3 METABOLIC NETWORK SYSTEMS BIOLOGY APPROACH FOR THE DISCOVERY OF METABOLIC TARGETS 55
2.3.3.1 Systems biology and metabolomics 55
2.3.3.2 Metabolic models as a tool for the discovery of new targeted therapies 56

3 OBJECTIVES 61

4 MATERIALS AND METHODS 65

4.1 CHEMICALS 65
4.2 CELL CULTURE AND MOLECULAR BIOLOGY EXPERIMENTS 65
4.2.1 CELL SOURCES, CULTURE AND MAINTENANCE 65
4.2.2 CELL DOUBLING TIME, VOLUME DETERMINATION AND SEEDING CONDITIONS 65
4.2.3 IC_{50} CURVE DETERMINATION USING HOECHST 66
4.2.4 CELL PROLIFERATION ASSAY USING FLUOROSPHERES 67
4.2.5 APOPTOSIS ASSAY 68
4.2.6 CELL CYCLE ANALYSIS 68
4.2.7 REACTIVE OXYGEN SPECIES (ROS) DETERMINATION ASSAY 68
4.2.8 SPHEROIDS ASSAYS IN LOW ATTACHMENT PLATES 69
4.2.9 SPHEROIDS ASSAYS IN MATRIGEL 69
4.2.10 WOUND HEALING ASSAY 70
4.2.11 WESTERN BLOTTING 70

4.3 METABOLIC AND METABOLOMIC EXPERIMENTS 72
4.3.1 EXTRACELLULAR METABOLITE MEASUREMENTS BY SPECTROPHOTOMETRY 72
4.3.2 TARGETED METABOLOMICS 72
4.3.3 STABLE ISOTOPE-RESOLVED METABOLOMICS (SIRM) 73
4.3.3.1 Polar intracellular metabolites 73
4.3.3.2 Other metabolites 74
4.3.3.3 SIRM data analysis 76
4.4 *IN VIVO* EXPERIMENTS 79
4.4.1 XENOGRAFT EXPERIMENTS 79
4.4.2 IMMUNOHISTOCHEMISTRY 79
4.4.3 STABLE ISOTOPE-RESOLVED METABOLOMICS *IN VIVO* 80
4.5 STATISTICAL ANALYSES 80

5 RESULTS AND DISCUSSION 85

5.1 CHAPTER 1. METABOLIC CHARACTERISATION OF THE METASTATIC PROGRESSION IN COLORECTAL CANCER 85
5.1.1 INTRODUCTION 85
5.1.1.1 The SW480 – SW620 cell lines model 85
5.1.1.2 Liver metastatic derivatives of SW620 88
5.1.2 RESULTS AND DISCUSSION 90
5.1.2.1 Characterisation of the metastatic phenotype 90
5.1.2.2 Metastatic cells display increased glucose and glutamine metabolism 97
5.1.2.3 Metabolic flexibility of the metastatic cells under glucose and glutamine deprivations 101
5.1.2.4 Amino acid profile of primary and metastatic colon cancer cell lines 105
5.1.2.5 The metabolic adaptation of the metastatic cell lines *in vitro* is maintained in an *in vivo* scenario 108
5.2 CHAPTER 2. THE METABOLIC VULNERABILITIES ASSOCIATED TO METASTASIS IN COLORECTAL CANCER. 113
5.2.1 INTRODUCTION 113
5.2.1.1 A genome-scale metabolic model for metastatic progression of colon cancer 113
5.2.1.2 Exploring and validating metabolic vulnerabilities of the metastatic progression of colon cancer 114
5.2.2 RESULTS AND DISCUSSION 115
5.2.2.1 Evaluation of the use of NCM460 cell line as a healthy control 115

5.2.2.2 Metastatic cell lines are dependent on cystine uptake and vulnerable to system xCT and glutathione reductase inhibition 118
5.2.2.3 The metastatic cell lines are vulnerable to inhibition of folate metabolism 126
5.2.2.4 Synergistic effect of the simultaneous inhibition of cysteine uptake and folate metabolism 133
5.2.2.5 Other inhibitions 138

6 GENERAL DISCUSSION 145

7 CONCLUSIONS 155

8 BIBLIOGRAPHY 159

9 APPENDIX I 195

9.1 MATERIALS AND METHODS 195
9.2 RESULTS 195

10 APPENDIX II 213

10.1 MATERIALS AND METHODS 213
10.2 RESULTS *IN VITRO* 213
10.3 RESULTS *IN VIVO* 229

11 APPENDIX III 235

11.1 MATERIALS AND METHODS 235
11.2 RESULTS 236

12 APPENDIX IV 241

12.1 MATERIALS AND METHODS 241
12.2 RESULTS 241

13 APPENDIX V 255

13.1 MATERIALS AND METHODS 255

13.1.1 TRANSCRIPTOMICS 255
13.1.2 INTEGRATING EXTRACELLULAR FLUX MEASUREMENTS 255
13.1.3 INTEGRATING OCR MEASUREMENTS, MITO STRESS AND MITO FUEL ASSAYS 255
13.1.4 INTEGRATING INTRACELLULAR AMINO ACID AND BIOGENIC AMINES MEASUREMENTS 256
13.1.5 USING LIPIDOMIC MEASUREMENTS TO PERSONALISE THE BIOMASS FUNCTION 256
13.1.6 INTEGRATING GROWTH RATES 257
13.1.7 ^{13}C MFA AND GSMM INTEGRATION 258
13.1.8 MINIMAL CUT SET ANALYSIS 258
13.1.9 GENE INACTIVATION MODERATED BY METABOLISM, AND EXPRESSION (GIMME) 260
13.1.10 FLUX SAMPLING AND REFERENCE FLUX DISTRIBUTION SELECTION 261
13.1.11 IDENTIFYING PUTATIVE METABOLIC TARGETS 262
13.2 RESULTS 262

14 APPENDIX VI 277

1. List of abbreviations

1 LIST OF ABBREVIATIONS

1,3BPG	1,3-bisphosphoglycerate
2PG	2-phosphoglycerate
3PG	3-phosphoglycerate
5,10-meTHF	5,10-methylenetetrahydrofolate
6PGD	6-phosphogluconate dehydrogenase
ACC	Acetyl-CoA carboxylase
AcCoA	Acetyl-CoA
ACLY	ATP-citrate lyase
ACO2	Aconitate hydratase, mitochondrial
ACSL	Long-chain fatty-acid-CoA ligase
ALDO	Fructose-bisphosphate aldolase
ALDOB	Fructose-bisphosphate aldolase B
ALL	Acute lymphocytic leukaemia
AML	Acute myeloid leukaemia
ANOVA	Analysis of variance
APC	Adenomatous polyposis coli
ARG1	Arginase 1
ARG2	Arginase 2, mitochondrial
ASNS	Asparagine synthetase
ASS1	Argininosuccinate synthase
BFGF	Basic fibroblast growth factor
CAFs	Cancer-associated fibroblasts
CHO-THF	10N-formyl tetrahydrofolate
CI	Respiratory complex I
CIII	Respiratory complex III
Cit	Citrate
CIV	Respiratory complex IV
CKB	Creatine kinase B-type
CML	Chronic myeloid leukaemia

CMS	Consensus molecular subtypes
CP	Computed tomography
CPT	Carnitine palmitoyltransferase
CRC	Colorectal cancer
CS	Citrate synthase, mitochondrial
CSC	Cancer stem cells
CTCs	Circulating tumour cells
ctDNA	Circulating tumour DNA
D2HG	D-2-hydroxyglutarate
DAP	Dihydroxyacetone phosphate
DHF	Dihydrofolate
DHFR	Dihydrofolate reductase
DMEM	Dulbecco's Modified Eagle Medium
dTMP	Deoxythymidine monophosphate
E4P	Erythrose 4-phosphate
EDTA	Ethylenediaminetetraacetic acid
EGF	Epidermal growth factor
EGFR	Epidermal growth factor receptor
EMT	Epithelial-mesenchymal transition
ENO	Enolase
ENO1	Alpha-enolase
ENO2	Gamma-enolase
ETC	Electron transport chain
F1,6BP	Fructose 1,6-bisphate
F6P	Fructose 6-phosphate
FA	Fatty acids
FAD	Flavin adenin dinucleotide
FASN	Fatty acid synthase
FBP	Fructose 1,6-bisphosphatase
FBP1	Fructose 1,6-bisphosphatase 1
FBS	Foetal bovine serum
FDA	Food and Drug Administration (USA)

FH	Fumarate hydratase, mitochondrial
Fum	Fumarate
G1P	Glucose 1-phosphate
G6P	Glucose 6-phosphate
G6PD	Glucose 6-phosphate 1-dehydrogenase
GAP	Glyceraldehyde 3-phosphate
GAPDH	Glyceraldehyde 3-phosphate dehydrogenase
GART	Trifunctional purine biosynthetic protein adenosine-3
GC-MS	Gas chromatography-mass spectrometry
GLS	Glutaminase
GLS1	Glutaminase, kidney isoform
GLUD	Glutamate dehydrogenase
GLUD1	Glutamate dehydrogenase 1, mitochondrial
GLUT	Glucose transporter
GLUT1	Glucose transporter 1
GLUT3	Glucose transporter 3
GOT1	Aspartate aminotransferase, cytoplasmatic
GOT2	Aspartate aminotransferase, mitochondrial
GPI	Glucose 6-phosphate isomerase
GPX2	Glutathione peroxidase 2
GSMM	Genome-scale metabolic model
GSR	Glutathione reductase
HDI	Human development index
HIF1α	Hypoxia-inducible factor 1-alpha
HK	Hexokinase
HK1	Hexokinase 1
HK2	Hexokinase 2
IDH	Isocitrate dehydrogenase
IDH1	Isocitrate dehydrogenase cytoplasmatic
IDH2	Isocitrate dehydrogenase mitochondrial
IL	Interleukin
Isocit	Isocitrate

Lac	Lactate
LC-MS	Liquid chromatography-mass spectrometry
LDH	L-Lactate dehydrogenase
LDHA	L-Lactate dehydrogenase A chain
LDHB	L-lactate dehydrogenase B chain
LPR6	Low-density lipoprotein receptor-related protein 6
Mal	Malate
MalCoA	Malonyl-CoA
MCT	Monocarboxylate transporter
MCT1	Monocarboxylate transporter 1
MCT4	Monocarboxylate transporter 4
MDH2	Malate dehydrogenase
ME1	NADP-dependent malic enzyme
ME2	NAD-dependent malic enzyme, mitochondrial
MET	Mesenchymal-epithelial transition
MFA	Metabolic flux analysis
MMP	Matrix metallopeptidase
MS	Mass spectrometry
MSI	Microsatellite instable
MSS	Microsatellite stable
MTHFD1	Methylenetetrahydrofolate dehydrogenase 1 ($NADP^+$ dependent), methenyltetrahydrofolate cyclohydrolase and formyltetrahydrofolate synthetase
MTHFD2	Methylenetetrahydrofolate dehydrogenase ($NADP^+$ dependent) 2, methenyltetrahydrofolate cyclohydrolase
mTOR	Mammalian target of rapamycin
NAC	N-acetylcysteine
NF-κB	Nuclear factor kappa-light-chain-enhancer of activated B cells
NMR	Nuclear magnetic resonance
NO	Nitric oxide
NOS	Nitric oxide synthase
NRF2	Nuclear factor erythroid 2-related factor 2
OAA	Oxalacetate

OCR	Oxygen consumption rate
ODC	Ornithine decarboxylase
OGDC	Oxoglutarate dehydrogenase complex
OTC	Ornithine carbamoyltransferase, mitochondrial
PBS	Phosphate-buffered saline
PC	Pyruvate carboxylase
PDH	Pyruvate dehydrogenase
PDK1	Pyruvate dehydrogenase lipoamide kinase isozyme 1, mitochondrial
PDP1	Pyruvate dehydrogenase phosphatase 1, mitochondrial
PDP2	Pyruvate dehydrogenase phosphatase 2, mitochondrial
PEP	Phosphoenolpyruvate
PET	Positron emission tomography
PFK	Phosphofructokinase
PFKP	Phosphofructokinase platelet
PGAM	Phosphoglycerate mutase
PGC-1α	Peroxisome proliferator-activated receptor gamma coactivator 1-alpha
PGK	Phosphoglycerate kinase
PGM	Phosphoglucomutase
PGM1	Phosphoglucomutase 1
PHD	Prolyl hydroxylase
PHGDH	D-3-phosphoglycerate dehydrogenase
PI3K	Phosphoinositide 3-kinase
PIM	Polar intracellular metabolites
PK	Pyruvate kinase
PKM2	Pyruvate kinase M2 isoenzyme
PPP	Pentose phosphate pathway
PRODH	Proline dehydrogenase
PSAT	Phosphoserine aminotransferase
PTEN	Phosphatase and tensin homolog
Pyr	Pyruvate
R5P	Ribose 5-phosphate
Ri5P	Ribulose 5-phosphate

ROS	Reactive oxygen species
RPIA	Ribose 5-phosphate isomerase
RRM1	Ribonucleotide reductase catalytic subunit M1
SAM	S-Adenosyl-methionine
SAT1	Diamine acetyltransferase 1
SCS	Succinyl coenzyme A synthetase
SD	Standard deviation
SDH (CII)	Succinate dehydrogenase (respiratory complex II)
SDS	Sodium dodecyl sulphate
SHMT1	Serine hydroxymethyltransferase, cytosolic
SHMT2	Serine hydroxymethyltransferase, mitochondrial
SIM	Single ion monitoring
SIRM	Stable isotope-resolved metabolomics
SMS	Spermine synthase
SRM	Spermidine synthase
Succ	Succinate
TF	Transcription factor
TGFβ	Transforming growth factor beta
THF	Tetrahydrofolate
TKT	Transketolase
TNM	Tumour, node, metastasis classification
TPI	Triosephosphate isomerase
TPO	Thrombopoietin
TYMS	Thymidylate synthetase
VEGF	Vascular endothelial growth factor
X5P	Xylulose 5-phosphate
xCT	Cysteine/glutamate transporter system xCI
ZEB1	Zinc finger E-box binding homeobox 1
ZEB2	Zing finger E-box binding homeobox 2
αKG	α-ketoglutarate

2. Introduction

2 INTRODUCTION

2.1 BIOLOGY OF CANCER AND METASTASIS

2.1.1 GENERALITIES ON CANCER

2.1.1.1 The genetic background of cancer

Cancer is a disease characterised by an uncontrolled proliferation of cells from a specific tissue that form a tumour. This happens in a context of cumulative genetic mutations that could have been previously inherited or caused by environmental factors such as physical or chemical carcinogens, diet, or infections. Specifically, mutations that are associated with cancer occur in proto-oncogenes, tumour suppressor genes, or DNA repair genes (Primo and Teixeira, 2019; Wang et al., 2018a).

Proto-oncogenes are genes related to the stimulation of cell division and survival, such as transcription factors. A point mutation, amplification, or epigenetic changes result in a dominant gain of function of the gene, converting it to an oncogene that is able to start or contribute to tumour progression. In contrast, tumour suppressors are genes that normally prevent cellular growth, such as proteins related to cell cycle regulation. In that case, a loss of function is required for malignancy, and therefore, mutations or epigenetic silencing are recessive and both copies of the gene need to be compromised in order to have a tumorigenic phenotype. For that reason, alterations in tumour suppressors are commonly found in hereditary syndromes where one copy of the gene is already mutated. Finally, DNA repair genes are considered to be another class of genes associated to cancer as the effect of their alteration is not directly related to uncontrolled cell proliferation, but to accelerate the mutation rate and therefore accelerate genetic events that affect oncogenes or tumour suppressors (Chae et al., 2019).

2.1.1.2 Types and subtypes of cancer

Depending on the tissue of origin, there are three main types of cancer. Cancers of epithelial origins are called carcinomas and are divided into two subtypes: Adenocarcinomas, which are originated in an organ or a gland, being the case of breast, lung, colon, prostate, or bladder cancer, and squamous cell carcinomas, which develop in the squamous epithelium and can occur in many parts of the body. The second major type of cancer are sarcomas, which are from connective tissues such as bones, cartilage, muscle, or fat. Examples of them are osteosarcomas, chondrosarcomas, leiomyosarcomas, or liposarcomas. Finally, when the origin of cancer is the white blood cells or the lymphatic system, we can distinguish between leukaemia or lymphomas, respectively (Koch, 2014).

Apart from the tissue of origin, different subtypes of cancers for each location are also established depending on the genetic lesion they present. At the same time, same genetic drivers

could be shared with tumours of different origin. For that reason, new classifications according to the molecular subtype are claimed by the scientific community in order to improve clinical care towards a precise and personalised treatments (Schneider et al., 2017; Zhao et al., 2019). Nevertheless, it is clear that the tissue of origin determines a common genetic alteration, especially for the hereditary cancer predisposition syndromes. This is the case of the familiar adenomatous polyposis syndrome of colorectal cancer or the hereditary diffuse gastric cancer, which have the genes *APC* (Adenomatous Polyposis Coli) and *CDH1* (E-cadherin) as tumour suppressor drivers (Muir and Nunney, 2015; Pena-Couso et al., 2018).

2.1.1.3 Cancer incidence, mortality and risk factors

Cancer is the second leading cause of death worldwide, after cardiovascular diseases. In 2018, 18.1 million people were diagnosed by cancer and 9.6 million died from this disease (Bray et al., 2018). Specifically, lung cancer is the most common type of cancer diagnosed and also the leading cause of cancer death, followed by female breast cancer, colorectal cancer, and prostate cancer in males. The distribution of the common cancer types is not homogenous among the countries, and both diagnosis and mortality of cancer types are substantially different. These patterns respond to different environmental factors that the different regions in the world are exposed to (Bray et al., 2018). Also, the human development index (HDI) is a factor that determines cancer incidence. In higher HDI regions, the cancer incidence is 2.5-fold higher compared to low HDI countries, as expectancy of life is longer. However, the mortality is similar because of a higher case fatality for many cancer types in lower HDI regions. Only 5-10% of all cancers are attributed to previous genetic or epigenetic alterations and are considered hereditary cancer syndromes. The other 90-95% is considered to be caused by the environment, lifestyle, and aging (Anand et al., 2008). The main environmental factors that are described to cause cancer are classified into physical carcinogens, chemical carcinogens, and infections, which produce DNA damage and mutations

The prevention of cancer, therefore, is of great importance in order to reduce as maximum as possible cancer incidence. However, at the moment, we face a great deal as a society of actually treating all the cancer cases and avoid mortality, which mainly comes from the malignant progression of tumours. Cancer metastasis is responsible for 90% of cancer deaths (Keum and Giovannucci, 2019). Such incidence can be explained by the fact that at the beginning of cancer development, most benign solid tumours affect non-essential structures and organs are able to keep their normal function. Then, when the metastatic spread is efficient and secondary tumours start to appear in other organs, they can affect essential functions and cause morbidities and an inflammatory state that could eventually lead to death. Furthermore, early detection could help to improve the survival rate as cancer could be treated before metastasis spread.

2.1.1.4 The hallmarks of cancer

Tumours are considered to be benign until they acquire the capacity to invade other tissues when start being considered as malign or metastatic. However, to date, the study of cancer has been centred mostly on tumorigenesis and tumour progression rather in the invasion and metastatic capacities, which are fewer known processes. There are at least ten hallmarks that define the biology of cancer, as Hanahan and Weinberg had proposed back in 2000 and revised in 2011.

The initial six characteristics that were proposed were sustained proliferation, evasion of growth suppressors, capacity for invasion and metastasis, enabled replicative immortality, angiogenesis, and cell death resistance (Hanahan and Weinberg, 2000). Great effort has been done for the last two decades to elucidate the mechanisms underlying these processes and some of them are targeted in the clinics, as explained in the next sections. Afterwards, scientific discoveries made clear that also immune evasion, inflammation, genome instability, and cellular energetics deregulation had to be considered as main hallmarks of cancer (Hanahan and Weinberg, 2011), and are nowadays at the cutting edge of cancer research.

Furthermore, not all cancer cells that form a tumour have the same characteristics, as genetic variations between them are observed and are responsible for the tumour heterogeneity (Hausser and Alon, 2020). Such heterogeneity can also be explained by the fact that there is a hierarchy of cancer cells with stem cell features that are able to self-renew, and its progeny with non-stem cell properties (Capp, 2019). Also, the tumour microenvironment, formed by stromal and immune cells also influence tumour progression and the metastatic capacity (Burgos-Panadero et al., 2019).

In the present work, we focus our attention on two of the hallmarks: the capacity for invasion and metastasis, and cellular energetics deregulation, although many other features are taken into account to have a global picture of how metastatic cells adapt their metabolism to invade and colonise other tissues.

2.1.2 MECHANISMS OF METASTASIS

2.1.2.1 The metastatic cascade

Metastasis is the process by which cancer cells from a primary tumour are able to originate another tumour in a new tissue or organ. Metastatic tumours are usually resistant to current therapies and cause the failure of vital organs. For that reason, metastasis is the leading cause of cancer death. However, it is a process with a lot of remaining questions, being much poorly understood than tumorigenesis. The mechanisms that drive metastatic development and progression are still full of controversy.

There are a series of steps that define the metastatic spread, starting from the local invasion of the nearby tissues and intravasation and arrival to circulation facilitated by angiogenesis. Then, in order to survive in circulation, immune evasion and anchorage-free capacities are needed. Circulating tumour cells (CTCs) are found as single cells or forming clusters that are usually accompanied by platelets (Pretzsch et al., 2019). After that, arrest to a new organ or tissue and specific adhesion is needed before extravasation and survival in the new environment to reinitiate a tumour, known as micrometastasis (Yamamoto et al., 2016). Finally, after a period of latency or dormancy, the last step of metastasis is the colonisation of the new organ with the formation of a clinically detectable tumour, which is called macrometastasis (Fares et al., 2020). Each step of the metastatic cascade implies a bottleneck for the cancer cells that select the clones that have developed the capacity to overcome all the scenarios, such as Darwinian selection (Lacina et al., 2019).

2.1.2.2 Cancer stem cells in the origin of metastasis

Growing scientific evidence implicates cancer stem cells (CSCs) in the origin of metastasis, as well as to tumour progression, therapy resistance, and recurrence (Ayob and Ramasamy, 2018). The CSC theory presents the tumour organised as a hierarchy where the CSCs are able to self-renew and differentiate to other tumour cells with no tumorigenic capacity and limited proliferative potential (mainly transit-amplifying progenitors and differentiated derivatives). The stem-like gene expression signature has been correlated with metastasis and poor survival outcome in patients (Riester et al., 2017). Therefore, cells that are able to proliferate and generate a new tumour in a distant site are considered to be CSCs, or metastatic stem cells (Oskarsson et al., 2014).

The origin of CSCs is not known and both the assumptions that come from previous normal stem cells where the tumour was originated or else a normal non-stem cell that has acquired proliferative capacities are possible. It is also possible that CSCs are dynamic cellular states that different tumour cells can acquire depending on the tumour microenvironment, as well as the selective pressure of metastatic progression or therapy. Despite all the controversies, CSCs surface expression markers such as CD133, CD44, CD90, CD24, and CD29 have been identified and observed to be associated with stemness. There are also a series of pathways that are related to the maintenance of CSC phenotype: Wnt/β-catenin, TGFβ (Transforming Growth Factor-β), Notch, Hedgehog and Hippo pathways, as well as microRNAs that promote pluripotency (miR290, 302, and 371), usually induced by the pluripotency transcription factors Oct, Sox2, Nanog, Tcf3, and Klf4 (Pattabiraman and Weinberg, 2014). The tumour microenvironment also plays a role in the maintenance of stemness properties of CSC and vice-versa, with positive feedback from inflammatory cytokine networks expressed by the surrounding immune cells or cancer associated fibroblasts (Prager et al., 2019; Ye et al., 2014). This is the case of the cytokines

IL-6 and IL-8 that activate the NF-κB (Nuclear factor kappa-light-chain-enhancer of activated B cells) pathway via Stat3 and Akt signalling.

2.1.2.3 Epithelial-mesenchymal transition, intravasation, and circulation

The first step of metastasis cascade, the invasion capacity, is also associated with stemness properties. In other words, metastatic CSCs are believed to be the cells that acquire the capacity to migrate and invade other tissues as well as reach circulation. Therefore, a transition from an epithelial to a mesenchymal state is thought to be an essential feature for CSCs to advance in metastatic progression. The epithelial-mesenchymal transition (EMT) is the loss of polarity and cell adhesion properties, the gain of migration capacity, and extracellular matrix components production (Figure 2.1.1).

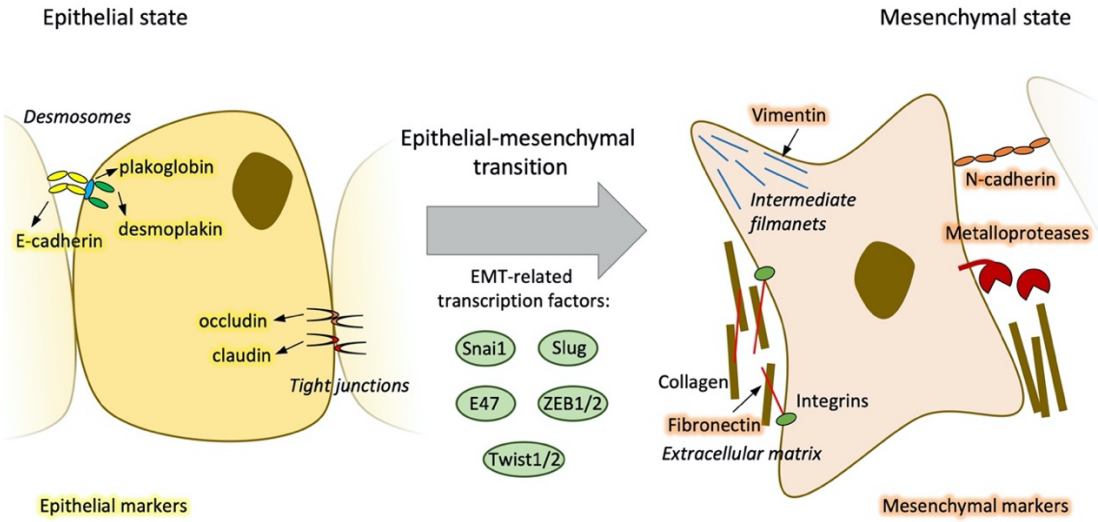

Figure 2.1.1. Epithelial-mesenchymal transition in cancer metastasis. Schematic representation of the epithelial-mesenchymal transition process, which allows cancer cells to initiate metastasis by loss of polarity and cell-cell adhesions, ability to migrate and remodel the extracellular matrix components.

The EMT was first described by Elisabeth Hay as a controlled process in embryogenesis and an uncontrolled process in cancer cells (Hay, 2005). Specifically, the increased production of transcription factors Snai1, Slug, Twist1/2, ZEB1/2 (Zinc finger E-box binding homeobox 1 and 2) and E47 is related to EMT. The resulting phenotype is a general decreased expression of molecules that are implied in epithelial cell-cell unions, mainly E-cadherin, claudin, occluding and desmoplakin. The loss of adhesion is accompanied by an increased expression of N-cadherin, which favours interactions with other types of cells, an increased vimentin expression, which forms intermediate filaments that favour migration, fibronectin, an extracellular matrix component, as well as matrix metalloproteinases that degrade the extracellular matrix. All these proteins are defined as the main EMT markers. When cells acquire mesenchymal properties also proliferate less, but usually, EMT transcriptions factors maintain and even increase stemness (Horvay et al., 2015; Yeung and Yang, 2017). In the case of colorectal cancer, a heterogenous

pattern of β-catenin is observed with increased expression in the invasive front, which has been related to higher proliferation and EMT activation (Qi et al., 2014; Teeuwssen and Fodde, 2019).

Recent research suggests that tumour microenvironment, apart from maintaining stemness, can induce EMT and help to maintain a mesenchymal phenotype. Mainly cancer-associated fibroblasts and immune cells such as tumour-associated macrophages, myeloid-derived suppressor cells and lymphocytes secrete cytokines, chemokines, and growth factors (EGF, HGF, TGFβ, IL-6, TNF, CCL18, and VEGF) that induce the expression of the EMT transcription factors (Dongre and Weinberg, 2019).

The process of mesenchymal cancer cells migration is accompanied by many stimuli in the invasive front. Migrating cells are exposed to environmental stress that comes from the surrounding tissue, such as hypoxia or immune surveillance. However, as explained above, cells of different types could help to migrate cancer cells with stimulating stimuli of survival and self-renewal factors (Sandberg et al., 2019). Also, tumour cells that are not CSCs help in the invasive front and may even undergo EMT and migrate (Gupta et al., 2011). Metastatic cells are finally able to intravasate and enter to lymphatic or vascular circulation as circulating tumour cells, which are able to survive by avoiding anoikis, a form of apoptosis cell death related with the loss of anchorage from the surrounding extracellular matrix (Strilic and Offermanns, 2017). Then, tumour cells, circulating as single cells or clusters, also face hemodynamic forces and the operating immune system circulating in the blood, giving back the immunosuppressive microenvironment.

At that point, circulating tumour cells that are able to extravasate in the metastatic site and form a new tumour after a period of dormancy need to undergo a reverse transition from EMT, known as mesenchymal-epithelial transition (MET), or at least re-acquire some epithelial properties. For example, it is observed that the re-expression of E-cadherin allows clonal outgrowth and confers advantages during the establishment of metastasis (Palen et al., 2016). Supporting that, it is also observed that late-stage metastatic cells exhibit gene signatures that are close to the primary tumour ones (Lawson et al., 2015).

The EMT theory is generally accepted although it is not always observed exactly in the same manner. The epithelial and mesenchymal markers are not always consistent or complete, and many other states rather than only the binary epithelial or mesenchymal states are observed (Pastushenko and Blanpain, 2019). Sometimes, E-cadherin is never repressed, and mesenchymal cells keep expressing it. Partial EMT or even no evidence of the EMT as traditionally understood are observed in some metastatic processes (Jolly et al., 2017; Saitoh, 2018).

2.1.2.4 Extravasation and organ-specific metastasis

The steps of the metastatic progression can vary among the different cancer types. There are cancer types that are more aggressive than others, or there are cases where a period of latency

before clinical manifestation of metastasis is longer. However, a characteristic of metastasis is the preference for a specific metastatic site depending on the organ of origin, which is called organ tropism. There are cancer types that spread to one specific organ, as it is the case of prostate cancer that metastasise to the bone, pancreatic cancer to the liver, etc. Other cancer types metastasise different organs sequentially, as colorectal cancer that colonises first the liver and then the lungs or the brain. Breast and lung cancers present multiorgan metastasis in the bones, liver, brain, lung, ovaries, and skin. Finally, melanomas usually metastasise to the skin or spleen (Obenauf and Massagué, 2015).

Organ tropism is in part determined by the physiology of the vascular system. For example, in the case of colorectal cancer, the liver is the preferential organ because of the enterohepatic circulation that brings colorectal cancer cells directly to the liver. However, not all organ-specific metastases are explained by physical questions and there are also molecular patterns that define an organ to be a good environmental niche for specific cancer types. Such theory is called the "seed and soil" hypothesis and was posed by Steven Paget in 1989 (Fidler and Poste, 2008), and establishes the formation of a pre-metastatic niche from the signals of the primary tumour, probably coming from CSCs, that prime the site of metastasis for receiving it, with a posterior interaction with the new microenvironment that facilitates colonisation (Doglioni et al., 2019; Sceneay et al., 2013).

There are many examples of molecular mechanisms that confirm this hypothesis: Cancer cells that reach to the bone benefit from survival signals (such as the chemokines CXCL12 and SDF1) before the activation of osteoclast for bone resorption, which is mediated by the release of intercellular adhesion molecule 1 (ICAM1) by cancer cells and helped by osteoblasts through the secretion of IL6 and by the same osteoclasts secreting TGFβ (Wang et al., 2015). In lung colonisation, cancer cells together with myofibroblast express a series of extracellular proteins such as periostin (POSTN) and tenascin C (TNC) that stimulate cancer cell survival, together with the expression of the vascular cell adhesion molecule 1 (VCAM1) that activate survival signals from macrophages (Tichet et al., 2015). In the case of the brain, cancer cells need to pass through the blood brain barrier and avoid astrocyte-mediated death signals and benefit from other several mediators such as cathepsin S, COX2, ST6GalNac5, matrix metallopeptidases (MMP2 and MMP9) and the expression of L1 cell adhesion molecule (L1CAM) (Rahmathulla et al., 2012). Finally, liver infiltration is facilitated by the hepatic endothelium, where Src signals protect from TNF-related apoptosis-inducing ligand (TRAIL)-mediated apoptosis. The recruitment of bone marrow-derived cells through stellate cells thanks to TGFβ, CCL2, and IL6 production from cancer cells is also important for liver colonisation, as well as the expression of claudin-2 to interact with hepatocytes (Mielgo and Schmid, 2020).

2.1.3 BIOLOGY OF COLORECTAL CANCER AND METASTASIS

2.1.3.1 Colorectal cancer epidemiology

Colorectal cancer is the third most frequently diagnosed cancer and the second in terms of mortality with 1.8 million new colorectal cancer cases and 881000 deaths every year (Bray et al., 2018; Siegel et al., 2020). It is predicted that by 2040 there will be up to 3 million new cases (Ferlay et al., 2019). The highest colon cancer rates are found in Europe, Australia, Northern America and Eastern Asia, while in most regions of Africa and Southern Asia the rates are lower. Colorectal cancer incidence has a wide variation it is considered to be a marker of socioeconomic development as incidence grow uniformly with rising HDI (Fidler et al., 2016). It is probably due to the lifestyle patterns that developed countries present such as unhealthy diet or alcohol consumption, although the better practices in cancer management and early detection help to lower mortality in comparison to undeveloped countries (Arnold et al., 2017).

The risk factors for colorectal cancer that are non-modifiable include age, with an increasing incidence from 50 years old, and it is infrequent at ages below 40 unless a previous disease is presented. Then, there is a predisposition in patients that suffer from Chron's disease or ulcerative colitis as well as genetic hereditary syndromes as familial adenomatous polyposis or Lynch syndrome. However, more around the 70% of the cases are sporadic (Keum and Giovannucci, 2019). Among the modifiable risk factors or environmental factors that are associated to colorectal cancer, there is enough evidence that red meat, processed meat and alcohol drinks increase risk of colorectal cancer (Rossi et al., 2018; Zhao et al., 2017). Another risk factor related to the diet or previous genetic condition is obesity, especially visceral fat (Dong et al., 2017). Finally, there is evidence that other components of diet such as dietary fibre, calcium, and D vitamin are protective against colorectal cancer (Ben et al., 2014; Bonovas et al., 2016; Choi et al., 2015), as well as physical activity (Shaw et al., 2018).

As explained before, metastasis is the main cause of cancer deaths. This is especially important in colorectal cancer, where there is a huge difference in survival depending on the stage of the tumour at the moment of diagnosis. If it is diagnosed at early stages, the 5-year survival rate is 95% whereas if it is diagnosed at late stages, survival is 5% (Arnold et al., 2017). It is of great importance, then, to set up early detection screenings such as colonoscopy or faecal occult blood test that help to increase survival and reduce mortality (Hamzehzadeh et al., 2017; Strul and Arber, 2007), as well as to establish more efficient therapies against metastatic colorectal cancer.

2.1.3.2 Genetic alterations in hereditary syndromes

Like many types of cancer, colorectal cancer has an observed common molecular progression that starts with loss of *APC* or, with less frequency, alterations in the mismatch repair

system (genes include *MLH1*, *MSH2*, *MSH6*, *MS1*, and *MS2*). In the case of hereditary colorectal cancer, which represents around 30% of colorectal cancer cases, it is clear that previous mutations in these genes favour the appearance of tumours. However, in the remaining 70% of sporadic colorectal cancers, it is also common that the initial point of carcinogenesis cascade is either loss of *APC* or loss of mismatch repair genes. Colorectal cancer is classified in two major subtypes according to the genes that are altered: The loss of function in mismatch repair system, which implicate a continuous genetic instability, determines colorectal cancer to be considered microsatellite instable (MSI), and represents around 15% of the total cases. The loss of *APC* is normally related to microsatellite stable (MSS) colorectal cancer and represents 85% of the cases (Díaz-Rubio et al., 2012).

Among all the hereditary syndromes, Lynch syndrome is the more frequent, with 2-3% of all colorectal cancer cases. This syndrome is related to a very high risk of colon cancer, but also endometrial, stomach, or pancreatic cancer. 90% of the mutations in Lynch syndrome appear in *MLH1* and *MSH2*, and 10% of the mutations appear in *MSH6*, *PMS2,* and *EPCAM*, all genes related to the mismatch repair system (Duraturo et al., 2019). Genetic lesions in this system cause a phenotype where multiple mutations are not repaired, mainly repetitions of mono and dinucleotides called microsatellites that are distributed along the genome and finally cause mutations in coding genes associated to cancer, giving to a carcinogenesis cascade that has every time more mutations as it develops (De Smedt et al., 2015). As explained above, tumours with defects in the mismatch repair system are classified as microsatellite instable (MSI).

Familial Adenomatous Polyposis accounts for 1% of total colorectal cancers and it is characterised by the presence of multiple polyps that may become tumours in the large intestine, and also osteomas and retinal hypertrophy. The genetic basis of the disease is the presence of mutations in the *APC* gene, which receives its name precisely for the disease, Adenomatous Polyposis Coli. As it was already described, *APC* is a tumour suppressor gene that is involved in the regulation of many cell processes including cell division, migration and adhesion, and several proteins can interact with it as Axin protein, microtubule protein, glycogen synthase kinase β-3 (GSKβ-3), β-catenin, y-catenin, p35, Tid56, and others. When *APC* is mutated, there is an accumulation of β-catenin in the nucleus that activates the Wnt pathway (see section 2.1.3.4) (Plawski et al., 2013).

Another syndrome that also produces multiple polyposes is the MUTYH-associated polyposis, associated to the *MUTYH* gene, which is related to base excision repair and therefore to DNA oxidative damage repair. When *MUTYH* is mutated, there is an increase of C:G to A:T transversions that can affect the coding region of *APC* or *KRAS*, causing again a carcinogenic cascade. Other minority colorectal cancer syndromes are the hereditary mixed polyposis, which is associated to mutations in the *GREM1* gene, the Peutz-Jeghers syndrome, that presents mutations in *STK11*, the Juvenile Polyposis Syndrome, associated with germline mutations of one

of three genes *SMAD4*, *BMPR1A,* or *ENG*, the Cowden syndrome, that is associated to mutations in *PTEN*, and the Serrated Polyposis Syndrome, whose genetic basis has not yet been established (Patel and Ahnen, 2012).

2.1.3.3 Carcinogenic cascade in colorectal cancer

As explained before, in both sporadic and hereditary colorectal cancer cases, the behaviour of the carcinogenesis cascade is similar (Figure 2.1.2). The differences come from the starting point that could be *APC* loss in case of MSS and mismatch repair genes loss in case of MSI. On one hand, when there is a loss of *APC* function, the epithelium of the colon turns to be hyperproliferative, although it is considered a benign adenoma. At that stage, there could be changes in the methylation state, normally hypomethylation that leads to an overexpression of genes related to cell proliferation, especially GTPase proteins of the MAPK/ERK pathway such as KRAS, which makes the benign adenoma more severe. Finally, some other genetic defects are needed to get the step of carcinoma and finally invasion and metastasis, such as loss of function of *DCC* (Deleted in Colorectal Cancer) or *TP53* genes, or else gain-of-function mutations in *PIK3CA* (Phosphatidylinositol-4,5-Bisphosphate 3-Kinase Catalytic Subunit Alpha) or *PTP4A3* (Protein Tyrosine Phosphatase 4A3) (Nguyen and Duong, 2018). *DCC* gene encodes for a transmembrane protein, netrin-1 receptor, that is involved in cell adhesion and interacts in the cytoplasm with the focal adhesion kinase pathway and is considered a tumour suppressor gene, frequently mutated in colorectal cancer (Finci et al., 2015). *TP53* gene encodes also for a tumour suppressor protein that promotes cell cycle arrest and apoptosis when DNA is damaged, therefore, its loss of function is related to unrestrained proliferation. However, other functions of p53 protein suggest that it also may act as an oncogene (Soussi and Wiman, 2015). Finally, both *PIK3CA* and *PTP4A3* are oncogenes that are involved in cell proliferation signalling pathways.

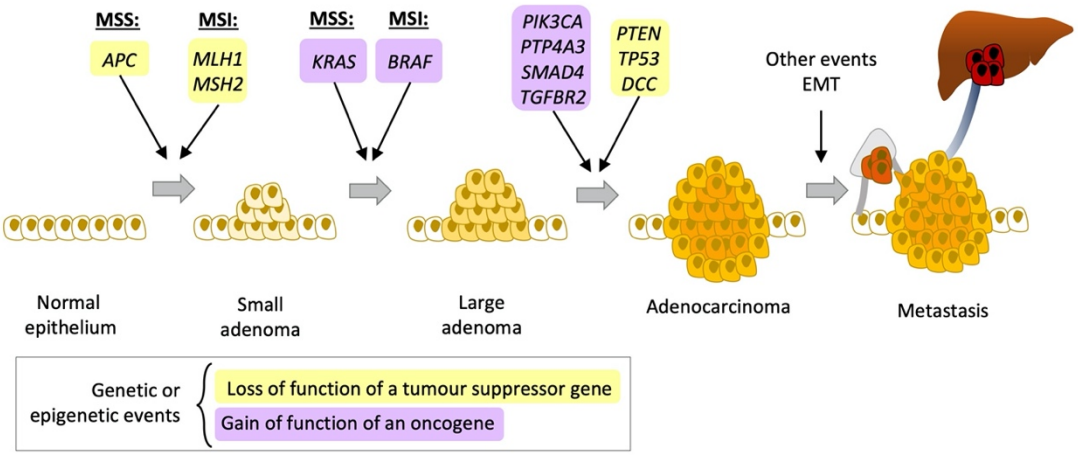

Figure 2.1.2. Colorectal cancer carcinogenic cascade. Schematic representation of the sequence of mutations that have been established to be more common in colorectal cancer. All abbreviations are listed in section 1.

On the other hand, colorectal cancers that start with germinal mutations or hypermethylation in the mismatch repair system genes present a loss of function of proteins that repair DNA mismatches (mainly *MLH1*, *MSH2*, *MSH6*, and *MS2* genes). Therefore, tumours present microsatellite instabilities, which implies frequent mutations at every cell division. In the case of MSI and differing from the MSS colorectal carcinogenesis, where *KRAS* was the most frequent oncogene mutated, the oncogene *BRAF* is normally mutated, which is a serine/threonine kinase also in the MAPK/ERK signalling pathway. Then, due to the microsatellite instability, the steps of the carcinogenic cascade, in that case, are not that clear and there are many more genes that can be affected and lead the adenoma to invasive carcinoma. Some mutations are the same as the ones that can be found in MSS carcinogenesis, such as gain of *PIK3CA* or loss of *TP53*. Another frequently mutated oncogene is the *TGFβR2* (Transforming Growth Factor Beta Receptor 2), which encodes for a transmembrane protein that binds TGFβ and activates a pathway related to cell proliferation, wound healing, immunosuppression and tumorigenesis. Other possible mutations are found in *IGF2R* (Insulin Like Growth Factor 2 Receptor), *BAX* (BCL2 Associated X Apoptosis Regulator), *E2F4* (E2F Transcription Factor 4), or *MRE11A* (Double-Strand Break Repair Protein MRE11A) (De Smedt et al., 2015).

2.1.3.4 Signalling pathways altered in colorectal cancer

One of the most frequently altered pathways in colorectal cancer is the Wnt/β-catenin pathway, where APC takes part. This pathway is required mainly for developmental processes that imply asymmetric cell proliferation or migration and it is expressed in the adult tissues that need regeneration such as skin or intestine. Precisely, Wnt signalling is expressed in the crypt stem cell compartments from the intestinal lumen. Wnt is an extracellular factor that binds its receptor frizzled (FZD) and low-density lipoprotein receptor-related protein (LRP), which then activates DVL protein that inhibits GSK3β. In turn, GSK3β is no longer able to phosphorylate β-catenin, which dissociates from the APC complex (formed by AXIN, APC, CK1, and GSK3) and goes to the nucleus where it removes expression repressors as Groucho and activates transcription factors as the T-cell transcription factor (TCF) or the lymphoid enhancer factor (LEF), activating the expression of *MYC*, *Jun*, *CCND1* (that codes for cyclin D1), *EGFR*, *CD44*, *CD133*, and leucine-rich repeat-containing receptor 5 (*LGR5*). Loss-of-function mutations in *APC*, observed in 80% of colorectal cancer cases, imply an abnormal and constitutive activation of the pathway. Other possible mutations are found in *CTNNB1* (β-catenin gene) or *AXIN* for 5-10% of the cases (Novellasdemunt et al., 2015).

Another usually overexpressed pathway in colorectal cancer is the EGFR/MAPK signalling pathway, which is usually related to proliferation and survival of normal cells. Epidermal Growth Factor Receptor (EGFR) is the transmembrane tyrosine kinase receptor (RTK) receptor that is activated by its ligand Epidermal Growth Factor (EGF). This and other growth-

factor receptors are upstream of MAPK pathways, that are characterised for consecutive phosphorylation of its members, starting with small GTPases that include HRAS, NRAS, or KRAS. The binding of the complexed form by the growth factor receptor bound protein 2 (Grb2) and the son of sevenless (SOS) to the phosphorylated tyrosine residues of EGFR activates RAS-GTP. After its activation, RAS-GTP activates through phosphorylation RAF, MEK, and ERK, which finally goes to the nucleus and activates many transcription factors related to cell growth, differentiation and survival. Aberrant expression of this pathway is very common in colorectal cancer, normally coming from a constitutively activated KRAS, but also overexpression of EGF or B-Raf (Mizukami et al., 2019).

The PI3K/Akt pathway is another important signalling pathway for cell growth and differentiation that is also activated by EGFR. Phosphatidylinositol 3-kinase (PI3K) class Ia is the most implicated type in cancer and it is formed by two subunits, one of them is *PIK3CA*, an oncogene commonly mutated and overexpressed in colorectal cancer. PI3K is recruited by Grb2 when EGFR is active and its function is to convert Phosphatidylinositol 4,5-bisphosphate (PIP_2) to Phosphatidylinositol (3,4,5)-trisphosphate (PIP_3), that in turn binds to PH domain of Akt that phosphorylates and inhibits TSC2. When TSC2 is not active, it stops the repression of RAS homolog enriched in brain (RHEB), a GTPase that subsequently activates mTORC1, a complex that when it is activated it phosphorylates S6K and 4EBP, that ultimately activate the ribosomal protein S6 and the transcription factor ELF4 that regulate and activate the expression of genes related to cell growth, protein synthesis, autophagy and angiogenesis. Apart from the overexpression of *PIK3CA* gene, colorectal cancer cases also report loss of function of Phosphatase and tensin homologue protein (PTEN), which represses the pathway by dephosphorylating PIP_3 or hyper-activation of the mTORC1 complex (Papadatos-Pastos et al., 2015).

The TGFβ signalling pathway is another signalling pathway relevant in colorectal cancer progression, that is also involved in cell proliferation, differentiation, migration, apoptosis and adhesion. TGFβ signalling can promote apoptosis and differentiation of epithelial cells and it is lost in some colorectal cancer cases, what makes TGFβ be considered a tumour suppressor. However, in the late stages of colorectal cancer, it was also observed to be highly expressed, acting as an oncogene. The TGFβ receptors are located in clathrin-rich membrane domains, which facilitates its internalisation of the receptors when the TGFβ ligand is present. TGFBR2 is the receptor that binds to the ligand and recruits TGFBR1 that phosphorylates and activate R-SMAD proteins, which form a complex with SMAD4 and translocate into the nucleus to regulate the transcription of the target genes, including CDKN1A, CDKN1B and CDKN2B, which are checkpoint genes that cause cell proliferation arrest. In 20-30% of colorectal cancer cases, loss of function of TGFBR2 or SMAD4 is found at late stages (Jung et al., 2017).

Finally, the Notch signalling pathway is important for the cell-to-cell interaction and maintain intestinal development and homeostasis by regulating the differentiation of stem cells. It has been observed to be overexpressed in colorectal cancer at primary stages and it is mainly conceived as an oncogenic pathway, but in some cases, it acts also as a tumour suppressor, depending on the context. The Notch ligands are endocytosed by Mind bomb-1 (Mib1) and E3 ubiquitin ligase and bind to Notch receptors, which lead to certain conformational changes. The extracellular domain of the Notch receptor is removed by ADAM through interaction with the S2 cleavage site, one of the extracellular domains of the Notch receptors, and the transmembrane domain is removed by γ-secretase at the S3 cleavage site, giving to the release of NICD (Notch intracellular domain), the intracellular domain. NICD is translocated into the nucleus and binds to the transcription factor CSL that forms a complex with MAML and induces the expression of the targets genes such as Hes family (Vinson et al., 2016). One of the observed roles of cell-to-cell interaction via Notch signalling and the VCAM1 adhesion molecule is to facilitate the extravasation of tumour cells through the endothelial cells that are around the tumour or have arrived via angiogenesis (Wieland et al., 2017).

2.1.3.5 Diagnosis and staging of colorectal cancer

As explained before, the early diagnosis of colorectal cancer is of great importance for the survival of the patients. Among the 30% of colorectal cancer cases that are hereditary, 5% are known hereditary syndromes and therefore, are easily predicted. Another 25%, have some family background, although any specific genetic background is described, and the rest 70% of cases are considered sporadic, and therefore, unpredictable. For that reason, population screening is very important, and programs of colonoscopies or faecal occult blood test have been implanted in some sanitary systems.

Optical colonoscopy is still the most reliable diagnostic method and has the advantage that it allows to both detect, perform biopsies, and extract polyps if necessary. However, it is difficult to extend the technique to all population and it is invasive, requires anaesthesia and has some potential complications (Seward, 2019). An alternative for optical colonoscopy is computed tomography colonography, which is non-invasive and allows to explore the light of the colon as well. The faecal occult blood test is the more extent screening method and it is not invasive, although it has quite low sensitivity and false-negative results are too common, especially in early stages (Garcia et al., 2015). An improved version of this test is the faecal immunochemical test, that specifically detects human haemoglobin and at much lower concentration (Moss et al., 2017).

After diagnosis, the way of determining the stage to set the best treatment and prognosis is by an Endoscopic Biopsy and Computed Tomography with Intravenous Contrast, both for the local extension and possible metastasis. However, in order to better establish the local staging, a Magnetic Resonance and Endorectal Ultrasound have been proven to increase efficiency in the

diagnosis. Another important diagnosis and staging technique is Positron Emission Tomography with ^{18}F-fluorodeoxyglucose (Macrae and Bendell, 2020).

The information of all these methods allows establish the stage of the disease following the tumour, node, metastasis (TNM) staging system, which is the preferred staging for colorectal cancer. The last version of the TNM system is represented in Table 2.1.1 (Amin et al., 2017; Puppa et al., 2010). Tumour (T) describes the size and how deeply has it grown into the intestine layers. Node (N) describes the regional lymph node affectation, whether the tumour has spread into them. Metastasis (M) describes spreading to other parts of the body, which implies distant metastasis for example to the liver or lungs. The TNM system has good prognosis correlation and facilitates treatment planning. However, the location in the colon or the rectum, the type of cancer evaluated through molecular characterisation as well as other health conditions also need to be taken into account.

	Primary tumour (T)
TX	The primary tumour cannot be evaluated
T0	No evidence of tumour in the colon or rectum
Tis	Carcinoma *in situ*, tumour found in intraepithelial or lamina propia
T1	The tumour invades submucosa
T2	The tumour invades muscularis propia
T3	The tumour growths through the muscularis propia into the subserosa or into the pericolorectal tissues
T4a	The tumour penetrates visceral peritoneum surface
T4b	The tumour invades and adheres to other organs or structures
	Regional lymph nodes (N)
NX	The regional lymph node cannot be evaluated
N0	There is no spread to the regional lymph nodes
N1a	There is one regional lymph node with tumour cells
N1b	There are 2 or 3 regional lymph nodes with tumour cells
N1c	There are nodules of tumour cells found in structures that are not lymph nodes such as mesenteric tissues or pericolorectal tissues.
N2a	There are 4 to 6 regional lymph nodes with tumour cells
N2b	There are more than 7 reginal lymph nodes with tumour cells
	Distant metastasis (M)
M0	There is no distant metastasis
M1a	Cancer has spread to one distant site or organ
M1b	Cancer has spread to 2 or more distant sites or organs
M1c	Cancer may have spread to distant organs and it has spread to peritoneum

Table 2.1.1. TNM system. Tumour, Node, Metastasis (TNM) system for the staging of colorectal cancer. Extracted from (Amin et al., 2017; Puppa et al., 2010).

Apart from the TNM, the overall stage (I-IV) is also used, representing non-invasive carcinoma (Tis) in stage 0, a developed tumour with good prognosis in stage I (T1 or T2) and with no metastasis (N0 and M0). Stage II is subdivided into three categories that all represent primary tumour with invasive characteristics but with no metastasis (N0 and M0): stage IIA (T3), Stage IIB (T4a), stage IIC (T4b). Then, stage III represents tumour with metastasis in regional lymph nodes but not metastasis in distant organs, also is subdivided into stage IIIA (T1/2+N1/N1c or T1+N2a), stage IIIB (T3/4a+N1/N1c or T2/3+N2a or T1/2+N2b) and stage IIIC (T4a+N2a or T3/4a+N2b or T4b+N1/2). Finally, stage IV is related to metastasis to distant organs and a poor prognosis and is also divided into three subcategories that correspond to the three M categories, i.e. stage IVA (T1-4+N1-2+M1a), stage IVB (T1-4+N1-2+M1b), stage IVC (T1-4+N1-2+ M1c).

Additionally, genomic biomarkers are currently used in clinical practices, especially in the case of metastatic cancers. To date, mainly MSI determination and mutational status of *RAS* and *BRAF* are used to design therapies and predict the response (see section 2.3.1.3). When genotyping tumours, tissue biopsies are generally used, but also the recently established liquid biopsy is being applied for genotyping circulating tumour DNA (ctDNA). The clear advantage of liquid biopsy is the non-invasiveness as well as the frequency at which it can be made, which allow not only diagnosis and prognosis but also monitoring of the treatment as well as assessing residual disease (Siravegna and Bardelli, 2016). Beyond genotyping, the liquid biopsy also allows the determination of circulating tumour cells (CTCs), which are cells that have escaped from the primary tumour and are susceptible to form a metastasis. CTCs determination is also an emerging practice to predict prognosis as well as chemoresistance if ex vivo studies are performed (Tsai et al., 2016).

Furthermore, five years ago, an international consortium compiled large amounts of multi-omics data and established the consensus molecular subtypes (CMS) of colorectal cancer (Guinney et al., 2015). According to them, there are four molecular subtypes, each related to certain genetic mutations and many other factors. The CMS1, accounting for 14% of the cases is the subtype that corresponds to MSI colorectal cancers with *BRAF* mutations and is characterised by being hypermutated and have a strong presence of immune cells. The CMS2 is the most common subtype and accounts for the 37% of the cases, it has epithelial characteristics and Wnt and MYC overactivation. The CMS3, with 13% of prevalence, is also epithelial and has a strong metabolic component as well as *RAS* mutations. Finally, the CMS4 represents the 23% of cases and has mesenchymal characteristics, invasion and angiogenic capacity and TGFβ activation, and normally the worse prognosis. However, the clinical utility of the CMS is still not clear, especially when dealing with metastatic colorectal cancer patients (Fontana et al., 2019). Therefore, it is even more urgent the need for specific and accurate therapies for metastasis in colorectal cancer.

2.1.3.6 Colorectal cancer metastasis

In the case of colorectal cancer, the liver is the most common site of metastasis, as the majority of the intestinal mesenteric drainage is directed to it through the hepatic portal venous system. Approximately 50% of colorectal cancer patients develop a metastatic disease to the liver. At that stage, if possible, hepatic resection is an option for potential cure combined with adjuvant chemotherapy (see section 2.3.1.3). However, 70% of patients develop recurrence, which is difficult to prevent. As explained in the previous section, molecular genotyping helps to identify and detect patients that are prone to recurrence and will benefit from adjuvant treatment (Zarour et al., 2017).

Other parts of the body that can be invaded by colorectal cancer are the thorax cavity, with an especially high frequency in rectal cancer at early stages, the peritoneum cavity, the bone, the lung, the nervous system, among other organs. Overall, the frequency of colorectal cancer metastasis to other sites is 38% in front of 62% in the liver. Furthermore, metastasis can occur to more than one site, especially when it is found in other organs. Lung metastases, for example, occur together with liver metastasis (in 73% of the cases in colon cancer), or else are often present in patients with nervous system metastasis (in 54% of the cases in colon cancer) (Riihimäki et al., 2016). Liver or other distant metastasis were originally thought to be originated by cells that previously spread to the lymph nodes, and that explained the mechanistic basis of the TNM staging system. However, recent discoveries underly that only 35% of the tumour cells that reached other organs had the same subclonal origin and the other 65% of liver metastasis are from different subclonal origin, suggesting that are metastasis independently originated directly from the primary tumour (Naxerova et al., 2017).

In case of a carcinoma such as colorectal cancer, tumour cells have an epithelial origin and therefore, to migrate and reach the blood vessels, EMT is thought to be a necessary step for metastasis. EMT in colorectal cancer is observed to be initiated by Wnt, TGFβ, or RAS signalling (Pretzsch et al., 2019) as well as other EMT-related transcription factors (see section 2.1.2.3). Also, microRNAs have been observed to regulate EMT in colorectal cancer, such as downregulation of miR-200 that allows the overexpression of ZEB1, or downregulation of miR-34a that leads to Notch signalling (Zhang et al., 2017), another crucial pathway in metastatic initiation of colorectal cancer (section 2.1.3.4). Other pathways associated with colorectal cancer metastasis are p53, NF-κB, COX, or JAKs/STAT3 (Koveitypour et al., 2019). Regarding the specific mechanisms that are observed to be implicated with liver metastasis from colorectal cancer, IL8 and its receptors have been observed to play a significant role in the establishment of the pre-metastatic niche in the liver and act as chemoattractants for CTCs from the colon (Bie et al., 2019).

2.2 METABOLIC REPROGRAMMING IN CANCER AND METASTASIS

2.2.1 METABOLIC PATHWAYS ALTERED IN TUMOUR CELLS

2.2.1.1 Otto Warburg and the first contributions to cancer metabolism

Cancer metabolic reprograming is nowadays considered as an important hallmark of cancer and it has received every time more attention from cancer researchers for the last two decades and many metabolic pathways and enzymes have been established to be altered in cancer (Figure 2.2.1). However, almost a hundred years ago, Otto Heinrich Warburg was the first to observe a different metabolism of cancer cells compared to other tissues. Specifically, he observed

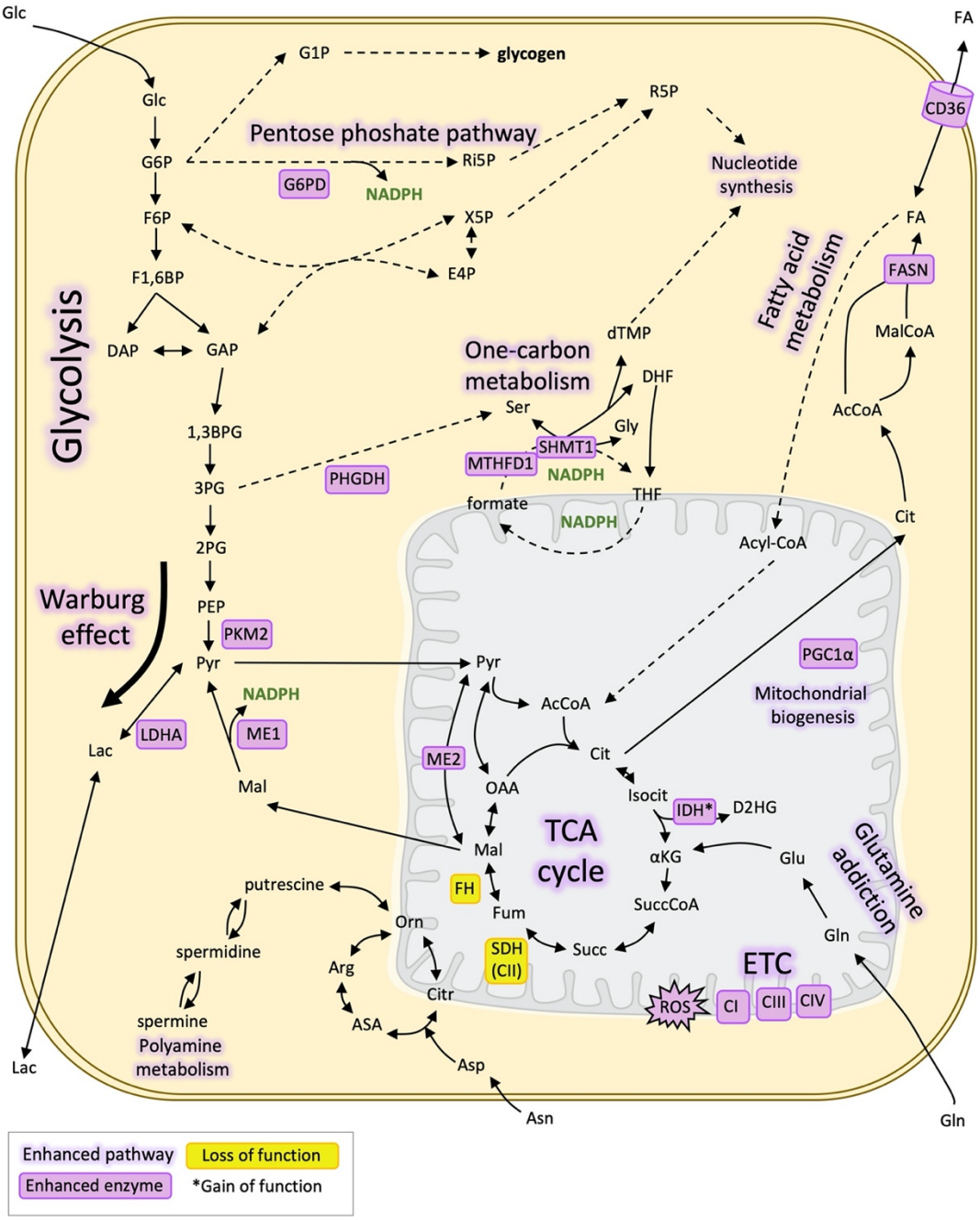

Figure 2.2.1. The main metabolic alterations in cancer. Schematic representation of the main metabolic pathways and metabolic enzymes altered in cancer. All abbreviations are listed at section 1.

that cancer cells had an enormous increase in glucose uptake and lactate production, even in the presence of oxygen (Warburg, 1925), and lately postulated that a dysfunctional mitochondria was also a feature of cancer cells (Warburg, 1956). However, Crabtree and other authors later discovered that respiration in cancer cells was not always inactive and that Warburg effect was compatible with an active mitochondrial metabolism (Crabtree, 1929).

Nowadays, it is widely accepted that the Warburg effect, understood as aerobic glycolysis, is one of the main metabolic adaptations of cancer cells. Although complete oxidation of glucose would be more efficient than glycolysis alone because it allows the synthesis of 36 molecules of ATP from 1 molecule of glucose, the rate of glycolysis and lactate production occurs 50 times faster than complete oxidation. It allows generating great amounts of ATP that are needed for the great energetic demand of proliferating cells (Slavov et al., 2014). Furthermore, the continuous lactate secretion decreases the pH of the tumour microenvironment, which involves malignant phenotype and immune evasion (Liberti and Locasale, 2016).

Another advantage of the increased glycolytic flux is the larger availability of glycolysis intermediates for biosynthetic pathways that also need to be increased in proliferating tumour cells such as the pentose phosphate pathway (PPP) that produces ribose-5-phosphate for nucleotide synthesis. Glucose-6-phosphate dehydrogenase (G6PD), the rate-limiting enzyme of the oxidative branch of the PPP, produces nicotinamide adenine dinucleotide phosphate (NADPH), and therefore is also one of the main contributors to redox balance. Then, the non-oxidative pathway of the PPP, which is the part of the pathway that finally generates ribose-5-phosphate, has transketolase (TKT) as the rate-limiting enzyme. Both enzymes, G6PD and TKT, are overexpressed in some types of cancer such as breast cancer and play a key role in metabolic reprogramming (Benito et al., 2017).

Apart from the pentose phosphate pathway, hexosamine pathway has recently been described to be altered in melanoma and other types of cancer. From fructose-6-phosphate, it generates uridine diphosphate N-acetylglucosamine, a substrate for protein glycosylation (de Queiroz et al., 2019). Additionally, serine biosynthesis from 3-P-glycerate is also of great importance in cancer due to its participation in one-carbon metabolism, generating methyl donors for nucleotide and amino acid biosynthesis as well as NADPH. The first enzyme of serine biosynthesis from glycolysis, 3-phosphoglycerate dehydrogenase (PHGDH), is overexpressed in many types of cancer (Jia et al., 2016; Locasale et al., 2011).

The last enzyme of glycolysis, pyruvate kinase (PK), catalyses the conversion from phosphoenolpyruvate and ADP to pyruvate and it is one of the enzymes that control the rate of the flux. The M2 isoform of his enzyme (PKM2), which is normally expressed during embryonic development, is also expressed in cancer cells. This isoform allows reducing the flux with respect to other isoforms, allowing the accumulation of glycolytic intermediaries for biosynthetic purposes (Ye et al., 2012). Furthermore, the PKM2 has other non-canonical functions that imply

cell cycle regulation and extracellular signalling that may promote metastasis (Hsu and Hung, 2018).

2.2.1.2 Beyond Warburg effect: Mitochondrial activity

The mitochondrial activity of cancer cells has always been in controversy. There are many examples in the literature of impaired mitochondria as an advantage for tumour cells (Hsu et al., 2016), as it was first postulated by Warburg. For example, mitochondrial DNA mutations are one of the drivers of mitochondrial defective phenotypes that are common in oncocytomas, benign tumours of most epithelia such as the renal epithelia (Joshi et al., 2015). Mutations in mitochondrial tricarboxylic acid (TCA) cycle enzymes such as succinate dehydrogenase (SDH), fumarate hydratase (FH), or isocitrate dehydrogenase (IDH) also cause deficiencies in mitochondrial activity (Zong et al., 2016). A study with fumarate hydratase deficient renal cancer cells reveals that the reductive carboxylation of glutamine supports tumour growth (Mullen et al., 2011). Another observation of mitochondrial activity impairment is in the case of p53-deficient cells that present diminished cytochrome c oxidase activity (Zhou et al., 2003). Furthermore, mitochondrial dysfunction has also been recently identified to promote cellular signalling related to EMT and cellular remodelling (Guerra et al., 2017).

However, being mitochondria the centre of energy production and anabolic growth, the most common mitochondrial phenotype in cancer is considered to be overactivated mitochondria, with high activity of the Krebs cycle, which provides intermediaries for biosynthetic pathway and allows complete oxidation of many substrates. Subsequently, also a high activity of the electron transport chain (ETC) to allow mitochondrial respiration as well as mitochondrial one-carbon metabolism is frequently observed in cancer cells (Zong et al., 2016). In the aforementioned example of mitochondrial DNA mutations that causes benign tumours, it is observed that these tumours have limitations in tumour growth, suggesting that respiration is needed for further tumour cell proliferation (Joshi et al., 2015). Apart from energy and building blocks, the mitochondrial activity also generates reactive oxygen species (ROS), that are thought to be essential for tumorigenesis (Weinberg et al., 2010; Xian et al., 2019). Mitochondrial biogenesis, driven by Peroxisome Proliferator-Activated Receptor Gamma Coactivator 1-Alpha (PGC-1α) is also considered to promote tumorigenesis in epithelial cancers such as breast cancer and other cancer types (Bost and Kaminski, 2019; Salem et al., 2012).

TCA cycle is a crucial pathway for cancer cells, especially for the generation the building blocks that will be important for biosynthetic pathways. However, as explained before, some types of cancer display mutations in its enzymes. Gliomas or acute myelogenous leukaemia commonly have mutations in IDH1 or 2, which generates D-2-hydroxyglutarate (D2HG), a reduced form of α-ketoglutarate, considered to be an oncometabolite (Dang et al., 2009; Ye et al., 2018). High levels of it interfere with many processes such as hydroxylation or histone

demethylation, that finally alters gene expression or epigenetic estate of differentiation programs, contributing to tumour development (Lu et al., 2012). Fumarate and succinate can also be considered as oncometabolites in certain types of tumours that present loss-of-function mutations in FH or SDH, respectively (Baysal et al., 2000; Tomlinson et al., 2002). Both fumarate and succinate have similar effects as D2HG as they display nonmetabolic functions such as epigenetic regulation (Martínez-Reyes and Chandel, 2020; Xiao et al., 2012).

2.2.1.3 Glutamine addiction and other amino acid addictions

Glutamine is the second most consumed nutrient after glucose. The main reason for that is the nitrogen source that glutamine represents for *de novo* biosynthesis of amino acids and nucleic acids, although its contribution as a carbon source is also important. Harry Eagle was the first to describe the high demand for glutamine in HeLa cells (Eagle et al., 1956). Nowadays it is widely conceived that glutamine addiction is one of the main characteristics of cancer metabolic reprogramming, with evidence of increased expression of glutamine transporters (SLC1A5), glutaminase (GLS) glutamate dehydrogenase (GLUD) and transaminases (Still and Yuneva, 2017).

Once inside the cell, and before being transformed to glutamate, glutamine itself is incorporated in the amino acid pool, as well as purine and pyrimidine synthesis and hexosamine biosynthesis pathway as a nitrogen donor. In turn, glutamate from glutamine has many fates such as taking part of glutathione, which is implicated in ROS homeostasis, proline biosynthesis and other amino acids biosynthesis through the aminotransaminase reactions as a carbon donor, such as serine, alanine, and aspartate. Glutamate is also transformed into α-ketoglutarate, which enters to TCA cycle, both in oxidative or reductive ways, depending on the cancer cell context. All these roles of glutamine are essential for cancer development, especially for KRAS-driven cancer cells (Bernfeld and Foster, 2019; Scalise et al., 2017).

However, recent discoveries suggest that other amino acids are equally important as glutamine for cancer cells, or else become critical in case of glutamine deprivation (Vettore et al., 2020). This is the case of asparagine, which has a similar structure with glutamine and can serve as a nitrogen and carbon donor at a similar way to glutamine, restoring the effects of glutamine deprivation associated apoptosis (Pavlova et al., 2018; Zhang et al., 2014). Arginine is another amino acid that becomes essential in some contexts as it is a good nitrogen source for many compounds such as polyamines and creatine. Another amino acid that also becomes a nutrient source under when other substrates are limited is proline, that can be derived from collagen, as it is observed in pancreatic ductal adenocarcinoma (Olivares et al., 2017). Cysteine, the rate-limiting enzyme for glutathione formation has also been discovered to promote tumorigenesis and sustain tumour proliferation probably for its contribution into redox homeostasis (Combs and DeNicola, 2019; Jiang et al., 2017). Finally, serine and glycine are another two amino acids that have recently

grabbed attention as they are direct substrates for one-carbon metabolism (Jain et al., 2012; Yang and Vousden, 2016).

2.2.1.4 One-carbon metabolism and redox balance

One-carbon metabolism consists in several reactions that transfer one-carbon units for a biosynthetic process that mainly include synthesis of purines and thymidine, methylation processes, redox homeostasis and control of the level of the amino acids glycine, serine, and methionine. The dihydrofolate-tetrahydrofolate cycle (or simply folate cycle) is the central pathway of one-carbon metabolism and it is compartmentalised between the cytosol and the mitochondria, where serine and glycine are directly implicated through the enzyme serine hydroxymethyltransferase 1 and 2 (SHMT1 and 2), cytosol and mitochondrial forms, respectively, although they are functionally redundant (Anderson and Stover, 2009). The enzyme catalyses the conversion between 5,10-methyltetrahydrofolate (5,10-meTHF) and THF with a single carbon derived from serine to glycine. There are some types of cancers such as breast or intrahepatic cholangiocarcinoma where SHMT2 overexpression is related to poor survival and prognosis (Ning et al., 2018; Zhang et al., 2016).

The other enzyme of the core folate cycle is methylenetetrahydrofolate dehydrogenase, methenyltetrahydrofolate cyclohydrolase and formyltetrahydrofolate synthetase 1, 1L or 2/L (MTHFD1, 1L, or 2/L). It is a multifunctional enzyme that completes the cycle with the interconversion between 5,10-meTHF, 10-formylTHF and formate. In the cytosol, the reactions are localised in only one enzyme (MTHFD1), while in the mitochondria there are two enzymes, MTHFD2/L, MTHFD1L. As SHMT1/2, this enzyme also appears to be upregulated in many types of cancers such as breast cancer or AML (Nilsson et al., 2014; Pikman et al., 2016).

Apart from the folate cycle, there are many other reactions in one-carbon metabolism that end up with the formation of purines, thymidine and methionine. The methionine cycle is considered another critical component of the one-carbon metabolic network implicated in cancer as it contributes to methylation reactions (Sanderson et al., 2019). DNA and RNA methylation in cytosine residues is of great importance for epigenetic mechanisms. For example, DNA hypermethylation of certain tumour suppressor genes is the cause of its loss of function. tRNA methylation is another recently discovered modification that stabilises and promotes translation (Shima et al., 2017). Histone methylation is another mechanism of gene expression regulation and some of the specific modifications are known to be activators (such as trimethylation of histone 3 at lysine 4, H3K4me3) or repressors (such as methylation of histone 3 at lysine 27, H3K27) of gene expression, although there are other multiple modifications that are still not characterised. Finally, another pathway directly branched from the methionine cycle and involved in rapid cell proliferation is polyamine metabolism. Overexpression of its enzymes has been

associated with cancer progression, especially ornithine decarboxylase (OCD) and adenosylmethionine decarboxylase 1 (ADM1) (Casero et al., 2018).

One-carbon metabolism has another important role in redox homeostasis that is shared also with other pathways such as PPP or malic enzyme, which is the production of NADPH from $NADP^+$, an important molecule for antioxidant defence. Specifically, the enzyme MTHFD1 and its mitochondrial forms of the folate cycle modulate mitochondrial and cytosolic NADPH levels. As explained before, in most cancer cells mitochondria is highly active and the electron transport chain with high levels of oxygen consumption produces ROS that is able to modify and damage cellular components. However, antioxidants such as ascorbic acid or glutathione are able to revert these modifications by its oxidation through enzymes such as superoxide dismutases (SOD), catalases, peroxiredoxins and glutathione peroxidases (GPX). Then, NADPH plays an important role in reducing these antioxidant molecules and restoring its antioxidant capacity, which is of great importance in proliferating tumour cells that have an increased ROS production, and therefore they need to avoid ROS-induced cell death (Panieri and Santoro, 2016). However, it is observed that most cancer cells show higher levels of ROS than normal cells, and these mild levels of ROS are needed for activation of signalling pathways involved in tumour progression (Hornsveld and Dansen, 2016) (see section 2.2.2.2).

Therefore, the role of amino acids and one-carbon metabolism in cancer redox homeostasis has major significance (Vučetić et al., 2017). For that reason, cancer cells have a higher consumption of amino acids needed for the formation of glutathione (glutamate, glycine, and especially cysteine), as well as higher activity of one-carbon metabolism enzymes that maintain high $NADPH/NADP^+$ ratios or its synthesis, especially consumption of serine. Glucose consumption also would contribute to redox homeostasis both for its contribution to the oxidative branch of PPP and serine synthesis. The conversion of malate to pyruvate in the cytosol by malic enzyme also produces NADPH and it is essential in certain scenarios such as glucose- or serine-restricted conditions and p53 suppression (Jiang et al., 2013; Maddocks et al., 2013; Murai et al., 2017).

2.2.1.5 Lipid metabolism

Among the metabolic demands proliferating cancer cells have, there is the need for phospholipid synthesis for membrane formation at every cell division. Both fatty acid uptake and endogenous biosynthesis are necessary for cancer cells and should be balanced depending on the conditions and the fatty acid availability at each moment. Moreover, lipid metabolism would also provide the cell with energy production and acetyl source for protein acetylation (Koundouros and Poulogiannis, 2020).

Depending on the cancer type, different enzymes of lipid metabolism are observed to be overexpressed. Enzymes of fatty acid synthesis, which are normally active only in liver and

proliferating tissues, are commonly overexpressed in many types of cancer (Khwairakpam et al., 2015; Li et al., 2017a). These are ATP citrate lyase (ACLY) is the first enzyme of fatty acid synthesis that catalyse the obtention of cytosolic acetyl-CoA from citrate, fatty acid synthase (FASN), which catalyses the synthesis of palmitate from acetyl-CoA and malonyl-CoA using NADPH, as well as stearoyl-CoA desaturase (SCD-1) that is involved in fatty acid desaturation, needed for phospholipid synthesis (Tracz-Gaszewska and Dobrzyn, 2019).

Fatty acid uptake is mediated by various transporters that are upregulated in cancer (Watt et al., 2019). These include fatty acid translocase (FAT) or CD36, fatty acid transport protein family (FATPs) and plasma membrane fatty acid-binding proteins (FABPpm). Specifically, in breast, ovarian, gastric, and prostate cancer increased CD36 expression has been associated with poor prognosis (Ladanyi et al., 2018). The accumulation of lipid droplets, cytoplasmatic organelles that store fatty acids is very common in cancer cells and serves to provide energy (through β-oxidation), maintain lipid homeostasis and prevent lipotoxicity. Fatty acid uptake and lipid droplets accumulation are particularly common in hypoxic cells, one of the metabolic scenarios that tumour cells would face and where lipid metabolism takes a prominent role (Munir et al., 2019).

Protein acetylation, and particularly histone acetylation is one of the main post-translational modifications that modulate cell signalling and gene expression linked with lipid metabolism. A source of acetyl-CoA is needed for Lysine Acetyltransferases (KATs) to catalyse this protein modification. The pool of acetyl-CoA comes β-oxidation of fatty acids, from citrate through ACLY, or directly from acetate through Acyl-CoA synthetase short chain family member 1/2 (ACSS1/2). Histone acetylation, as an epigenetic modification is known to affect gene expression. In general, hyperacetylated histones result in relaxed, open chromatin that in cancer cells would allow gene expression of proto-oncogenes, whereas hypoacetylated histones would result in repression of tumour suppressors (Audia and Campbell, 2016). Specifically, in cancer cells, it is common to find acetylation of H4 at lysine 16, which could have a potential prognostic value. Moreover, acetylation has been found to modify many metabolic enzymes that are important for cancer such as PKM2, G6PD, or LDHA (lactate dehydrogenase A chain) (Lv et al., 2011; Wang et al., 2014; Zhao et al., 2013).

2.2.2 THE CANCER METABOLIC REPROGRAMMING IN ITS CONTEXT

2.2.2.1 Signalling pathways and cancer metabolism

During tumorigenesis, the overexpression of oncogenes and the repression of tumour suppressor genes are responsible for changes in signalling pathways that ultimately regulate metabolic reactions among other processes (Seth Nanda et al., 2019). In other words, the metabolic reprogramming observed during tumour development is driven by altered signalling

pathways, resulting in oncogene-directed nutrient uptake and intracellular reprogramming. However, at the same time, alterations in metabolite levels or metabolic enzymes are able to modulate signalling pathways, causing metabolite-directed changes in cell behaviour and function (Pavlova and Thompson, 2016). Therefore, metabolic and signalling pathways are completely linked and interconnected during cancer development (Figure 2.2.2).

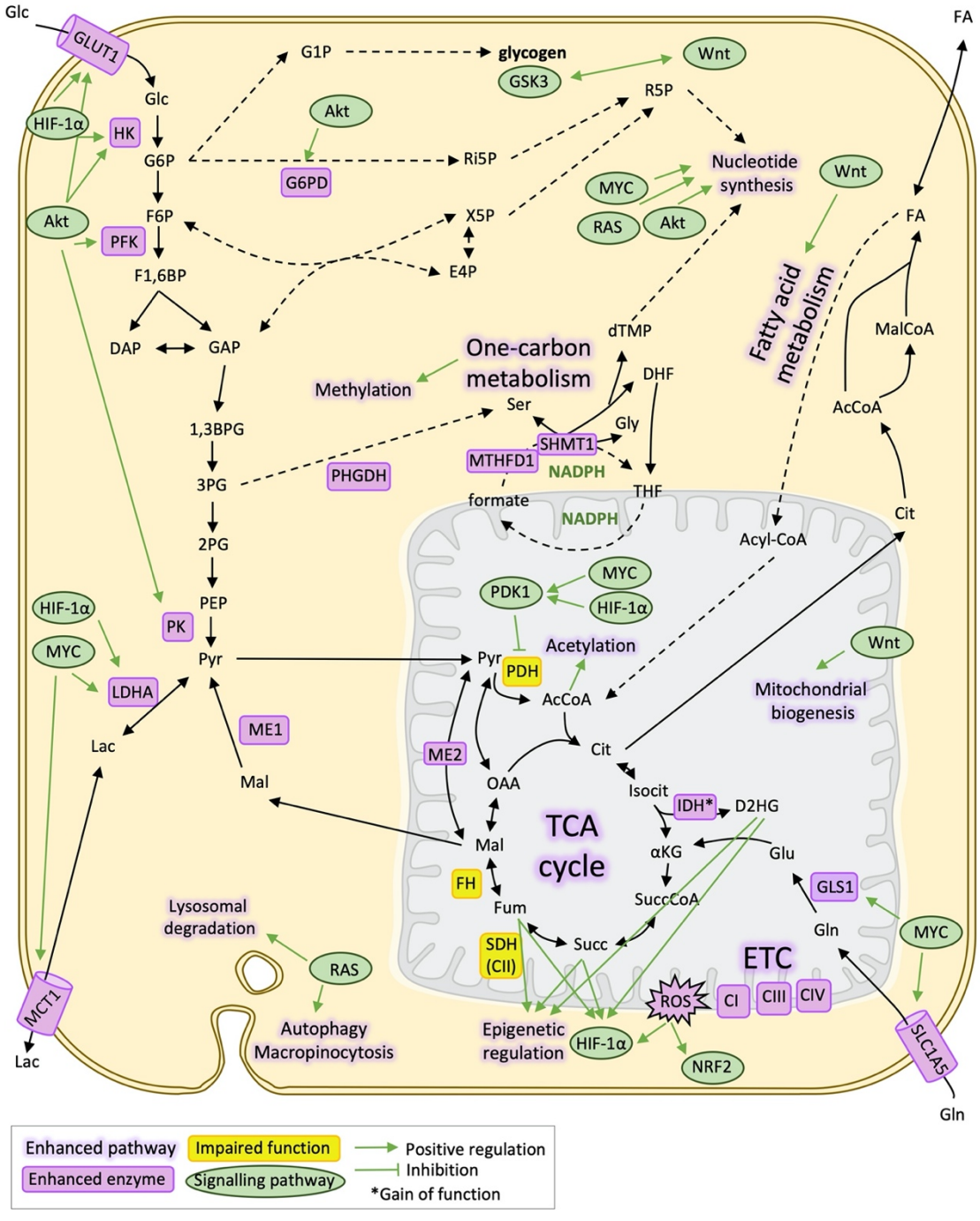

Figure 2.2.2. Relationship between metabolic reprogramming and signalling pathways in cancer. Schematic representation of the main metabolic pathways and metabolic enzymes altered in cancer and its relationship with signalling pathways that positively regulate them mainly through transcriptional activation. All abbreviations are listed at section 1.

The aberrant expression of growth factor signalling pathways stimulates substrates uptake. A clear example is PI3K/Akt signalling, which regulates glucose uptake by promoting the expression of glucose transporters (mainly GLUT1) and glycolytic enzymes such as hexokinase (HK) and phosphofructokinase (PFK), that together with PK are the three steps that control glycolytic flux (Hoxhaj and Manning, 2020). Also, MAPK/RAS signalling is found to regulate GLUT1 (Kimmelman, 2015). On the other hand, MYC pathway is the main driver of glutamine uptake (through its transporter SLC1A5) and glutaminolysis (through GLS1), promoting TCA cycle anaplerosis and also stimulating cysteine uptake as they exchange in the cysteine antiporter system xCT (Wise et al., 2008). MYC also regulates glucose metabolism as it increases the expression of LDHA, PDK1 and monocarboxylate transporter (MCT1), as well as enzymes of the nucleotide biosynthesis pathway (Goetzman and Prochownik, 2018). Wnt/β-catenin pathway is another pathway that drives metabolic reprogramming, as it has been observed to directly upregulate mitochondrial biogenesis as well as lipid metabolism (Vergara et al., 2017).

After tumorigenesis, when tumours are growing, it is frequent the appearance of hypoxic areas that lack vascular nutrient delivery. In these cases, few oxygen levels activate HIF1α signalling through the inhibition of Prolyl hydroxylases (PHDs) that in normal levels of oxygen degrades HIF1α through the proteasome (Semenza, 2013). However, not only hypoxia is able to inhibit PHDs and activate HIF1α but also oncometabolites such as succinate, fumarate, α-ketoglutarate, lactate, or high ROS levels have the same capacity. Therefore, it means that during tumour development HIF1α may be aberrantly activated without having reached a hypoxic state. In any case, HIF1α contributes to malignant progression activating the transcription of metabolic enzymes such as GLUT1 and 3, HK1 and 2, LDHA, or PKD1 (Kim et al., 2006; Papandreou et al., 2006), as well as angiogenic, cell survival, and cell proliferation-related genes (Masoud and Li, 2015; Al Tameemi et al., 2019). Furthermore, HIF1α signalling activates the import of unsaturated fatty acids from the surrounding to supplement the lack of fatty acid unsaturation and grow faster (Kamphorst et al., 2013).

Apart from upregulating transporters and metabolic enzymes of certain pathways, oncogenic signalling is also able to activate other modes of nutrient uptake. For example, RAS signalling, but not PI3K/Akt signalling, stimulates autophagy, lysosomal degradation of extracellular proteins and macropinocytosis, as well as phagocytosis of apoptotic cells (Guo et al., 2016; Schmukler et al., 2014). Autophagy-deficient cells are much more dependent on glutamine and other amino acids uptake (Zhang et al., 2018).

As mentioned before, a consequence of the overactivation of metabolic pathways is the accumulation of certain metabolites that have signalling roles. Among these metabolites there is acetyl-CoA as it is the substrate for acetylation and especially histone acetylation is very sensitive to its levels, thus, nutritional status (Carrer et al., 2019). Analogously, SAM levels are also determinant for DNA and histone methylation. Many enzymes such as deacetylases (sirtuins) and

demethylases (lysine-specific demethylase 1, LSD1) are also sensitive to the levels of its cofactors, NAD^+ and FAD, respectively (Wang et al., 2017b). α-ketoglutarate is also a key player in signalling as many dioxygenases need the α-ketoglutarate to succinate reaction to perform its function. Examples are TET DNA methylases, mRNA demethylases, Jumonji C histone demethylases and PHDs that regulates HIFα.

However, the metabolites that are considered to have a great effect on signalling during tumour development are the aforementioned oncometabolites. On one hand, the loss of SDH or FH results in an accumulation of succinate and fumarate, respectively, that inhibit dioxygenases by product inhibition, therefore leading to a global increase in DNA methylation or elevated levels of HIF1α among other alterations. On the other hand, the gain of function of IDH1 or 2 produces D2HG that also act as a competitive inhibitor of α-ketoglutarate dependent dioxygenases. As a consequence of D2HG increased levels, IDH-driven cancers display hypermethylation of CpG islands, similarly to SDH- and FH-deficient cancers with succinate or fumarate (Martínez-Reyes and Chandel, 2020). However, levels of D2HG have been also found in other types of cancers that do not display any mutation in TCCA cycle enzymes, such as triple-negative breast cancer driven by MYC (Terunuma et al., 2014). The L enantiomer of 2HG has also been found in clear cell renal carcinoma with similar inhibitory effects on dioxygenases as well as increasing response to hypoxia (Shim et al., 2014).

2.2.2.2 ROS signalling and homeostasis

As a result of the increased metabolic pathways, especially mitochondrial function, cancer cells present increased levels of ROS (Panieri and Santoro, 2016). At moderate levels, such ROS levels play an important signalling role in enhancing tumour development. ROS cause DNA damage and that contributes to generating genomic instability (Naik and Dixit, 2011; Vafa et al., 2002). Certain ROS levels are also able to inhibit phosphatases that are tumour suppressors such as PTEN and activate the transcription factors HIF1α and NRF2, as explained before, and therefore reprogramming metabolism and inducing inflammatory response (Sayin et al., 2017).

On the other hand, excess of ROS has damaging consequences that may underlie oncogene-induced cellular senescence and irreversible growth arrest. Therefore, one of the challenges for cancer cells is to manage ROS levels and compensate them. One of the mechanisms that cancer cells develop is the overexpression of PDK1 and repression of PDH phosphatase 2 (PDH2), described by many oncogenes such as MYC or HIF1α, that negatively regulates the activity of PDH, resulting in an attenuated entrance of pyruvate to TCA cycle and diminished activity of the electron transport chain and attenuated ROS levels (Kim et al., 2006).

However, cancer cells that increase ROS detoxification capacity will survive better to oxidant conditions. Increasing the expression or activity of antioxidant enzymes such as superoxide dismutatses (SODs), catalases, glutathione peroxidases, and thioredoxins could be

crucial for cancer cells. Most of them depend on the metabolite glutathione for its antioxidant capacity. Therefore, increasing glutathione synthesis (formed by glutamate, glycine, and cysteine) and recycling is also a manner of increasing antioxidant capacity (Bansal and Simon, 2018). For that reason, cancer cells increase GLS and GLUD1, as to increase the uptake glutamine and glutamate generation directly for glutathione synthesis and a source of nitrogen for glycine and cysteine formation (Vučetić et al., 2017). Also, glycine and especially cysteine uptake is increased as it is considered to be the rate-limiting enzyme for glutathione production (Combs and DeNicola, 2019; Gout et al., 1997; Prabhu et al., 2014).

Finally, the generation of NADPH is also important as it is the master reductant. Many antioxidant enzymes and glutathione recycling depend on NADPH levels. As explained before, in cancer cells, the metabolic pathways that generate NADPH are of great importance: Oxidative branch of PPP (Benito et al., 2017), cytosolic and mitochondrial isoforms of malic enzyme (ME1 and ME3, respectively) (Murai et al., 2017), cytosolic and mitochondrial isoforms of isocitrate dehydrogenase (IDH1 and IDH2, respectively) (Jiang et al., 2016a; Wise et al., 2011), and cytosolic and mitochondrial folate cycle (MTHFD1 and 2 enzymes, respectively) (Fan et al., 2014; Shin et al., 2017).

2.2.3 METABOLIC REPROGRAMMING UNDERLYING METASTASIS

2.2.3.1 Glucose metabolism and EMT

The research about metabolic reprogramming associated with the metastatic process is still widely unknown, although some researchers have been working in that specific field during the last few years. Such research has focused more on breast cancer metastasis than colorectal metastasis (Bu et al., 2018; Christen et al., 2016; Elia et al., 2019). The first step of metastasis, which is the transition of the metastatic stem cells from an epithelial to a mesenchymal state, has been observed to be accompanied by metabolic changes (Morandi et al., 2017) that frequently are similar to the metabolic reprogramming associated to tumorigenesis and tumour growing (Figure 2.2.3).

Glycolysis and glycolytic enzymes are enhanced when cells undergo EMT, as well as in CSC phenotype. Energetic and biosynthetic precursors demand in metastatic cells are equally or even more important than in differentiated non-tumorigenic cancer cells. It has been observed that GLUTs, LDH and MCTs favour the invasion capacity by interacting with invadopodium (Attanasio et al., 2011). The loss of the gluconeogenetic enzyme fructose 1,6-bisphosphatase (FBP) is associated with E-cadherin loss through Snai1 signalling (Dong et al., 2013). Loss of FBP implies higher flux through the glycolytic enzyme PFK, which is one of the enzymes that regulate glucose metabolism. Furthermore, the relationship between metabolic reprogramming and EMT inducing is also explained by other factors that induce both processes, which is the case

of TFGβ, TNFα signalling pathways as well as HIF1α. Induced by oxygen low levels in the less vascularised tumour zones or else or certain metabolites that are accumulated (see section 2.2.2.1), HIF1α induces EMT-related genes such as Snai1, Slug, and Twist and regulates the autocrine mobility factor (AMF), which is the secretion form of the glucose phosphate isomerase that also mediates EMT (Yang et al., 2017).

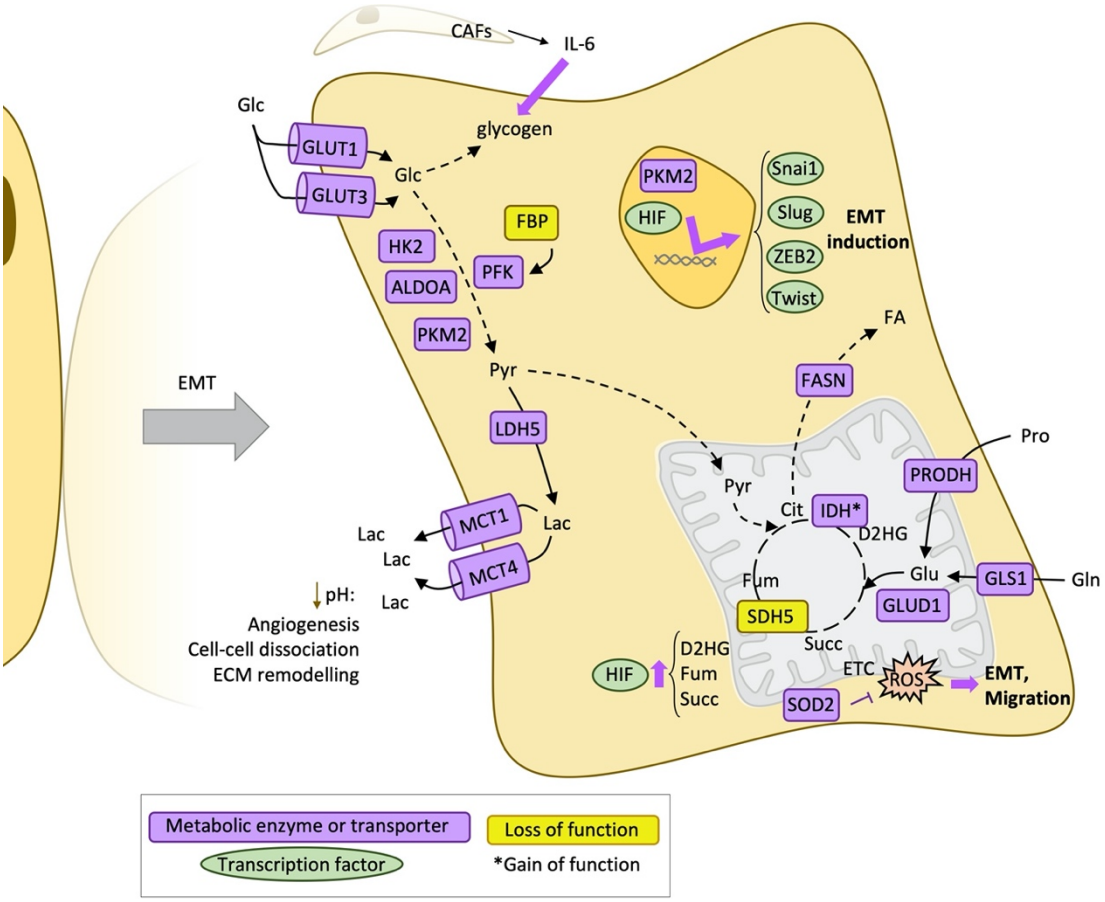

Figure 2.2.3. Metabolic reprogramming during epithelial-mesenchymal transition (EMT). Schematic representation of the main metabolic changes described during the epithelial-mesenchymal transition process. All abbreviations are listed in section 1.

The specific glycolytic enzymes that are related to the EMT process are GLUT1 and GLUT3, both associated with EMT transcription factors and matrix metalloproteases (MMP2) and correlated to poor prognosis. HK2, ALDOA, and PKM2, which are activated by HIF1α, are stimulated also by EMT transcription factors. Moreover, PKM2 is translocated to the nucleus and induce EMT through the upregulation of both ZEB2 and Snai1. In lower steps of glycolysis, the overexpression of enzymes that catalyse lactate production from pyruvate, as well as its transport such as LDH5, MCT1, and MCT4 also correlate with migration capacity, extracellular matrix remodelling and MMP2 (Izumi et al., 2011). Acidification of the surrounding extracellular environment caused both by an increased Warburg effect and by the overexpression of carbonic anhydrase IX (CAIX), also help to the first steps of the metastatic process. The effects of an acidic

extracellular pH include angiogenesis stimulation, adherents junctions dissociation, extracellular matrix remodelling through activation of hydrolases and MMPs (Kato et al., 2007; Suzuki et al., 2014). Moreover, acidification do not only occur in the core and hypoxic regions of the tumour but also in the invasive front, inducing an RNA splicing program that helps invasion (Rohani et al., 2019). The invasive front is not only formed by metastatic cells but also CAFs help in this process and induce invasion by secreting soluble factors that promote nuclear translocation of PKM2, HIF1α activation and ends up with upregulation of ZEB2 and Snai1 through miR-205 (Giannoni et al., 2015). In a model of ovarian cancer cells, CAFs help to mobilise the tumour cell glycogen through IL-6, CXCL10, and CCL5, promoting proliferation, invasion and metastasis (Curtis et al., 2019).

2.2.3.2 Mitochondrial metabolism and EMT

The evidence about mitochondrial alterations related to the invasion capacity and EMT are even more contradictory than the ones related to tumorigenesis and cancer cell growth. An example of that is the transcription factor PGC-1α that stimulates mitochondrial biogenesis. On one hand, in breast cancer, PGC-1α correlates with the formation of distant metastasis and it is observed to be overexpressed in invasive cells, promoting mitochondrial biogenesis, and enhanced mitochondrial activity (LeBleu et al., 2014), as well as overall bioenergetic capacity, flexibility and drug resistance (Andrzejewski et al., 2017). On the other hand, PGC-1α is observed to suppresses melanoma and prostate metastasis by a different pathway from biogenesis. PGC-1α interacts with ID2 and inactivates the transcription factor TCF4, which in turn inactivate genes related to metastasis such as integrins (Luo et al., 2016; Torrano et al., 2016).

Other contradictory results are about mitochondrial respiration associated with EMT. Both upregulation (Kordes et al., 2015) and downregulation (Gaude and Frezza, 2016) of the electron transport chain have been observed to be related to the acquisition of mesenchymal phenotype and invasion. Correspondingly, mitochondrial ROS production may induce EMT and migratory capacities through the activation of Src and Pyk2 (Porporato et al., 2014), although excessive ROS can lead to cell death, being therefore equally important the expression of SOD2 controlled by ZEB2 and NF-κB that would maintain ROS at levels that induce a mesenchymal phenotype (Kinugasa et al., 2015). Moreover, the overexpression of ME1, a NADPH producing enzyme, has been correlated to hepatocellular carcinoma (Wen et al., 2015). In cancers that have deregulated TCA cycle enzymes, accumulation of succinate, fumarate, or D2HG cause HIF1α stabilisation and epigenetic modifications that lead to overexpression of EMT transcription factors. For example, ZEB1 expression in the case of IDH-mutated gliomas or leukaemias is induced by D-2HG levels (Grassian et al., 2012). Finally, other TCA cycle enzymes that are related to EMT are SDH5, which acts as a tumour suppressor gene and SDH5 loss promotes

metastasis in lung cancers interacting with GSK-3β and inducing the inhibition of β-catenin (Liu et al., 2013).

2.2.3.3 Other pathways supporting EMT

Regarding amino acid metabolism, glutamine uptake and glutaminolysis have been related to EMT and metastasis (Lee et al., 2016; Liu et al., 2015). Another amino acid that could have similar roles than glutamine in the metastatic progression is asparagine, whose metabolisation by L-asparaginase and also synthesis asparagine synthase are correlated with invasive and metastatic potential in breast cancer cells (Knott et al., 2018). Proline is another example of amino acid that has been postulated to be important for metastasis formation, as its catabolism through proline dehydrogenase (PRODH) supports proliferation in 3D culture of breast cancer cells (Elia et al., 2017). Previous work of our research group has observed an enhanced amino acid uptake in CSC phenotype but not EMT phenotype in a model of prostate cancer (Aguilar et al., 2016).

Finally, lipid metabolism is also observed to be implicated in invasion and metastasis. The storage of produced lipids and cholesterol in lipid droplets and destabilisation of lipid rafts driven by FASN is associated with aggressiveness and maintenance of a mesenchymal state trough the induction of VEGF and TFGβ signalling (Beloribi-Djefaflia et al., 2016; Luo et al., 2017). However, diminished fatty acid synthesis could be also an advantage as it facilitates the availability of acetyl-CoA, implicated in the acetylation of histones that control genes that regulate EMT such as ZEB1/2 and mesenchymal markers such as N-cadherin and vimentin (Zhang et al., 2013). This is consistent with the observation that histone deacetylase inhibitors induce EMT genes in prostate cancer (Kong et al., 2012). Fatty acid uptake and lipogenesis (genes such as *CAV1*, *CD36*, *MLXIPL*, *CPT1C*, *CYP2E2*) are also associated with EMT of multiple cancer types and metastasis and poor prognosis (Nath and Chan, 2016; Pascual et al., 2017).

2.2.3.4 Antioxidant metabolism in CTCs

When cells finally reach circulation, they become detached. Normal detached cells compromise glucose uptake and result in depressed mitochondrial potential and decreased ATP levels. However, constitutively active Akt or other signals prevents a decrease in ATP levels triggered by the loss of cellular attachment (Grassian et al., 2011; Schafer et al., 2009). Detachment also causes an apoptotic cell death called anoikis (Paoli et al., 2013) induced by high levels of ROS. Specifically, it has been proved in a model of melanoma metastasis *in vivo* that high ROS levels and oxidative stress limited the observed distant metastasis (Piskounova et al., 2015). Therefore, enhanced antioxidant mechanisms allow the CTC to survive in circulation (Kreuzaler et al., 2019) (Figure 2.2.4).

For example, anchorage-independent cells were observed to be dependent on cytosolic IDH1 and produced citrate in a reductive carboxylation manner, that entered to the mitochondria and through IDH2 generated NADPH, which was necessary to compensate high ROS levels (Jiang et al., 2016b). Also, Erbb2 pathway, which was overexpressed in non-transformed mammary epithelial cells, increased survival of this cells by upregulating pentose phosphate pathway and also generating NADPH (Schafer et al., 2009), something that was also observed in metastatic pancreatic ductal adenocarcinoma cells, which displayed a dependence on the oxidative branch of PPP (McDonald et al., 2017b). Concurrently, glucose oxidation is diminished with matrix detachment, which attenuates the ROS levels that can be produced from the mitochondrial metabolisation of glucose (Kamarajugadda et al., 2012). Another antioxidant mechanism activated in CTCs is the increased expression of the activating transcription factor 4 (ATF4) and the nuclear factor-erythroid 2 related factor 2 (Nrf2) that induces heme oxygenase 1 (HO-1) that in turn help to diminish the concentration of prooxidant heme (Dey et al., 2015). An *in vivo* research proved that antioxidant mechanisms favour metastatic cells and specifically circulating tumour cells as mice bearing melanoma and treated by N-acetylcysteine (NAC) developed more metastasis (Le Gal et al., 2015).

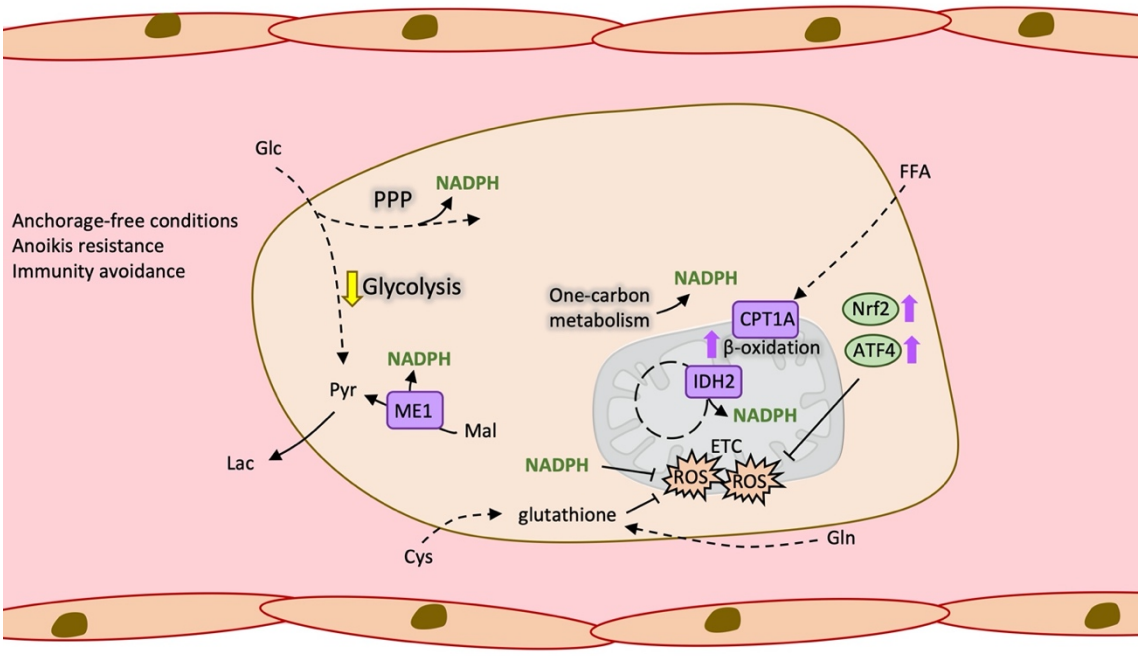

Figure 2.2.4. Antioxidant metabolism in circulating tumour cells (CTC). Schematic representation of the metabolic changes that favour CTCs survival under anchorage-free conditions, mainly enhanced ROS. All abbreviations are listed in section 1.

2.2.3.5 Metabolic flexibility in the metastatic site

As described in section 2.1.2.4, cancer cells release certain factors in the blood that favour a premetastatic niche in the place of metastatic site. A metabolic example of that is the secretion of miR-122 that suppress glucose uptake and downregulates PK in the premetastatic niche, which

will increase glucose availability for cancer cells once they reach the metastatic site (Fong et al., 2015). In fact, nutrient availability in the tissue or organ of destiny and the adaptation to it by metastatic cancer cells defines the efficiency of metastasis. This is the case of breast cancer metastasis, as observed in a transcriptomics study that revealed differences in the metabolic gene expression between the different metastasis sites (Kim et al., 2014).

Regarding metabolic adaptations observed specific to the organ of origin, there is evidence that confirmed that breast cancer metastatic cells expressed PPP enzymes differently, being the brain the place with the highest expression (Cha et al., 2017). Another example of metabolic reprogramming of cells that metastasise to the brain is an increased capacity of acetate metabolisation and oxidation in the TCA cycle. This metabolic feature is also observed in tumours that are from the brain, such as glioblastoma, but not in the primary tumours of other sites (Mashimo et al., 2014). Even more, it is also observed that brain metastatic cells from breast are able to grow independently of glucose and even overexpressing gluconeogenic enzymes (Chen et al., 2015), and even acquire the capacity to catabolise GABA to succinate, overexpressing GABA receptor, transporter and transaminase (Neman et al., 2014).

When breast cancer cells metastasise specifically to the lung, another study revealed that metastatic cells become dependent on pyruvate carboxylase in response to the pyruvate availability of the lung microenvironment (Christen et al., 2016). Antioxidant systems such as peroxiredoxin-2 (PRDX2) were also upregulated in metastatic cells in the lungs as the lung is one of the organs with higher oxygen concentration that metastatic cells have to face (Stresing et al., 2013). Proline catabolism by PRODH also supports metastasis of breast cancers to the lung (Elia et al., 2017).

When the site of metastasis is the liver, breast cancer cells reduced mitochondrial metabolism as a response of the low oxygen levels that exist some parts of the liver by overexpressing PDK1 that inhibits PDH and reduces oxidative phosphorylation (Dupuy et al., 2015). The same study indicated that this pattern was unique for liver metastasis compared to breast cancer that metastasised to the lung or bones.

Regarding bone metastasis, breast cancer cells show increased serine biosynthesis through the expression of phosphoglycerate dehydrogenase (PHGDH), phosphoserine aminotransferase, (PSAT1), and phosphoserine phosphatase (PSPH). This is probably occurring due to the fact that serine is released and required for the formation of osteoclasts that would help bone metastasis through osteolysis (Pollari et al., 2011). Another metabolite that has been observed to fuel osteoclasts through the MCT1 is lactate that breast cancer cells produce in excess through Warburg effect and released through monocarboxylate transporter 4 (MCT4) (Lemma et al., 2017).

Finally, regarding lymph node metastasis, fatty acid oxidation is observed to acquire an important role. Enzymes such as FAO are overexpressed by the transcriptional coactivator yes-

associated protein (YAP) that were probably activated by bile acids accumulation in the metastasis of lymph nodes through the vitamin D receptor (Lee et al., 2019).

2.2.4 METABOLIC REPROGRAMMING IN COLORECTAL CANCER AND METASTASIS

2.2.4.1 Metabolic alterations in the primary stages of colorectal cancer

In the context of colon cancer, it is observed that at very initial steps of tumorigenesis and progression, cancer-initiating cells present a significant metabolic reprogramming, mainly characterised by increased glycolysis, TCA cycle, cysteine, and methionine metabolism (Chen et al., 2014). This changes, that could be initially mediated by Wnt signalling, one of the first pathways that are found deregulated in the colon cancer cascade, also included activation of pyruvate dehydrogenase kinase 1 (PDK1), that inhibits PDH, suggesting a decreased flux of glucose to mitochondrial respiration (Pate et al., 2014). Wnt pathway is also directly activating the lactate/pyruvate transporter MCT1 which contributes to an increased flux of glycolysis lactate secretion (Sprowl-Tanio et al., 2016). Another enzyme of the glycolytic pathway, PKM2 is observed to be activated by O-GlcNAcylation and serine phosphorylation (Chaiyawat et al., 2015).

Apart from direct Wnt pathway-related metabolic alterations in adenoma stage also MYC is observed to be upregulated, probably induced by Wnt, bringing an early metabolic reprogramming including the major biosynthetic pathways such as PPP, nucleotide synthesis, fatty acid synthesis or one-carbon metabolism. At the same time, MYC reduces the expression of genes related to mitochondrial metabolism such as PGC-1α (Satoh et al., 2017). Furthermore, in the context of colon cancer initiation, the metabolic pathways that are altered in cancer-initiating cells in the colon epithelia is greatly influenced by the microbiome and vice versa (Garza et al., 2020).

As previously seen in section 2.1.3.4 and 2.2.2.1, there are other signalling pathways important in colorectal cancer that could have an effect in metabolic pathways. This is the case of KRAS mutations, that were observed to give some metabolic advantages such as survival under glucose-depletion conditions (Miyo et al., 2016). Also, PI3K/Akt and p53 are described to be involved in the colon cancer metabolic reprogramming (Brown et al., 2018).

Regarding glutamine metabolism, GLS1, GLUD1 and the mitochondrial aspartate glutamate carrier 2 SLC25A13 are associated to tumour growth and poorer outcome in colon cancer (Miyo et al., 2016; Xiang et al., 2019).

Many metabolic alterations in the initial steps of colorectal cancer also occur in lipid metabolism. β-oxidation is another of the specific signatures observed in colon cancer cell lines compared to other types of cancer (Halama et al., 2015). Other changes in lipid metabolism

included increased fatty acid synthesis through FASN, increased elongation of saturated fatty acids, desaturation, and polyunsaturation (Pakiet et al., 2019).

2.2.4.2 Metabolic alterations in metastatic colorectal cancer

As explained before, the metabolic alterations underlying metastatic colorectal cancer are much less studied than other types of cancer such as breast. However, there are some relevant studies that compared primary tumour and metastatic colon metabolism and found that expression of ACSL and SCD correlates with poor clinical outcome inducing energetic capacity and invasive and migratory characteristics (Sánchez-Martínez et al., 2015). Another study of clinical relevance found an increased expression of GLUT3 and PKM2 in metastatic colon cancer cells through the Yes-associated protein (YAP) pathway (Kuo et al., 2019). In fact, YAP pathway is also associated with lymph node metastasis through the upregulation of fatty acid oxidation (Lee et al., 2019).

Other studies have discovered some of the metabolic properties that would allow colorectal cancer cells to survive in circulation and initiate metastasis in the liver. Detached colorectal CTCs overexpressed enzymes also of the fatty oxidation pathway. Specifically, CPT1A, the rate-limiting enzyme of this pathway, is found to be essential for anoikis resistance and survival of CTCs from the colon (Wang et al., 2018b).

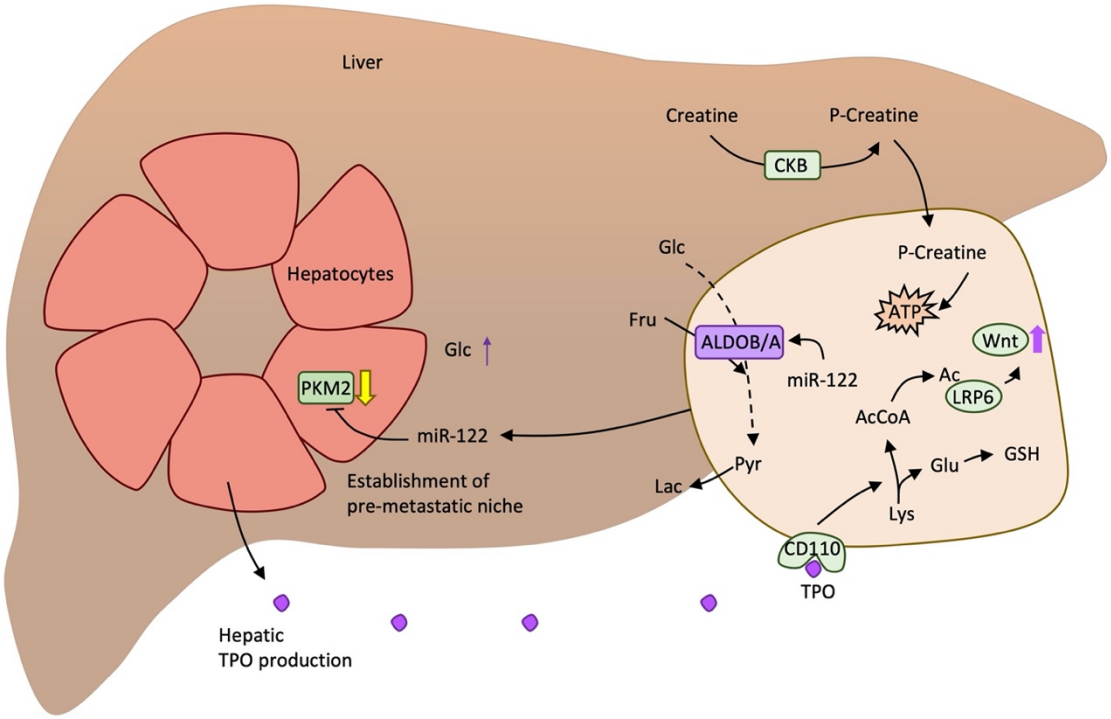

Figure 2.2.5. Metabolic flexibility of metastatic colorectal cancer cells colonising the liver. Schematic representation of the known metabolic changes that help cancer cells from colon to colonise the liver. All abbreviations are listed in section 1.

Another example of a characteristic pattern in colorectal cancer cells that metastasised to the liver is the induction of creatine phosphorylation in the extracellular environment by secreting

creatine kinase (CKB) and then import the resulting phosphocreatine through SLC6A8 transporter and use it as a fuel to generate ATP (Loo et al., 2015) (Figure 2.2.5). Also, thrombopoietin (TPO) produced by hepatic cells activate lysine catabolism through the TPO receptor CD110 expressed in CTCs from the colon. Lysine catabolism generates Acetyl-CoA necessary for LDL receptor related protein 6 (LRP6) acetylation that in turn leads to Wnt signalling, which promotes self-renewal of colorectal cancer tumour cells that colonise the liver. It also generates glutamate that contributes to glutathione formation (Wu et al., 2015). Finally, as previously seen in section 2.2.3.5, metastatic cells secrete miR-122 to downregulate PKM2 in hepatocytes and increase glucose availability (Fong et al., 2015). In colorectal cancer, miR-122 is found to be upregulated and promote ALDOA overexpression (Li et al., 2019b). Precisely, another isoform of this enzyme, ALDOB, is found to enhance fructose metabolism in colorectal metastatic cancer cells as a response of elevated fructose concentration that is present in the liver (Bu et al., 2018).

2.3 CANCER THERAPY AND METABOLIC-BASED STRATEGIES

2.3.1 CURRENT AND NEW THERAPIES OF CANCER

2.3.1.1 Generalities on cancer treatment

The cancer disease has been diagnosed and treated since the Egyptian era. Until the invention of radiotherapy in the late XIX century, surgery had been the main treatment for cancer in the cases that it was possible. Nowadays, surgery is still being broadly used especially in early stages of cancer and when the tumour is easily extricable, and in the cases when it is possible, it remains to be the most effective therapy. Even in the case of metastatic cancer, surgery is applied if it is convenient. Surgery is being continuously improved by the use of modern techniques that are less invasive such as laparoscopic colectomy for colorectal cancer, breast-conserving surgery, and surgeries including robotic systems, radiosurgery, etc. (Arruebo et al., 2011; Matsuda et al., 2018). However, even the primary tumour has been extracted, metastasis could appear later as it was previously undetectable or due to the existence of circulating tumour cells or dormant cells in the metastatic sites that further developed into clinically manifested metastasis. Then, even when surgery is possible, metastatic disease treatments are commonly accompanied by adjuvant radiotherapy and/or chemotherapy.

From the discovery of X-rays by Becquerel and Marie Curie, radiotherapy has been in the first line of cancer treatment, together with surgery and chemotherapy. It has also been improved during the last decades, concentrating X-rays to the tumour and achieving the least possible side effects in the healthy tissue. Intensity-modulated radiation therapy (IMRT) combined with the use of computed tomography (CP) provides a three-dimensional perspective that favours tracing the tumour and avoids toxicity. Even better, four-dimensional radiotherapy

using a dynamic CP allows to takes into account any movement of the patient (Garibaldi et al., 2017).

Finally, the third main clinical strategy against cancer, chemotherapy, began later than radiotherapy, during the first years of the XXth century, and since then is normally used as a complement to surgery and radiotherapy or as a unique treatment if the other two strategies are not possible. In fact, from the first alkylating agents to targeted therapies, chemotherapy is nowadays the major hope in treating cancers in advanced stages and with poor prognosis (Falzone et al., 2018).

2.3.1.2 Pharmacological treatment of cancer

The first drugs used to treat cancer were nitrogen mustard and alkylating drugs like cyclophosphamide and chlorambucil that prevented DNA duplication and led to cancer cell death, being also very toxic for healthy tissue (Gilman, 1946). With the development of the synthesis of new compounds as well as the definition of DNA structure, chemotherapy advanced and new alkylating agents were developed. Nowadays, alkylating platinum compounds are still widely used, such as cisplatin or oxaliplatin. Another class of chemotherapeutic agents that arose in the middle of the XXth were antimetabolites, which block the enzymes that are essential for cancer cell growth, mainly synthesis of nucleic acids (Farber and Diamond, 1948). Antifolates such as aminopterin and methotrexate, purine analogues such as mercaptopurine and pyrimidine analogues such as 5-fluorouracil and gemcitabine are still used in chemotherapy, normally in combination with alkylating agents or other compounds (see section 2.3.2.3). However, a problem of most alkylating agents and antimetabolites is that are not specific for cancer cells. Another problem is that cancer cells tend to generate resistance to such chemotherapies (Falzone et al., 2018).

Other classes of chemotherapeutics frequently used in cancer are antimitotic from natural origin such as microtubule depolymerizing agents (Vinca alkaloids such as vinblastine, vincristine, vinorelbine, or vindesine), microtubule stabilising molecules (paclitaxel, docetaxel and cabazitaxel) topoisomerase I inhibitors (topotecan, irinotecan), and topoisomerase II inhibitors (teniposide and etoposide). Antibiotics such as doxorubicin, actinomycin D, mithramycin and bleomycin are also being used in cancer treatment and also act as inhibitors of DNA synthesis, topoisomerase inhibitors, DNA intercalates, and other mechanisms. Finally, polyamine inhibitors (such as difluoromethylornithine, DFMO) and iron-modulating drugs, such as desferrioxamine, are also used. Some of these drugs emerged in the middle of the XXth and others are nowadays still being explored and under clinical trials, mainly in combination with alkylating agents and/or antimetabolites (Chabner and Roberts, 2005). Combination regimes show overall higher efficacy of the administrated drugs and allow to reduce the dose of each drug

and help to overcome resistance. However, most of the drugs and regimes present undesirable cytotoxicity and side effects, mainly related to collateral damage to healthy stem cells.

With the development of molecular biology and the recent discoveries, a second era of pharmacological cancer treatment started at the beginning of the 80s with the first selective kinase inhibitors and monoclonal antibodies (Bernstein et al., 1980). These treatments, called "targeted therapies" are selective for a specific target that is normally a component of an altered signalling pathway and generally affect only cancer cells and not normal cells, diminishing the side effects. Together with the advances in DNA sequencing and omics sciences, targeted therapies allow a more personalised medicine. From the first monoclonal antibody, trastuzumab, which was directed against HER2, a lot of antibodies were developed. Nowadays some antibodies have been approved and are being effective in the clinics, such as bevacizumab against VEGF or cetuximab and panitumumab against EGFR. Some antibodies are used also in diagnosis or are conjugated with cytotoxic molecules or radioactive isotopes so that the antibodies direct the toxicity to tumour cells (Pento, 2017).

Apart from monoclonal antibodies, targeted therapies also include specific inhibitors, mainly against kinases. The first selective tyrosine kinase inhibitor was imatinib, which was directed to the fusion protein BCR-ABL that is found in Philadelphia chromosome-positive CML and ALL patients (Druker et al., 1996). Gefitinib and erlotinib were the second tyrosine kinase-specific inhibitors, directed to the EGFR ATP-binding site and therefore avoiding the overactivation of MAPK and PI3K/Akt signalling pathways. Other inhibitors that have been emerging from the beginning of the present century are inhibitors against HER1 and 2 (lapatinib), inhibitors against VEGF (sunitinib and sorafenib), which are considered to be antiangiogenic, mTOR inhibitors (temsirolimus and everolimus, derived from rapamycin), BRAF inhibitors (vemurafenib and dabrafenib), MEK inhibitors (trametinib and cobimetinib), proteasome inhibitors (bortezomib and carfilzomib), cyclin-dependent kinases 4/6 (CDK4/6) inhibitors (palbociclib), among others (Xie et al., 2020).

Unfortunately, it is very common that tumours treated with targeted therapies (either with antibodies or inhibitors) develop resistance. It also happens with traditional chemotherapy, but the mechanisms of resistance are simpler and better known, such as overexpression of DNA repair genes, drug efflux transporters or antioxidant mechanisms. In the case of targeted therapies, resistance is mostly related to a selection process due to tumour heterogeneity. Even though most of the tumour cells can be treated with an specific inhibitor, some small population of the tumour may not harbour the specific mutation that is being targeted and will be resistant to the treatment, giving to recurrence. Even more, tumour cells can acquire a new mutation or epigenetic event that bypasses the specific inhibition, through the overexpression of another member of the pathway that is downstream of the target or else the overexpression of another concomitant pathway. For that reason, also combination patterns have been established in targeted therapies. MYC addiction

and higher glutaminase activity emerge when colorectal cancer cells try to overcome CDK4/6 inhibition (Tarrado-Castellarnau et al., 2017), and combination of telaglenastat with palbociclib has been proposed and is currently under clinical trials for solid tumours (Qie et al., 2019). Another example applied in the clinics is the combination of BRAF inhibitors with MEK inhibitors to avoid such resistance (Sabnis and Bivona, 2019).

Immunotherapy for cancer emerged from 2010 with the first monoclonal antibodies against T-cell receptors that favour cancer development and downregulate the immune response. Specifically, ipilimumab, an anti-cytotoxic T-lymphocyte-associated antigen 4 (anti-CTLA4) was the first immune checkpoint inhibitor to be approved and is able to activate T-cells against cancer cells. Then, nivolumab, pembrolizumab and durvalumab were developed as an antibody against programmed cell death protein 1 (PD1), which normally downregulates T-cells and are not able to recognise cancer cells. These treatments are also combined with other targeted therapies or traditional chemotherapy and are increasing the survival of patients with metastasis (Seidel et al., 2018).

Other possible therapies that are being nowadays developed such as chimeric-antigen receptor (CAR)-T cell therapy, which consists in the *in vitro* genetic modification of T-cells from the patient in order to selectively induce cell death to cancer cells but not to normal cells by detecting specific antigens. Some CAR-T therapies are approved for diffuse large B-cell lymphoma (DLBCL) (Xu et al., 2018). Vaccines are also being designed and developed to prepare the immune system against cancer. Polypurine reverse Hogsteen hairpins are also useful therapeutic tools to specifically target cancer-associated genes (Ciudad et al., 2017). Finally, CRISPR/Cas9 technology is also being explored to allow fast genome editing and correct known genetic aberrations of cancer (Zhan et al., 2019).

2.3.1.3 Current therapies of colorectal cancer

Surgical treatment remains to be the main clinical strategy for the first stages of colorectal cancer when the resection of the primary tumour is possible. The laparoscopic technique is the most used approach to perform mesorectal excision, but new approaches are arising such as transanal total mesorectal excision, laparoscopic lateral pelvic lymph node dissection and robotic surgery. (Matsuda et al., 2018). After surgery, the 5-year survival rate of stages I to III of CRC is 80%, however, for stage IV is only 18% of cases. Surgery is also applied in colorectal liver metastasis when it is possible, especially when there is only one resectable metastatic tumour. When there are multiple metastases the general recommendations are to perform surgery when possible or apply chemotherapy and evaluate resectability afterwards (Oki et al., 2018).

Nowadays chemotherapy is applied normally after surgery (both of primary tumour in stages II or III liver metastasis at stages IV) as adjuvant treatment or else as the main treatment when surgery is not possible. In stage II patients, there is controversy about the use of adjuvant

chemotherapy, usually fluorouracil based. It is not clear to what extent it could be useful, and it is observed that only a selection of the patients would really benefit from it. Patients at higher risk (T4) and that present the first lymph node metastasis possibly benefit from it. Also, molecular determinations of aggressivity should be taken into account to make therapeutic decisions about adjuvant chemotherapy. For example, MSI patients usually do not benefit from 5-fluorouracil as they develop resistance to the treatment (Bender et al., 2019).

In stage III, it is widely demonstrated that adjuvant therapy is useful, and it is very common to apply 5-fluorouracil-leucovorin (5-FU-LV) normally in combination with oxaliplatin (FOLFOX). 5-fluorouracil is an antimetabolite that has been used to manage colorectal cancer since 1957 and it inhibits thymidylate synthase, which is necessary for RNA and DNA synthesis and induces apoptosis in proliferating cells. Leucovorin (folinic acid) increases the stability of the complex that 5-FU forms with TS, increasing its antitumoral activity. Capecitabine is also used in colorectal cancer and it is metabolised to 5-FU. Oxaliplatin is an alkylating agent that forms adducts with DNA structure inhibiting its synthesis and causing cell death by apoptosis (Lee and Chu, 2018).

Regarding stage IV CRC patients, chemotherapy is widely applied, both as an adjuvant therapy to metastatic liver resection or as a single treatment if surgery is not possible. Schemes that combine 5-FU-LV with oxaliplatin (FOLFOX), or else using capecitabine (CAPOX) are very common. Irinotecan is another drug used for advanced colorectal cancer. It is an inhibitor of topoisomerase I and therefore inhibits relieving of the DNA double-strand supercoiling. The combination of 5-FU and irinotecan (FOLFIRI) is another one of the main choices for advanced colorectal cancer treatment. The triple treatment (FOLFOXIRI) has also been proved with no effectivity although sometimes the sequential administration of the three drugs is used. Acute cytotoxicity of chemotherapy is very common and despite the improvements that have supposed some of the treatments such as the oral administration of fluoropyrimidines or the combination therapies there are still many undesirable side effects. Palm diathesis, ulceration, infections, or neurotoxicity (in the case of oxaliplatin) are very common in patients treated with all these chemotherapies. Therefore, treatments have to be strictly controlled in order to avoid severe cytotoxicity (Oki et al., 2018).

Additionally, in order to avoid cytotoxicity of traditional chemotherapy, targeted therapies are being nowadays also applied and in development for treating colorectal cancer. Cetuximab or panitumumab, approved in 2004 and 2006, respectively, are monoclonal antibodies against EGFR and are effective in combination with FOLFIRI. This strategy is exclusively for *RAS* native patients as patients bearing *RAS* mutations would not benefit from an anti-EGFR, which is upstream RAS GTPases. Another effective approach is the use of monoclonal antibodies against VEGF or VEGFR, that help to avoid angiogenesis. In that sense, bevacizumab,

aflibercept, regorafenib and ramucirumab were anti-VEGF and VEGFR antibodies approved between 2004 and 2015 for the treatment of colorectal cancer.

Nowadays, patients that present unresectable metastatic disease are treated according to the mutational status of *RAS* and *BRAF*, as well as MSI state. Double combination of traditional chemotherapeutics (normally FOLFOX, CAPOX, or FOLFIRI) is given together with anti-EGFR in RAS wildtype cases and with bevacizumab in *RAS* mutant patients. When *BRAF* is mutated (normally in MSI, see section 2.1.3.3) then the triple combination FOLFOXIRI is given together with bevacizumab. Aflibercept or ramucirumab are commonly used as second-line treatments, as the progresses (Van Cutsem et al., 2016). During the last years 2017 and 2018, three new drugs that are immunotherapeutic agents (immune checkpoint inhibitors against PD1 and PD-L1) were approved: pembrolizumab, nivolumab, and ipilimumab have started being used, with higher effectivity in patients with MSI than MSS colorectal cancer (Jácome and Eng, 2019). The decisions about which treatment is the best also depend on the medical goal, for example, cytoreduction in patients that there are being evaluated for possible surgery, or cytoreduction because of aggressive biology of the tumour and existing severe symptoms, disease control, among other scenarios.

In order to better select the most convenient therapy for each patient, plenty clinical trials are evaluating the clinical value of more biomarkers, apart from *RAS*, *BRAF* and MSI testing, such as mutations in *PIK3CA* at exon 20, *PTEN* loss, EGFR levels of expression, *HER2* amplification and mutations, or HER3 overexpression. The applicability of consensus molecular subtypes (CMS) is also being studied. At the moment, it is considered that CMS1, being MSI-like would probably benefit from anti-PD1/L1, CMS2 could benefit from anti-EGFR, CMS4 probably a TGFβ inhibitor and CMS3 is still to be defined. Circulating tumour cells determination, liquid circulating tumour DNA and whole genome, exome and transcriptome analysis are also being explored for patient stratification and improvement of personalised medicine in cancer treatment.

Furthermore, many targeted therapies and immunotherapies are in clinical trials for colorectal cancer, which include inhibitors of PI3K, mTOR, Akt, STAT3, MAPK, MEK, EGFR, HER2/3/4, Src, BRAF, VEGFR, Wnt, Notch, DR5, Hedgehog, TGFβ, IGF-1R as well as immune checkpoint modulators against PD1, PD-L1, CTLA-4, LAG-3, TIM-3, TIGIT, and A33 (Xie et al., 2020).

2.3.2 METABOLISM IN CANCER TREATMENT

2.3.2.1 Metabolic-based cancer diagnosis

One of the most remarkable applications of metabolism in cancer treatment is positron emission tomography (PET), which uses metabolite analogues labelled with radioisotopes that

emit positrons which can be followed by imaging. PET is usually used in order to determine the malignancy and help on the staging of the disease as well as on the definition of volume in order to determine the dose of radiotherapy or chemotherapy and further monitoring the disease. The most widely used tracer is ^{18}F-fluorodeoxyglucose (^{18}F-FDG), which is an analogue of glucose and its effectivity is based on the fact that tumours display Warburg effect, and therefore consume much more glucose than other cells in the body. However, glucose analogues are not the only tracers used. Amino acids analogues, such as ^{18}F-fluoro-ethyl-tyrosine or l-[methyl-()11C]methionine are more commonly used for brain tumour imaging than ^{18}F-FDG (D'Souza et al., 2014). It is also common to use ligands targeting the somatostatin receptor such as ^{68}Ga-DOTATOC and ^{68}Ga-DOTATATE for meningioma, as they target more specific features of that type of cancer, rather than glucose metabolism (Unterrainer et al., 2020).

Metabolic reprogramming of cancer can also be exploited for biomarker research. One of the main problems of cancer disease is that frequently is not detected as early as it would be necessary for the treatment to be effective and assure survival. For that reason, it is necessary to develop early detection biomarkers that allow clinicians to deal with the disease in early stages, if it is possible when there is still no metastasis and surgical resection is enough to completely eradicate the disease (Muthu and Nordström, 2019). The problem with metabolic-based biomarkers is that, with some exceptions, there is not any specific metabolite for cancer, and if it was, it would be very diluted in the bloodstream. Additionally, metabolites that can be used as a biomarker of cancer are also altered in other diseases. This is the case of alteration of glutamate serum levels, that is altered in breast cancer but also in Wilson's disease, Alzheimer's disease, depression, chronic obstructive pulmonary disease and multiple sclerosis, among others (Muthu and Nordström, 2019; Yuan et al., 2019). To date, the evaluation of DNA methylations in ctDNA is more efficient and reliable than metabolic-based biomarkers.

However, some researchers have found clinically valuable metabolic biomarkers, although none of them has reached the clinics yet. This is the case of some amino acids and biogenic amines such as polyamines, short-chain fatty acids and others. However, the reason why they have not been established in the clinics is that it lacks more information about the different values that these metabolites can reach when a tumour is present, compared to normal levels. In some cases, it is also unknown the relationship between the altered metabolite levels and the cancer metabolic adaptations that explains it (López-López et al., 2018).

In the case of colorectal cancer, many amino acids (alanine, arginine, aspartate, glutamate, glutamine, glycine, histidine, leucine, lysine, methionine, ornithine, phenylalanine, proline, threonine, tryptophan, tyrosine, valine) have been observed to be altered in blood samples, compared to healthy patients. Also, carbohydrates such as lactate, pyruvate, and the fatty acids hydroxybutyrate and 18:2 lysophosphatidylcholine are altered in the blood (Farshidfar et al., 2016). Urine and faecal samples also present promising biomarkers that are different from the

blood and that could be more specific of colorectal cancer disease, such as trigonelline, cytidine, methyladenosine, methanol, 2,2-methylguanosine or pseudouridine in urine and β-glucose, acetate, butyrate and propionate in faecal samples (Erben et al., 2018).

2.3.2.2 Metabolic-based therapeutic strategies

Metabolic reprogramming has been exploited for cancer therapy almost since the beginning of chemotherapy, with the discovery of aminopterin for the treatment of acute lymphoblastic leukaemia in children (Farber and Diamond, 1948) and nowadays there are plenty of metabolic enzyme inhibitors that are approved or being explored for cancer therapy (Figure 2.3.1).

Aminopterin was the first of one of the main classes of chemotherapeutics, antimetabolites, and was the precursor of methotrexate and pemetrexed, which are drugs currently used for many types of cancer. Specifically, these drugs are also called antifolates or folate analogues as they act inhibiting enzymes of folate pathway that are involved in nucleotide synthesis, mainly dihydrofolate reductase (DHFR), although not all of them have the same targets. Since then, it is widely recognised that folate metabolism is one of the main overactivated pathways in cancer, although it is also a crucial pathway for stem cell metabolism and immune system precursors. For that reason, there are many side effects and cytotoxicity related to bone marrow, intestinal crypts and hair follicles affectation (Luengo et al., 2017).

Another commonly used antimetabolites are those also inhibiting the nucleotide synthesis but in biosynthetic pathways of purines and pyrimidines, which is also overactivated in cancer cells. There are purine analogues (6-mercaptopurine and 6-thioguanine), which target amidophosphoribosyltransferase (PRPP amidotransferase), and pyrimidine analogues (5-fluorouracil and its prodrug capecitabine), which target thymidylate synthase (TS). There are also inhibitors of dihydroorotate dehydrogenase (DHODH) (brequinar and leflunomide), one of the steps in the pyrimidine nucleotide synthesis pathway. Despite being widely used in chemotherapy they also showed similar cytotoxic effects as antifolates.

However, there are many other metabolic-based strategies that are approved or in clinical trials and are more specific for cancer cell metabolic reprogramming. This is the case of the treatment of cancers that present mutations in IDH1 or 2, mainly glioblastoma multiforme (GBM) or acute myeloid leukaemia (AML) (see section 2.2.1.2). Specific inhibitors for IDH1 (AG-120 or ivosidenib, IDH305, BAY143602, FT-2102), IDH2 (AG-221 or enasidenib) or both IDH1/2 (AG-881) have been proven to be effective and approved or currently in clinical trials, being enasidenib and ivosidenib the first mutant-IDH FDA-approved for AML patients in 2017. However, not all IDH-mutant tumours have a good response to the treatment, or exhibit resistance, for what a further exploring of the possible drug combinations is needed (Golub et al., 2019).

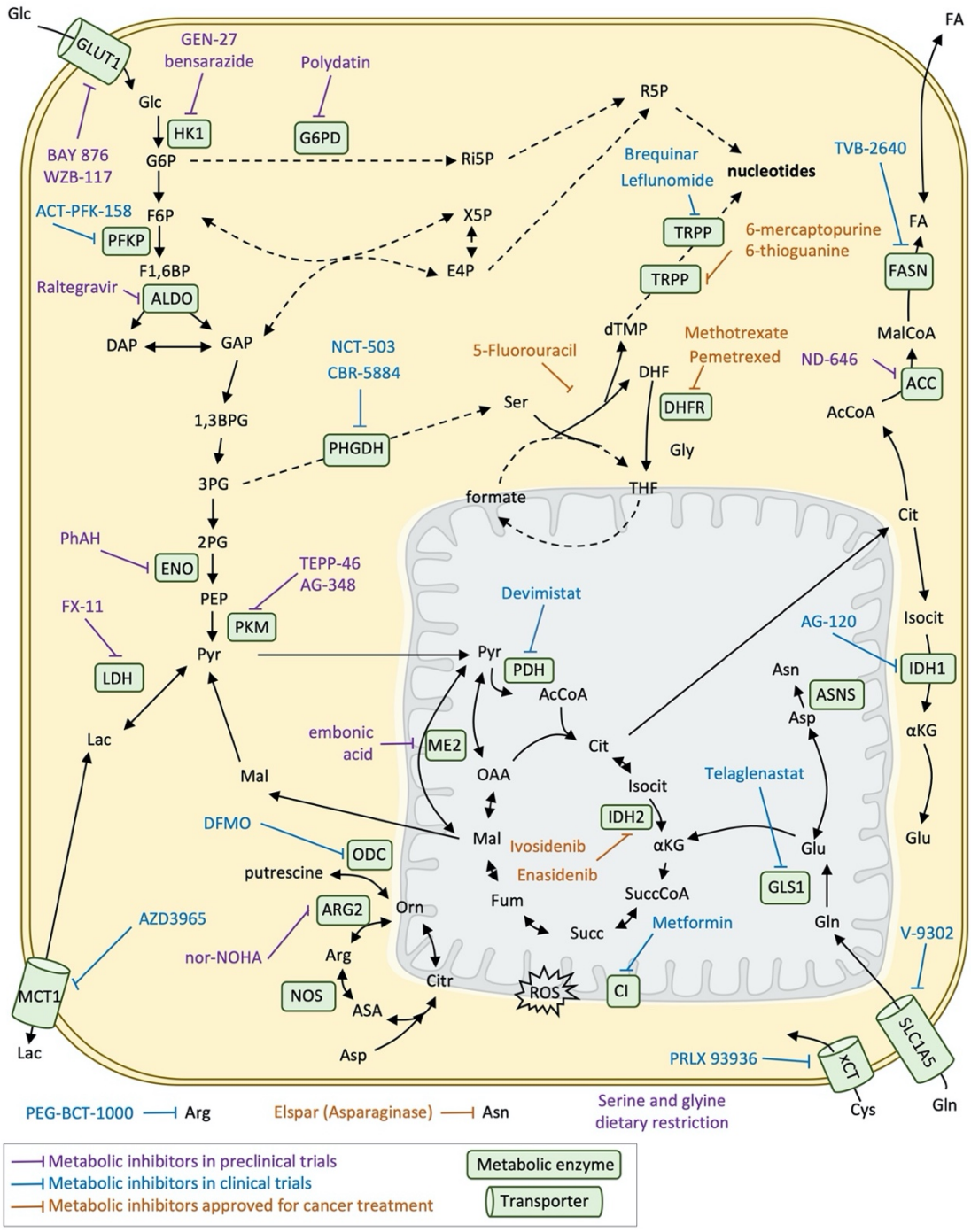

Figure 2.3.1. Metabolic inhibitors for cancer treatment. Schematic representation of the main metabolic pathways and the main metabolic inhibitors that are being nowadays explored preclinical or clinical trials as well as those approved for cancer treatment. All abbreviations are listed in section 1.

There are other targets related to glucose metabolism and TCA cycle. Alpha-Enolase (ENO1) is one of the enzymes of glycolysis that has shown to be overexpressed and contribute to Warburg effect and its inhibition using phophonoacetohydroxamate (PhAH) or SF-2312 has been proven to be effective for many cancer cell lines *in vitro* (Capello et al., 2016). Inhibition of ENO1 also activates plasmacytoid dendritic cells in multiple myeloma patients, enhancing the immune

response against tumour cells (Ray et al., 2020). The inhibition of the last step of glycolysis, the enzyme PK and specifically its isoform M is another of the most explored spots of cancer metabolic reprogramming and its inhibition (by TEPP-46 or AG-348) has proven to be effective in preclinical models of pancreatic cancer, and in combination with the lactate dehydrogenase inhibitor FX-11. One of the central enzymes of carbon metabolism and that is frequently enhanced in cancer cells is pyruvate dehydrogenase (PDH) (McFate et al., 2008). Its inhibition has been demonstrating to tackle the metabolic reprogramming of cancer cells, which impairs cell growth and invasion (Commander et al., 2020; Yonashiro et al., 2018) and the inhibitor devimistat (CPI-613) is nowadays in phase III trial in patients with AML. Another target that is being explored is the import and export of lactate mediated by monocarboxylate transporter 1 (MCT1), which allows both the secretion of lactate from highly glycolytic cancer cells as well as the utilization of lactate from the tumour microenvironment. AZD3965, an inhibitor of MCT1, decreases tumour aggressiveness by increasing immune cell infiltration and inhibiting lipid biosynthesis. The inhibitor is nowadays in phase I of clinical trials (Beloueche-Babari et al., 2020). Finally, metformin, a drug that is used in the treatment of diabetes and it is known to inhibit the mitochondrial respiratory chain complex I is nowadays being explored for cancer prevention and treatment, although its benefits are still not clear (Saraei et al., 2019; Yu et al., 2019).

Glutamine addiction is another metabolic feature of cancer cells that is being exploited for therapy. Targeting glutaminase 1 or 2 activity with the inhibitor telaglenastat (CB-839) is currently in clinical trials for the treatment of renal cell carcinoma or other solid tumours in combination with other drugs (Hoerner et al., 2019; Meric-Bernstam et al., 2019). Another amino acid that is being explored for cancer therapy is serine, especially *de novo* serine from glucose. The first enzyme of this pathway, phosphoglycerate dehydrogenase (PHGDH) is overexpressed in many types of cancers such as breast, lung and melanoma. Inhibitors of PHGDH have been designed (NCT-503 and CBR-5884) (Wang et al., 2017a), although they present brain cytotoxic effects and its effectivity depends on environmental serine availability. In fact, some cancer types such as intestinal cancer or lymphoma that are not KRAS mutant rely on exogenous serine uptake and dietary restriction of serine and glycine have an anti-tumour effect in mouse models (Maddocks et al., 2017).

Other chemotherapeutic treatments related to amino acid metabolism are the depletion of circulating arginine using PEG-BCT-100 or AEB-1102, which are human recombinant arginases or arginine deaminases, respectively. Such therapies are in phase 1 of clinical studies in combination with immune checkpoint inhibitor antibodies (De Santo et al., 2018), in the context of argininosuccinate synthase 1 (ASS1) – deficient cancers, normally melanoma, lymphoma, glioma or prostate cancers that rely on circulating arginine. The same approach is applied for circulating asparagine using L-asparaginase, which is currently used in the first-line treatment of ALL (Brumano et al., 2018) and it is also being tested for solid tumours and nanoparticles carrying

the enzyme are also being developed in order to improve efficiency (Orhan and Aktaş Uygun, 2020).

Finally, fatty acid metabolism rewiring in cancer is also currently being explored for cancer therapy. Specifically, *de novo* lipogenesis is a requirement of cancer cells and targeting fatty acid synthase (FASN) using the TVB-2640 FASN inhibitor is nowadays in phase I or II clinical trials for breast, lung and colon cancers (Koundouros and Poulogiannis, 2020). Inhibition of acetyl-CoA carboxylase (ACC), the previous enzyme of the lipogenesis pathway, is also being explored in preclinical models using the inhibitor ND-646 (Li et al., 2019a).

2.3.2.3 Metabolic-based therapeutic strategies in colorectal cancer

There are many metabolic inhibitors that are being tested for the treatment of colorectal cancer in cell lines, preclinical models and also in clinical trials such as GLS1 or FASN inhibitors. An example of specifically targeting a colorectal cancer metabolic adaptation is 3-bromopyruvate sensitivity, taking advantage that the colorectal cancer cells present overexpression of MCT1, induced by Wnt pathway (Ferro et al., 2016; Sprowl-Tanio et al., 2016). In that sense, the drug AZD3965, which targets MCT1, is being tested for colorectal cancer in preclinical models (Beloueche-Babari et al., 2017). Furthermore, the presence of acetate and other short-chain fatty acids could come also from the microbiome and could have an important role in cancer prevention. Other examples of inhibitors being tested in colorectal cancer cell lines are WZB117, which targets GLUT1, to overcome 5-Fluorouracil resistance (Liu et al., 2014). Also, metformin, which targets the mitochondrial electron transport complex I, has been widely explored in colorectal cancer in both preclinical and clinical trials (Kamarudin et al., 2019).

Nevertheless, although there are many metabolic alterations observed in colorectal cancer and other cancer types have started to benefit from metabolic strategies, none of these metabolic approaches is being used nowadays in the treatment of colorectal cancer (La Vecchia and Sebastián, 2020). Therefore, more research is needed for a better comprehension of the metabolic reprogramming in colorectal cancer and metastasis that would allow discovering new metabolic targets and finally reach the clinics.

2.3.3 METABOLIC NETWORK SYSTEMS BIOLOGY APPROACH FOR THE DISCOVERY OF METABOLIC TARGETS

2.3.3.1 Systems biology and metabolomics

During the last years, there has been a change in the paradigm of scientific discovery in the biological sciences field. The XXth century was dominated by a reductionist approach of biological systems that allowed to identify and characterise many components of them (genes, proteins, metabolites, etc) and identify mechanisms of diseases. However, such components and

their interactions were mainly evaluated individually. Nowadays, with the technological advances and the appearance of the omics sciences from the beginning of the XXIth century, it is possible to apply a holistic approach to biological systems that allows having a more complete picture. A better comprehension of many biological processes is possible due to the comprehension of the whole system.

Biomedicine and specifically cancer research have benefitted from all these new approaches. Genomics, one of the first omics science to appear thanks to massive genome sequencing, was rapidly applied to cancer research and the first cancer genome sequence appeared in 2006. Advances in mass spectrometry and other protein characterisation techniques allowed proteomics also to emerge as an important field for cancer research. Other two emerging omics that have acquired great importance in the last few years in biomedicine: metabolomics and fluxomics, which deal with the complete knowledge of the metabolites as well as the metabolic reaction fluxes, respectively. The research about cancer metabolic reprogramming is nowadays linked to the application metabolomics and fluxomics approaches (Balcells et al., 2019).

The experimental techniques that are used for metabolomics research are mass spectrometry (MS), nuclear magnetic resonance (NMR) spectroscopy and Fourier transform IR spectroscopy. MS is usually coupled to a previous separation technique as gas chromatography (GC-MS), liquid chromatography (LC-MS) or capillary electrophoresis (CE-MS). With metabolomics techniques we have the information of which metabolites are present at a certain point in a cell or any biological system, usually referred to as untargeted metabolomics (Zamboni et al., 2015). However, this static picture is not always enough for a good metabolomics characterisation. Fluxomics allows us to define the fluxes or rates of the reactions that happen inside the system and between the outside, the consumption and productions rates of metabolites using isotope-labelled substrate previous to the techniques mentioned before, what is called stable isotope-resolved metabolomics (SIRM). Secondly, although substrate contribution or pathway activity analysis formulas can be used in order to have an idea of specific reactions or local predictions, the use of computational tools are needed to fully characterise the fluxes of a. biological system, what is called as metabolic flux analysis (MFA) (Balcells et al., 2019). The isotope-labelled substrates commonly used in SIRM, known as tracers, are glucose, glutamine, and palmitate, and usually bear ^{2}H, ^{13}C, ^{15}N, and ^{18}O isotopes.

2.3.3.2 Metabolic models as a tool for the discovery of new targeted therapies

A metabolic model is a computational tool that consists of the description of a set of metabolic reactions forming a network, which can represent a certain pathway, groups of pathways or the whole metabolism of an organelle, cell or any biological system. The model contains the information of the stoichiometry of each reaction together with the measured isotopic distribution from a SIRM experiment. With that, it is possible to estimate the fluxes of all the

reactions from the experimental data, which is limited. To perform a model, an iteration that minimises the variation of simulated *vs* experimental isotope distribution is needed, as well as certain assumptions (Antoniewicz, 2018).

Among the types of models, we can distinguish between stationary and dynamic MFA. Stationary MFA assumes a metabolic and isotopic steady state, which means that metabolic fluxes and isotope distribution patterns and metabolic fluxes are constant in time. The steady state can be reached within some minutes for intracellular metabolites but hours in case of a big network. It uses only an experimental time point (Noack et al., 2011; Reimers and Reimers, 2016). Dynamic MFA does not assume the steady-state and are simulated by a system of ordinary differential equations from an initial experimental point until the final point, which means it needs several experimental time points to be performed. It also uses information about kinetic equations and properties, such as affinities for substrates and allosteric regulations and it is much more computationally complex (Foguet et al., 2016).

Both models have not only one solution but a space of solutions for each predicted flux values, that can be more or less concise according to the complexity of the model, the amount of available experimental data (such as one or more than one tracer). Tracers can also be optimised for a given set of reactions. For example, [1,2-^{13}C]-glucose and [U-^{13}C]-glutamine are the best tracers for the study of central carbon metabolism (Walther et al., 2012).

Metabolic models can be combined with information from other omics. For example, genome-scale metabolic models (GSMM) integrate information about the genes that encode each enzyme that correspond to a reaction as well as the experimental data about transcriptomics, apart from isotope distribution (Nilsson and Nielsen, 2017). With that, the space of solutions of genome-scale metabolic models are constrained and can be used to make predictions about adaptability to distinct substrate availability and other simulations of any biological system, such as cancer cells (Auslander et al., 2017; Yizhak et al., 2014). Furthermore, proliferation simulations with knockouts for each metabolic gene could be done in order to determine which genes are essential for proliferation and therefore determining gene essentiality (Katzir et al., 2019). In the present work, we apply such approach in metastatic colorectal cancer cells, where it can be used to predict specific metabolic targets that emerge from cancer cell metabolic vulnerabilities, which could be further exploited in the clinics.

3. Objectives

3 OBJECTIVES

Metastatic colorectal cancer is causing 90% of colorectal cancer deaths and the molecular mechanisms underlying metastasis are still poorly understood and not applied in therapies (Fares et al., 2020). Since it is clear that tumour development is driven by a series of genetic alterations on tumour suppressors and oncogenes, the metastatic process is described to be less driven by genetic alterations and more by epigenetic events and other molecular processes, such as metabolic changes (Kreuzaler et al., 2019; Teeuwssen and Fodde, 2019).

The metabolic reprogramming of cancer has been widely studied in the last two decades (Frezza, 2020), and there are also some studies covering metabolic changes associated to the EMT processes and metastasis, especially in breast cancer (Christen et al., 2016; Du et al., 2016; Dupuy et al., 2015; Elia et al., 2017, 2019). However, few studies have been focused on the metabolic adaptation associated with colorectal cancer metastasis (Bu et al., 2018; Loo et al., 2015).

Current chemotherapeutic treatments are still based on traditional chemotherapies that tackle the capacity of cancer cells to divide and cause many side effects. While the development of targeted therapies and immunotherapies is broad, including metabolic strategies, they have inefficient application in the clinical approach of colorectal cancer.

The hypothesis of the present work is that metabolic adaptation plays a crucial role in the metastatic progression of colorectal cancer and metabolic vulnerabilities exploitable for colorectal cancer therapy will emerge from studying it. Therefore, the main objectives of the present thesis are the following:

1. Characterisation of the metastatic features and the metabolic reprogramming of the same-patient derived colon cancer cell lines SW480 (from the primary tumour), SW620 (from lymph node metastasis), LiM1 and LiM2 (from liver metastasis).

2. Application of a systems biology approach to identify and validate specific metabolic vulnerabilities of metastatic cells that could be exploitable in colorectal cancer therapy.

4. Materials and methods

4 MATERIALS AND METHODS

All products were purchased from Merck (USA) unless otherwise specified.

4.1 CHEMICALS

LY345899 (inhibitor of MTHFD1), clofarabine (inhibitor of RRM1), shikonin (inhibitor of PKM2), A939572 and MK-8245 (inhibitors of SCD-1) were purchased from Med Chem Express (USA). SHIN2 (inhibitor of SHMT1/2) was purchased from Glixx Laboratories (USA). methotrexate (inhibitor of DHFR), pemetrexed (inhibitor of DHFR, TYMS, and GART), 2-AAPA (inhibitor of GSR), sulfasalazine and erastin (inhibitors of system xCT) were purchased from Merck (USA).

4.2 CELL CULTURE AND MOLECULAR BIOLOGY EXPERIMENTS

4.2.1 CELL SOURCES, CULTURE AND MAINTENANCE

SW480 cell line was obtained from the American Type Culture Collection (ATCC, USA). SW620 and its metastatic derivatives SW620-LiM1 and SW620-LiM2 (hereafter referred to as LiM1 and LiM2) were obtained from Dr Gomis at IRB Barcelona (Urosevic et al., 2014), both lines were authenticated and *KRAS* mutation confirmed. NCM460 cell line (Moyer et al., 1996) was a kind gift from Dr Mary Pat Moyer (INCELL, USA). All cells were grown in DMEM with 12.5 mM glucose (unless differently specified), 4 mM glutamine, 5% Foetal Bovine Serum (10270, Gibco, Thermo Fisher Scientific, USA), and 1% Streptomycin/penicillin at 37ºC in a 5% CO_2 atmosphere. Cells were grown in 100mm dishes and Trypsin EDTA solution (0.05% trypsin – 0.02% EDTA) from Biological Industries (Israel) was used to split the cells. Centrifugations were done at 500 g in the case of SW480, SW620, LiM1, and LiM2 cell lines and 300 g for the NCM460 cell line. A contrast-phase microscope was used to observe and take pictures of the cells.

4.2.2 CELL DOUBLING TIME, VOLUME DETERMINATION AND SEEDING CONDITIONS

In order to establish the best incubation times to perform the molecular and metabolic measurements (see section 4.3), cell proliferation curves were first performed by measuring both cell number and cell volume using a Scepter™ Handheld Automated Cell Counter (Merk Millipore, USA). Results of cell volume and cell proliferation curves are shown in Appendix I. It was determined that for a correct relationship between cell confluence and cell growth, in order to obtain measurements from exponential growth of the cells but with a maximum confluence of

80% in the SW480 cell line and 60% in the SW620, LiM1, and LiM2 cell lines (as established by Dr Gomis' group), the initial seeding confluence would be $1{,}5 \cdot 10^5$ cells / p6 plate well (9,6 cm^2) for SW480 and $2 \cdot 10^5$ cells / p6 pate well for SW620, LiM1, and LiM2 cells and the ideal incubation time to reach just below the maximum confluence was 48h. For the case of NCM460, the same initial confluence as SW480 was determined. However, not all the experiments were performed at these conditions due to technical reason.

4.2.3 IC_{50} CURVE DETERMINATION USING HOECHST

When determining IC_{50} values using various concentrations of a specific inhibitor or a combination in p96 well plates, cell proliferation was estimated by assessing DNA content using Hoechst staining (HO33342). Cells were seeded at a density of $6 \cdot 10^3$ cells / p96 well plate (0.32 cm^2) in the case of SW480 and NCM460 and $8 \cdot 10^3$ cells / p96 well plate in the case of SW620 and LiM2. When cells were properly adhered, generally 24 hours after seeding, the medium was washed and medium with different concentrations of the inhibitor was applied, taking into account dimethyl sulfoxide (DMSO) concentrations in case the inhibitor was dissolved in DMSO (without reaching the maximum 1% of DMSO, the concentration at which cells would be affected). After 72 hours of incubation, the cell plates were washed with PBS, lysed with 0.01% SDS and frozen at -20ºC, thawed at 37ºC and incubated with 4 µg/mL of HO33342 in 1M NaCl, 1 mM EDTA, 10 mM Tris-HCl pH 7.4 for 1 hour at 37ºC in the darkness. Fluorescence was measured at 460 nm after excitation with 337 nm in a FLUOstar OPTIMA Microplate Reader (BMG LABTECH GmbH, Germany).

When establishing an IC_{50} value, a first experiment trying to cover the maximum range of concentration of each inhibitor was performed, and the following experiments tried to concentrate in the IC_{50} value having at least two values with 100% of proliferation, three or four that were around the 50% (the IC_{50} value), and two values that corresponded to 0% proliferation. When testing drug combinations, the same ratio between the two drugs was always maintained (see 3.5 for combination index value determination), and values above the IC_{50} were used in order to better assess the effect of the combination.

At some point, the IC_{50} curves were also assessed by imaging using IncuCyte® (Sartorius, Germany), an incubator that allows monitoring cells by live imaging. IncuCyte® software allowed to estimate cell proliferation by measuring the cell confluence (Figure 4.1.1A and B). Although the method worked well for SW480 cells (Figure 4.1.1C and E), the metastatic cell lines form aggregates growing on top of each other (Figure 5.1.4A), and therefore the confluence does not correspond with the real cellular content, which is better estimated by DNA content (Figure 4.1.1D and F). For that reason, we decided not to use IncuCyte data from confluence to determine IC_{50}, although it is a very powerful machine for high-throughput performance.

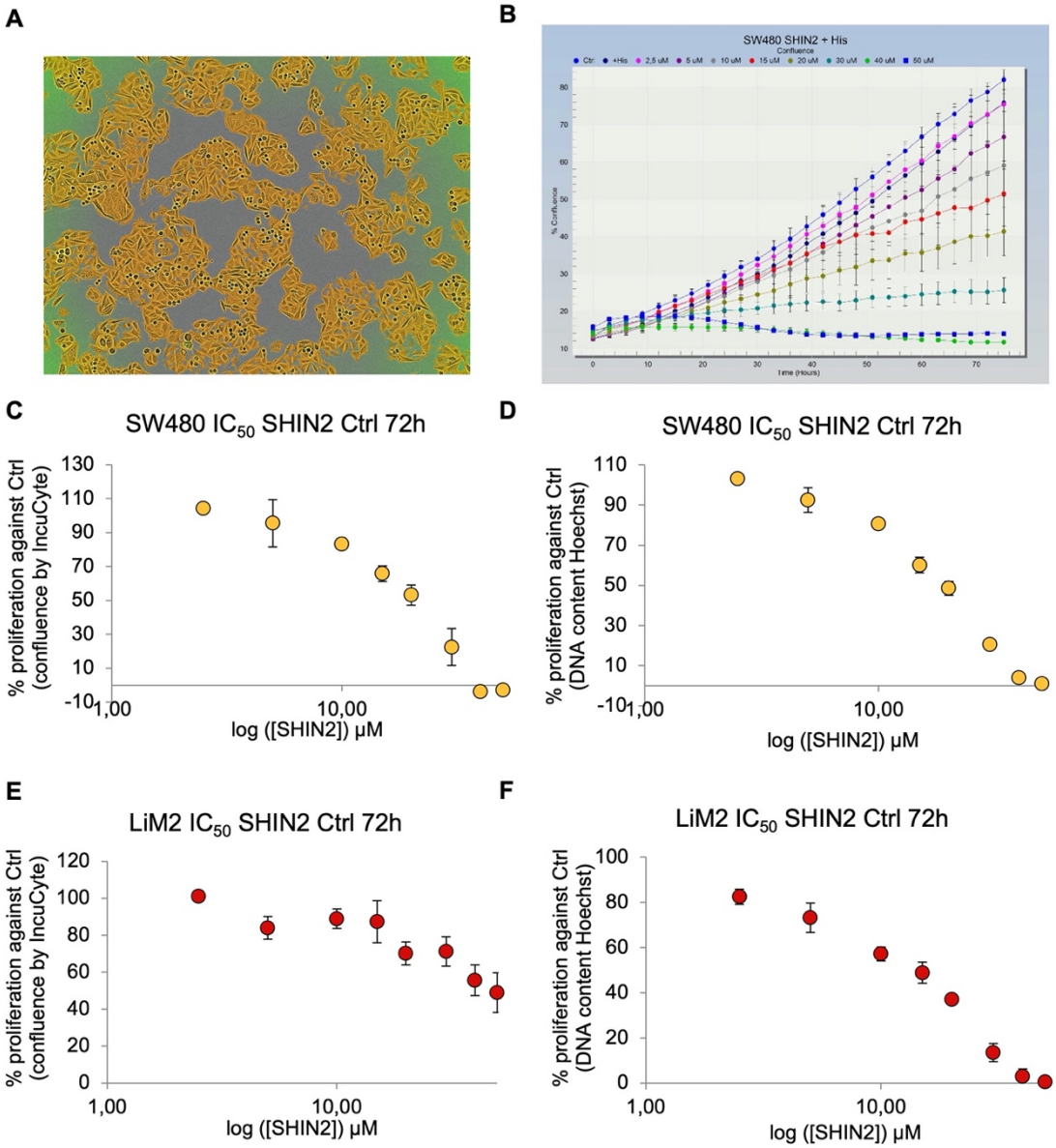

Figure 4.1.1. IC50 curve determination comparison between IncuCyte® confluence and DNA content approximation. A. IncuCyte® image with the confluence mask detecting the presence of cells. **B.** Growth curves from confluence live quantification of each p96 well with different concentrations of the SHMT1/2 inhibitor SHIN2. **C.** and **E.** IC50 curve of SHIN2 estimated with cell proliferation from confluence detected by IncuCyte® in SW480 (C) and LiM2 (E). **D.** and **F.** Same experiment in C and E but estimated with cell proliferation from DNA content determination by Hoechst staining in SW480 (D) and LiM2 (F).

4.2.4 CELL PROLIFERATION ASSAY USING FLUOROSPHERES

In specific experiments where a more precise number of cells was needed (more precise than the one obtained from the automated cell counter Scepter™ or the estimation using DNA content by Hoechst staining), cell count was determined by flow cytometry using flow-count fluorospheres (7547053, Beckman Coulter, USA). This was the case of glucose and glutamine deprivations, glucose deprivation adding pyruvate, cysteine deprivation and cysteine deprivation

adding N-acetylcysteine. Cells were seeded at the conditions specified in 3.2.2. At the end of each incubation (24, 48, and 72 hours, specified in each figure), cells were washed with PBS, trypsinised, centrifuged at 500g and resuspended with media containing 100000 fluorospheres / mL and immediately analysed by Gallios™ Flow Cytometer (Beckman Coulter, USA).

4.2.5 APOPTOSIS ASSAY

Apoptotic cells were determined by flow cytometry using Annexin V coupled with fluorescent isothiocyanate (FICT). In the case of apoptosis determination after cell deprivations, cells were seeded at the conditions specified in 3.2.2 and incubated for 24, 48, or 72 hours. In the case of apoptosis determinations after inhibitors incubations, cells were seeded at the same conditions specified in 3.2.2 and incubated for 72 hours at the IC_{50} concentration of the inhibitor. At the end of incubation, cells were washed with PBS (which was recovered), trypsinised, centrifuged at 500g and resuspended together with the detached cells in 10 mM Hepes pH 7.4, 140 mM NaCl, 2.5 mM $CaCl_2$ buffer. Annexin V-FICT was added according to the kit's instructions (Bender System MedSystem, Austria) and an incubation was performed in the darkness during 30 minutes at room temperature. Propidium iodide (PI) was added at 20 µg/mL before starting the analysis at the Gallios™ Flow Cytometer (Beckman Coulter, USA), which detected both Annexin and PI fluorescence.

Apoptosis was also assessed in some of the IC_{50} experiments (and therefore under conditions specified in 3.2.3) by imaging using IncuCyte® (Sartorius, Germany), after incubation in the presence of a caspase 3/7 green reagent (Sartorius 4440, Germany) at 1:200 dilution.

4.2.6 CELL CYCLE ANALYSIS

Cell cycle analysis was determined by flow cytometry for the glucose and glutamine deprivation experiments. Cells were seeded at the conditions specified in 3.2.2 and incubated for 24, 48, or 72 hours. After that, cells were washed with PBS, trypsinised, centrifuged at 500g and resuspended in 0.5 mL PBS. The cell suspension in PBS was added drop by drop to 4.5 mL of cold ethanol (70% v/v). After fixation, cells were centrifuged washed with PBS, resuspended in PBS that contained 0.2 mg/mL of DNAse free RNAse (Roche, Switzerland) and incubated at 37ºC for 1 hour. Then, PI was added at 20 µg/mL before starting the analysis at the Gallios™ Flow Cytometer (Beckman Coulter, USA), which determined PI fluorescence.

4.2.7 REACTIVE OXYGEN SPECIES (ROS) DETERMINATION ASSAY

Intracellular ROS levels were determined by flow cytometry using the H_2DCFDA reactive (Invitrogen, Thermo Fisher Scientific, USA). After seeding cells at the conditions specified in 3.2.2 and incubating for 72 hours, the medium was removed, and cells were incubated

with 5.5 mM glucose solution in PBS containing 5 µM of H_2DCFDA at 37ºC for 30 min in the cell culture incubator. After the probe was incorporated into de cells, the solution was removed and replaced by culture medium and incubated at 37ºC for 45 minutes. This step facilitates the activation of the probe by intracellular esterases. Finally, the cells were washed with PBS, trypsinised and resuspended in PBS containing 50 uM of H2DCFDA and 20 uM of PI prior to analysis at the Gallios™ Flow Cytometer (Beckman Coulter, USA), which detected the fluorescent probe that exciting at 492 nm, emitted at 520 nm, as well as PI fluorescence.

4.2.8 SPHEROIDS ASSAYS IN LOW ATTACHMENT PLATES

Cell lines were seeded on p24 well plates (10^3 cells/well) that with ultra-low attachment surface (Corning, USA) and with medium specified in 3.2.1 without FBS and containing 0.02 µg/mL EGF, 0.02 µg/mL BFGF, 10 µg/mL heparin, B27 supplement (50X) (Thermo Fisher Scientific, USA), 5 µg/mL insulin, and 0.5 µg/mL hydrocortisone. Cells were incubated for one week. For secondary spheroids assay, after the one-week incubation, the spheroids formed were disrupted by pipetting, filtered with 70 µm strainer and seeded again at the same conditions for one week more. Spheroids were analysed by phase-contrast microscopy and stained incubating them with 0.5 mg/mL MTT (3-[4,5-dimethylthiazol-2-yl]-2,5-diphenyltetrazolium bromide) at the end of incubation for 4h. Quantification was made by ImageJ software scanned images with the tool Analyse particles applying a size of a particle from 0.0000785 – infinite cm^2 and "total area" was taken as the value to estimate and compare spheroid formation capacity between samples.

4.2.9 SPHEROIDS ASSAYS IN MATRIGEL

Using low attachment plates is a good technique for spheroid formation assay but it is established that using a Matrigel matrix is even better representing the *in vivo* context (Kapałczyńska et al., 2018). For that reason, we used this second technique when studying spheroid formation under inhibitors treatment. Trypsinsed and centrifuged cell lines were resuspended on a mix of 50% medium (specified in 3.2.1) and 50% Matrigel Matrix (Corning, USA) at a total $4 \cdot 10^4$ cell/mL density, keeping all the time the Matrigel solution, Matrigel mix and cell suspension on ice. Then, 4 spots of 5uL each were done on each well of a p24 well plate that was previously warmed at 37ºC. Then, the plate was placed in the incubator at 37ºC for 10 minutes so that the spots could be gelled and after that warm medium (containing IC_{50} concentration of the inhibitor when specified) was added and incubated for one week. Spheroids were analysed by phase-contrast microscopy and stained incubating them with 0.5 mg/mL MTT (3-[4,5-dimethylthiazol-2-yl]-2,5-diphenyltetrazolium bromide) for 4h. Quantification was made by ImageJ software scanned images with the tool Analyse particles applying a size of a particle

from 0.0000785 – infinite cm^2 and "total area" was taken as the value to estimate and compare spheroid formation capacity between samples.

4.2.10 WOUND HEALING ASSAY

Cell lines were seeded on p24 well plates ($6 \cdot 10^4$ cells/well for SW480 and $8 \cdot 10^4$ cells/well for SW620 and LiM2). The media was replaced after 24h by another media containing 0.5% of mitomycin and 0% FBS. After 1h incubation, an artificial wound was performed by scratching the monolayer using a pipette tip. The wound's width was measured at 0, 3, 7, 24 and 48h using phase-contrast microscope images and ImageJ software.

4.2.11 WESTERN BLOTTING

Protein extracts were obtained from the cultured cells or dry tissue incubating for 20 minutes at 4ºC with RIPA buffer (50 mM Tris pH 8.0, 150 mM sodium chloride, 1% Triton X-100, 0.5% sodium deoxycholate, 0.1% sodium dodecyl sulphate (SDS), 1% protease inhibitor cocktail and 1% phosphatase inhibitor cocktail (Thermo Fisher Scientific, USA) and scrapping, sonicating and centrifuging at 12000g, 4ºC for 20 minutes.

Equal amounts of protein extracts, previously measured by Pierce Bicinchoninic Acid assay (Thermo Fisher Scientific, USA), were diluted in 5X loading buffer (250 mM Tris pH 6.8, 50 mM DTT, 10% SDS, 50% glycerol and 0.02% bromophenol blue) and incubated for 5 minutes at 100ºC. Then, the denaturised protein extracts were separated by SDS-PAGE gel (stacking gel: 5% acrylamide/bisacrylamide in 125 mM Tris pH 6.8, 1% SDS, 1% ammonium persulfate (APS) and 0.01% N,N,',N'-tetramethylethylenediamine (TEMED); resolving gel: 8-12% depending on the size of the proteins that were analysed at each case in 375 mM Tris pH 8.8, 1% SDS, 1% APS and 0.01% TEMED) using an electrophoresis buffer (25 mM Tris pH 8.3, 192 mM glycine and 1% SDS). When the gel is resolved, it was transferred to polyvinylidene fluoride transfer membranes with a transfer buffer (25 mM Tris pH 8.3, 192 mM glycine, 20% methanol). Membranes were blocked with 5% non-fat milk in PBS-0.1% Tween 20 and incubated with a specific primary antibody (Table 4.1.1) o/n at 4ºC. The next day, incubation with the appropriate Horseradish peroxidase (HRP)-labelled secondary antibody was performed for 1h at room temperature. HRP activity was assessed with Immobilon ECL Western Blotting Detection Kit Reagent and detected by exposition with photographic film. Quantification of the bands was performed using ImageJ software, normalising the quantification using the TATA box levels as a loading control. When ratios between phosphorylated forms and total forms of a protein are calculated, first the bands are quantified and normalised by TATA box levels and then calculating the ratio.

Antibody	Source	Reference	Dilution
Primary antibodies			
Rabbit anti-E-cadherin	Abcam, UK	ab1416	1:1000
Mouse anti-N-cadherin	BD Transductions Lab, USA	610920	1:1000
Rabbit anti-Fibronectin 1	Merck Sigma Aldrich, USA	F3648	1:2000
Mouse anti-vimentin	Thermo Fisher Scientific, USA	MS-129	1:1000
Rabbit anti-ZEB1	Merck Sigma-Aldrich, USA	ABE596	1:1000
Rabbit anti-ZEB2	Merck Sigma-Aldrich, USA	AV33694	1:1000
Rabbit anti-Twist 1/2	Genetex, USA	GTX127310	1:1000
Rabbit anti-Snai1	Genetex, USA	GTX125918	1:1000
Rabbit anti-NF-κB	Santa Cruz Biotechnology, USA	sc-8008	1:2000
Rabbit anti-β-catenin	Merck Millipore, USA	06-599	1:500
Mouse anti-γ-catenin	Santa Cruz Biotechnology, USA	sc-8415	1:10000
Mouse anti-EGFR	Santa Cruz Biotechnology, USA	sc-373746	1:500
Rabbit anti-ERK2	Santa Cruz Biotechnology, USA	sc-154	1:1000
Rabbit anti-Akt	Cell Signalling Technology, USA	9272S	1:500
Rabbit anti-P-Akt (S473)	Cell Signalling Technology, USA	9271	1:1000
Rabbit anti-PTEN	Cell Signalling Technology, USA	9188S	1:1000
Rabbit anti-mTOR	Cell Signalling Technology, USA	2972	1:1000
Rabbit anti-P-mTOR (S2448)	Cell Signalling Technology, USA	55365	1:1000
Rabbit anti-cMyc (Y69)	Abcam, UK	ab32072	1:10000
Mouse anti-HIF1α	Santa Cruz Biotechnology, USA	sc-13515	1:5000
Mouse anti-p53	Chalbiochem	OP09	1:200
Mouse anti-PDH (sub E1)	Abçcam, UK	ab110330	1:1000
Rabbit anti-P-PDH (S293)	Merck Millipore, USA	ABS204	1:10000
Mouse anti-PDK1	Santa Cruz Biotechnology, USA	sc-293160	1:200
Goat anti-PDK3	Santa Cruz Biotechnology, USA	sc-14490	1:100
Rabbit anti-PDP2	Abcam, UK	ab99170	1:500
Rabbit anti-PC	Abcam, UK	ab126707	1:10000
Rabbit anti-GLS	Abcam, UK	ab93434	1:1000
Rabbit anti-GLUD1	Abcam, UK	ab166618	1:1000
Rabbit anti-KGA	Proteintech, USA	20170-1AP	1:2000
Rabbit anti-SHMT2	Abcam, UK	ab155230	1:10000
rabbit anti-TATA (TBS)	Abcam, UK	ab63766	1:1000
Secondary antibodies			
Anti-Mouse	Abcam, UK	GR304350-1	1:20000
Anti-Rabbit	Abcam, UK	GR297013-4	1:20000
Anti-Goat	Santa Cruz Biotechnology, USA	sc-2020	1:10000

Table 4.1.1. Primary and secondary antibodies. Primary and secondary antibodies used in order of appearance.

4.3 METABOLIC AND METABOLOMIC EXPERIMENTS

4.3.1 EXTRACELLULAR METABOLITE MEASUREMENTS BY SPECTROPHOTOMETRY

Glucose, lactate, glutamine, glutamate and pyruvate uptake and secretion rates were measured from cell culture media concentrations at initial and final incubation time (see Appendix I for optimisation of incubation times and cell seeding conditions) using a COBAS Mira Plus spectrophotometer (Horiba ABX, Japan). Determination of glucose was performed using hexokinase and D-glucose-6-phosphate dehydrogenase coupled reactions (kit ABX Pentra Glucose HK CP, Horiba ABX, Japan) and NADPH release was measured at 340 nm. Lactate was measured using lactate dehydrogenase (LDH) mixing the samples with a buffer containing the enzyme LDH at 87.7 U/mL, 28.6 mM $(NH_4)_2SO_4$, 1.55 mg/mL NAD^+ in 0.2 M hydrazine, 12 mM EDTA pH 9 at 37ºC and NADH release was measured at 340nm. Glutamate was quantified by glutamate dehydrogenase (GLUD1) mixing the samples in a buffer containing GLUD1 at 39 U/mL, 2.41 mM ADP, 3.9 mM NAD^+ in 0.5 M hydrazine, 0.5 M glycine pH 9 at 37ºC and NADH release was measured at 340 nm. Glutamine was measured indirectly by first transforming it to glutamate by glutaminase (GLS), mixing the samples with a buffer containing 125 mU/mL of GLS and 125 mM acetate pH 5 at 37ºC for 30 minutes in agitation and subsequently performing the same reaction as for glutamate concentration determination. Pyruvate was quantified by mixing the samples with a buffer containing LDH at 790 mU/mL, 11.6 mM $(NH_4)_2SO_4$, 0.28 mM NADH in 0.53 M triethanolamine, 5.3 mM EDTA-Na_2 pH 7.8 at 37ºC and NADH extinction was measured at 340 nm.

The estimation of metabolite uptake and secretion rates was done from the spectrophotometric measurement variation between the final and initial point of the incubation and taking into account the cell number at both points assuming exponential growth that was previously verified (Appendix I) following the equation 1:

$$\begin{cases} \dfrac{dN_t}{dt} = N_t \cdot \mu \\ \dfrac{dM_t}{dt} = N_t \cdot J_{met} \end{cases}$$

Equation 1

where N is the cell number (the difference between final and initial cell number), M is the metabolite quantity (the difference between final and initial measurement) and μ is the growth rate and J_{met} is the metabolite uptake or secretion rate.

4.3.2 TARGETED METABOLOMICS

Intracellular metabolite profiling and determination of uptake and secretion rates were performed using the Biocrates Absolute IDQ™ p180 kit (Biocrates Life Sciences AG, Austria).

For the quantification of intracellular metabolites, cells were seeded at high confluence conditions in order to obtain the maximum quantity of cell pellet ($5 \cdot 10^6$ cells for NCM460 and SW480 and $7.5 \cdot 10^6$ cells for SW620, LiM1 and LiM2) in 100 mm plates. After 24 hours of incubation, cells were trypsinised and centrifuged at 500g for 5 minutes to obtain the cell pellet and cell medium. Pellet was resuspended in 70 µL of 85:15 ethanol:PBS buffer and sonicated 3 times for 5 seconds each, then submerged in liquid nitrogen for 30 seconds and thawed at 95ºC. Then, it was centrifuged 20000 g, 5 minutes at 4ºC, the supernatant was collected, and protein content was measured. For the determination of metabolites uptake and production, metabolites were extracted from cell media taken from the beginning and the end of the incubation in the same conditions as intracellular measurements. Both extracts from pellets and media were plated in the Biocrates plate together with the calibration standards, and derivatised to be ready for UHPLC-MS reading (for amino acids and biogenic amines) and FIA-MS/MS (for lipids, sugars and acylcarnitines) according to the manufacturer's instructions. A total of 21 amino acids, 19 biogenic amines, 90 glycerophospholipids, 15 sphingolipids, 40 acylcarnitines and hexose sugars were analysed. The data were normalised by protein and transformed into a Log2 scale. Clustering and heatmap and statistical analysis were performed using the Metaboanlyst webserver (Chong et al., 2019). In order to determine the metabolite uptake and secretion rates, the same estimation specified at 4.3.2 was used.

4.3.3 STABLE ISOTOPE-RESOLVED METABOLOMICS (SIRM)

For ^{13}C-resolved metabolomics, cells were seeded at $2 \cdot 10^6$ (NCM460 and SW480) and $2.5 \cdot 10^6$ (SW620 and LiM2) cells were seeded in 100 mm plates and after 24 hours the media was changed for either 12.5 mM glucose 50% enriched in [1,2-^{13}C]-glucose, or 4 mM glutamine 50% enriched in [U-^{13}C]-glutamine, or unlabelled substrates. Cells and media were obtained and measured immediately or frozen at -80ºC for metabolite extractions at 6 and 24 hours after the labelled substrates were added. Extracellular metabolite measurements were also performed by spectrophotometry for these samples according to the method 3.3.2.

The analyses of ^{13}C-labelled intracellular and extracellular metabolites for isotopologue distribution were performed using an Agilent 7890A gas chromatograph (Agilent Technologies, USA) with an HP-5 capillary column coupled to an Agilent 5975C mass spectrometer. For analysis, 1 ul of each sample was injected together with helium gas as a carrier at a 1 mL/min of flow rate.

4.3.3.1 Polar intracellular metabolites

For polar intracellular metabolites analysis, cells were washed with ice-cold PBS and scrapped with 1:1 metanol:water (adding first 1 mL of methanol, waiting for 1 minute and adding

1 mL of milliQ water afterwards). At that point, 5 uL of norvaline 1 mg/mL was added for quantification purposes to minimise the differences that could be associated with efficiency of extraction. Then, the samples were sonicated (3 cycles of 5 seconds) and 2 mL of cold chloroform was added. After gentle shaking (30 minutes at 4ºC) the samples were centrifuged (20000 g, 15 minutes at 4ºC) and the supernatant was completely dried under airflow. The extracted metabolites were derivatised by adding 50 µL of 2% methoxamine hydrochloride in pyridine for 90 minutes at 37ºC and (N-methyl-N-tert-butyldimethylsilyl) trifluoroacetamide + 1% tertbutyldimethylchlorosilate) for 60 minutes at 55ºC before GC-MS analysis using electron impact mode. The oven temperature variations were programmed as follows: 100ºC during 3 minutes, then increased to 165ºC at 10ºC/min, to 225ºC at 2.5ºC/min, to 265 at 25ºC and finally to 300ºC at 7.5ºC/min. The detector was run at single ion monitoring (SIM) mode. In the next table all the intracellular metabolites that were analysed are specified (Table 4.1.2).

4.3.3.2 Other metabolites

For intracellular ribose analysis, RNA was isolated from cell pellets using Trizol reagent, mixing it with chloroform. The aqueous phase was obtained, and cold isopropanol was added and centrifuged 12000 g, 15 minutes at 4ºC. The samples were washed several times using cold 75% ethanol and isolated RNA was quantified using a Nanodrop spectrophotometer (ND 1000 V3.1.0, Thermo Fisher Scientific). The samples of purified RNA were hydrolysed in 2 mL of 2 M HCl at 100ºC for 2 hours, dried under airflow and resulting ribose was derivatised into its aldonitrile acetate derivative using 100 µL of 2% hydroxylamine hydrochloride in pyridine at 100ºC for 30 minutes and 75 µL of acetic anhydride at 100ºC for 1 hour. Then, samples were dried under N_2 flow and resuspended in ethyl acetate before GC-MS analysis using chemical ionisation mode. The oven temperature variations were programmed as follows: 150ºC during 1 minute, then increased to 275ºC at 15ºC/min, to 300ºC at 40ºC/min, and hold for 2 minutes. The detector was run at SIM mode. Ribose complete fragment C1-C5 was detected at 5.3 minutes of retention time monitoring the cluster 257 m/z from the range 256-261 m/z.

For extracellular glucose analysis, glucose from cell culture media was isolated using Dowex-1X8/Dowex-50WX8 ion-exchange columns and samples were dried under airflow. Purified glucose was derivatised by incubation with 100 µL of 2% hydroxylamine hydrochloride in pyridine at 100ºC for 30 minutes and 75 µL of acetic anhydride at 100ºC for 1 hour. Then, samples were dried under N_2 flow and resuspended in ethyl acetate before GC-MS analysis using chemical ionisation mode. The oven temperature variations were programmed as follows: 230ºC for 2 minutes, then increased to 260ºC at 10ºC/min, to 270 at 25ºC/min, and hold for 2 minutes. The detector was run at SIM mode. Glucose complete fragment C1-C6 was detected at 3.7 minutes of retention time by monitoring the cluster 328 m/z from the range 327-336 m/z.

Compound	Fragment	Retention time (min)	m/z cluster	m/z cluster range	m/z control
Pyruvate	C1-C3	7,9	174,1	173.1-179.1	216,1
Lactate	C1-C3	11,4	261,1	260.1-266.1	303,1
Alanine	C1-C3	12,2	260,1	259.1-265.1	232,1
Alanine	C2-C3	12,2	232,1	231.1-237.1	260,1
Glycine	C1-C2	12,6	246,1	245.1-250.1	218,1
Glycine	C2-C3	12,6	218,1	217.1-221.1	246,1
Valine	C1-C5	14,5	260,2	259.2-267.2	288,1
Norvaline	C1-C5	14,7	260,2	259.2-267.2	288,1
Leucine	C1-C6	15,4	274,2	273.2-282.2	302,1
Isoleucine	C1-C6	16,1	302,2	301.2-310.2	274,1
Succinate	C1-C4	16,84	289,1	288.1-295.1	331,2
Proline	C1-C5	17	286,1	285.1-293.1	258,2
Proline	C2-C5	17	258,2	257.2-264.2	286,1
Itaconate	C1-C5	17,25	301,1	300.1-309.1	343,1
Fumarate	C1-C4	17,55	287,1	286.1-293.1	329,1
Oxaloacetate	C1-C4	20	374	373-384	-
Methionine	C1-C5	22,5	320,2	319.2-327.2	292,2
Methionine	C2-C5	22,5	292,2	291.2-298.2	320,2
Serine	C1-C3	23,2	390,2	389.2-395.2	362,2
Serine	C2-C3	23,2	362,2	361.2-366.2	390,2
α-ketoglutarate	C1-C5	23,8	346,1	345.1-353.1	388,2
Threonine	C1-C4	24	404,2	403.2-410.2	376,2
Phenylalanine	C1-C9	26,2	336,2	335.2-347.2	308,2
Malate	C1-C4	26,9	419,2	418.2-425.2	461,3
Aspartate	C1-C4	28	418,2	417.2-424.2	390,2
Aspartate	C2-C4	28	390,2	389.2-396.2	418,2
Cysteine	C1-C3	29,5	406,2	405.2-411.2	378,2
Cysteine	C2-C3	29,5	378,2	377.2-382.2	406,2
2-hydroxyglutarate	C1-C5	29,3	433,2	432.2-443.2	475,2
Glutamate	C1-C5	31,6	432,3	431.3-439.3	474,3
Ornithine	C1-C5	31,8	474,4	473.4-481.4	417,3
Asparagine	C1-C4	32,8	417,3	416.3-423.3	459,2
Lysine	C1-C6	34,5	431,2	430.2-439.2	488,4
Cis-aconitic acid	C1-C6	34,7	459,3	458.3-467.3	501,3
Histidine	C1-C6	37	440,3	439.3-448.3	482,3
Kynurenine	C1-C10	37,1	379,2	378.2-391.2	436,3
Citric acid	C1-C6	37,3	591,4	590.4-599.4	459,2
Tyrosine	C1-C9	37,5	466,3	465.3-477.3	438,3
Tryptophan	C1-C11	38	375,2	374.2-388.2	302,2
Pyruvate	C1-C3	7,9	174,1	173.1-179.1	216,1

Table 4.1.2. Intracellular metabolites quantified by GC-MS. Intracellular metabolites and fragments that were quantified with its theoretical retention time (the real retention time was recorded for each run), and the monitored clusters and ranges, that were previously optimised for maximum detection. An extra cluster was detected for control purposes.

For extracellular lactate analysis, lactate from cell culture media was isolated using HCl and ethyl acetate previous to airflow drying. Lactate was derivatised to lactate acid n-propylamide-heptafluorobutiric ester by incubation with 200 µL of 2,2-dimethoxypropane and 50 µL of 0.5 N methanolic HCl at 75ºC for 1 hour and then adding 60 µL of n-propylamine at 100ºC for 1 hour more. After drying under N_2 flow, samples were filtered using glass wool through a Pasteur pipette and dried again under N_2 flow. Then, samples were resuspended and incubated with 200 µL of dichloromethane and 15 µL of heptafluorobutyric anhydride at room temperature for 10 minutes, dried under N_2 and resuspended under ethyl acetate before GC-MS analysis under chemical ionisation mode. The oven temperature variations were programmed as follows: 100ºC for 3 minutes, then increased to 160ºC at 20ºC/min, and hold for 2 minutes. The detector was run at SIM mode. Lactate complete fragment C1-C3 was detected at 5.4 minutes of retention time by monitoring the cluster 328 m/z from the range 327-332 m/z.

For extracellular amino acids analysis (glutamate and glutamine), these were isolated from cell culture media using Dowex-50WX8 ion-exchange columns and elution with NH_4OH before samples were dried under airflow. Then, samples were resuspended in 1 mL of H_2O, passed through the Dowex-1X8 ion-exchange column and either eluted with 10 mL of H_2O for glutamine isolation or eluted with 10 mL of acetic acid after H_2O washes for glutamate isolation. In order to Amino acids were derivatised to their n-trifluoroacetyl-n-butyl ester by incubation with 200 µL of butanolic HCl at 100ºC for 1 hour, followed by drying with N_2 flow to remove the excess of reagent. Then, the precipitate was re-dissolved in 100 mL of dichloromethane and 25 mL of trifluoroacetic anhydride and incubated at room temperature for 20 minutes. Samples were dried under N2 flow and dissolved in dichloromethane for GC-MS analysis under chemical ionisation mode. The oven temperature variations were programmed as follows: 110ºC during 1 minute, then increased to 125ºC at 10ºC/min, to 153ºC at 5ºC/min, to 200ºC at 50º/C/min and to 216ºC at 5ºC minute and for 1 minute more, ending to 250ºC at 25ºC/Minute, and hold for 2 minutes more. The detector was run at SIM mode. Glutamate/glutamine complete fragments C1-C5 were detected at 12.8 minutes of retention time by monitoring the cluster 228 m/z from the range 227-231 m/z.

4.3.3.3 SIRM data analysis

Raw MS data was examined using MSD5975C Data Analysis (Agilent Technologies). The data obtained by mass spectrometry represents a spectral distribution of ions with its molecular weights (m/z) at each retention time. The ion clusters, which were specified for each case, were used to determine the distribution of ^{13}C at each carbon of the fragment. Therefore, manual integration of peak areas was needed to quantify the distribution of each compound, as at the same time and with the data of the present work, a software called “Ramid” for automated integration was being performed by the computational team of our research group (see Appendix

VI.3) (Selivanov et al., 2020). The software, based in "R", allow extraction of the NetCDF files containing the m/z raw time course to isotopologue distributions.

However, the values of peak areas, which are proportional to the 13C incorporation to each molecule of the compound, need to be corrected for the presence of natural abundance of ^{13}C as well as Si isotopes that are present from the derivatisation reagents and contribute to the mass isotopologue distribution. The correction was performed from isotopologue distributions extracted before, using the "Midcor" software package (Selivanov et al., 2017, 2020).

Afterwards, data was analysed and represented as direct substrate contribution of to specific isotopologues (m1, m2, m3, etc. according to the number of ^{13}C that were labelled) normalised by total contribution: (mn / Σm). In the case of glucose contribution to lactate, m2 was represented (Figure 4.1.2A) and for glucose contribution to TCA cycle, m2 isotopologues of citrate, malate and fumarate were represented (Figure 4.1.2B), obtained from polar intracellular metabolites analysis. In the case of glutamine contribution to the TCA cycle, isotopologues from oxidative and reductive carboxylation were represented (Figure 4.1.3), also obtained from PIM analysis.

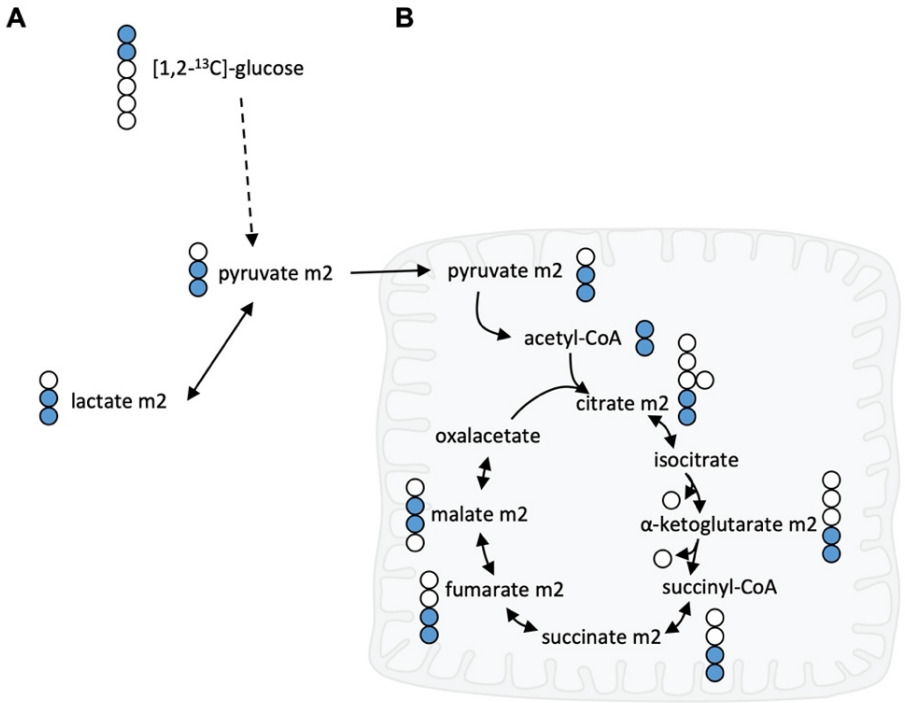

Figure 4.1.2. [1,2-^{13}C]-glucose contribution to lactate and the TCA cycle. A. and **B.** Schematic representation of the ^{13}C (in blue) and ^{12}C (in white) distribution to intracellular lactate (A) or TCA intermediaries (B) from [1,2-^{13}C]-glucose.

Glucose contribution to the pentose phosphate pathway can be determined by the analysis of intracellular ribose and different isotopologues from oxidative and non-oxidative branches of the pathway can be represented (Figure 4.1.4).

Finally, SIRM data was also integrated into the genome-scale metabolic model that was done by the computational team of our research group as explained in Appendix V, section 13.1.7.

A central carbon metabolism flux map was performed by using the framework of ^{13}C metabolic flux analysis (MFA).

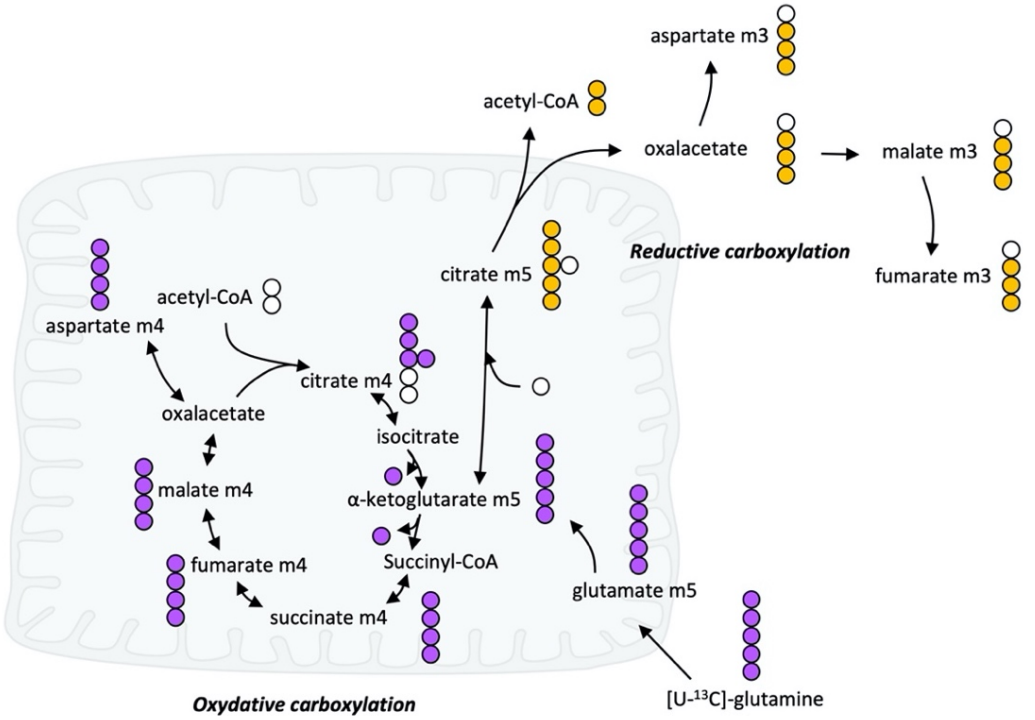

Figure 4.1.3. [U-^{13}C]-glutamine contribution to lactate and the TCA cycle. Schematic representation of the ^{13}C (coloured) and ^{12}C (in white) distribution TCA cycle by oxidative carboxylation (purple) or reductive carboxylation (orange) from [U-^{13}C]-glutamine.

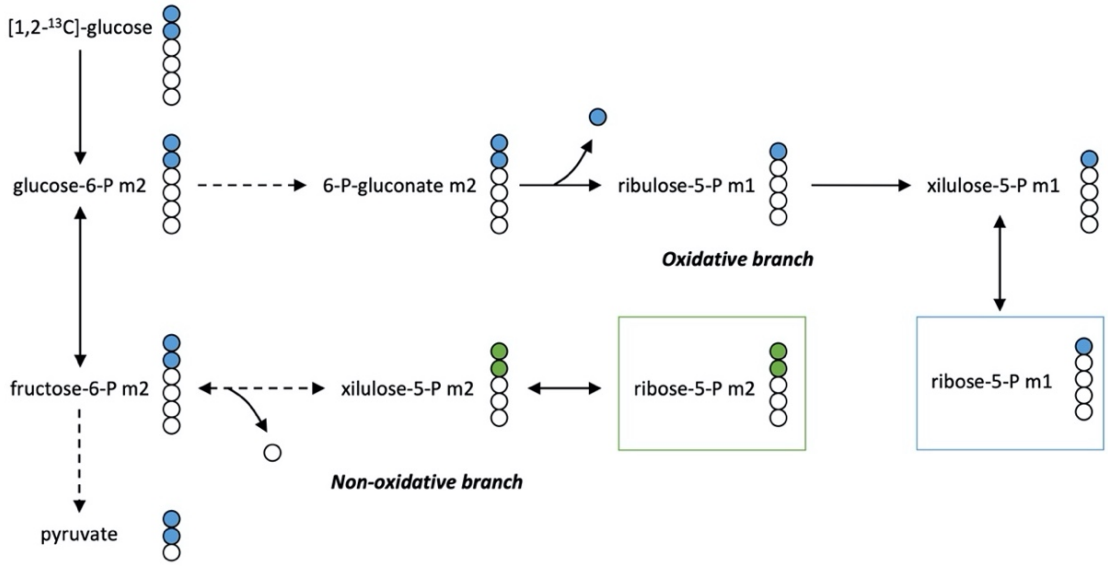

Figure 4.1.4. [1,2-^{13}C]-glucose contribution to ribose through the pentose phosphate pathway. Schematic representation of the ^{13}C (coloured) and ^{12}C (in white) distribution to intracellular ribose through the oxidative branch of PPP (blue) or non-oxidative branch of PPP (orange) from [1,2-^{13}C]-glucose.

4.4 *IN VIVO* EXPERIMENTS

4.4.1 XENOGRAFT EXPERIMENTS

SW480, SW620, and LiM2 cell lines (1 million cells/mouse) were injected subcutaneously into immunosuppressed NOD/SCID male mice, previous to a test for mycoplasma contamination. Before injections, the cells were trypsinised and resuspended in 50% Extracellular Matrix gel (E6909, Sigma-Aldrich, USA) : 50% DMEM 12.5 mM Glc and 4 mM Gln, 5% FBS, and 1% S/P. A total of 29 mice were injected, 10 mice per cell lines (except for LiM2, for which we injected 9 mice). Tumour volume was measured two times per week with a calliper until the tumours reached 8-10 mm in diameter. All procedures were carried out at the Francis Crick Institute under pathogen-free conditions and assuring animal well-being according to the Local Ethics Comitee.

4.4.2 IMMUNOHISTOCHEMISTRY

Tumour tissue, liver, lung and spleen were obtained from mice wearing a tumour of 8-10 mm in diameter. After fixation in 4% paraformaldehyde the tissues were paraffin-embedded and mounted slides were obtained (part of the slides were stained by haemotoxylin and eosin for tissue and others were led in paraffin for immunohistochemistry). Then, deparaffination was achieved by washes with xylene and decreasing ethanol concentrations until rehydration of the slides (2 times 3 minutes wash with 100% xylene, 3 minutes with 1:1 xylene:ethanol, 2 times 3 minutes with 100% ethanol, 3 minutes with 95% ethanol in water, 3 minutes with 70% ethanol in water, 3 minutes in 50% ethanol in water and 3 minutes in 100% water). Then, antigen unmasking was performed in 95-100ºC bath for 20 minutes with high pH retrieval solution (from Dako kit EnVision dual Link System-HRP DAB+ K4065, Agilent Technologies, USA). Then, the slides were blocked with the Dual Endogenous Enzyme Block solution from the same kit for 10 minutes at room temperature, washed with the wash buffer from the kit (2 washes of 5 minutes) and incubated O/N at 4ºC in a humidified chamber with the corresponding antibodies diluted with the antibody dilutant from the kit. The antibodies used were rabbit anti-GLS (ab93434, Abcam, UK) diluted at 1:100 with antibody diluent solution, rabbit anti-E-cadherin (GTX629691, Genetex, USA) diluted at 1:500, rabbit anti-Vimentin (GTX629744, Genetex, USA) diluted at 1:500. The next day, after washing twice for 5 minutes with the wash buffer, the slides were incubated with the labelled polymer (-HRP) from the kit for 30 minutes and after another 2 washes of 5 minutes, the antibody binding was stained by the DAB+ chromogen solution. The slides were dehydrated (same hydration steps in the opposite direction) and mounted with Dako Mounting Medium CS703. Images of the stained slides were taken in an optical microscope (40X) and analysed with ImageJ software.

4.4.3 STABLE ISOTOPE-RESOLVED METABOLOMICS *IN VIVO*

After cell line injections into immunocompromised NOD/SCID mice (see section 4.4.1) and once tumours reached 8-10 mm in diameter mice were given a bolus of either [U-^{13}C]-glucose (1 bolus of 20 mg / 35 g) or [U-^{13}C]-glutamine (2 boluses of 6 mg / 35 g each, with 15 minutes interval). 15 minutes after the last bolus, the mice were terminally anaesthetised, and blood was taken by cardiac puncture. Tumour tissue was snap-frozen in liquid nitrogen and keept at -80ºC. Then, tumour samples were ground in liquid nitrogen to form a powder, which was lyophilised. Metabolites were extracted from 10 mg of dry tissue with methanol:chloroform 1:2. First, 600 µL of cold methanol containing 5 nmols of scyllo-inositol, 10 nmols of N-norleucine and 1.5 nmols of ^{15}N^{13}C-valine were added as internal standards. Then, 1200 µL of chloroform was added and after extensive vortexing, the tubes were sonicated (3 times, 8 minutes, 4ºC) and centrifugated (20 minutes, 4ºC, 20000g). The supernatant is dried in a speed-vacuum machine and 500 µL of methanol:water is added to the pellet for a second extraction following the same steps as before, adding it to the first dried supernatant and drying it as well. Separation of polar and apolar phase is performed by addition of 3:3:1 methanol:water:chloroform (150:150:50 µL) and vortexing and centrifugation (30 minutes, 4ºC , 20000g). The extracted metabolites in the polar phase were derivatised by adding 50 µL of 2% methoxamine hydrochloride in pyridine for 90 minutes at 37ºC and (N-methyl-N-tert-butyldimethylsilyl) trifluoroacetamide + 1% tertbutyldimethylchlorosilate) for 60 minutes at 55ºC before GC-MS analysis (Agilent 7890A gas chromatography coupled to an Agilent 5975C mass spectrometer, Agilent Technologies, Santa Clara, CA, USA) using electron impact mode. The oven temperature variations were programmed as follows: 100ºC for 3 minutes, then increased to 165ºC at 10ºC/min, to 225ºC at 2.5ºC/min, to 265 at 25ºC, and finally to 300ºC at 7.5ºC/min. The detector was run at single ion monitoring (SIM) mode.

The polar intracellular metabolites that were analysed are the same as specified in Table 4.1.2 and the posterior data analysis was performed as explained in section 4.3.3.3.

4.5 STATISTICAL ANALYSES

All experiments were performed at least in triplicates and repeated at least two or three times. All data were represented as mean ± standard deviation. For the comparisons that are between the cell lines (NCM460, SW480, SW620, LiM1 and LiM2) we used a one-way ANOVA for the factor “cell line”, and Scheffe’s test for multiple comparisons. Groups that show the same letter are not significantly different with α=0.05. In other cases, for comparisons between two conditions, we used Student’s *t* test with $p<0.05$, and we used asterisk (*) to indicate significant differences. Furthermore, we used Shapiro-Wilk test to assess normal distribution of the experimental data and Dixon’s Q-test to identify outliers and Levene’s test to test homogeneity of variances. “R” software was used to perform all statistical analysis, except for the combined

drug treatments statistical analysis, which was performed with CompuSyn software (ComboSyn, Inc., USA). The software allows determining the Combination Index for each drug combination treatment (done by respecting the same ratio of concentrations between the two drugs). In that case, CI<1, CI=1 and CI>1 indicates synergy, additive effect, and antagonism, respectively, as described by Chou and Talalay (Chou, 2010).

5. Results and discussion

5 RESULTS AND DISCUSSION

5.1 CHAPTER 1. METABOLIC CHARACTERISATION OF THE METASTATIC PROGRESSION IN COLORECTAL CANCER

5.1.1 INTRODUCTION

5.1.1.1 The SW480 – SW620 cell lines model

Cell lines are one of the main biological resources that researchers use to study physiological and biochemical mechanisms at the level of cell biology. Different from primary cells directly derived from humans or animals, cell lines have been permanently established through different methods in cell cultures and proliferate indefinitely, having become immortalised. Specifically, in the field of cancer biology, cultured cancer cells are broadly used, because in culture conditions, cancer cells are thought to behave similarly as in the human body in terms of proliferation.

SW480 and SW620 are two established colon cancer cell lines derived from the same patient, a 50 years Caucasian male (Leibovitz et al., 1976). SW480 was isolated from the primary colon adenocarcinoma, which was Duke's type B. Duke's classification has been replaced nowadays by the TNM staging and is no longer used in clinical practice. Duke's B meant there was invasion through the serosa but not lymph node metastasis. SW620 was extracted from the lymph node of the same patient at 51 years old when the patient had a colon adenocarcinoma Duke's type C, which implies lymph node invasion. Both lines bear a *KRAS* mutation in G12V codon. Remarkably, among the possible mutations found in *KRAS*, G12V is related to poor prognosis and higher metastatic efficiency (Alamo et al., 2015; Hayama et al., 2019). The cell lines are also positive for the oncogenes *MYC*, *MYB*, *RAS*, *FOS*, *SIS*, and *TP53*, and negative for *ABL*, *ROS* and *SRC*.

Therefore, SW480 and SW620 is a very valuable model for the study of metastasis progression and the multiple alterations associated with it. It has been further validated as a good model of metastasis, as SW620 appeared to be more tumorigenic and malignant *in vivo* (Hewitt et al., 2000) and present gradual metastatic capacities. The model has been widely studied in terms of cellular and molecular phenotype. Some of the molecular traits with potential consequences for metastasis that have been published are an enhanced anti-apoptotic adaptation of SW620 with respect to SW480 (Maamer-Azzabi et al., 2013), as well as increased cytoskeleton dynamics (Ghosh et al., 2011). In addition, prior metabolic studies have been performed with SW480 and SW620, which provide a preliminary metabolic insight into the differences between these cell lines (Figure 5.1.1). In this regard, higher levels of polyamines metabolism are present in SW620

(Duranton et al., 2003). In addition, SW620 shows decreased levels of Nitric Oxide (NO), which reduces vasodilatation and induces platelet aggregation and metastasis (Radomski et al., 1991).

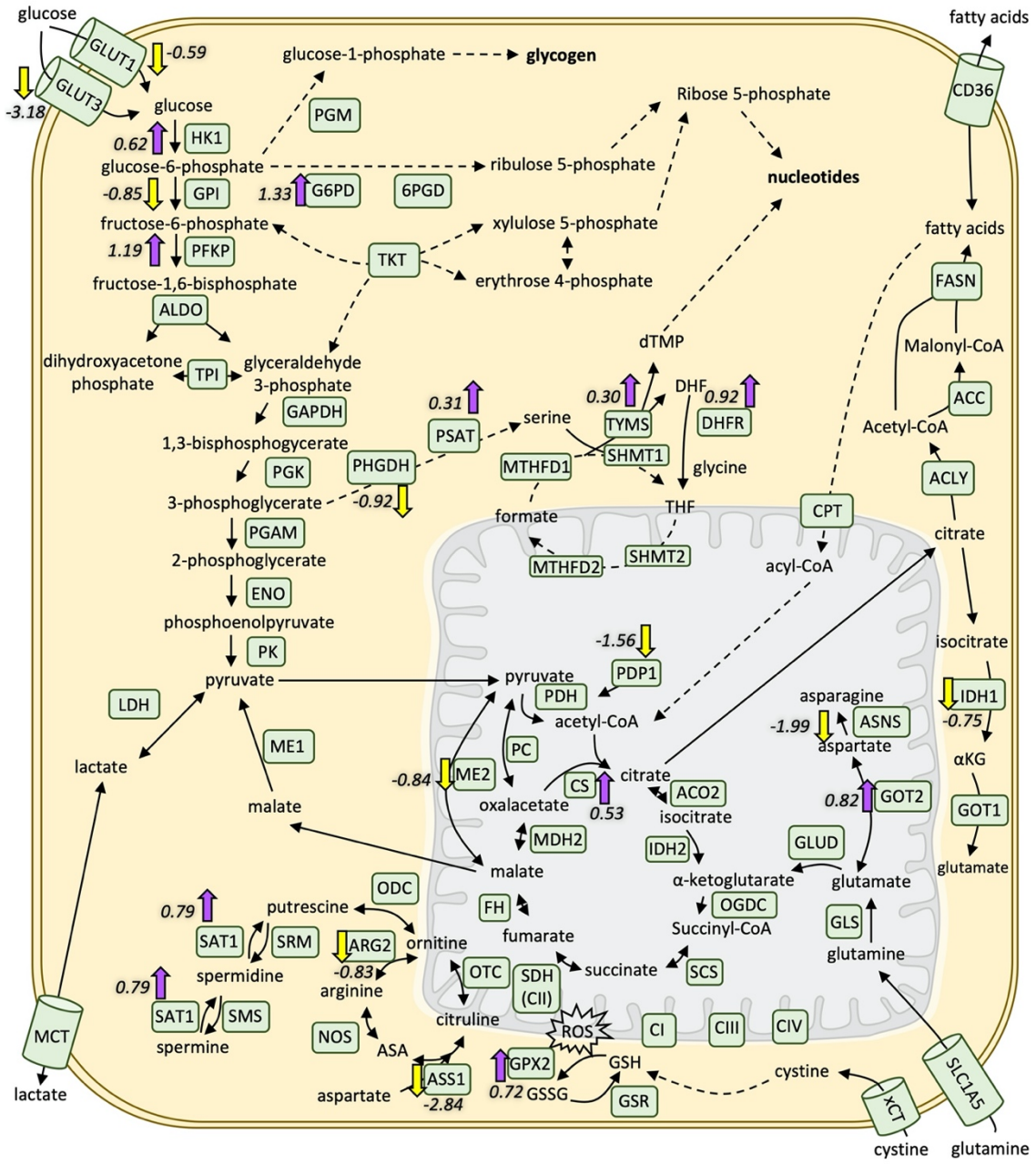

Figure 5.1.1. Differential expression of the metabolic genes in a comparison between SW620 vs SW480 (primary vs metastatic colon cancer cell lines). Schematic representation of the main metabolic pathways and enzymes with the significantly overexpressed (purple arrow) or underexpressed (yellow arrow) genes and the fold-change value from a transcriptomics study (Provenzani et al., 2006). All abbreviations are listed in section 1.

Transcriptomic and proteomic studies have been performed on the colon cancer cell lines SW480 and SW620. Microarray analysis comparisons between the primary cell line SW480 and the lymph node metastasis SW620 by gene set enrichment analysis (GSEA) show a differential expression for many signalling and metabolic pathways (Provenzani et al., 2006). For instance, as previously described for these cell lines, important regulators such as MYC and p53 appear to

be upregulated in SW620 with respect to SW480 while mTOR and HIF1α are downregulated. Regarding metabolic pathways, genes related to glycolysis show some contradictory results. While some of them are downregulated in SW620 with respect to SW480 (*GLUT1*, *GLUT3*, and *GPI*), others are upregulated (*HK1* and *PFK*). PPP, folate metabolism, branched-chain amino acid metabolism and polyamine metabolism genes also upregulated (Figure 5.1.1). The proteomic data comparing SW480 and SW620 had similar results than the transcriptomics (Lee et al., 2015) (Figure 5.1.2). Data for regulators show concordance with the array data. Many enzymes of

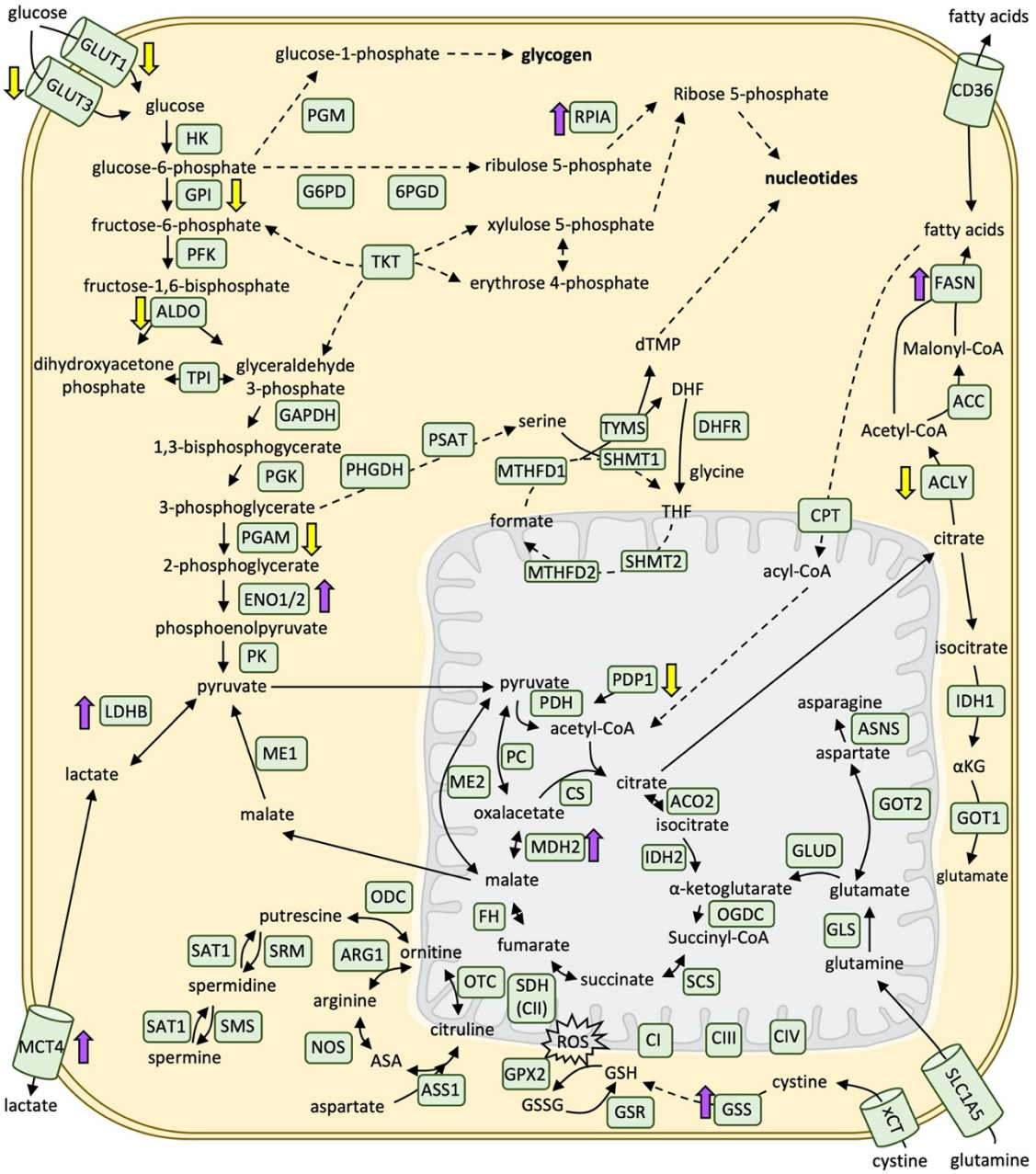

Figure 5.1.2. Differential protein levels of metabolic enzymes of SW620 *vs* SW480 (primary vs metastatic colon cancer cell lines). Schematic representation of the main metabolic pathways and enzymes with the significantly upregulated (purple arrow) or downregulated (yellow arrow) protein levels from a proteomics study (Lee et al., 2015). All abbreviations are listed in section 1.

glycolysis and PPP appear to be downregulated in SW620 with respect to SW480 except for enolase and pyruvate kinase, and the lactate transport, which is upregulated. Some other enzymes related to glutaminolysis, fatty acid synthesis and mitochondrial 1C cycle are also upregulated.

However, there is still a lack of knowledge regarding the contribution of metabolism to the development of increasing metastatic potential in the SW480-SW620 model, and it only represents part of the metastatic process, which is the invasion to lymph node metastasis, but not other distant organ colonisation such as the liver or lungs. Therefore, in order to have a complete picture, we searched other cell lines that could represent further steps of metastasis.

5.1.1.2 Liver metastatic derivatives of SW620

In an attempt to establish the molecular mechanisms that allow colon cancer cells to colonise the liver and the lung, a group from the Institute of Biomedical Research of Barcelona led by Dr Roger R. Gomis generated two metastatic-enriched derivatives from SW620 (Urosevic et al., 2014). LiM1 were isolated from liver metastatic cells resulting from the inoculation of SW620 into the portal circulation of immunodeficient mice. LiM2 were isolated from a second round of *in vivo* selection from LiM1. Gomis' group observed differences in MAPK signalling pathways between the highly metastatic cells LiM2 and the parental cell line SW620. Specifically, they established that ERK2 overactivation in LiM2 modulated EMT through FRA1 and ZEB1 transcription factors and to drive liver metastasis, but not lung metastasis. It was downregulation of p38, which promoted Ca^{2+}-dependent apoptosis of the pulmonary endothelial cells through the expression of PTHLH, that was observed to drive lung metastasis from the liver.

Microarray data were also available for LiM2 vs SW620 (Urosevic et al., 2014). The three main expression signatures differentially expressed between LiM2 and SW620 were nitrogen metabolism, cell adhesion molecules and MAPK and p53 signalling pathways. Some of the metabolic pathways that appear to be upregulated in LiM2 with respect to SW620 are glycolysis and pentose phosphate pathway (GLUT3 and FBP1 upregulation), fatty acid uptake (CD36 upregulation) (Figure 5.1.3). At the same time, some enzymes pathways of glycogen synthesis and serine synthesis from glucose appear to be downregulated (PGM1 and PHGDH, respectively) Also, PDP1 was determined as increased in the metastatic cell lines, which would dephosphorylate and activate PDH, indicative of increased flux of pyruvate through the TCA cycle and the mitochondrial respiration.

With that, our study is based on a highly valuable cell model to study the metabolic adaptation of the metastatic progression: SW480, SW620, LiM1, and LiM2. As the model is isogenic, it allows to better understand the metabolic changes in the same genetic background, something that would be not possible if the cell lines were of different origin. In that first part of the study, we performed deep metabolic characterisation and its relationship with metastatic

features with the aim to establish a metabolic pattern that would allow us to identify therapeutic targets against metastasis in colorectal cancer.

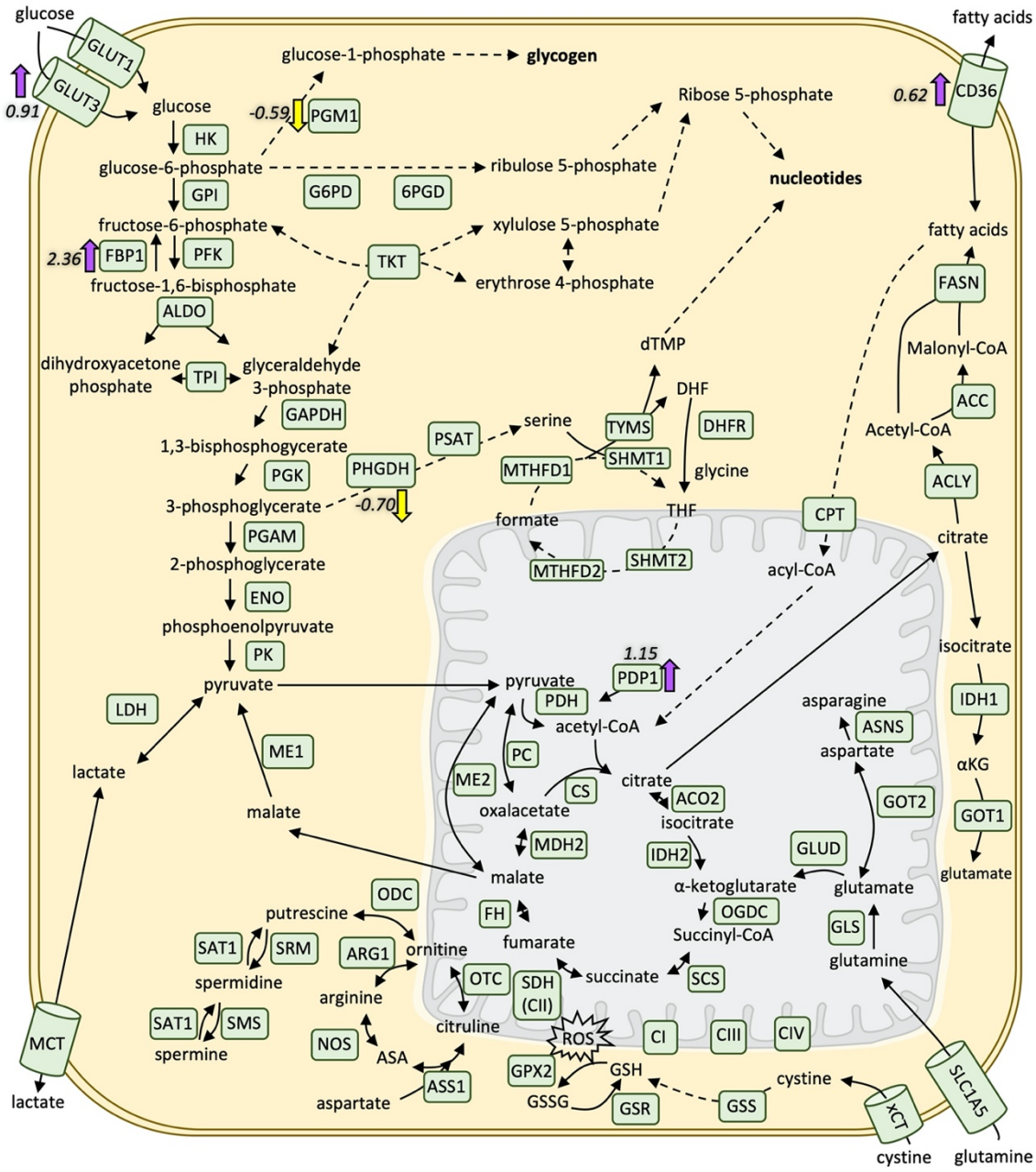

Figure 5.1.3. Differential expression of metabolic enzymes of LiM2 vs SW620 metastatic colon cancer cell lines. Schematic representation of the main metabolic pathways and enzymes with the significantly overexpressed (purple arrow) or underexpressed (yellow arrow) genes and the fold-change value from a transcriptomics study (Urosevic et al., 2014). All abbreviations are listed in section 1.

5.1.2 RESULTS AND DISCUSSION

5.1.2.1 Characterisation of the metastatic phenotype

In order to evaluate the metabolic adaptations underlying metastasis, we first characterised the metastatic phenotype of our cell line model in terms of proliferation, 3D growth, migration, EMT markers, and signalling pathways. In that manner, we could establish a link between the metastatic and the metabolic phenotypes and further exploit possible metabolic vulnerabilities of metastasis in cancer therapy.

Firstly, a general characterisation of the cell lines was performed by evaluating cell proliferation, duplication time and cell volume (Figure 5.1.4). Such features were deeply characterised in order to establish the best conditions for metabolic measurements (see Appendix I). When observed under a contrast-phase microscope, SW480 cells grew forming a layer

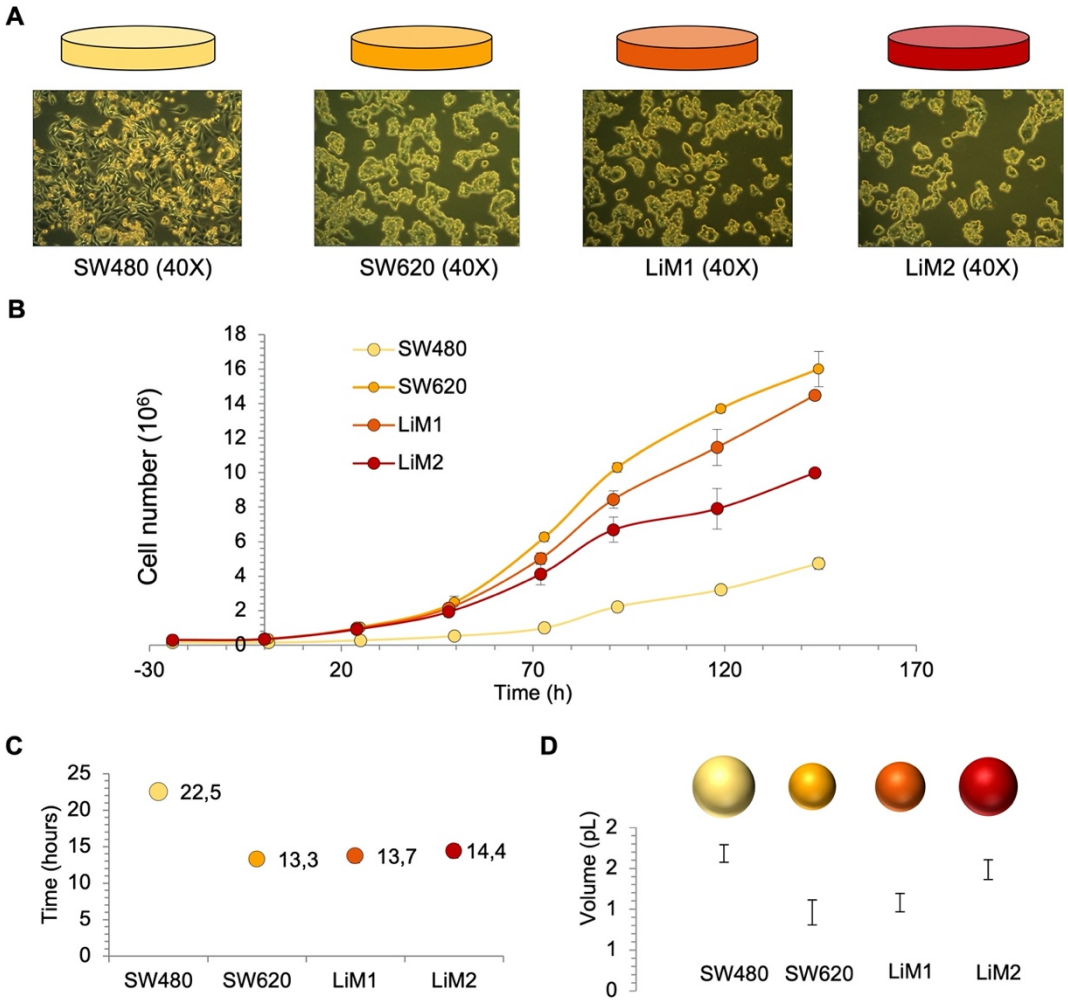

Figure 5.1.4. Growing characteristics of primary (SW480) and metastatic (SW620, LiM1, and LiM2) colon cancer cell lines. A. Contrast-phase microscopy images at 40X. **B.** Cell number in a p6 plate measured by the automatic cell counter Scepter™ up to 144h, changing the medium (DMEM 25 mM Glc, 4 mM Gln, 5% FBS, and 1% S/P) every 24h. **C.** Doubling time for each cell line measured from different experiments (See Appendix I, Figures A.I.1 – A.I.8 and A.I.9) **D.** Cell volume measured by the automatic cell counter Scepter™ measured from different experiments (See Appendix I, Figures A.I.1 – A.I.8).

and cells appear to be more elongated. Meanwhile, SW620, LiM1, and LiM2 have a rounded shape and grew on top of each other, forming aggregates (Figure 5.1.4A). Proliferation and cell-doubling data measured by an automatic cell counter indicated that SW480 was the slowest-growing cell line, followed by LiM2, LiM1, and finally, SW620, which grew the fastest (Figure 5.1.4B and C). Between the metastatic cell lines (SW620, LiM1, and LiM2) it is interesting to observe that the liver metastatic derivatives, and specifically the more metastatic cell line, LiM2, is proliferating at a slower rate than SW620, which means that the acquisition of more metastatic capacities is not fully related with the maximum growth rate. In fact, cell volume had an inverse correlation with cell proliferation in line with the notion that smaller cells tend to proliferate faster than larger cells (Dolfi et al., 2013) (Figure 5.1.4D).

Although 2D culture is the most frequent culture technique used in biomedical research, in the case of studying tumour biology, a layer of cells growing in 2D is very different from a tumour. For that reason, 3D cultures are emerging as more representative of *in viv*o situation and, specifically, of metastatic and colonisation capacities (Kapałczyńska et al., 2018). Furthermore, the capacity to generate a new tumour from a single cell could be as well attributable to a stem cell phenotype (Chaicharoenaudomrung et al., 2019). Thus, in order to confirm the distinct metastatic capacity described for our cell lines, a primary spheroid assay was performed, in which the metastatic cell lines showed an increased spheroid-formation and 3D growth capacity than the primary cell line SW480, but no differences were detected among them (Figure 5.1.5A and C). Additional experiments uncovered that when primary spheroids were disrupted and seeded again to obtain secondary spheroids, the result was that LiM2 had the highest spheroid-formation capacity (Figure 5.1.5B and D). These results validate the distinct metastatic capacities of the cell lines and are also indicative that the metastatic cell lines, and especially LiM2 would have a stronger cancer stem cell phenotype.

In order to simplify the study, from that point on, we decided to exclude LiM1 cells. This decision was made because the metastatic characteristics of LiM1 as well as its metabolic characteristics were very similar to SW620 (see Appendix I). On the contrary, the liver metastatic derivative LiM2 showed some remarkable differences with SW620.

Regarding migration capacity, tested by wound-healing assays, the result was, somehow, unexpected. Considering that SW480 were isolated from the primary tumour one could expect this cell line to have less migratory capacity than the cell lines that were isolated from metastatic sites SW620 and LiM2. Surprisingly, SW480 the cells were the ones to have the highest ability to migrate and wound the heal, while SW620 had the least capacity, with almost no movement of the cells (Figure 5.1.5E and F). Interestingly, LiM2 cells were not able to wound the heal but migrated more than SW620. Together, the spheroid and wound healing assays seem to indicate that SW480 could have already acquired some invasive capacities that would allow them to start

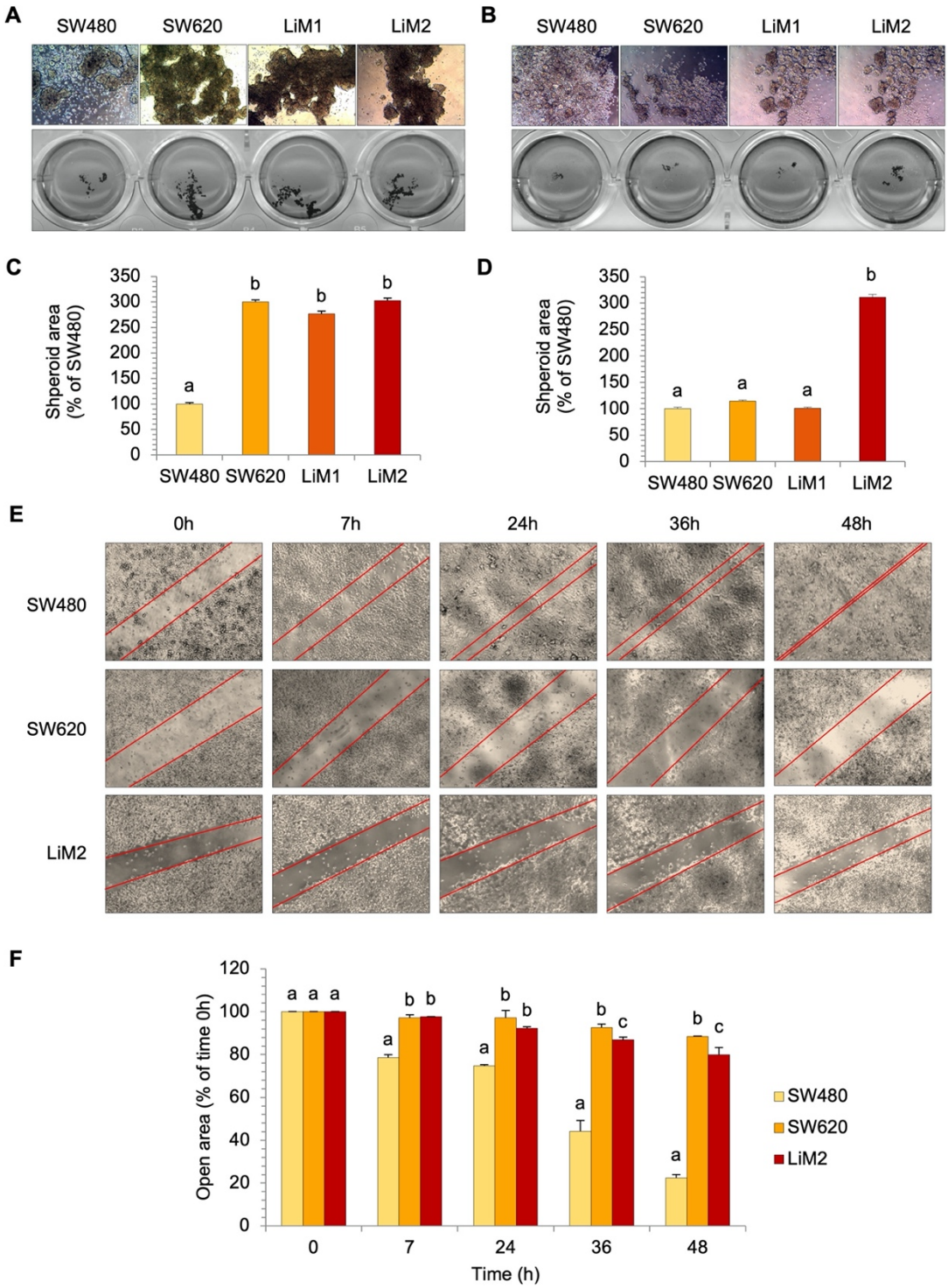

Figure 5.1.5. 3D growth and migration capacities of primary (SW480) and metastatic (SW620, LiM1, and LiM2) colon cancer cell lines. A. Spheroid formation assay in low attachment plates and medium containing EGF, Bfgf, heparin, B27, insulin and hydrocortisone for one week, images of a contrast-phase microscope (40X) above and scanner of the plate (1X) below. **B.** Secondary spheroid formation assay, reseeded from the primary spheroid assay in D, using the same plates and medium for one more week. Images of a contrast-phase microscope (40X) above and scanner of the plate (1X) below. **C.** and **D.** Quantification of the spheroid area using ImageJ software from the scanner images. **E.** Images of a wound-healing assay up to 48h, being 0h the time that mitomycin was added. **F.** Migration area quantification from the experiment in E. [a,b,c] In all cases, a one-way ANOVA and Scheffe's test for multiple comparisons was performed for the factor "cell line". Groups with different letter show significant differences with α=0.05.

the metastatic process (Mittal, 2018), but SW620 and LiM2 are the cells that possess colonisation capacities, necessary in further steps of metastasis.

Next, in order to better understand the metastatic capacities that each cell line had, the epithelial-mesenchymal transition (EMT) status was evaluated by testing protein levels of the main EMT markers using the western blotting technique. Being SW480 from the primary tumour one could expect that SW480 should have higher levels of the epithelial markers than SW620 and LiM2, and these, from metastatic sites and metastatic capacities, should have higher levels of mesenchymal markers. However, the findings on migration capacity anticipated us to think that the EMT markers would not be exactly as expected and indeed, E-cadherin, which is the main epithelial marker, behaved the contrary: SW480, that came from the primary tumour, had low levels of E-cadherin while the metastatic cell lines clearly showed much more E-cadherin levels (Figure 5.1.6A and B). The presence of such levels of E-cadherin suggest a reinforced cell-cell

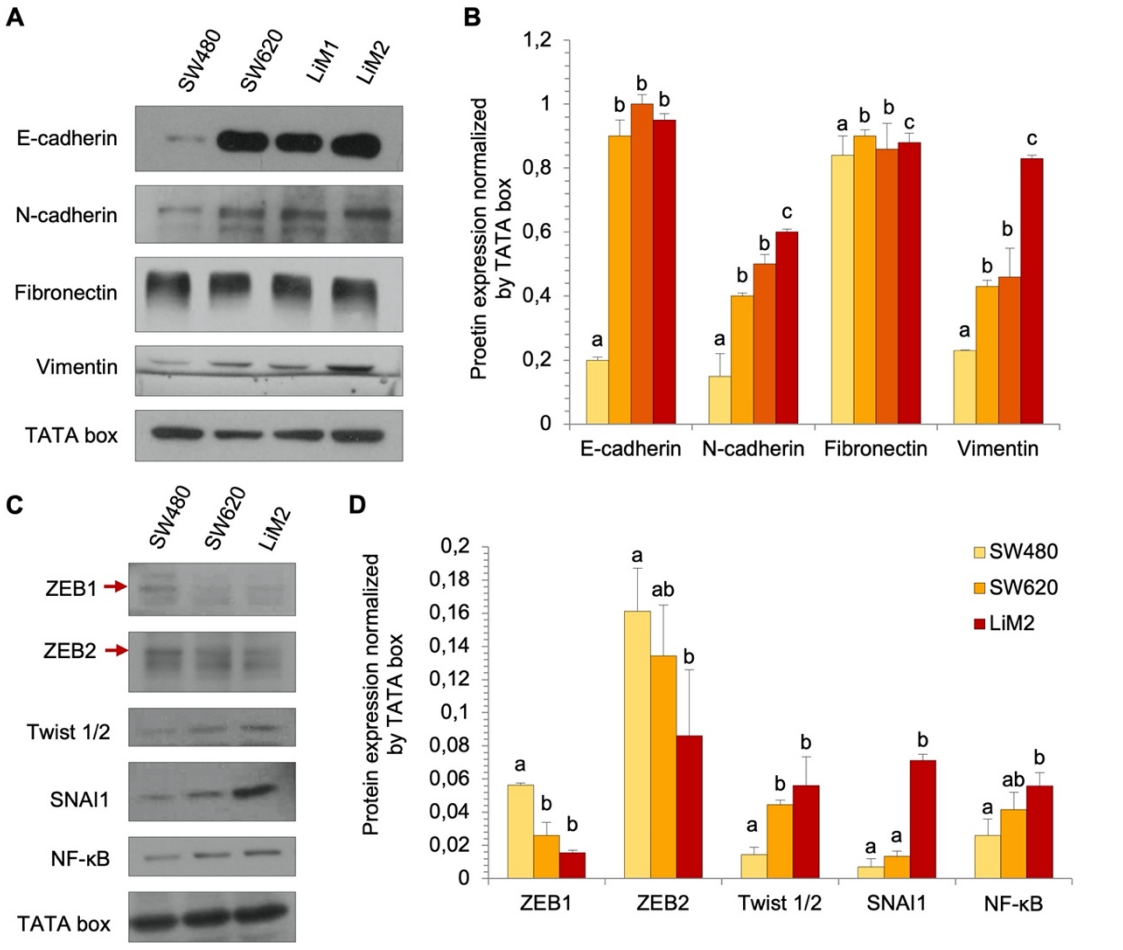

Figure 5.1.6. Protein levels of epithelial-mesenchymal transition (EMT) markers and transcription factors of SW480, SW620 and LiM2 cell lines. A. Western blotting images of the main EMT markers and TATA box used as a loading control. **B.** Quantification of the experiment in A using ImageJ software. **C.** Western blotting images of the main EMT-related transcription factors and TATA box used as a loading control **D.** Quantification of the experiment in C using ImageJ software. [a,b,c] A one-way ANOVA and Scheffe's test for multiple comparisons was performed for the factor "cell line". Groups with different letter show significant differences with α=0.05.

interaction capacity that is in line with the observed aggregates in 2D culture or the higher capacity for 3D culture growth.

On the other hand, the mesenchymal markers were in line with the expected and especially N-cadherin and vimentin levels are increasingly higher in the SW620, LiM1, and LiM2, and therefore in agreement with the overall metastatic capacities. The main transcription factors that induce EMT were also examined and the results showed that while the levels of ZEB1 and 2 where higher in SW480, the metastatic cells showed higher levels of the other EMT transcription factors Twist1/2, NF-κB, and Snai1 (Figure 5.1.6C and D). Remarkably, LiM2 showed much higher levels of Snai1 than SW620 cells, which reinforces the assumption that LiM2 has a higher stem cell phenotype, as Snai1 is not only a mesenchymal marker but also a stem cell marker (Horvay et al., 2015). Altogether, these results suggest that we could be in front of a model of a partial EMT or intermediate estates of EMT (Pastushenko and Blanpain, 2019) (see section 2.1.2.3).

After having explored the molecular status of EMT, other signalling pathways were explored with the aim to identify the drivers of metastasis and its crosstalk with EMT and also with the metabolic features. In colorectal cancer, especially in MSS cases, the main signalling pathway that results to be altered and it is considered to be the first tumorigenic driver is Wnt signalling. APC loss results in the inactivation of the destruction complex of β-catenin, which in turn activates Wnt signalling. Wnt stimulates cell proliferation, stemness and also EMT activation (Teeuwssen and Fodde, 2019). It is also observed that β-catenin is overexpressed in the invasive front of the tumour (Fodde and Brabletz, 2007). In line with the migratory capacity of SW480, as well as its E-cadherin loss, levels of β-catenin are higher in this cell line with respect to the metastatic cell lines (Figure 5.1.7A and B). This could be indicative for the possibility that EMT is already induced in the SW480 primary tumour cell line. The β-catenin paralogue γ-catenin, also called plakoglobin, is an alternative Wnt signalling transducer and also a component of desmosomes and therefore implicated in cell-cell adhesion, and possibly in circulating tumour cell clusters (Aceto et al., 2014). Interestingly, its levels are inversely correlated with β-catenin and increased in the metastatic cells with respect to SW480, in line with the levels of E-cadherin (Figure 5.1.7A and C).

The second most important driver in colorectal cancer is the oncogene *KRAS*, which results to be mutated in 30-40% of the CRC cases and it has been related to poor prognosis and metastasis (Porru et al., 2018). As explained before, the isogenic cell lines of our study, SW480, SW620 and LiM2 are *KRAS* mutated in G12V codon. We explored the key members of the MAPK and PI3K/Akt signalling that are upstream and downstream of the mutated GTPase KRAS, which is supposed to be permanently active. EFGR, upstream of KRAS, and one of the most relevant tyrosine kinase receptors are much higher in SW480 but not in the metastatic cell lines (Figure 5.1.7D and E). This is in line with previous observations in the literature that EGFR is

downregulated to facilitate EMT and metastatic progression in models of breast cancer and hepatocellular carcinoma (López-Luque et al., 2019; Wendt et al., 2015).

Regarding MAPK signalling downstream of KRAS (measured by the levels of ERK2) and PI3K/Akt signalling (measured by the activating phosphorylation levels of Akt at S473 and by PTEN, an inactivator of PI3K) were equal among the three cell lines (Figure 5.1.7D and F-H). This suggests that signalling downstream of KRAS is equally activated and both pathways are overactivated due to aberrant KRAS-mutated signalling.

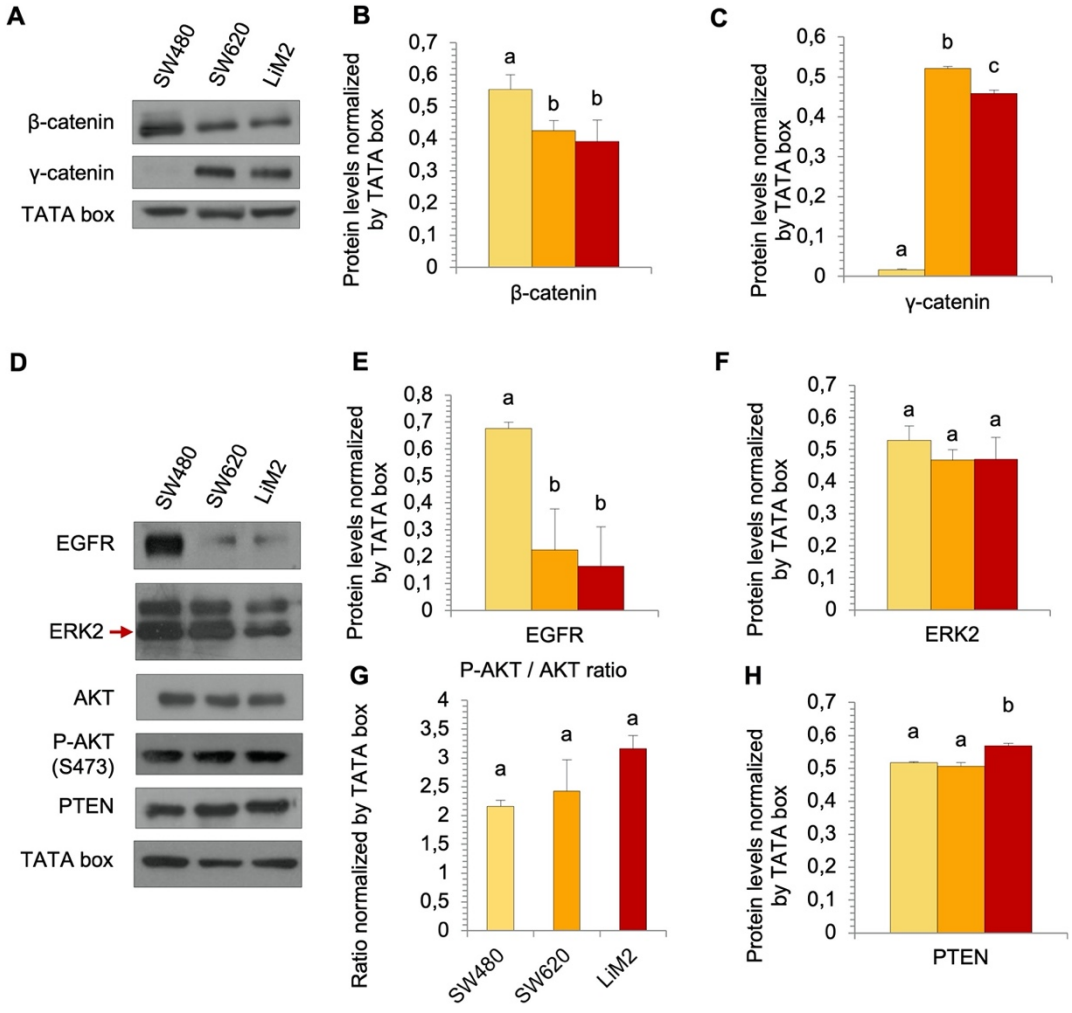

Figure 5.1.7. Protein levels of key members of the main signalling pathways in primary (SW480) and metastatic (SW620 and LiM2) colon cancer cell lines. A. and **D.** Western blotting images of Wnt, MAPK, and Akt signalling pathways members and TATA box used as a loading control. **B, C, E – H.** Quantification of the experiments in A and D using ImageJ software. [a,b,c] In all cases, a one-way ANOVA and Scheffe's test for multiple comparisons was performed for the factor "cell line". Groups with different letter show significant differences with α=0.05.

Then, the differences in cell proliferation among the explored cell lines could not be explained by MAPK or PI3K/Akt signalling. For that reason, we examined the role that mTOR signalling could have, as it coordinates cell growth and metabolism and protein synthesis, and its signalling is not only dependent on growth factors (i.e. coming from PI3K/Akt signalling) but

also nutrient status, especially amino acid uptake (Saxton and Sabatini, 2017). We checked the levels activating phosphorylation in S2448 of mTOR protein and they resulted to correlate with the cell volume as well as protein content (Figures 5.1.4D and 5.1.8A-C) and were not specifically induced in the metastatic cells.

Finally, in an attempt to find a signalling pathway that correlated with the proliferation as well as the overall metastatic capacities and metabolic features, we also checked MYC, HIF1α and p53 levels. MYC has a central role also in proliferation and metabolism and it is considered to be one of the main drivers of metastasis, being deregulated in more than 50% of human cancers (Chen et al., 2018) (see section 2.2.2.1). As expected, increased MYC protein levels were correlated with increased proliferation in metastatic cell lines (Figure 5.1.8D and E). Another driver of tumour progression and metastasis is HIF1α, that is normally being activated by low levels of oxygen but also other stimuli such as the oncometabolites fumarate and succinate aberrantly activate it in tumours. Taking into account that the metastatic cells of our model grow forming aggregates and are able to grow forming spheroids we wondered if HIF1α signalling could play a role in the inner parts of the aggregates. However, the results indicated that HIF1α

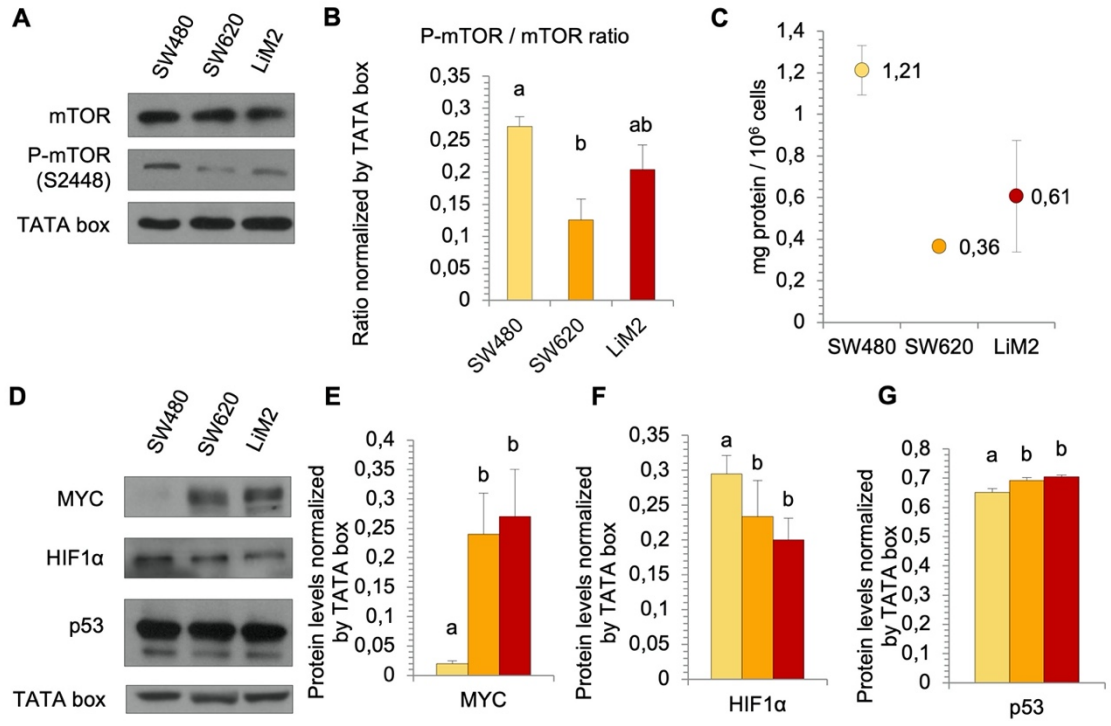

Figure 5.1.8. Protein levels of key members of the main signalling pathways in primary (SW480) and metastatic (SW620 and LiM2) colon cancer cell lines. A. and **D.** Western blotting images of mTOR, MYC, HIF, and p53 signalling pathways members and TATA box used as a loading control. **B.** Ratio of mTOR phosphorylation from the protein levels of phosphorylated mTOR (at S2448) and total mTOR, normalised by TATA box **C.** Protein content measured using bicinchoninic acid (BCA) protein assay. **E – G.** Quantification of the experiments in D using ImageJ software. [a,b,c] In all cases, a one-way ANOVA and Scheffe's test for multiple comparisons was performed for the factor "cell line". Groups with different letter show significant differences with α=0.05.

levels are similar in all cell lines, and even SW480 had higher levels than the metastatic cell lines (Figure 5.1.8D and F). Finally, we also check the levels of p53 in order to know if it can be playing a role in the survival of metastatic cells, but no differences were observed between the three cell lines (Figure 5.1.8D and G).

5.1.2.2 Metastatic cells display increased glucose and glutamine metabolism

In order to characterise the metabolic differences between the primary and metastatic cell lines, we used spectrophotometric measurements, stable isotope-resolved metabolomics and other metabolomic and molecular biology measurements. Firstly, we established the best conditions for metabolic measurements according to the growing experiments (see section 4.2.2, 5.1.2.1 and Appendix I). The spectrophotometric measurements results determined that the metastatic cells had a stronger Warburg effect than SW480, as they consumed more glucose and secreted more lactate (Figure 5.1.9A and B). Subsequent analysis of the production of intracellular lactate from

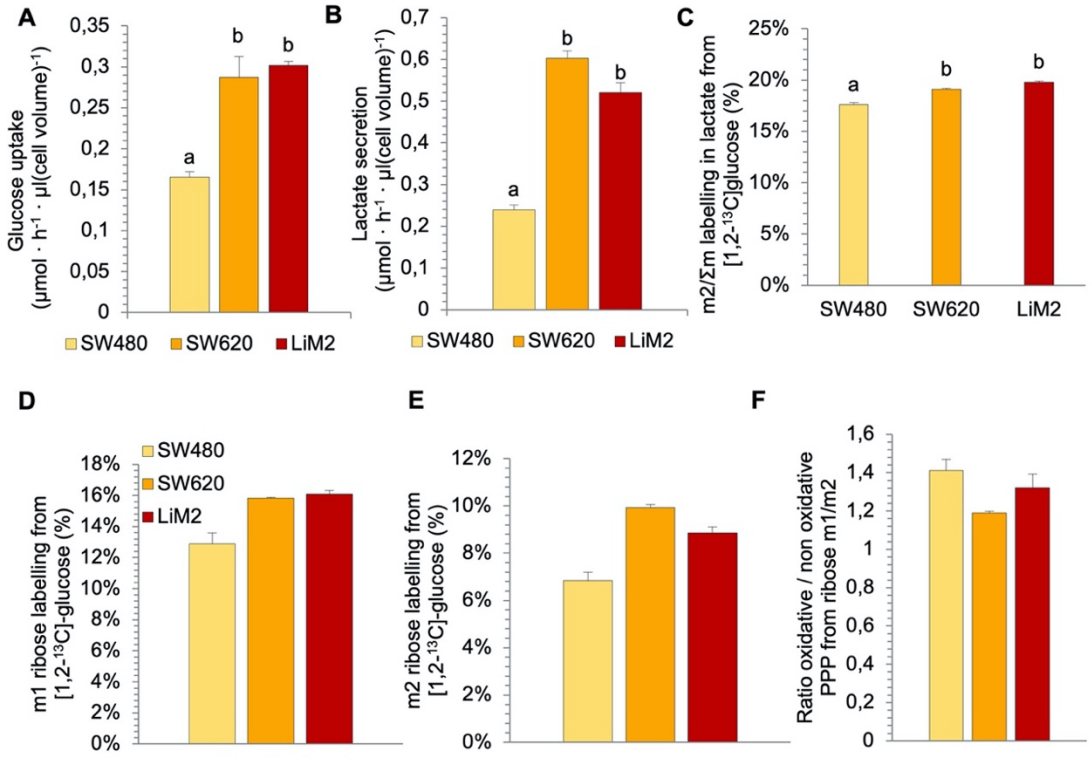

Figure 5.1.9. Changes in glucose metabolism in primary (SW480) and metastatic (SW620 and LiM2) colon cancer cell lines. A. and **B.** Glucose uptake and lactate secretion rates measured by spectrophotometry after 48h of cell culture in DMEM 12.5 mM Glc and 4 mM Gln, 5% FBS, and 1% S/P (see Tables A.I.1 – A.I.8). **C.** Glucose contribution to lactate measured in the presence of [1,2-^{13}C]-glucose at 12.5 mM after 24h incubation. Lactate was isolated and analysed by GC-MS for isotopologue distribution (see Table A.II.3, A.II.5, A.I.8 and A.II.12) **D.** and **E.** Glucose contribution to the oxidative branch of pentose phosphate pathway (PPP) measured by m1 labelling in ribose (D) and the non-oxidative branch of PPP estimated by m2 labelling in ribose (E) from the same experiment in C, isolating and analysing intracellular ribose and analysing it by GC-MS for isotopologue distribution (see Table A.II.10) **F.** Ratio from the experiment in E and F. ^{a,b,c} In all cases, a one-way ANOVA and Scheffe's test for multiple comparisons was performed for the factor "cell line". Groups with different letter show significant differences with α=0.05.

[1,2,-^{13}C]-glucose incubation confirmed that increase in the glycolytic pathway (Figure 5.1.9C and Appendix II). The isotopologue distribution of ribose allowed to infer the direct contribution to the oxidative (Figure 5.1.9D) and non-oxidative (Figure 5.1.9E) branch of pentose phosphate pathway, which was increased in both cases in the metastatic cell lines. However, the contribution of the oxidative and non-oxidative branches to ribose synthesis is similar in all the cell lines (Figure 5.1.9F).

As long as metastatic cells were more glycolytic than the primary cell lines, we then wondered if the entrance of glucose to the TCA cycle of pyruvate coming from glucose through PDH was lower. For that purpose, we first examined the phosphorylation status of pyruvate dehydrogenase (PDH) enzyme. On the contrary, we found it to be more active (dephosphorylated) in metastatic cells than in SW480 (Figure 5.1.10A and B), which could mean that metastatic cell

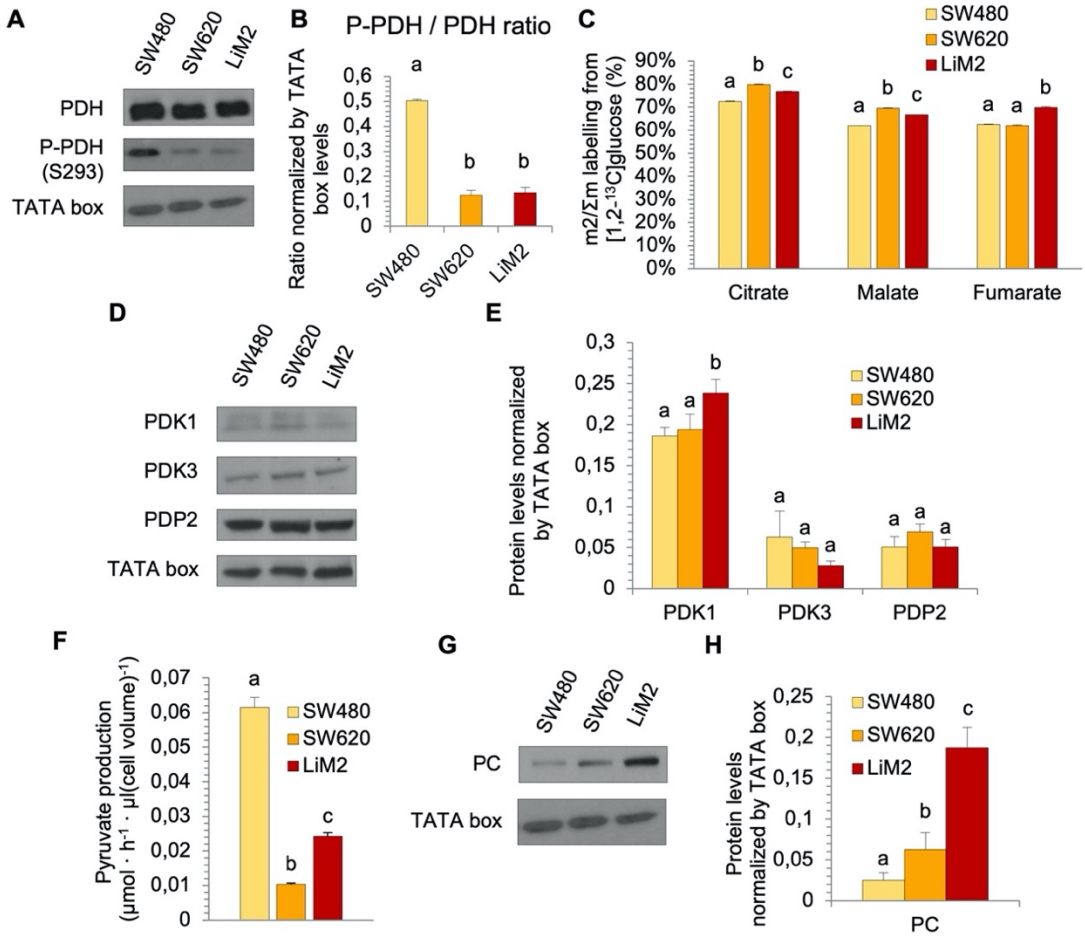

Figure 5.1.10. Glucose and pyruvate metabolism in primary (SW480) and metastatic (SW620 and LiM2) colon cancer cell lines. A. and **B.** PDH phosphorylation tested by western blotting (A) and ratio determination (B). **C.** Glucose contribution to the TCA cycle measured in the presence of [1,2-^{13}C]-glucose at 12,5 mM after 24 h incubation. TCA intermediates were isolated and analysed by GC-MS for isotopologue distribution (see Tables A.II.1 and A.II.6). **D.** Regulation of PDH phosphorylation tested by western blotting. **E.** Quantification from the experiment in D. **F.** Pyruvate production rate measured by spectrophotometry after 48h of cell culture. **G.** and **H.** PC levels tested by western blotting (G) and quantification (H). ^{a,b,c} In all cases, a one-way ANOVA and Scheffe's test for multiple comparisons was performed for the factor "cell line". Groups with different letter show significant differences with α=0.05.

lines have enhanced both glycolysis and tricarboxylic acid (TCA) cycle coming from glucose. To confirm that, we evaluated the glucose entrance into the TCA by [1,2-^{13}C]-glucose incubation and there were significant increases in the incorporation of the TCA cycle intermediates citrate, malate and fumarate (Figure 5.1.10C).

Having observed the differences in PDH phosphorylation we explored if any of the enzymes that phosphorylate or dephosphorylate PDH are differentially expressed among the different cell lines. However, no differences were found in PDK1, 3, nor in PDP2 (Figure 5.1.10D and E). We then examined the possible role of pyruvate in the activation of PDH (Patel et al., 2014), measuring the pyruvate levels in the medium, in order to find a possible relationship with PDH phosphorylation levels. The results were that pyruvate is less secreted in the metastatic cell lines (Figure 5.1.10F), a possible explanation of the intracellular utilisation of this metabolite and activation of PDH. Furthermore, metastatic cells, especially LiM2 cells, had higher pyruvate carboxylase (PC) levels (Figure 5.1.10G and H), an anaplerotic enzyme that metabolises pyruvate to replenish the TCA by transforming it to oxaloacetate. Overall, these results suggest a rewiring of pyruvate metabolism concomitant with increased metastatic capacity. In fact, enhanced pyruvate metabolism and specifically PC activity have been observed to have a crucial role for metastatic progression in the case of breast cancer metastasis colonisation of the lung (Christen et al., 2016; Shinde et al., 2018).

Glutamine is the second major substrate used by cancer cells and it is not only carbon but also a nitrogen source. We observed that metastatic cells consumed more glutamine and secreted more glutamate (Figure 5.1.11A and B). Increased uptake in the metastatic cell lines is correlated with increases in protein levels of key glutamine catabolising enzymes glutaminase (GLS) and glutamate dehydrogenase (GLUD1) (Figure 5.1.11C and D). As we did with glucose, the incorporation of glutamine to the TCA cycle was also analysed by using stable isotope-resolved metabolomics. We observed increased labelling from [U-^{13}C]-glutamine to TCA cycle intermediates, in both of the isotopologues that correspond to the oxidative and the reductive pathways (Figure 5.1.11E and F). Intracellular glutamate and aspartate were included as TCA cycle intermediaries as it is considered that its label is equivalent to α-ketoglutarate and oxaloacetate, respectively. Therefore, in our cell models, metastatic capacity is underlined by higher glutaminolysis, which is consistent with the higher MYC expression that we observed in the metastatic cell lines. Interestingly, a recent study has reported the functional importance of GLS1 for metastatic colonisation in colorectal cancer cells (Xiang et al., 2019). However, in this case, they observed GLS1 to be induced by hypoxia, which does not correspond with our results of HIF1α.

In line with the metabolic changes observed above, previous experiments of our research group showed enhanced mitochondrial function in both SW620 and LiM2, which displayed an increased oxygen consumption rate (OCR) compared to SW480 (Appendix III, Figure A.III.1A).

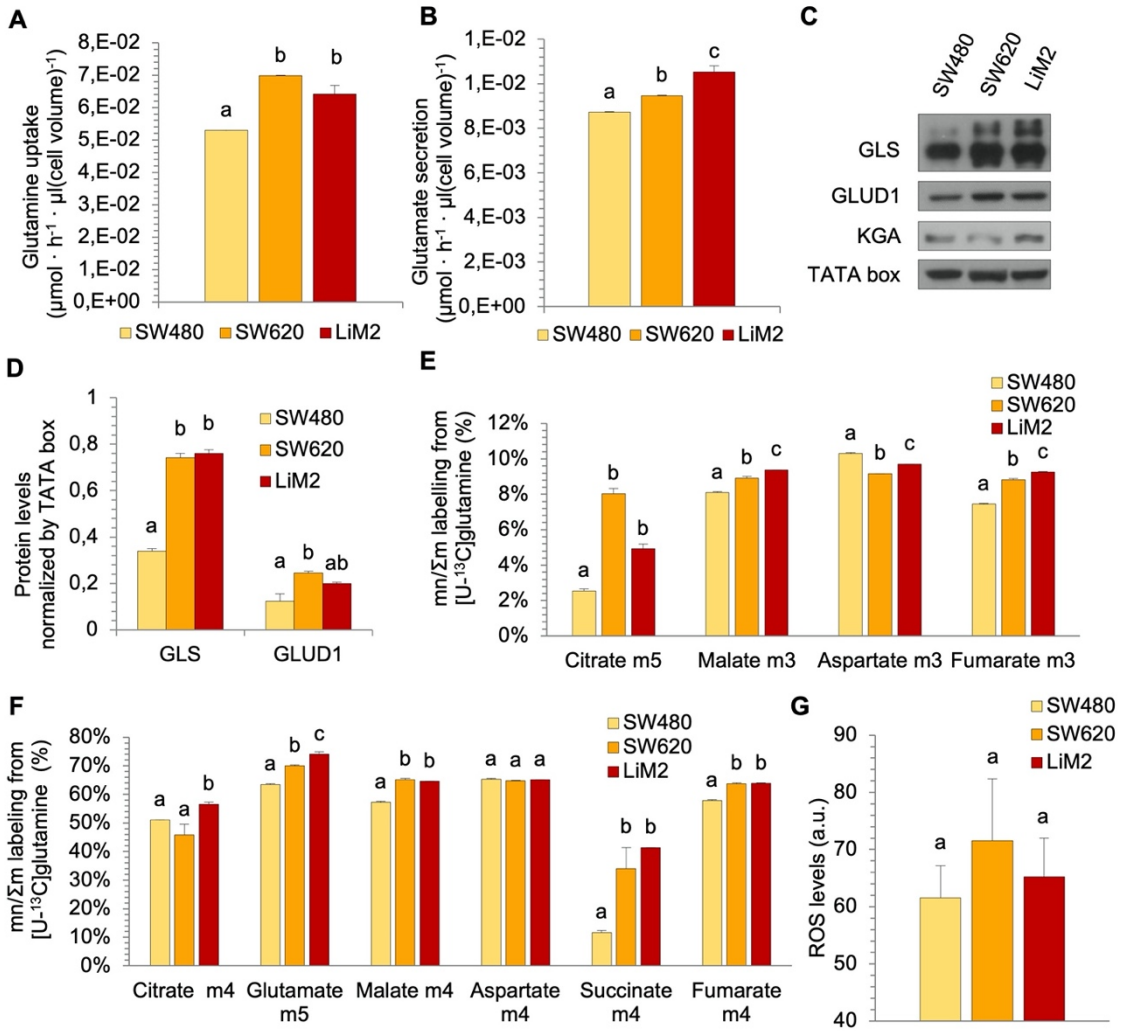

Figure 5.1.11. Glutamine metabolism in primary (SW480) and metastatic (SW620 and LiM2) colon cancer cell lines. A. and **B.** Glutamine uptake and glutamate secretion rates measured by spectrophotometry after 48h of cell culture, normalised by cell volume. Medium DMEM 12.5 mM Glc and 4 mM Gln, 5% FBS, and 1% S/P. **C.** and **D.** Glutaminolysis enzymes tested by western blotting (C) and its quantification (D). **E.** and **F.** Glutamine contribution to the TCA cycle and some amino acids measured in the presence of [U-^{13}C]-glutamine at 4 mM after 24 h incubation. TCA intermediates were isolated and analysed by GC-MS for isotopologue distribution. (E) represents the isotopologues that correspond to reductive carboxylation of glutamine and (F) represents the isotopologues that correspond to oxidative carboxylation of glutamine (see Tables A.II.4 and A.II.11). **G.** ROS levels measured by flow cytometry after 24 hours of incubation. [a,b,c] In all cases, a one-way ANOVA and Scheffe's test for multiple comparisons was performed for the factor "cell line". Groups with different letter show significant differences with α=0.05.

In spite of the significant differences in OCR, when performing a Mito Stress assay to elucidate the respiratory characteristics of the three cell lines (i.e. ATP production, basal respiration, maximal respiration, non-mitochondrial respiration, proton leak and spare capacity), no differences were observed in any of them. However, if the concentration of glucose, glutamine, or palmitate is gradually increased, then the metastatic cell lines display higher OCR compared to the SW480 (Figure A.III.1C-E). This corresponds with our results on ROS levels, that showed

a tendency to increase, although it was not significant, in the metastatic cell lines (Figure 5.1.11G).

Mito Fuel assays, performed with specific inhibitors to block the utilisation of the three major respiratory substrates, revealed that the metastatic cell lines had similar capacity but lower dependency and higher flexibility for the three substrates (Figure A.III.2A-C), when compared to the SW480 cell line. This unique increased capacity is further evident in the consistent increase in OCR found for titrations with alternative substrates (i.e. arginine, leucine, proline, glycine, serine and uridine) exclusively in the metastatic cell lines (Figure A.III.2D-I). Overall, mitochondrial function experiments confirmed an enhanced mitochondrial metabolism of the main carbon substrates, increased metabolic flexibility as well as adaptation to the presence of alternative substrates and capacity to use them for mitochondrial respiration. Concomitantly, increased oxidative phosphorylation has also been recently attributed to being a feature of breast cancer metastasis (Davis et al., 2020).

5.1.2.3 Metabolic flexibility of the metastatic cells under glucose and glutamine deprivations

The results from the previous section revealed that both glucose and glutamine metabolism was enhanced in the metastatic cell lines, which suggests a potential reliance on these metabolites for their increased growth rate. To investigate the metabolite addiction to these two substrates as well as metabolic stress conditions, we incubated cell lines in the absence of either glucose or glutamine and measured proliferation at 24, 48, and 72 hours (Figure 5.1.12A-C). We found that the proliferation of the metastatic cell lines is more affected by glutamine deprivation than by glucose deprivation, suggesting that glutamine could be more essential than glucose for metastatic cells. When comparing the deprivations between the cell lines, it is clear that in both deprivations, metastatic cell line proliferation decreased significantly more than the primary cell line (Figure 5.1.12D).

In order to elucidate if the effect of metabolite deprivations on proliferation was due to cell death by apoptosis or else cell survival by stopping cell cycle, we performed the convenient assays under the same conditions explained before. We observed that the effect of both deprivations on proliferation is attributable to a partial cell cycle arrest rather than cell death, as both metastatic cell lines displayed increased G1 and S phase, and reduced G2 phase (Figure 5.1.13A-C). The evidence was clearer when we observed that early apoptosis is reduced in the metastatic cell lines under glucose or glutamine deprivations (Figure 5.1.13D and E). These results suggest that despite metastatic cell lines SW620 and LiM2 proliferation is impaired under these deprivations, they are able to survive and avoid apoptosis. Such capacity is not found in SW480, taking into account the observed higher cell death in an attempt to keep cell proliferation.

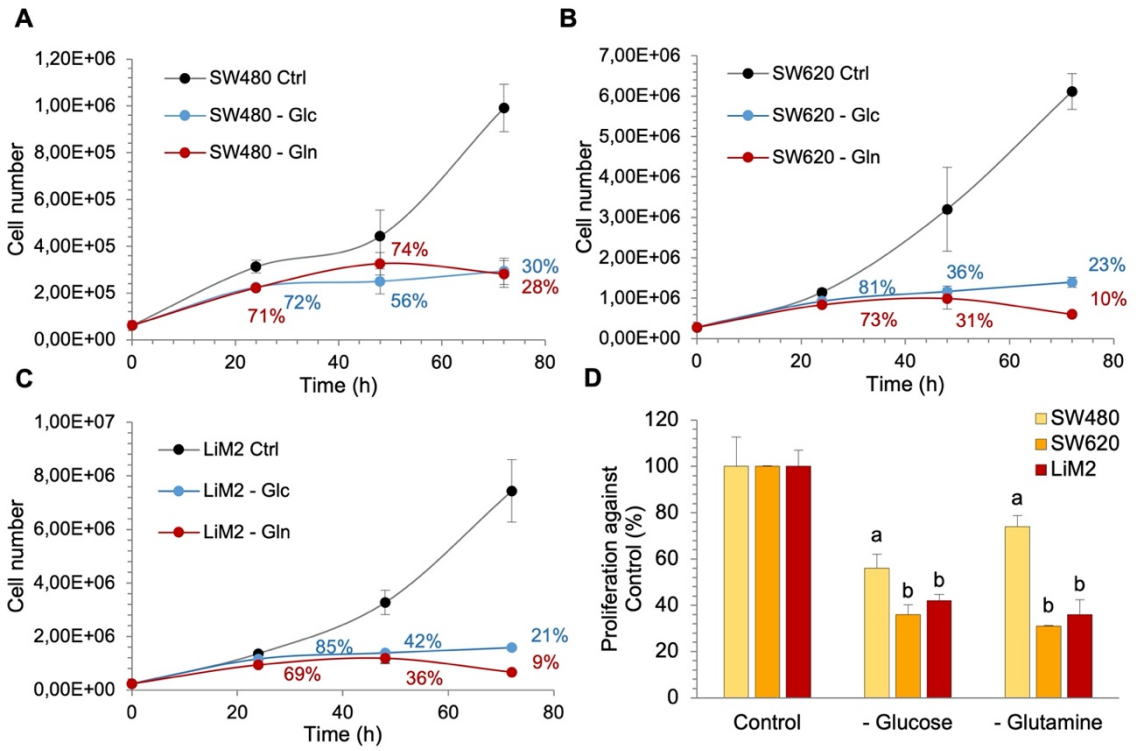

Figure 5.1.12. Glucose and glutamine deprivation effects on cell proliferation in primary (SW480) and metastatic (SW620 and LiM2) colon cancer cell lines. A. - C. Cell proliferation measured by flow cytometry (beads counting) after 24, 48 or 72 hours of incubation under control conditions (12.5 mM Glc, 4 mM Gln) and in the absence of either glucose or glutamine. **D.** Representation of the same experiment in A-C comparing between cell lines at 48 hours. A one-way ANOVA and Scheffe's test for multiple comparisons was performed for the factor "cell line". Groups with different letter show significant differences with α=0.05. [a,b] A one-way ANOVA and Scheffe's test for multiple comparisons was performed for the factor "cell line". Groups with different letter show significant differences with α=0.05.

Then, we analysed the 3D growth capacity under the same deprivations in order to know if there was any difference compared to 2D growth. Interestingly, under glucose deprivation, only the metastatic cell lines, and especially LiM2, were able to form spheroids (Figure 5.1.14A and B). Regarding glutamine deprivation, none of the cell lines was able to form spheroids, confirming the higher essentiality of the amino acid glutamine upon glucose. Additionally, in the absence of glucose, only the metastatic cell lines increased glutamine uptake. This suggests that pathways such as glutaminolysis compensate for glucose deprivation and support 3D growth in metastatic cells (Figure 5.1.14C), although the spectrophotometric determination was made in 2D growth. Having seen the differences on pyruvate dehydrogenase and glutaminase among the cell lines, it was interesting to see if the phosphorylation status of PDH and GLS levels were also changing differently under metabolic stress conditions such as glucose and glutamine deprivations. Under such conditions, we confirmed again that PDH is phosphorylated in SW480 and less phosphorylated in the metastatic cell lines (Figure 5.1.14D and E). Then, we observed that in all

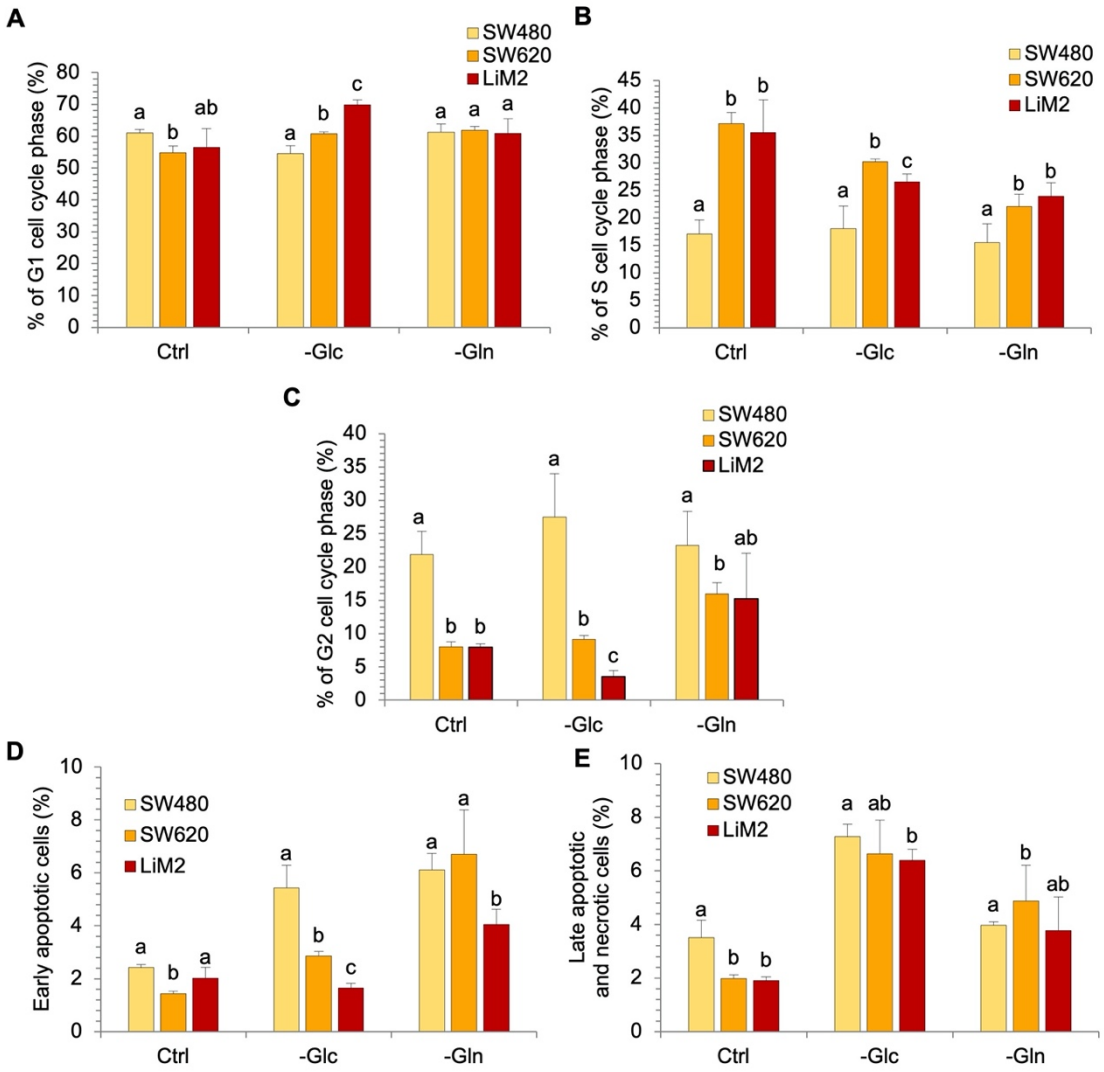

Figure 5.1.13. Glucose and glutamine deprivation effects on cell cycle and apoptosis in primary (SW480) and metastatic (SW620 and LiM2) colon cancer cell lines. A. - **C.** Percentage of cell cycle phase measured by flow cytometry after 48 hours of incubation under control conditions (12.5 mM Glc, 4 mM Gln) and either glucose or glutamine deprivation. **D.** and **E.** Percentage of early apoptotic (D) and late apoptotic and necrotic (E) cells measured by flow cytometry after 48 hours of incubation under control conditions and either glucose or glutamine deprivation. [a,b,c] In all cases, a one-way ANOVA and Scheffe's test for multiple comparisons was performed for the factor "cell line". Groups with different letter show significant differences with α=0.05.

cell lines, PDH is phosphorylated (inactivated) when glucose availability is compromised. Subsequently, when glutamine availability is compromised, only the metastatic cell lines SW620 and LiM2 display significantly less phosphorylation with respect to glucose deprivation (Figure 5.1.14D-G), showing more adaptability to the diverse situations. Regarding glutaminase, only the metastatic cell line LiM2 but not SW620 neither SW480 cells increase GLS protein levels under glucose deprivation (Figure 5.1.14H). Under glutamine deprivation, the three cell lines show decreased GLS levels.

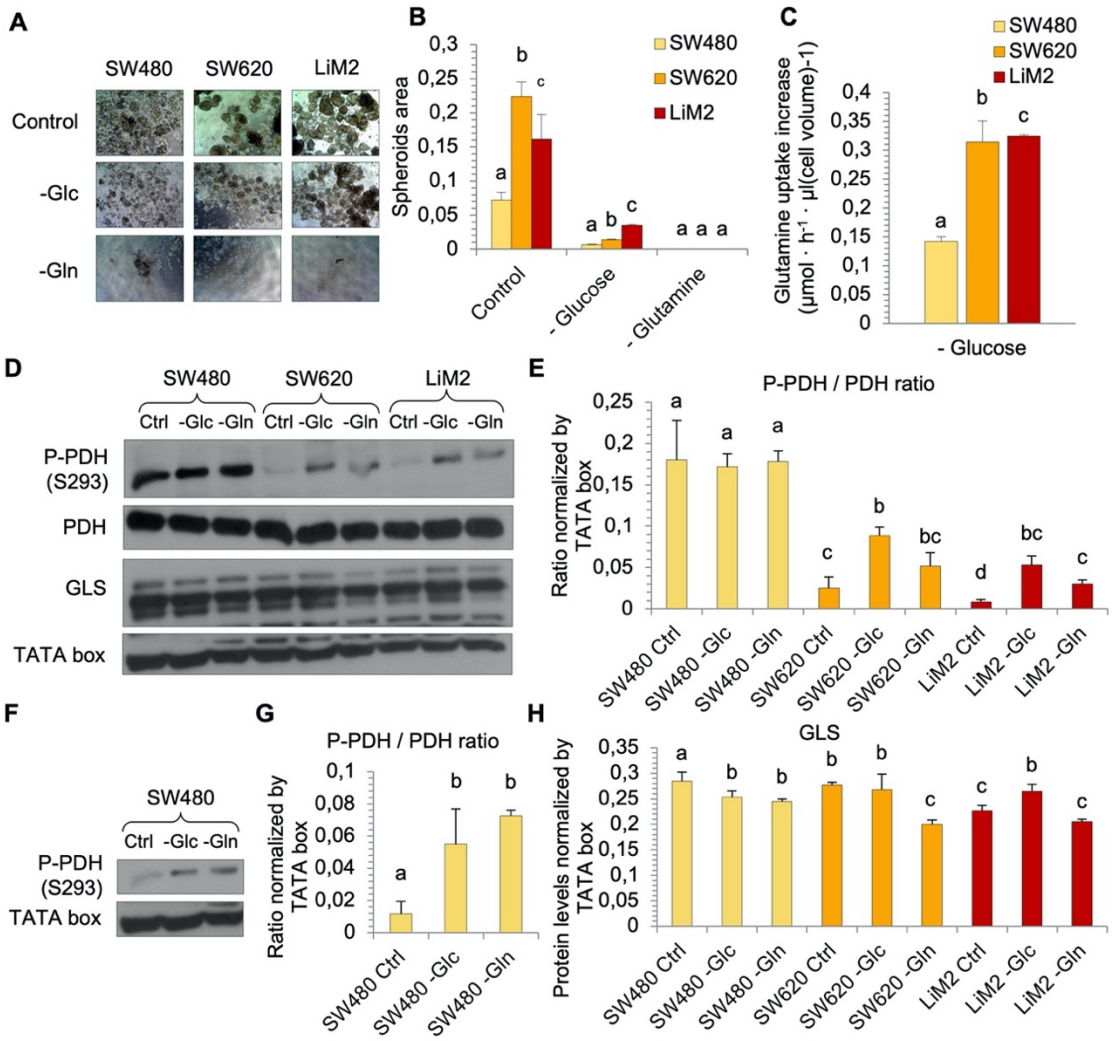

Figure 5.1.14. Glucose and glutamine deprivation effects on 3D growth and metabolic enzymes in primary (SW480) and metastatic (SW620 and LiM2) colon cancer cell lines. A. Spheroid formation assay done in low attachment plates and medium containing EGF, Bfgf, heparine, B27, insulin, and hydrocortisone for one week under control conditions (12.5 mM Glc and 4 mM Gln), glucose deprivation (-Glc) and glutamine deprivation (-Gln). Images of a contrast-phase microscope (40X). **B.** Quantification of the experiment in A. using ImageJ software. **C.** Glutamine uptake rate measure by spectrophotometry from 0 to 48h. **D.** PDH phosphorylation status and GLS levels tested by western blotting under control conditions (Ctrl), glucose deprivation (-Glc) and glutamine (-Gln) deprivation. **E.** and **H.** Protein level quantification from the experiment in D. **F.** From the experiment in D, a lower exposition of the western blotting film from the same experiment in D. **G.** Protein level quantification from the experiment in F. using ImageJ software. [a,b,c] In all cases, a one-way ANOVA and Scheffe's test for multiple comparisons was performed for the factor "cell line". Groups with different letter show significant differences with α=0.05.

Finally, after the evidence of enhanced pyruvate metabolism in our cell models previously seen in section 5.1.2.2, we decided to compare the cell proliferation under glucose or glutamine deprivation in the presence of 10 mM pyruvate. Indeed, we found that the presence of pyruvate under glucose deprivation is able to partially rescue cell proliferation of only the more metastatic cell line, LiM2 (Figure 5.1.15A-C). We also checked the phosphorylation status of PDH in these conditions (glucose deprivation and adding pyruvate), confirming that in the absence of glucose,

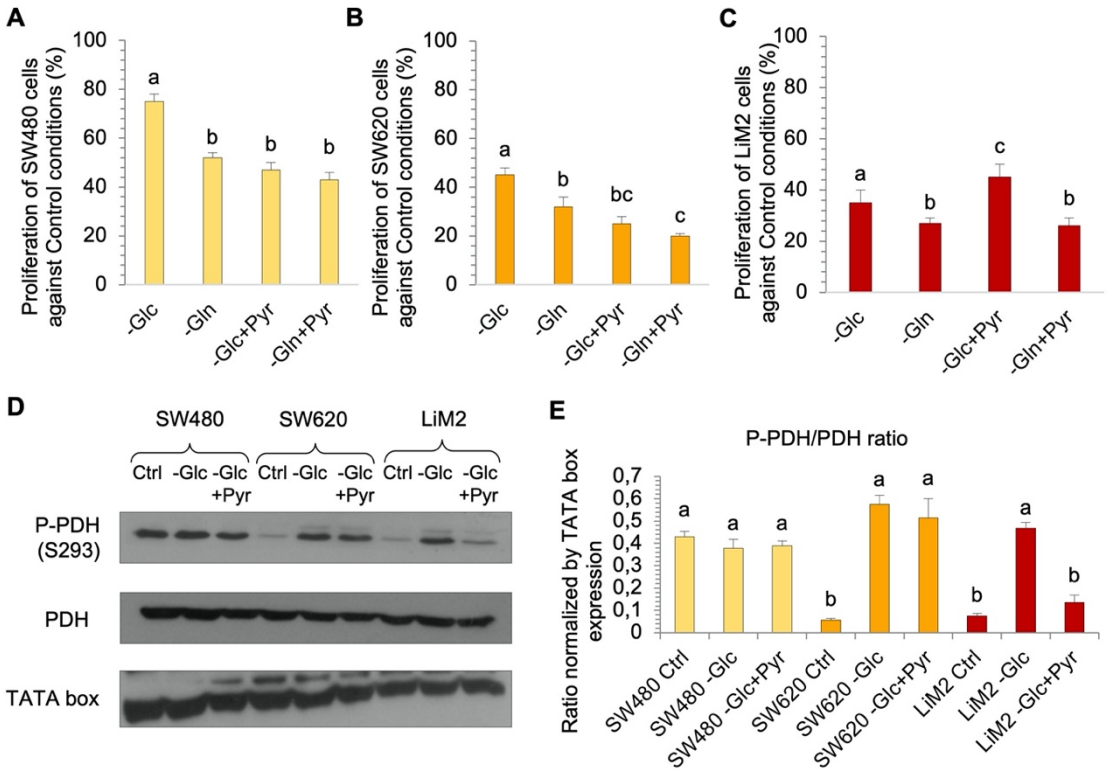

Figure 5.1.15. Effects of pyruvate on PDH phosphorylation and growth in primary (SW480) and metastatic (SW620 and LiM2) colon cancer cell lines. A. – C. P-PDH (phosphorylated pyruvate dehydrogenase at S293), PDH (pyruvate dehydrogenase), protein levels and TATA box, used as a loading control, tested by western blotting under control conditions (12.5 mM glucose and 4 mM glutamine), glucose deprivation (-Glc) and glucose deprivation adding 10 mM of pyruvate (-Glc+Pyr). **D.** Quantification of the experiment in A. using ImageJ software. **E.** Cell proliferation measured by flow cytometry (beads counting) after 48 hours of incubation under control conditions (Ctrl), glucose deprivation (-Glc), glutamine deprivation adding 10 mM pyruvate (-Glc+Pyr), glutamine deprivation (-Gln) and glutamine deprivation adding 10 mM of pyruvate (-Gln+Pyr). [a,b,c] In all cases, a one-way ANOVA and Scheffe's test for multiple comparisons was performed for the factor "cell line". Groups with different letter show significant differences with α=0.05.

PDH was inactivated by phosphorylation in both metastatic cell lines and that pyruvate addition only induced PDH activation (dephosphorylation) in LiM2 cells (Figure 5.1.15D and E). All these experiments prove that the metastatic cell lines, and especially LiM2, display higher metabolic flexibility and adaptation to distinct perturbations, which confer an advantage in circulation or changing environments, crucial events for metastatic progression (Lehuédé et al., 2016).

5.1.2.4 Amino acid profile of primary and metastatic colon cancer cell lines

In order to complete the characterisation of metabolic traits associated with metastatic capacity in colon cancer, we measured intracellular metabolite concentrations (Appendix IV, Table A.IV.1, and Figure A.IV.1 and 2) as well as metabolite exchange fluxes with cell culture media (Appendix IV, Table A.IV.2, and Figure A.IV.3 and 4) using the Absolute IDQ p18 kit (Biocrates Life Sciences AG).

Intracellular glutamate and glutamine intracellular concentrations were significantly higher in metastatic cell lines (SW620 and LiM2), consistent with their higher rate of glutamine uptake and glutaminolysis (Figure 5.1.16A, B and Figure 5.1.11). Similarly, we observed increased intracellular serine and glycine concentration (Figure 5.1.16C and D), as well as increased serine consumption and reduced glycine production in the metastatic cell lines (Figure 5.1.16E and F). This suggests an increased serine hydroxymethyltransferase (SHMT) activity, which was confirmed by western blotting (Figure 5.1.16G and H), and thus, probably enhanced folate metabolism and nucleotide synthesis in the metastatic cell lines.

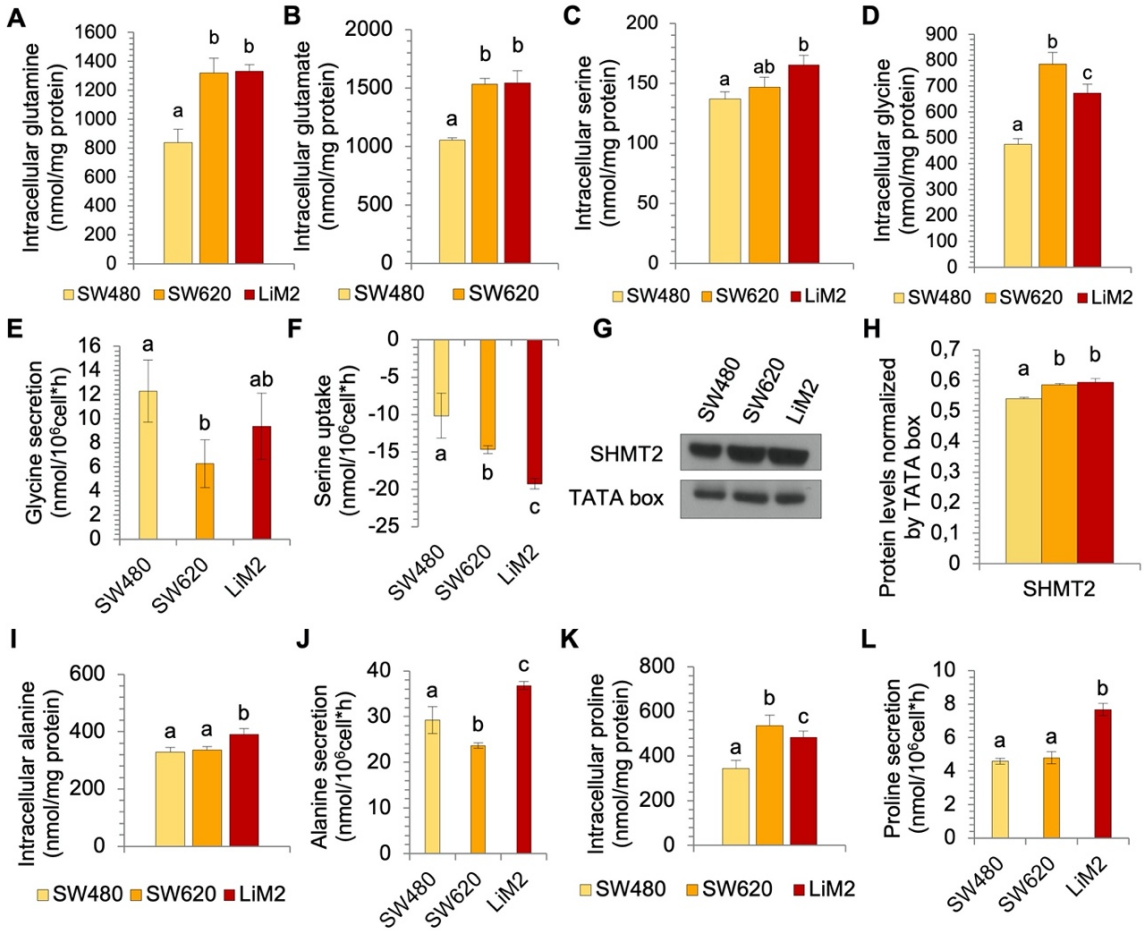

Figure 5.1.16. Amino acid metabolism in primary (SW480) and metastatic (SW620 and LiM2) colon cancer cell lines. A. - D., I and **K.** Intracellular content of amino acids obtained by the Absolute IDQ p180 kit (Biocrates Life Sciences AG) after 24 hours of incubation with DMEM 12.5 mM Glc and 4 mM Gln, 5% FBS, and 1% S/P. **E, F, J** and **L.** Amino acid uptake and secretion rates obtained by measuring the culture medium by the Absolute IDQ p180 kit (Biocrates Life Sciences AG) before and after 24 hours of incubation with DMEM 12.5 mM Glc, 4 mM Gln, 5% FBS, and 1% S/P. **G.** SHMT2 protein levels tested by western blotting **H.** Quantification of the experiment in G using ImageJ software. [a,b,c] In all cases, a one-way ANOVA and Scheffe's test for multiple comparisons was performed for the factor "cell line". Groups with different letter show significant differences with α=0.05.

Regarding other amino acid levels, in concordance with the previous results about pyruvate metabolism, intracellular alanine and alanine secretion are higher in LiM2 cells (Figure 5.1.16I and J). It is reasonable to think that if pyruvate metabolism enhanced in LiM2 cells, also its metabolisation to alanine is increased. Furthermore, alanine is metabolised directly from pyruvate through alanine aminotransferase, whose activity has been explored as a biomarker of hepatic carcinoma (Zhang et al., 2019).

Proline is another amino acid that we observed to be gradually altered with metastatic capacity: its intracellular levels are higher in SW620 and LiM2 than in SW480 and its secretion is increased in LiM2 cells (Figure 5.1.16K and L). Proline metabolism is also enhanced in cancer metabolic reprogramming (Tanner et al., 2018) and its production and secretion could be related to the ability of metastatic cells to synthesise collagen and form extracellular matrix in a cluster-migration environment or during the colonisation process (Phang et al., 2015).

The metabolomics profile analysis also allowed us to observe that the metastatic cells displayed decreased intracellular concentrations and increased consumption of the essential amino acids (EAA) pool, specifically arginine, tyrosine, valine, phenylalanine, lysine and tryptophan (Figure 5.1.17A-K and Figure A.IV.1 and 2). This could be an indicator of either enhanced protein synthesis or increased catabolism of EAA to fuel the TCA and respiratory chain. It is also consistent with the results of alternative substrates respirations where OCR of the metastatic cell lines was increased after arginine and leucine injections (Figure A.III.2). Regarding the results of the secretion of some essential amino acids is probably attributable to technical details that are not properly solved. However, there is a clear tendency of the values to be lower in the final medium with respect to the initial medium as the metastatic capacity of the cell lines increases.

Additionally, acyl-carnitines and free carnitine were detected as significantly higher concentrations in SW480 compared to metastatic cell lines (Table A.IV.1), potentially indicative of differences the β-oxidation observed in the fatty acid mitochondrial fuel assay (Figure A.III.2). It is possible that SW480 display enhanced β-oxidation as they showed to be more dependent on this pathway, although fatty acid uptake is increased in the metastatic cell lines according to the proteomics and transcriptomics studies of our cell line models (Urosevic et al., 2014).

Finally, the metastatic cell lines have also an enhanced polyamine metabolism, as they consumed less taurine and produced more spermidine and putrescine (Figure 5.1.17L-N), which is correlated with an increased arginine consumption (Figure 5.1.17A). This observation is consistent with many research that have related polyamine metabolism to cancer proliferation and metastasis (Casero et al., 2018) even in the same SW480 - SW620 cell model (Duranton et al., 2003).

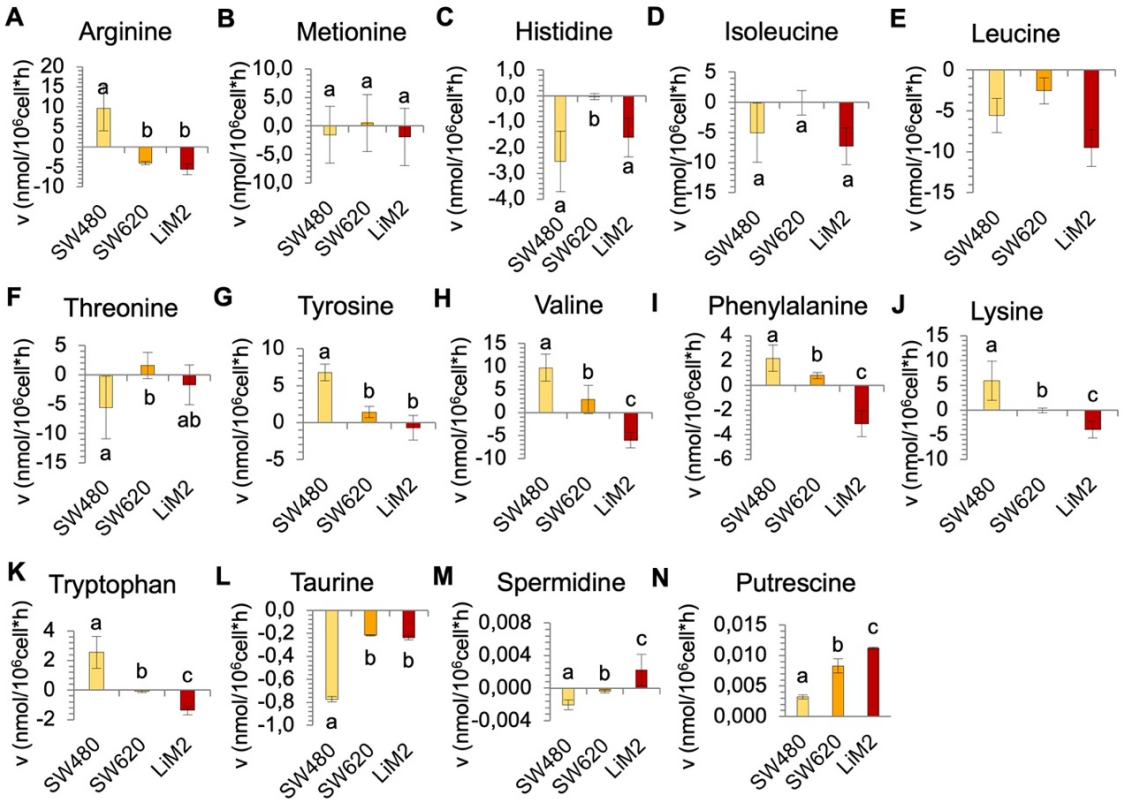

Figure 5.1.17. Non-essential amino acids and polyamine metabolism in primary (SW480) and metastatic (SW620 and LiM2) colon cancer cell lines. A. - N. Non-essential amino acids (A – K) and polyamines (L – N) uptake and secretion rates obtained by measuring the culture medium by the Absolute IDQ p180 kit (Biocrates Life Sciences AG) before and after 24 hours of incubation with DMEM 12.5 mM Glc, 4 mM Gln, 5% FBS and 1% S/P. [a,b,c] In all cases, a one-way ANOVA and Scheffe's test for multiple comparisons was performed for the factor "cell line". Groups with different letter show significant differences with α=0.05.

5.1.2.5 The metabolic adaptation of the metastatic cell lines *in vitro* is maintained in an *in vivo* scenario

A significant concern working with *in vitro* models is that the metabolic phenotype can be significantly different from those encountered *in vivo* (Kreuzaler et al., 2019). When studying the metabolic adaptation of such a complex process that is metastasis it is of great importance to consider as much as possible the interaction of cancer cells with their microenvironment, for example substrate availability or oxygen concentration can change significantly from the *in vitro* culture. Furthermore, many examples in the literature show metabolic interactions between the tumour stroma and cancer cells (Lyssiotis and Kimmelman, 2017). For that reason, we used *in vivo* models to determine if key features of our cellular models were conserved, which would validate our results *in vitro*. Specifically, the three cell lines SW480, SW620 and LiM2 were injected subcutaneously into immunocompromised NOD/SCID mice and once tumours reached 8-10 mm in diameter, mice were given a bolus of either [U-^{13}C]-glucose or [U-^{13}C]-glutamine in

order to examine the metabolic fluxes *in vivo* through metabolite extraction from the frozen tumour and subsequent analysis by GC-MS.

Firstly, we observed that tumour growth rate in mice correlated with the metastatic phenotype characterised *in vitro* (Figure 5.1.18A), being LiM2 cells the cells that formed tumours faster, even though its growth in cell culture is lower than SW620. We also extracted and paraffined tissues where there could have been metastasis, such as the livers, lung, and spleen. However, no metastasis was detected in any these tissues for any of the cell lines (Figure 5.1.18B). A possible explanation is that more time would be needed to develop metastasis, which was not possible to achieve as the primary tumour would have exceeded the allowed diameter for mice well-being.

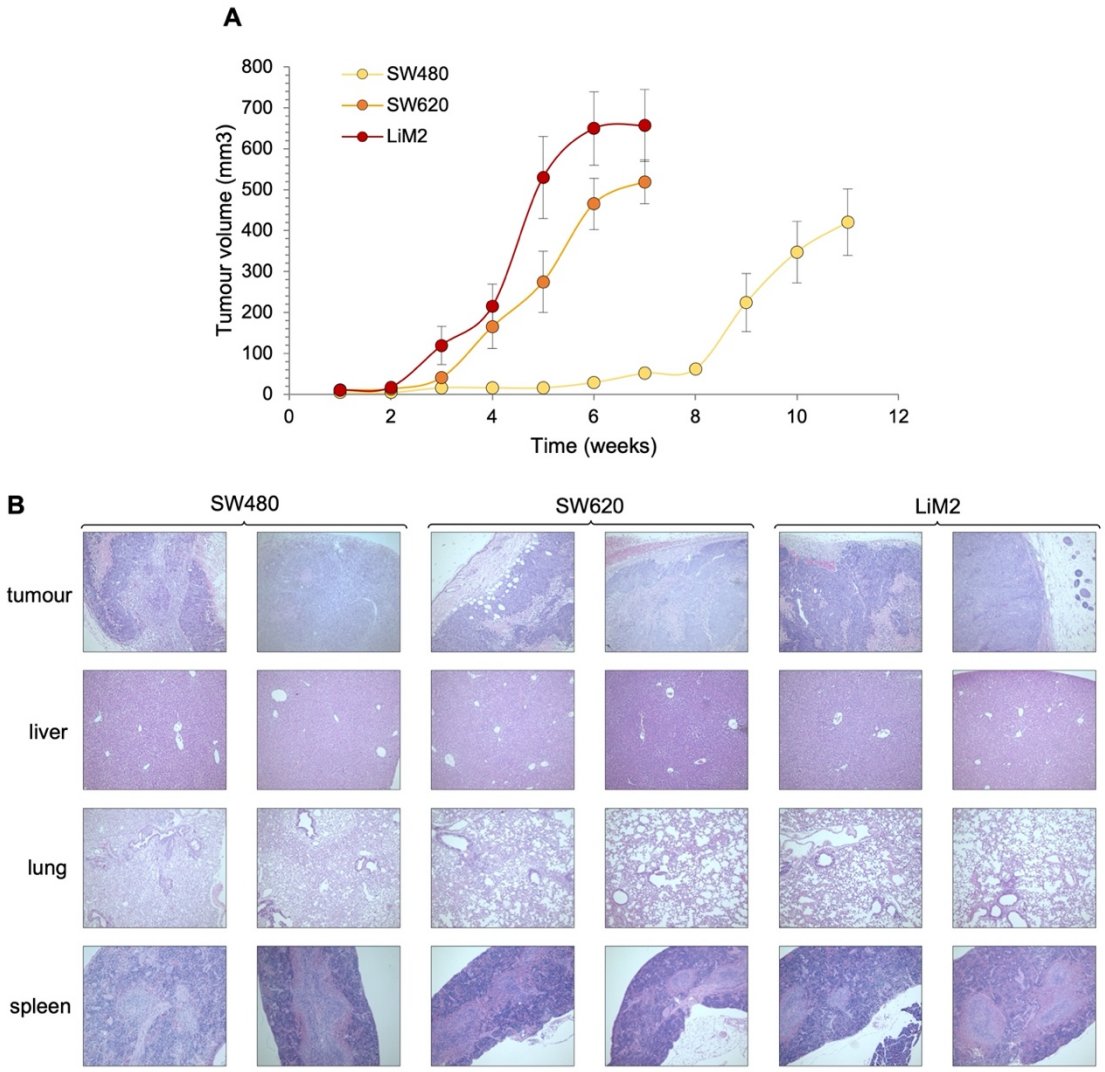

Figure 5.1.18. *In vivo* growth and metastasis of the primary (SW480) and metastatic (SW620 and LiM2) colon cancer cell lines. A. Mean of tumour volume evolution of each cell line injected in immunocompromised NOD/SCID mice measured by calliper. **B.** Haematoxylin and eosin staining of paraffin-embedded tissues (tumour, liver, lung, and spleen) at the end of the experiment, when tumours reached 8-10 mm in diameter. Images of two different mice for each cell line (40X).

Most of the tumour piece of each mice was deep-frozen in liquid nitrogen for metabolite extraction, but a part of it was paraffin-embedded in order to analyse the tissue characteristics as well as perform immunohistochemistry. From haematoxylin and eosin staining of that slides, we observed that tumours of metastatic cell lines SW620 and LiM2 have an infiltrating pattern, while SW480 cells form tumours that have a more defined edge (Figure 5.1.18B), consequent with the previous *in vivo* studies with SW480 and SW620 (Hewitt et al., 2000).

Immunohistochemical experiments allowed us to identify some of the proteins that have been explored *in vitro* that were changed between primary and metastatic cells. We focused mainly on EMT markers and metabolic enzymes. An excellent agreement with *in vitro* cell data was observed for EMT markers, as both E-cadherin and vimentin were increased in the metastatic cell lines, suggesting that the metastatic phenotype at the level of epithelial-mesenchymal transition is maintained *in vivo* (Figure 5.1.19A and B).

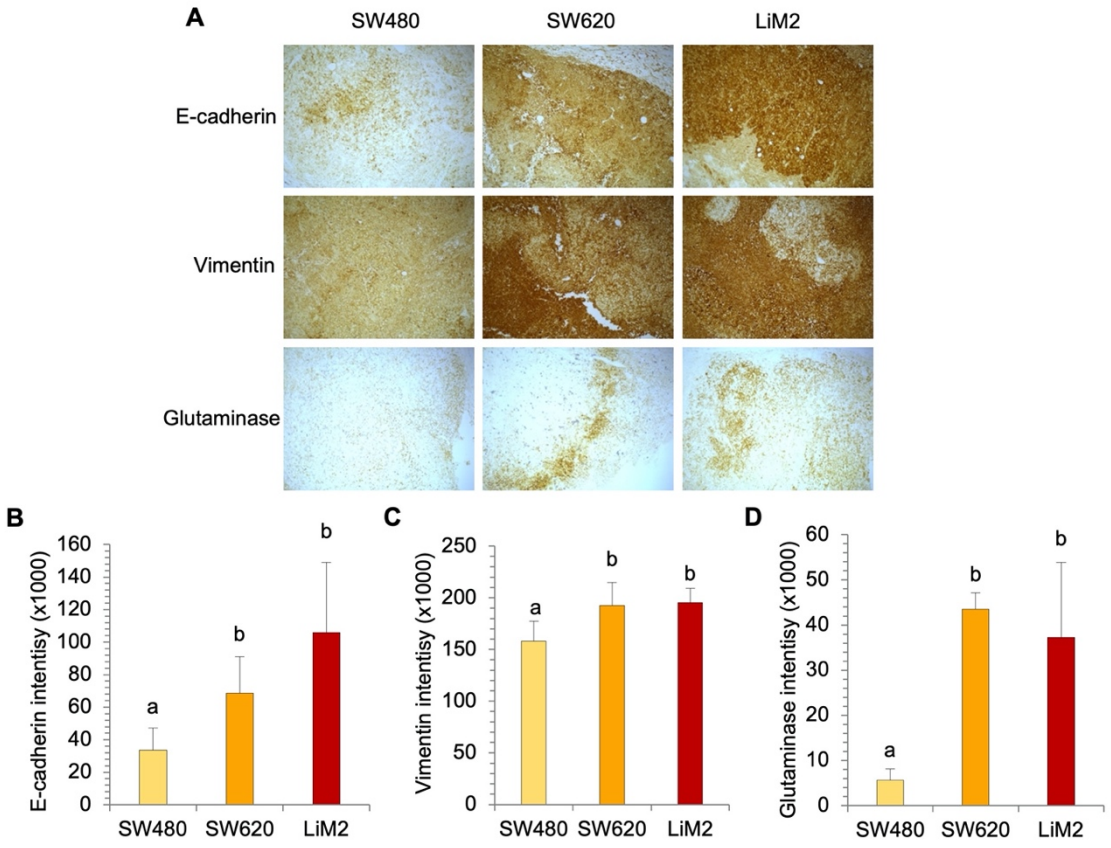

Figure 5.1.19. Immunohistochemistry of the tumours from mice injected with the primary (SW480) and metastatic (SW620 and LiM2) colon cancer cell lines. A. Immunohistochemical staining of paraffin-embedded tumour slides of each cell line after deparaffination, antigen unmasking and staining using E-cadherin, vimentin and glutaminase antibodies (40X). **B.** Quantification of the experiment in A using ImageJ software. [a,b,c] In all cases, a one-way ANOVA and Scheffe's test for multiple comparisons was performed for the factor "cell line". Groups with different letter show significant differences with α=0.05.

Regarding metabolic enzymes, we observe glutaminase is increased in the metastatic cell lines as it was in the *in vitro* experiments (Figure 5.1.19A and B). In order to analyse the phosphorylation status of PDH, immunohistochemistry was not suitable as the P-PDH antibody was not sensitive enough to detect PDH phosphorylation. Therefore, we opt for performing a western blot experiment from a protein extract of the same frozen tumour sample that we used for the SIRM experiment. Remarkably, PDH phosphorylation also followed the same pattern as *in vitro* with the metastatic cell lines having a less phosphorylated (more active) PDH enzyme (Figure 5.1.20A and B).

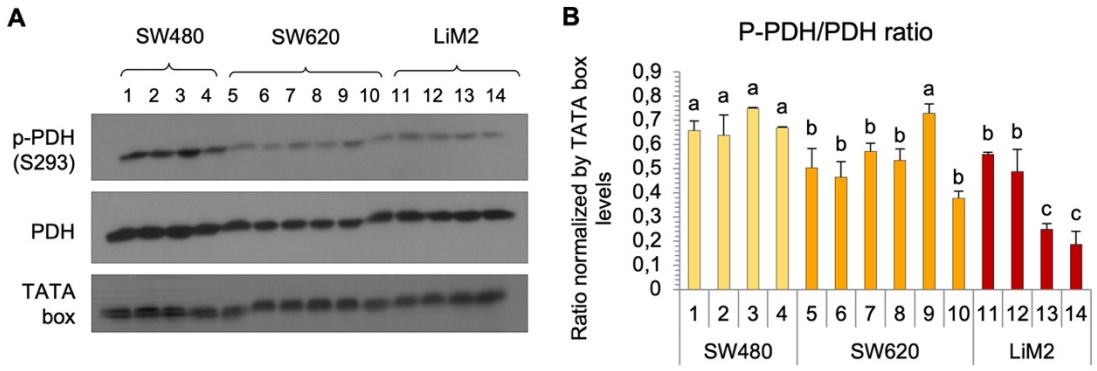

Figure 5.1.20. PDH phosphorylation status of the tumours from mice injected with the primary (SW480) and metastatic (SW620 and LiM2) colon cancer cell lines. A. PDH phosphorylation status tested by western blotting of tumour protein extracts. **B.** Quantification of the experiment in A using ImageJ software. [a,b,c] A one-way ANOVA and Scheffe's test for multiple comparisons was performed for the factor "cell line". Groups with different letter show significant differences with α=0.05.

At the level of ^{13}C label incorporation, isotopologue labelling patterns obtained after a bolus of either [U-^{13}C]-glucose or [U-^{13}C]-glutamine, were similar to results *in vitro* as the previous experiment on PDH phosphorylation and GLS anticipated. Incorporation of glucose to the TCA cycle was maintained in the *in vivo* environment in citrate and malate TCA intermediaries (Figure 5.1.21A). In the case of glutamine incorporation to the TCA cycle in the oxidative manner, the pattern perfectly corresponds with the observed *in vitro*, a clear increase in all the TCA cycle intermediaries that were analysed (Figure 5.1.21B). Finally, the reductive carboxylation from glutamine was not following the same pattern than *in vitro* and glutamine incorporation to citrate is higher in the primary tumour cells SW480, which could have developed a higher fatty acid *de novo* synthesis from citrate in an *in vivo* environment. At the same time, LiM2 cells have diminished the reductive carboxylation compared to SW620 cells (Figure 5.1.21C).

Altogether, these data obtained *in vivo* generally confirm a similar metabolic behaviour of the cell lines *in vitro* and *in vivo*. Such correspondence gives more value and reliability to all the previous findings *in vitro*, which were the base for the search of metabolic weaknesses that could be explored for possible metastatic colorectal cancer therapies.

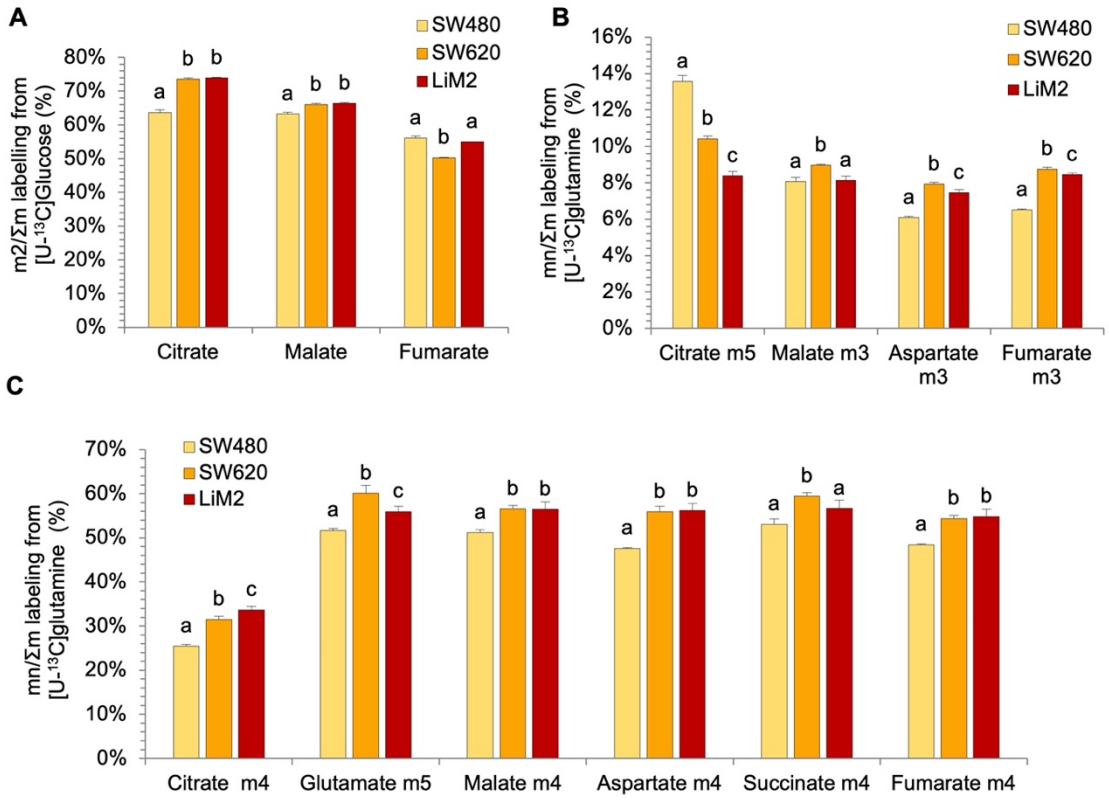

Figure 5.1.21. Stable isotope-resolved metabolomics experiment in the tumours from mice injected with the primary (SW480) and metastatic (SW620 and LiM2) colon cancer cell lines. A. Glucose contribution to the TCA cycle measured from a tumour extract after a 15 minutes bolus of [U-^{13}C]-glucose (20 mg / 35 g) before the mice were culled. TCA intermediates were isolated from the tumour and analysed by GC-MS for isotopologue distribution (see Table A.II.13). **B.** and **C.** Glutamine contribution to the TCA cycle measured from a tumour extract after two boluses of [U-^{13}C]-glutamine (6 mg / 35 g, with 15 minutes interval) before the mice were culled. TCA intermediates were isolated from the tumour and analysed by GC-MS for isotopologue distribution. Letter (B) represents the isotopologues that correspond to reductive carboxylation of glutamine and (C) represents the isotopologues that correspond to oxidative carboxylation of glutamine (see Table A.II.14). ^{a,b,c} A one-way ANOVA and Scheffe's test for multiple comparisons was performed for the factor "cell line". Groups with different letter show significant differences with α=0.05.

5.2 CHAPTER 2. THE METABOLIC VULNERABILITIES ASSOCIATED TO METASTASIS IN COLORECTAL CANCER.

5.2.1 INTRODUCTION

5.2.1.1 A genome-scale metabolic model for metastatic progression of colon cancer

After having performed a deep metabolic characterisation of the same-patient derived cell lines SW480, SW620, and LiM2, we have an overall idea of how tumour cells rewire their metabolism in order to adapt to different environments and undergo the metastatic process. These metabolic characteristics can be exploited for target discovery that could eventually improve metastatic colorectal cancer treatments. However, the best way to integrate all the data that we have obtained and predict which would be the best targets against metastasis is to perform a computational metabolic model. For that purpose, the bioinformaticians in our research group integrated the experimental data explained in the results section of the first chapter of the present thesis, as well as previously published data and built a genome-scale metabolic model (GSMM).

The workflow used consisted of many steps that are further specified in Appendix V and Figure A.V.1. In a few words, they firstly obtained a central carbon metabolism flux map using ^{13}C-based metabolic flux analysis (MFA) (Antoniewicz, 2018). To perform the MFA, data from measured growth rates, rates of metabolite uptake and secretion, respiration parameters as well as the SIRM experiments that we performed incubating our cells with [1,2-^{13}C]-glucose and [U-^{13}C]-glutamine was used. The flux map performed using MFA was integrated into the human GSMM model Recon2 (Swainston et al., 2016). Then, they integrated targeted metabolomics from the experiment done using the Absolute IDQ p18 kit (Biocrates Life Sciences AG). This was done in order to constrain GSMMs to produce intracellular metabolites at a rate proportional to their concentrations and the proliferation rate of each cell line. Finally, Minimal Cut Set Analysis (MCS) was used to integrate reported essential metabolic genes from project DRIVE (deep RNAi interrogation of viability effects in cancer) database (McDonald et al., 2017a) were also integrated and the GIMME algorithm (Becker and Palsson, 2008; Schmidt et al., 2013) was used to restrict the maximum flux through reactions based on gene expression evidence.

Once the model is created, flux sampling was used to compute flux combinations consistent with the above-integrated data. For each of the flux samples, gene knockouts were simulated, and flux samples were ranked based on their consistency with gene dependency data. The later step served both to minimise the false positives of gene essentiality and integrate partial dependences on non-essential genes. The top 100 ranked flux samples were selected to obtain the cell line-specific flux maps (Table A.V.3).

As expected, the cell line-specific flux maps showed significantly higher glycolytic flux in the metastatic cell lines, as exemplified by the flux through hexokinase 1 and lactate dehydrogenase (Figure A.V.2). Furthermore, consistent with the phosphorylation status of PDH,

the flux maps presented a higher flux through PDH and citrate synthase in SW620 and LiM2 than in SW480. It was worth noting that the computed flux maps showed that in the metastatic cell lines the PDH/lactate dehydrogenase flux ratio was quite low (roughly 15%), suggesting that despite the PDH activity, the metastatic cell lines still predominantly relied on aerobic glycolysis. Likewise, cell line-specific flux maps predicted increased glutaminase activity in the metastatic cell lines, and LiM2 in particular, in concordance with the increased glutaminase levels and glutamine consumption rates (Figure A.V.2). Together, that means that the results of the model are consistent with the experimental data, which is indicative of good performance and gives reliability to the workflow applied.

The main application of the computational model was to identify single or synthetic lethal target pairs that could selectively inhibit growth in the metastatic cell lines. Overall, 10 single targets and 237 target combinations were predicted to impair the proliferation of SW620 and LiM2 (Table A.V.5). Of these targets, we chose to focus mainly on related to cysteine metabolism (*GSR*, *SLC7A9*+*SLC7A11*, *SLC7A9*+*SLC3A2*, *SLC3A1*+*SLC7A11*, and *SLC3A1*+*SLC3A2*) and folate metabolism (*MTHFD1*), as were the ones to be more selective for the metastatic cell lines, although other targets were also validated in order to further verify the model as well as to broaden the possible therapeutic strategies against metastasis in colorectal cancer.

5.2.1.2 Exploring and validating metabolic vulnerabilities of the metastatic progression of colon cancer

After having obtained the results and target predictions from the GSMM generated from our cell lines, the next step was to validate these targets using specific inhibitors, metabolic deprivations or other disruptions. An important part of the validation was the search for suitable inhibitors and the design of strategies that allowed us to properly identify how our cells were affected by these inhibitors. The main technique that was used was a proliferation screening by using 96-well plates with different concentrations of the drugs and evaluation of the cell number after a certain incubation by detecting the DNA. Moreover, also apoptosis and 3D growth were evaluated for the most promising inhibitors in order to further evaluate its effect.

In addition, we introduced to our research a new cell line that is isolated from the healthy colon mucosa, NCM460 (Moyer et al., 1996), and that was previously validated as a suitable control in antitumour strategies by the research group (Alcarraz-Vizán et al., 2014). This constitutes an important validation step in order to assess the inhibitors and see how specific are for cancer cells with respect to healthy cells. Having in mind that most of the traditional chemotherapies cause severe side effects it was very important to evaluate *in vitro* the effects of the inhibitors on a healthy cell line to make decisions about their suitability. In our case, with the strategy of specifically targeting vulnerabilities of metastatic cells, we expect that both primary tumour cells and healthy cells would not be affected.

5.2.2 RESULTS AND DISCUSSION

5.2.2.1 Evaluation of the use of NCM460 cell line as a healthy control

Before starting the validation of the targets predicted by the model in the cell lines SW480, SW620, LiM2, and the non-tumoral cell line NCM460, we wanted to explore some characteristics of this lately incorporated cell line in order to evaluate its suitability as a healthy control in our scenario, focusing on growth characteristics and metabolism and comparing them with the previous cell lines. First of all, the growth rate was determined, as well as 3D growth capacity. We expected that proliferation of the healthy cell line would be lower than SW480. However, the growth rate in 2D was in between SW480 and LiM2 (Figure 5.2.1A). The fact that a healthy cell line's growth is higher than a primary tumour cell lines is not alarming, because even though it is a healthy cell line, it has been immortalised and, therefore, it is logic that possessess enhanced growth characteristics. Even more, it makes NCM460 a better control than if it had less growth rate: If its proliferation is not affected by the inhibitors, it would mean that the inhibitors are not blocking just proliferation capacities but specific characteristics of the metastatic cancer cells.

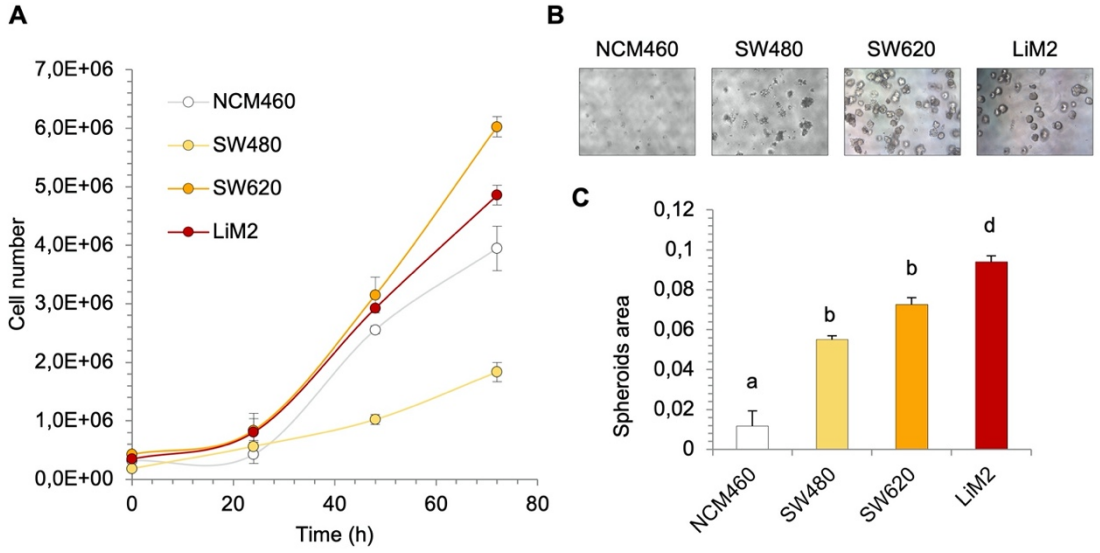

Figure 5.2.1. Growing characteristics of the healthy colon cell line NCM460 compared to the primary tumour and metastatic colon cancer cell lines SW480, SW620 and LiM2. A. Cell number in a p6 plate measured by the automatic cell counter Scepter™ up to 72h (DMEM 12.5 mM Glc, 4 mM Gln, 5% FBS, and 1% S/P) every 24h. **B.** Spheroid formation assay done in low attachment plates and medium containing EGF, Bfgf, heparin, B27, insulin and hydrocortisone for one week, images of a contrast-phase microscope (40X). **C.** Quantification of the spheroid area using ImageJ software from the scanner images. ^{a,b,c,d} A one-way ANOVA and Scheffe's test for multiple comparisons was performed for the factor "cell line". Groups with different letter show significant differences with α=0.05.

As expected, NCM460 were not able to form spheroids (Figure 5.2.1B and C). In proper conditions, it would be possible that healthy colon cells form intestinal organoids (Dedhia et al.,

2016). However, at our experimental conditions, we did not expect that the healthy cell line would form nor an organoid neither a tumoroid (spheroid), which is a feature exclusively of cancer cells, especially the ones that present a cancer stem cell phenotype (Chaicharoenaudomrung et al., 2019). Therefore, this result is consistent with the fact that NCM460 is from a healthy cell line from the colon mucosa and makes the cell line a reliable control.

We then focused on the metabolic characteristics, specifically ^{13}C incorporation into central carbon metabolism from [1,2-^{13}C]-glucose and [U-^{13}C]-glutamine, as it was done with SW480, SW620, and LiM2 cells. We thought it was important to have the information about how NCM460 behave at the level of metabolic fluxes, as that was the basic data to build the GSMM model. Metabolic fluxes result from NCM460 would allow us to understand if the model predictions are really specific against metastatic cells and do not affect healthy cells. Although the incorporation of glucose to intracellular lactate that NCM460 presents, which is a measure of the direct glycolytic flux, is similar to metastatic cell lines (Figure 5.2.2A), as well as the pattern of incorporation of glucose into the pentose phosphate pathway (Figure 5.2.2B and C). Furthermore, both glucose and glutamine incorporation into the TCA cycle (Figure 5.2.2D and E) was lower than all the cancer cell lines. That confirms a metabolic reprogramming in our cancer cells as well as even an enhanced reprogramming in the case of metastatic cells with respect to the primary cell lines.

Finally, the same analysis of intracellular amino acid concentration and uptake and secretion rates done by the Absolute IDQ p180 kit (Biocrates Life Sciences AG) for the cancer cell lines was performed for NCM460. Many of the changes observed at both intracellular concentration or exchange rates are in agreement with the fact that NCM460 is not a cancer cell line with a reprogrammed metabolism. For example, both intracellular levels of glutamate and glutamine are lower than the cancer cell line (Figure 5.2.3A and B). In the case of serine uptake, it is almost insignificant in NCM460 (the values are between uptake and production), compared to the cancer cell lines, which clearly increased serine uptake in agreement with the metastatic potential (Figure 5.2.3C). Some essential amino acids also behave very different from cancer cell lines: Its intracellular levels are much higher than the cancer cell lines, and the value of uptake/secretion rate is in the opposite direction (Figure 5.2.3D-H), although technical issues that could have been given a secretion of essential amino acids as a result.

Overall, the results on growth and metabolic characteristics of the healthy colon NCM460 cell line confirmed that it could be used as a control for the validations of the targets predicted in our model. Even more, we consider it to be an excellent control for our validations due to the fact that the growth rate is similar to the metastatic cell lines but they are not able to form spheroids, added to metabolic characteristics that are generally opposed to the metabolic adaptation of the metastatic cell lines.

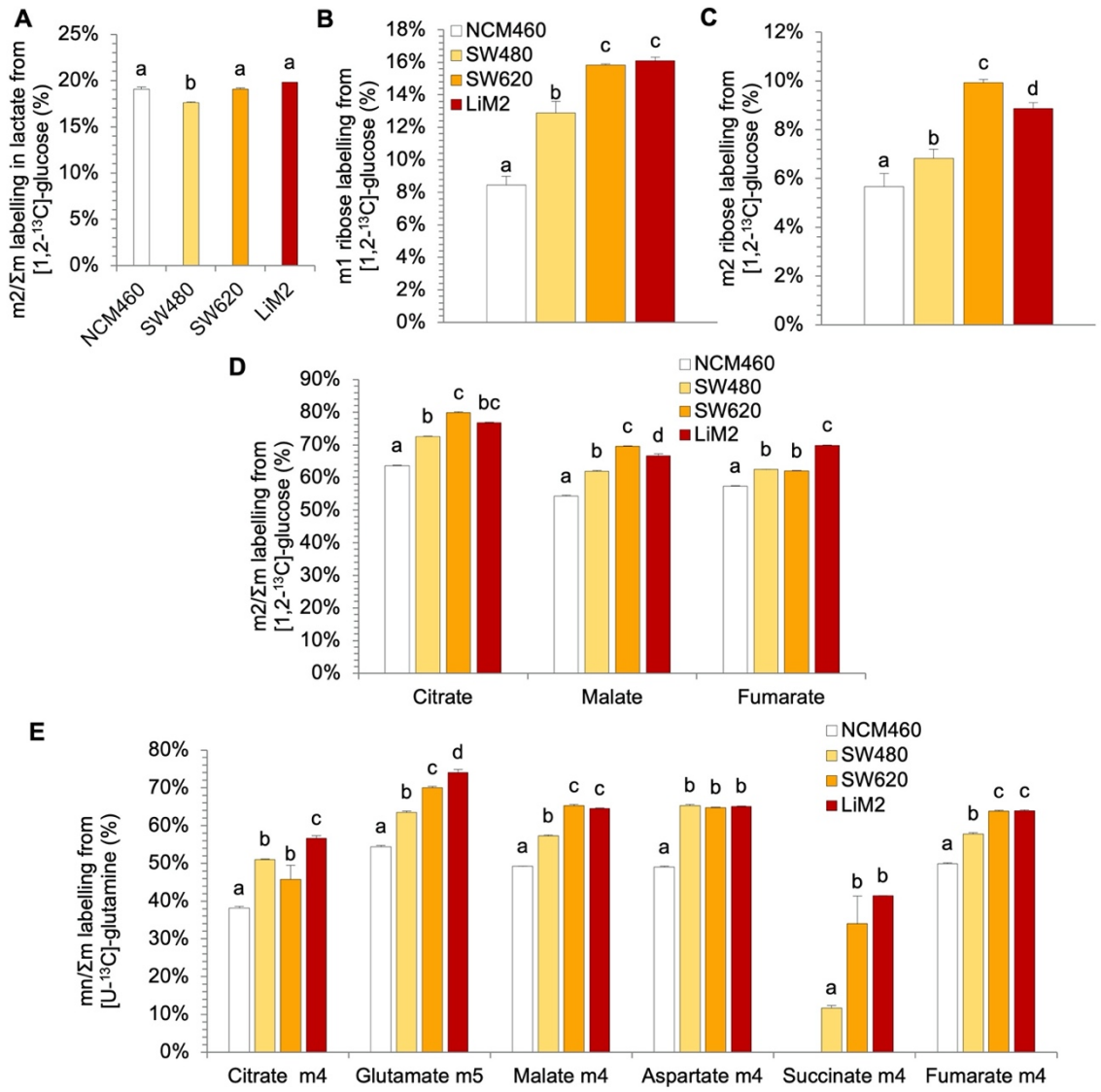

Figure 5.2.2. Glucose and glutamine metabolism in the healthy colon cell line NCM460 compared to the primary tumour and metastatic colon cancer cell lines SW480, SW620, and LiM2. A. Glucose contribution to intracellular lactate measured in the presence of [1,2-^{13}C]-glucose at 12,5 mM after 24h incubation. Lactate was isolated and analysed by G-/MS for isotopologue distribution (see Table A.II.3 and A.II.8). **B.** and **C.** Glucose contribution to the oxidative branch of pentose phosphate pathway (PPP) measured by m1 labelling in ribose (D) and the non-oxidative branch of PPP estimated by m2 labelling in ribose (E) from the same experiment in C, isolating and analysing intracellular ribose and analysing it by GC-MS for isotopologue distribution (see Table A.II.10). **D.** Glucose contribution to the TCA cycle measured in the presence of [1,2-^{13}C]-glucose at 12,5 mM after 24 h incubation. TCA intermediates were isolated and analysed by GC-MS for isotopologue distribution (see Table A.II.1 and A.II.6). **E.** Glutamine contribution to the TCA cycle and some amino acids measured in the presence of [U-^{13}C]-glutamine at 4 mM after 24 h incubation. TCA intermediates were isolated and analysed by GC-MS for isotopologue distribution (see Table A.II.4 and A.II.11). ^{a,b,c,d} In all cases, a one-way ANOVA and Scheffe's test for multiple comparisons was performed for the factor "cell line". Groups with different letter show significant differences with α=0.05.

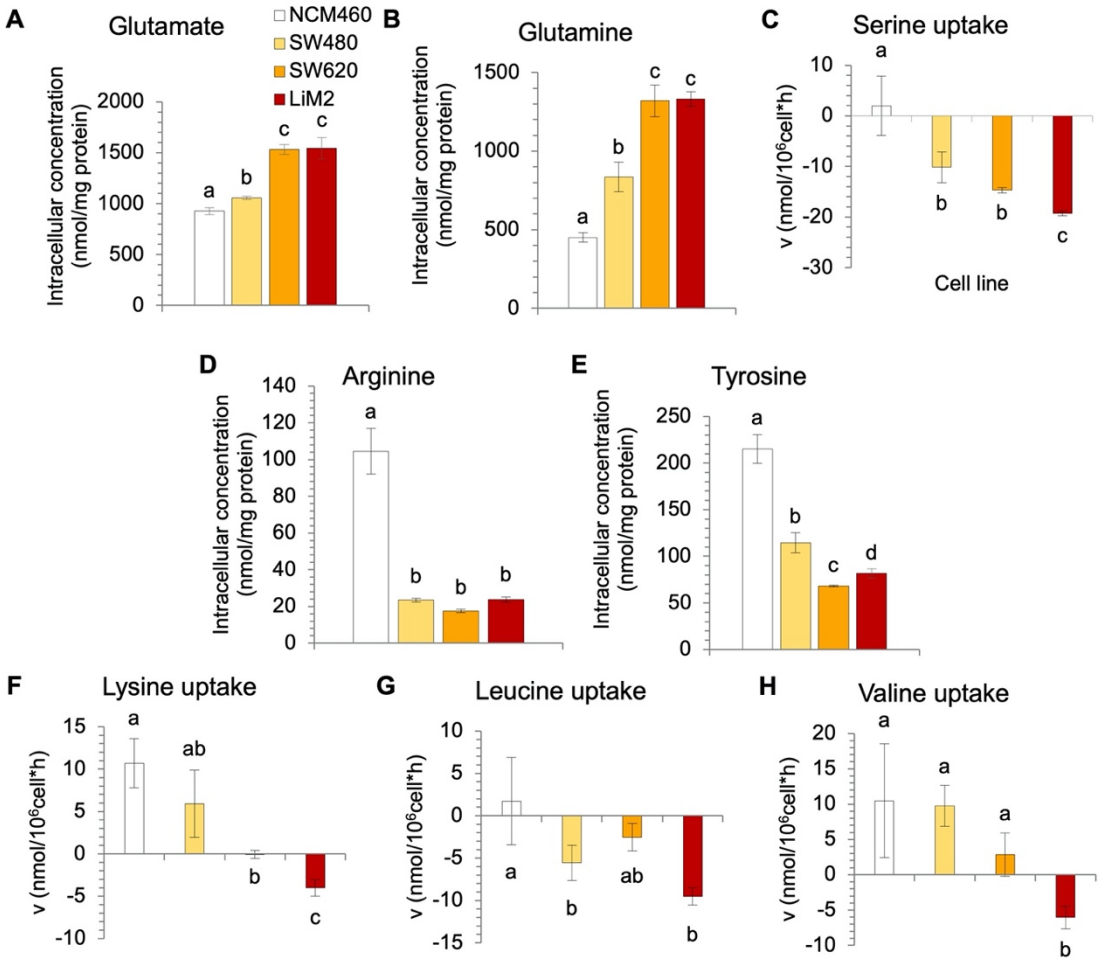

Figure 5.2.3. Amino acid metabolism in the healthy colon cell line NCM460 compared to the primary tumour and metastatic colon cancer cell lines SW480, SW620, and LiM2. A, B, D and **E.** Intracellular content of amino acids obtained by the Absolute IDQ p180 kit (Biocrates Life Sciences AG) after 24 hours of incubation with DMEM 12.5 mM Glc and 4 mM Gln, 5% FBS, and 1% S/P (see Table A.IV.1 and Figures A.IV.1 and 2). **C** and **F – H.** Amino acid uptake and secretion rates obtained by measuring the culture medium by the same kit (Biocrates Life Sciences AG) before and after 24 hours of incubation with DMEM 12.5 mM Glc, 4 mM Gln, 5% FBS, and 1% S/P (see Table A.IV.2 and Figures A.IV.3 and 4). [a,b,c] In all cases, a one-way ANOVA and Scheffe's test for multiple comparisons was performed for the factor "cell line". Groups with different letter show significant differences with α=0.05.

5.2.2.2 Metastatic cell lines are dependent on cystine uptake and vulnerable to system xCT and glutathione reductase inhibition

We first focused on the targets predicted in cysteine metabolism. The reason was that among all single targets and targets pairs, cysteine metabolism targets were the ones that affected more the metastatic cell lines compared to the primary tumour cell line (Table A.V.5). Cystine is the oxidised form of cysteine and the predominant form in blood and culture media (Chawla et al., 1984). Cystine can be transported inside the cell through the cystine/glutamate antiporter system xCT (coded by the genes *SLC7A11* and *SLC3A2*) and through the cystine/neutral amino antiport acid system $b^{0,+}$ (coded by the genes *SLC7A9* and *SLC3A1*) (Figure 5.2.4A). One of the predictions from the GSMMs simulations was the simultaneous inhibition of the two main cystine

transport systems, the system xCT and the system $b^{0,+}$ (Figure 5.2.4B) (i.e. the combination of *SLC7A9* + *SLC3A2*, or *SLC3A1* + *SLC3A2*, or *SLC7A9* + *SLC7A11*, or *SLC7A11* + *SLC3A1*). Cysteine is not only a proteogenic amino acid but also the limiting substrate of glutathione synthesis (Estrela et al., 2016), formed by glutamine, glycine and cysteine.

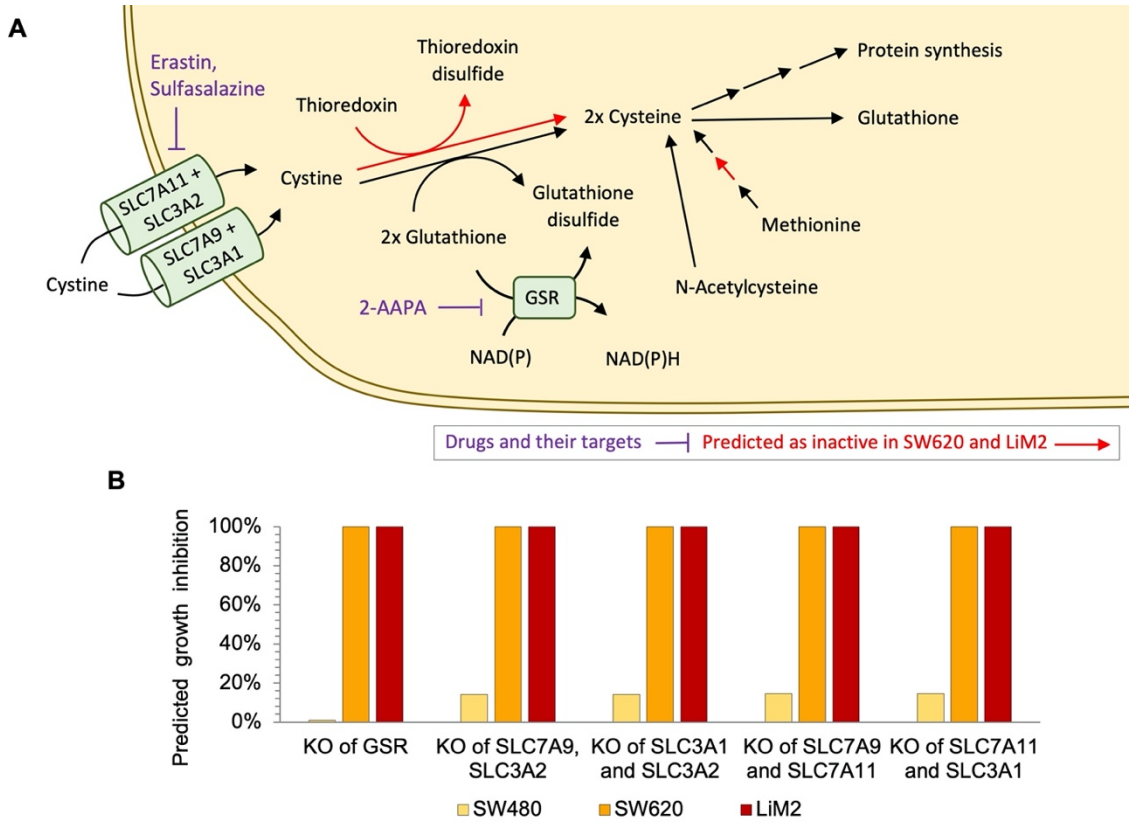

Figure 5.2.4. Predictions in cysteine and glutathione metabolism from a genome-scale metabolic model of SW480, SW620, and LiM2. A. Graphical representation of cysteine and glutathione metabolism, targets predicted and their possible inhibitors and pathways predicted to be inactive in SW620 and LiM2. GSR: Glutathione-disulfide reductase. SLC3A1: $B^{0,+}$-type amino acid transport protein. SLC3A2: Solute carrier family 3 (activators of dibasic and neutral amino acid transport), member 2. SLC7A11: Amino acid transport system xCT. SLC7A9: $B^{0,+}$-type amino acid transporter 1. TXNRD: Thioredoxin reductase. **B.** Predicted growth inhibition under inactivating genes or gene pairs associated with cystine and glutathione metabolism. Growth inhibition is computed as 1-(Biomass production KO/ Biomass production Wild Type) as simulated with the cell line-specific GSMMs.

Glutathione reductase (*GSR*), which catalyses the reduction of oxidised glutathione (glutathione disulfide), was also predicted as a target. In order to synthesise glutathione *de novo*, firstly cystine has to be reduced in the cytoplasm to obtain cysteine, primarily by reacting with reduced glutathione (Tietze et al., 1972). At that point, GSR plays a role in glutathione recycling, in order to obtain more cysteine from cystine, which makes all these targets interdependent. However, the reaction of cysteine from cystine is also possible through the thioredoxin reductase system (Holmgren, 1977). Alternatively, cysteine can also be derived from methionine by the transsulfuration pathway (Sbodio et al., 2019). The GSMM revealed that the metastatic cell lines were largely cystine/cysteine auxotrophs as a result of a predicted insufficient activity of the

transsulfuration pathway. Likewise, the dependence on GSR probably emerged due to a predicted insufficient thioredoxin-dependent cystine reduction (Figure 5.2.4A).

In order to validate the predicted dependence on cystine uptake, we first incubated SW480, SW620, and LiM2 in a culture medium with or without cystine. We observed that under cystine deprivation, proliferation was more significantly reduced in the metastatic cell lines, confirming that they were more dependent on cystine uptake from the media (Figure 5.2.5A). As expected, cell proliferation was rescued through the addition of N-acetyl cysteine (NAC) which can be deacylated to form cysteine (Whillier et al., 2009).

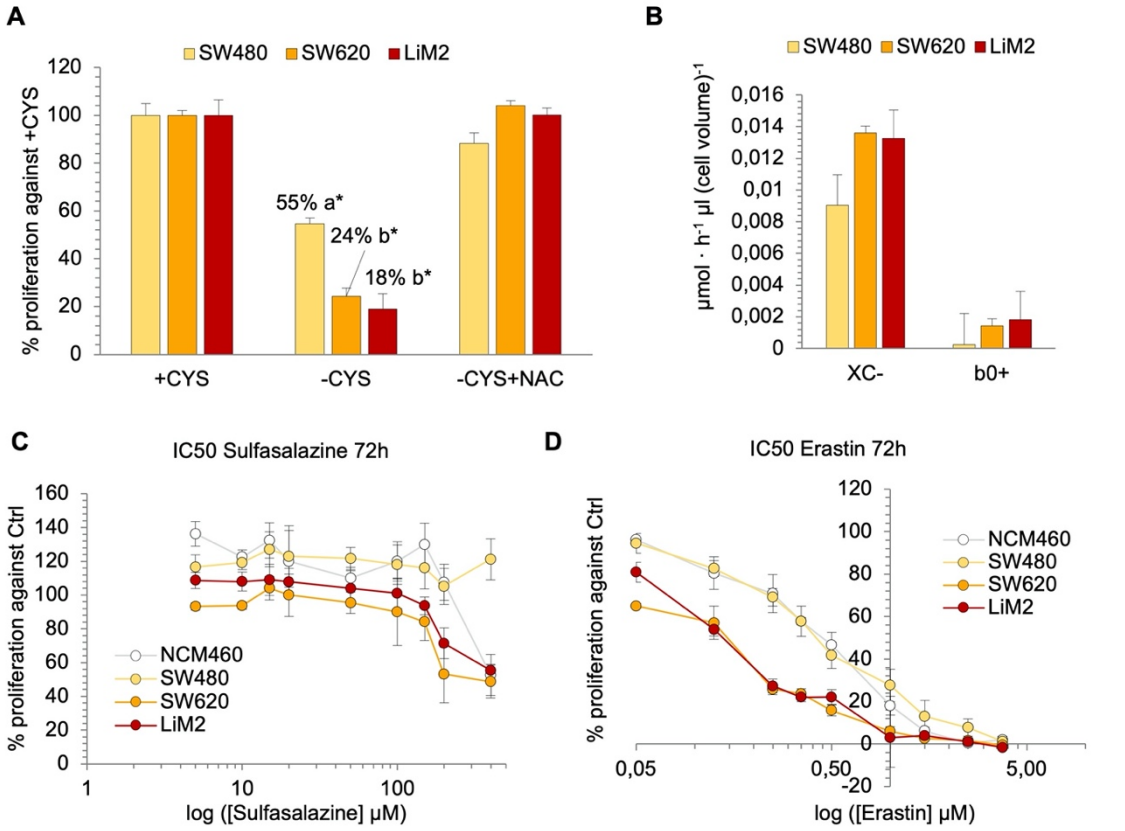

Figure 5.2.5. Cysteine uptake inhibition in the healthy colon NCM460, primary tumour colon cancer cell line SW480, and metastatic derivatives SW620 and LiM2. A. Cell proliferation measured by DNA content using HO33342 under control conditions (+CYS), under cystine deprivation (-CYS) and adding N-acetylcysteine to cystine deprivation (-CYS+NAC). *Student's *t* test for –CYS or -CYS+NAC vs Control conditions, $p<0.05$. [a,b]A one-way ANOVA and Scheffe's test for multiple comparisons was performed for the factor "cell line". Groups with different letter show significant differences with $\alpha=0.05$. **B.** Precited fluxes through the system xCT and $b^{0,+}$ system. **C.** and **D.** IC_{50} curve for (C) sulfasalazine (system xCT inhibitor) and (D) erastin, both system xCT inhibitors assessed by DNA content using HO33342 after 72h incubation.

Having established the dependence of the metastatic cell lines on cystine uptake, we proceeded to evaluate the therapeutic potential of inhibiting cystine transporters. As simulations showed significantly higher flux through the system xCT (Figure 5.2.5B) than through the system $b^{0,+}$, we chose to focus on targeting it. Furthermore, there is previous evidence that system xCT

inhibition impairs cell proliferation and tumorigenic capacity in several cancer types (Gout et al., 1997; Lo et al., 2008; Ma et al., 2015; Savaskan et al., 2008; Shin et al., 2018). With this aim, we evaluated in the SW480, SW620, LiM2 cells and the non-tumour colon NCM460 cell line the effects of two system xCT inhibitors: sulfasalazine and erastin.

The inhibition of cysteine transport by sulfasalazine is approved for the treatment of rheumatoid arthritis (Abbasi et al., 2018) and the drug was first tried for lymphoma and pancreatic cancer cells with a modest IC_{50} of 0.1-0.2 mM (Gout et al., 2001; Lo et al., 2010). Later, another drug for the inhibition of system xCT was discovered, erastin (Dolma et al., 2003) which has an IC_{50} much lower than sulfasalazine for cancer cells and causes a non-apoptotic, iron-dependent cell death which is called ferroptosis (Dixon et al., 2012, 2014). Erastin was also identified as a drug selective for cell lines with mutant RAS, making it an attractive drug choice for our cell models. Even more, the erastin analogue PRLX 93936 is currently in phase I/II clinical trials for the treatment of multiple myeloma (Voorhees et al., 2014). As expected, erastin exhibited IC_{50} values up to three orders of magnitude lower than those of sulfasalazine (Figure 5.2.5C,D and Table 5.2.1), and both drugs had lower IC_{50} values for the metastatic cells.

Inhibitor	IC_{50} values			
	NCM460	SW480	SW620	LiM2
Sulfasalazine (μM)	518 ± 43	534 ± 58	429 ± 66	415 ± 56
Erastin (μM)	1.35 ± 0.32	1.00 ± 0.05	0.86 ± 0.27	0.52 ± 0.13
2-AAPA (μM)	175 ± 76	61 ± 38	28 ± 10	20 ± 2

Table 5.2.1. IC_{50} values of cysteine and glutathione metabolism inhibitors for NCM460, SW480, SW620, and LiM2 cell lines. List of tested inhibitors and its IC_{50} values from various proliferation experiments. The IC_{50} curves were performed assessing cell proliferation by staining DNA with HO33342 under various concentrations of the inhibitors. Sulfasalazine and erastin are specific inhibitors of system xCT and 2-AAPA is a specific inhibitor of GSR (glutathione reductase).

As mentioned before, glutathione reductase (GSR) is another target predicted to be selective for the metastatic cell lines. In order to inhibit GSR we tried 2-AAPA (2-Acetylamino-3-[4-(2-acetylamino-2-carboxyethylsulfanylcarbonylamino) phenyl carbamoylsulfanyl] propionic acid), which is a specific inhibitor of GSR (Seefeldt et al., 2009). However, thioredoxin reductase was proposed recently to be another target (de Souza et al., 2017). This inhibitor was already tested in melanoma, colon, and oesophagal cancer cell lines with IC_{50} values around 20-40 μM (Chen et al., 2012; Li et al., 2017b), causing protein S-glutathionylation, microtubule depolymerisation, and arrest at G2/M phase.

In our cell model, 2-AAPA had lower IC_{50} values for the metastatic cell lines than for the primary cell lines, confirming that targeting GSR is a possible vulnerability of metastatic colon

cancer cells and that there could be not enough activity in the thioredoxin-dependent cystine reduction. The range of IC_{50} values for the metastatic cell lines is similar to the range of concentrations described in the literature (Figure 5.2.6A and Table 5.2.1). In order to check the specificity of the inhibitor to GSR, we incubated the cells in the presence of 2-AAPA and NAC, increasing the concentration of direct cysteine availability (so that cysteine reduction step from cystine would be not necessary) to produce *de novo* glutathione. Indeed, NAC was able to rescue proliferation of the cell lines treated with 20 µM of 2-AAPA (Figure 4.2.6B) but not at higher doses of 2-AAPA.

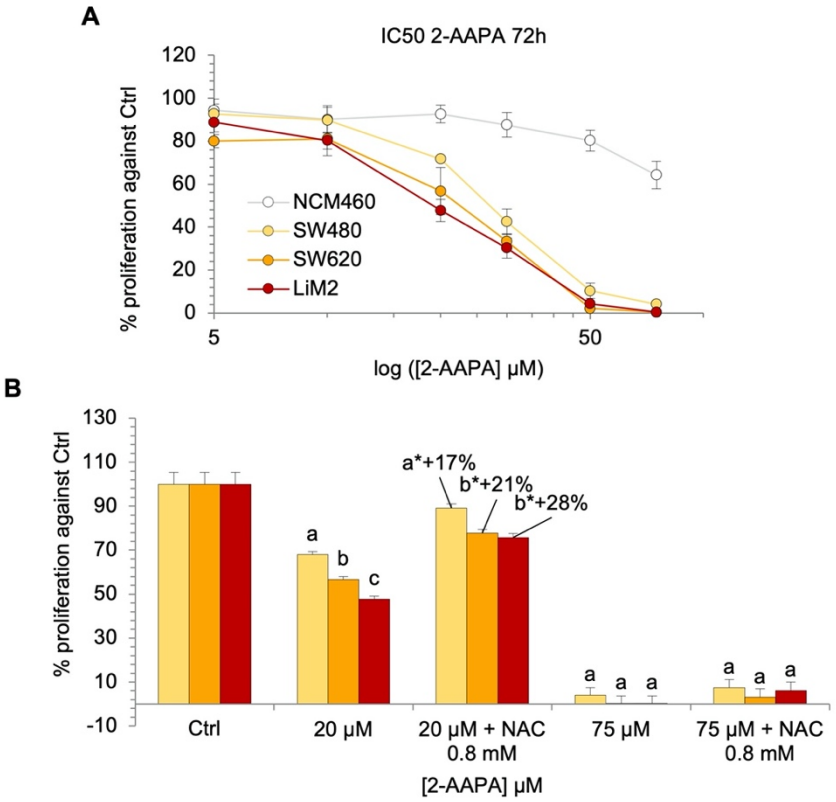

Figure 5.2.6. GSR inhibition in the healthy colon NCM460, primary tumour colon cancer cell line SW480, and metastatic derivatives SW620 and LiM2. A. IC_{50} curve for 2-AAPA (glutathione reductase inhibitor) assessed by cell proliferation measured by DNA content using HO33342 under various erastin concentrations after 72h incubation. **B.** Cell proliferation measured by DNA content using HO33342 under control conditions (Ctrl), under 2-AAPA treatments, and adding N-acetylcysteine to 2-AAPA treatments (-CYS+NAC). * *t* Student test for "2-AAPA 20 uM + NAC 0.8 mM" vs "2-AAPA 20 uM" conditions, $p<0.05$. ^{a,b}A one-way ANOVA and Scheffe's test for multiple comparisons was performed for the factor "cell line". Groups with different letter show significant differences with $\alpha=0.05$.

After these observations, we considered that erastin and 2-AAPA are good inhibitors of metastatic cell growth. However, it is of great importance to further check the effects that these inhibitors have on cell death, as metastatic cells could have the ability to stop their cell cycle but survive at the treatment, as we have seen with glucose and glutamine deprivation in previous sections. For that reason, we analysed cell apoptosis with both inhibitors at the IC_{50} concentration

after 72h and the result was that erastin caused significant cell death by apoptosis in the metastatic cell lines and not in the primary cell line SW480, being that one more proof that metastatic cell lines are largely dependent on cystine uptake and its viability is compromised when cystine importers are inhibited (Figure 5.2.7A). Furthermore, it is consistent with the apoptosis cell death type called ferroptosis that was already described in cystine uptake inhibition for ovarian cancer cells or retinal pigment epithelial cells (Liu et al., 2019; Sun et al., 2018). Ferroptosis cell death is due to a depletion of antioxidant defence that causes an accumulation of lipid peroxides generated from excessive ROS and iron (Abdalkader et al., 2018). On the other hand, inhibition of GSR by 2-AAPA is not causing the same amount of apoptosis as erastin, although there is a significant increase in the metastatic cell lines (Figure 5.2.7B).

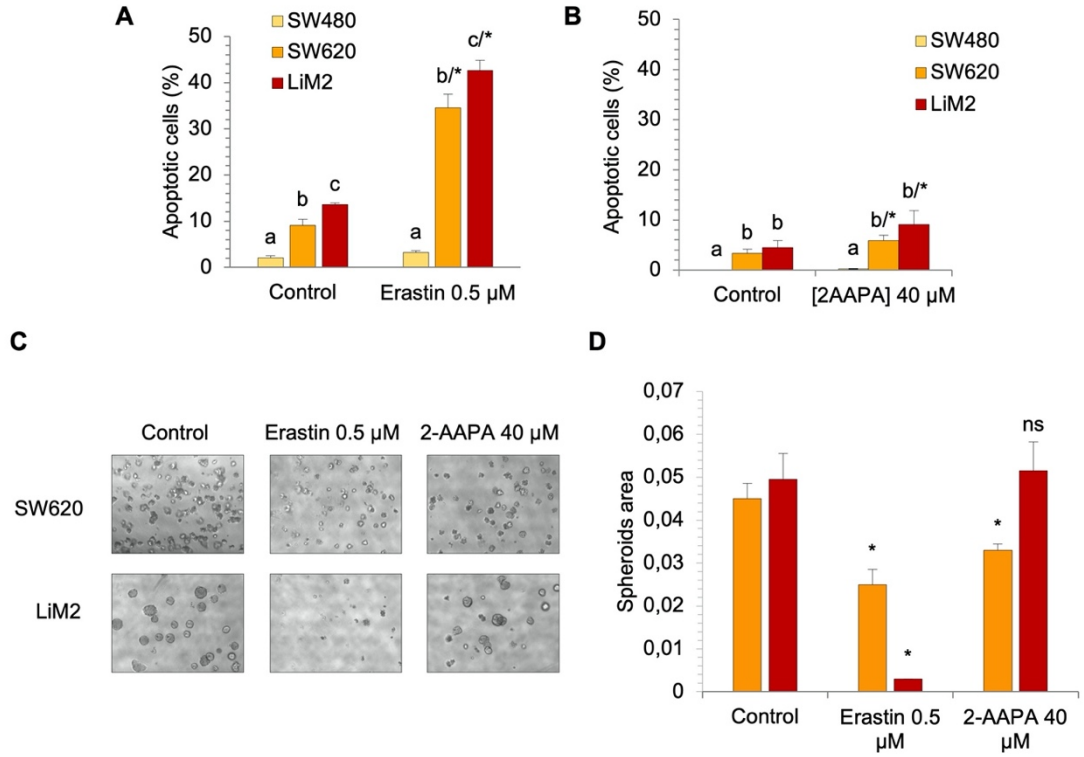

Figure 5.2.7. Cysteine and glutathione metabolism inhibition effects on apoptosis and 3D growth in the primary tumour colon cancer cell line SW480, and metastatic derivatives SW620 and LiM2. A. and **B.** Percentage of early apoptotic cells measured by flow cytometry using Annexin V-PI under a concentration of 0.5 µM of erastin (A) or 40 µM of 2-AAPA (B) after 72h incubation. **C.** Spheroid formation assay done in the presence of 50% medium (DMEM 12,5 mM Glc and 4 mM Gln, 5% FBS, and 1% S/P) and 50% Matrigel matrix, adding the inhibitors erastin (0.5 µM) and 2-AAPA (40 µM) for one week. Images of a contrast-phase microscope (40X). **D.** Quantification of spheroid area in C using ImageJ software from scanner images below. * *t* Student test for erastin or 2-AAPA vs control conditions, $p<0.05$. ^{a,b} A one-way ANOVA and Scheffe's test for multiple comparisons was performed for the factor "cell line". Groups with different letter show significant differences with $\alpha=0.05$.

The capacity to form spheroids was also analysed for both inhibitors in the metastatic cell lines, as the primary tumour and healthy cell lines do not have that capacity (see Figure 5.1.5 and Figure 5.2.1). 3D growth is indicative of how the inhibitors impair not only cell proliferation but

also metastatic and colonisation capacities, and it is a suitable model to test effectivity and resistance to therapeutic drugs (Nunes et al., 2019). Indeed, cystine import inhibition by erastin reduced the capacity to form spheroids (Figure 5.2.7C and D), a proof that the dependence that metastatic cells have on extracellular cystine could be also related to the capacity to grow in suspension and colonise other tissues. However, GSR inhibition by 2-AAPA is not causing the same effect on 3D growth capacity and only SW620 are mildly affected, but not LiM2 (Figure 5.2.7C and D).

The fact that 2-AAPA is causing almost no effect on 3D growth is in line with the few apoptosis that the drug at its IC_{50} is causing, as well as its less potency compared to system xCT inhibitor erastin. For that reason, we tried higher concentrations of 2-AAPA than the IC50. Cell death by apoptosis was indeed increased at 50 or 100 µM of 2-AAPA, but 3D growth was not impaired at any of these high concentrations (Figure 5.2.8). Together, it could mean metastatic cells are more vulnerable to the inhibition of cystine import than GSR, which could be explained by the fact that as long as the cells have cysteine imported from extracellular cystine to synthesise

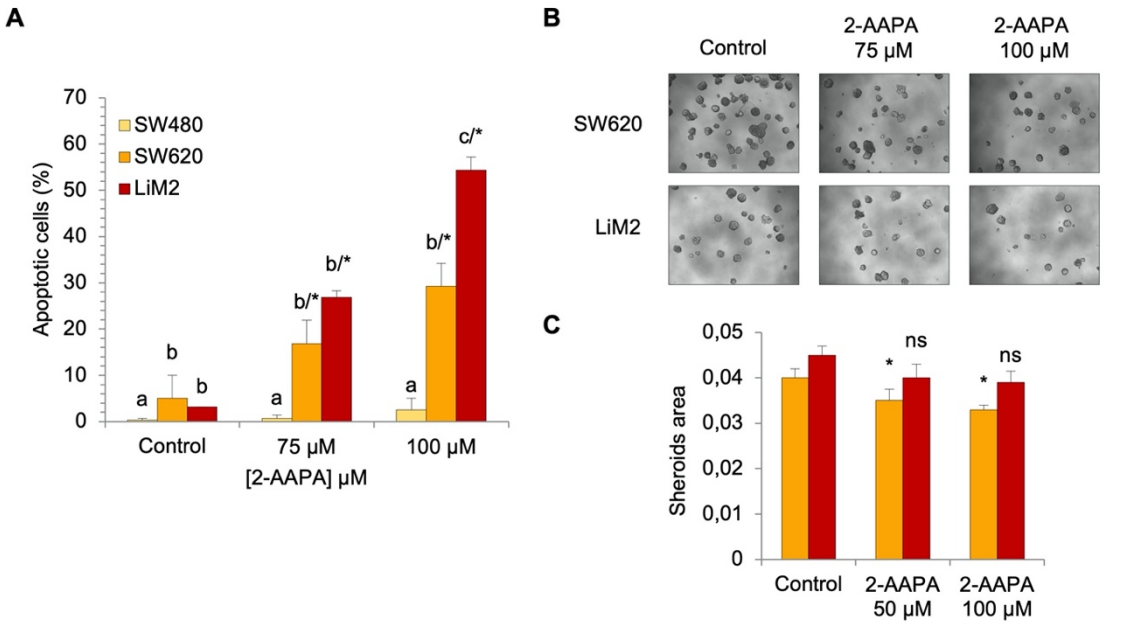

Figure 5.2.8. Glutathione metabolism inhibition effects on apoptosis and 3D growth the colon metastatic cell lines SW620 and LiM2. A. Percentage of early apoptotic cells measured by flow cytometry using Annexin V-PI under a concentration of 50 or 100 µM of 2-AAPA after 72h incubation. **B.** Spheroid formation assay done in the presence of 50% medium (DMEM 12,5 mM Glc and 4 mM Gln, 5% FBS, and 1% S/P) and 50% Matrigel matrix, adding the inhibitor 2-AAPA at 50 or 100 µM for one week. Images of a contrast-phase microscope (40X). **C.** Quantification of spheroid area in B using ImageJ software from scanner images below. * *t* Student test for erastin or 2-AAPA vs control conditions, $p<0.05$. ^{a,b,c} A one-way ANOVA and Scheffe's test for multiple comparisons was performed for the factor "cell line". Groups with different letter show significant differences with $\alpha=0.05$.

de novo glutathione, they do not need to recover it from oxidised glutathione by GSR. However, these results do not correspond with the previous observation that NAC is not able to rescue cell proliferation at high doses of 2-AAPA when cells are growing in 2D. It is possible that when cells form spheroids, they acquire distinct capacities such as the ability to increase cystine import. Whatever the case may be, it is proof of how different the two culture approximations are and how significant can be to work with one or the other.

Then, in an attempt to improve the efficacy of both treatments, especially 2-AAPA, we tested the combination of both inhibitors. In that manner, inhibiting cystine transport and GSR, both *de novo* glutathione synthesis and glutathione recycling are impaired at the same time. The combination was done first adding erastin for 72h, so that the cystine import inhibition is totally effective and simulates a situation of cystine deprivation, and then adding 2-AAPA (and renewing erastin) for a total duration of 120h. The treatment was synergetic for the metastatic cell lines from a concentration of 0.38 µM of erastin and 15 µM of 2-AAPA (Figure 5.2.9 and Table 5.2.2). The combination is improving the potency of both inhibitors as it significantly lowers the IC_{50} values.

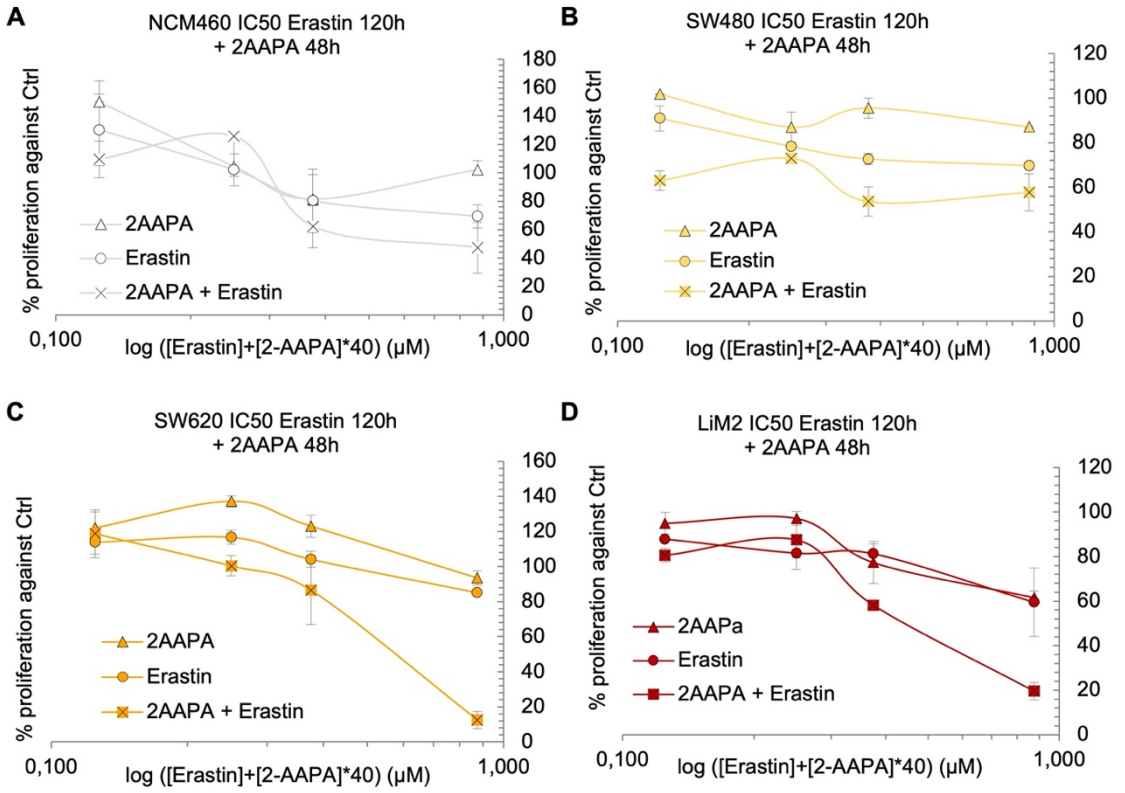

Figure 5.2.9. Combination of cysteine uptake and GSR inhibition in the healthy colon NCM460, primary tumour colon cancer cell line SW480, and metastatic derivatives SW620 and LiM2. A. – D. IC_{50} curve for erastin alone (120h), 2-AAPA alone (120h) and the combination of both inhibitors (erastin 72h and erastin + 2-AAPA until 120h) for NCM460 (A), SW480 (B), SW620 (C), and LiM2 (D) assessed by cell proliferation measured by DNA content using HO33342.

Combinations (CI values)	[Erastin] + [2-AAPA]			
Dose (μM)	**0.125 + 5**	**0.25 + 10**	**0.38 + 15**	**0.88 + 35**
NCM460	1.43	1.17	1.46	1.56
SW480	0.91	0.81	0.36	1.24
SW620	1.21	1.36	1.24	0.06
LiM2	1.28	2.56	0.56	0.52

Table 5.2.2. Combination index values for the combination of erastin and 2-AAPA. Combination index (CI) values calculated with CompuSyn, Inc, software (Chou-Talalay's CI method) of the combinations Erastin + 2AAPA at 120h, adding 2AAPA after 72h of Erastin treatment alone. CI<1, CI=1 and CI>1 indicates synergy, additive effect and antagonism, respectively.

5.2.2.3 The metastatic cell lines are vulnerable to inhibition of folate metabolism

The second vulnerability that we chose to focus on was folate metabolism, as methenyltetrahydrofolate dehydrogenase 1 (MTHFD1) was another of the single predicted targets by the GSMM model that affected more the metastatic cell lines in compared to the primary tumour cell line (Table A.V.5). Even more, as it could be inferred from the experimental results about amino acid metabolism, the model predicted that SW620 and LiM2 cell lines displayed significantly higher fluxes through the cytosolic folate pathway. MTHFD1, in fact, is one of the enzymes of that pathway.

Folate metabolism or folate cycle is a part of one-carbon metabolism, a series of reactions that support nucleic acids synthesis (purines and thymidine), amino acid synthesis and methylation reactions, which are important for epigenetic maintenance (Ducker and Rabinowitz, 2017) (see section 2.2.1.4). Such pathways are compartmentalised between the mitochondria and the cytosol and are interconnected through intermediates that are transported between both sites: tetrahydrofolate (THF), serine, glycine, 10N-formyl tetrahydrofolate (CHO-THF) and formate (Figure 5.2.10). Folate metabolism is also one of the most commonly altered pathways in cancer and its inhibition has been largely exploited and there are examples of current treatments that inhibit enzymes from this pathway (Yang and Vousden, 2016). In most cancer types, when inhibiting an enzymatic activity of one of either cytosolic or mitochondrial branches of folate metabolism, redundancy has been observed and one branch can compensate another (Anderson and Stover, 2009; Zheng et al., 2018). However, it has also been observed that in some cases, cancer cells can be vulnerable to one of the enzymes of a specific branch (Ding et al., 2018; Nishimura et al., 2019).

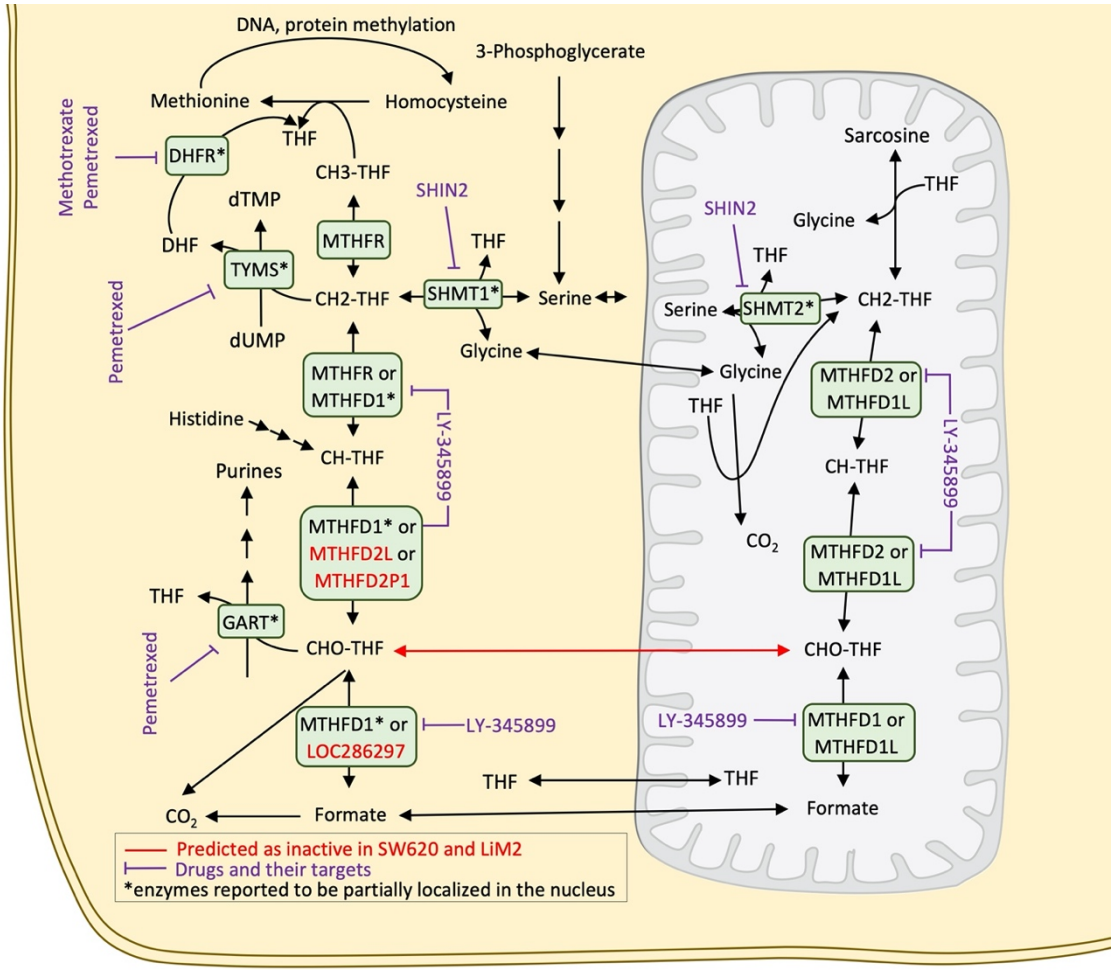

Figure 5.2.10. Predictions of folate metabolism from a genome-scale metabolic model of SW480, SW620, and LiM2. Graphical representation of folate metabolism. All abbreviations are specified as some of them do not appear in section 1. CH2-THF: N^5,N^{10} methylene-THF. CH3-THF: N^5-methyl tetrahydrofolate. CHO-THF: N^{10}-formyl tetrahydrofolate. CH-THF: N^5,N^{10}-methenyl tetrahydrofolate. THF: Tetrahydrofolate. DHFR: Dihydrofolate reductase. GART: Trifunctional purine biosynthetic protein adenosine-3. LOC286297: Methylenetetrahydrofolate dehydrogenase (NADP+ dependent) 1 like pseudogene. MTHFD1: Methylenetetrahydrofolate dehydrogenase, dyclohydrolase, and formyltetrahydrofolate synthetase 1. MTHFD1L: Methylenetetrahydrofolate dehydrogenase (NADP+ dependent) 1 like. MTHFD2: Methylenetetrahydrofolate dehydrogenase (NADP+ dependent) 2, methenyltetrahydrofolate cyclohydrolase. MTHFD2L: Methylenetetrahydrofolate dehydrogenase (NADP+ dependent) 2 like. MTHFD2P1: Methylenetetrahydrofolate dehydrogenase (NADP+ dependent) 2, Methenyltetrahydrofolate cyclohydrolase pseudogene 1. MTHFR: Methylenetetrahydrofolate reductase. SHMT1/2: Serine hydroxymethyltransferase 1/2. TYMS: Thymidylate synthetase.

In this regard, the GSMM model predicted that the transport of CHO-THF between the cytosol and the mitochondria is inactive, as well as other enzymes that take part of the cytosolic branch of folate metabolism (Figure 5.2.10). According to the model, the dependency on MTHFD1 could have emerged due to these deficiencies (Figure 5.2.11A). MTHFD1 is able to catalyse three steps of the branch of folate metabolism. Additionally, the model predicted significantly higher fluxes through the cytosolic folate pathway than the mitochondrial (Figure

5.2.11B). In other words, the inhibition of MTHFD1 in the folate cytosolic pathway in the metastatic cell lines, could not be compensated by the redundant folate mitochondrial pathway, as the CHO-THF generated by the mitochondrial isoenzyme (MTHFD2) could not be transported to the cytosol. Therefore, we consider that in the metastatic cell lines, folate metabolism was uncoupled between the two branches, which makes them vulnerable to cytosolic folate pathway inhibitors.

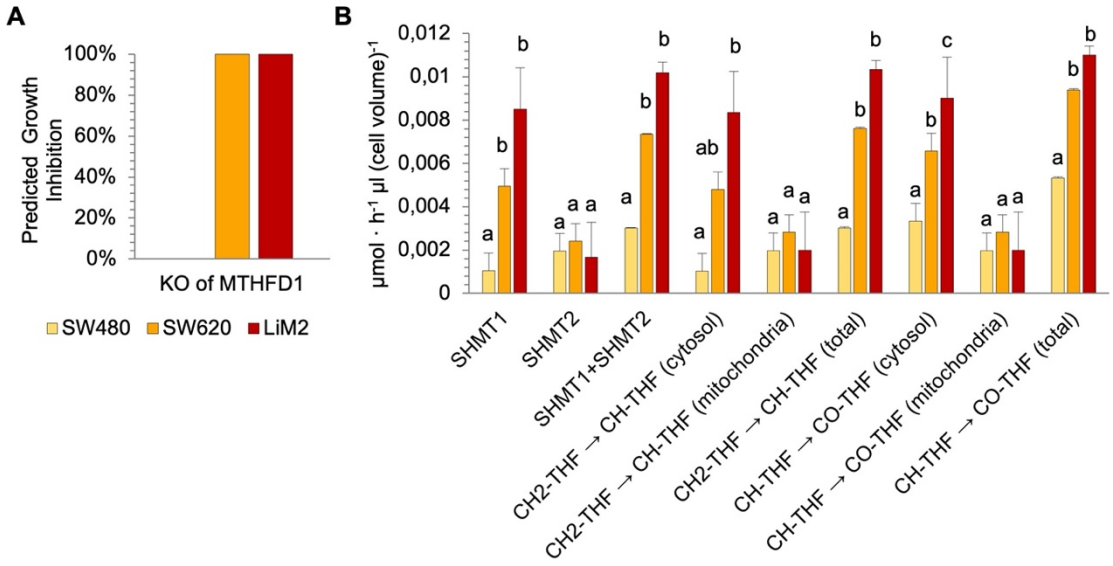

Figure 5.2.11. Predictions of folate metabolism vulnerabilities from a genome-scale metabolic model of SW480, SW620 and LiM2. A. Predicted growth inhibition under inactivating MTHFD1. Growth inhibition is computed as 1-(Biomass production KO/ Biomass production Wild Type) as simulated with the cell line-specific GSMMs. **B.** Predicted flux values for different steps reactions of cytosolic, mitochondrial folate and metabolism. Letters a,b,c denote cell lines where there is an overlap of the sampled flux values.

In order to confirm such dependency, NCM460, SW480, SW620, and LiM2 were incubated with LY345899. LY345899 is an inhibitor of both MTHDF1 and MTHFD2 but with a significantly lower K_i for the former (Gustafsson et al., 2017; Schmidt et al., 2000). Such inhibitor had been previously tested on the SW480/SW620 and reported to be selective for SW620 (Ju et al., 2018). Our validation confirms the prior reports and shows that the inhibitor is selective not only for SW620 but also for the highly metastatic derivative of SW620, LiM2, while having little effect on the proliferation of both the primary tumour cell line SW620 and the heathy colon epithelial, here represented by NCM460 (Figure 5.2.12A and Table 5.2.3). This makes an excellent inhibitor to selectively impair metastatic cell line proliferation.

Then, in order to confirm the general dependence of the metastatic cell lines on cytosolic folate branch upon the mitochondrial branch, we tried to target both branches by using SHIN2 (Ducker et al., 2017), a chemical inhibitor of both SHMT1 (cytosolic) and SHMT2 (mitochondrial). We chose SHMT1/2 because it was an enzyme that takes part of both branches and its activity is not affected according to the model. We observed a similar growth inhibitory

effect on both the primary and metastatic tumour cell lines but a significantly lower growth inhibitory effect on NCM460 at higher SHIN2 concentrations (Figure 5.2.12B and Table 5.2.3). This result is one more proof of the possible dependence that metastatic cells have on folate metabolism, as when both branches are inhibited, both primary and metastatic cell lines are equally affected.

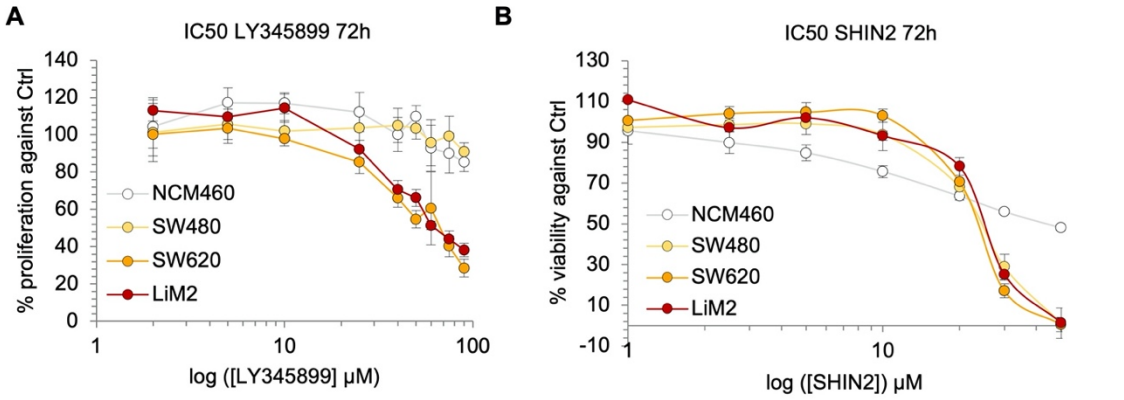

Figure 5.2.12. MTHFD1/2 and SHMT1/2 inhibition in the healthy colon NCM460, primary tumour colon cancer cell line SW480, and metastatic derivatives SW620 and LiM2. A. IC_{50} curve of the MTHFD1/2 inhibitor LY345899 determined by cell proliferation measured by DNA content using HO33342 under various LY345899 concentrations after 72 hours incubation. **B.** IC_{50} curve of the SHMT1/2 inhibitor SHIN2 assessed by cell proliferation measured by DNA content using HO33342 under various SHIN2 concentrations after 72h incubation.

Inhibitor	IC_{50} values			
	NCM460	SW480	SW620	LiM2
LY345899 (µM)	191.1 ± 9.9	178.3 ± 45.3	57.5 ± 9.2	58.1 ± 12.7
SHIN2 (µM)	55.9 ± 5.7	19.8 ± 3.5	19.7 ± 3.3	20.8 ± 4.2
Methotrexate (nM)	72.8 ± 5.2	14.9 ± 2.5	10.9 ± 3.4	9.7 ± 2.3
Pemetrexed (nM)	68.1 ± 4.3	29.9 ± 4.2	15.8 ± 3.2	16.3 ± 2.5

Table 5.2.3. IC_{50} values of folate metabolism inhibitors for NCM460, SW480, SW620, and LiM2 cell lines. LY345899 is a specific inhibitor of MTHFD1/2 (methylenetetrahydrofolate dehydrogenase 1/2), SHIN2 is a specific inhibitor of SHMT1/2 (serine hydroxymethyltransferase 1/2), methotrexate is an inhibitor of DHFR (dihydrofolate reductase), pemetrexed is an inhibitor of DHFR, TYMS (thymidylate Synthetase) and GART (trifunctional purine biosynthetic protein adenosine-3).

We next analysed the effect of both inhibitors, the MTHFD1 inhibitor LY345899 and the SHMT1/2 inhibitor SHIN2, in cell death by apoptosis. Surprisingly, the MTHFD1 inhibitor, which was only inhibiting the cytosolic folate pathway, was not causing apoptotic cell death at its IC_{50}, while the SHMT1/2 inhibitor causes significant apoptosis in the three cell lines, especially in the metastatic cell lines (Figure 5.2.13A and B). The apoptosis results may seem contradictory with respect to the model, but it is important to take into account that the model predictions are done by simulating biomass production, which corresponds to cell proliferation but not cell death.

Such predictions, therefore, give rise targets whose inhibition would impair cell proliferation but it does not mean that it causes cell death. That could explain the perfect agreement between the model predictions and the results of cell proliferation inhibition (Figure 5.2.12), which is the experiments that better correspond to what the model has predicted. All these results suggest that although the metastatic cell lines could be dependent on the cytosolic folate pathway in terms of cell proliferation, when it comes to cell death, inhibiting both branches could be more efficient for colorectal cancer treatment. The results on SHMT1/2 inhibition were consistent with previous studies where it has been found that such inhibition causes apoptosis in lung cancer cells (Paone et al., 2014), suppresses cell proliferation and tumorigenesis in hepatocellular carcinoma (Woo et al., 2016). Furthermore, its overexpression is related to poor prognosis in intrahepatic cholangiocarcinoma (Ning et al., 2018) and breast cancer (Zhang et al., 2016).

In terms of 3D growth capacity, both inhibitors were able to significantly reduce spheroid formation at the IC_{50} value. However, neither of the inhibitors caused a complete impairment of

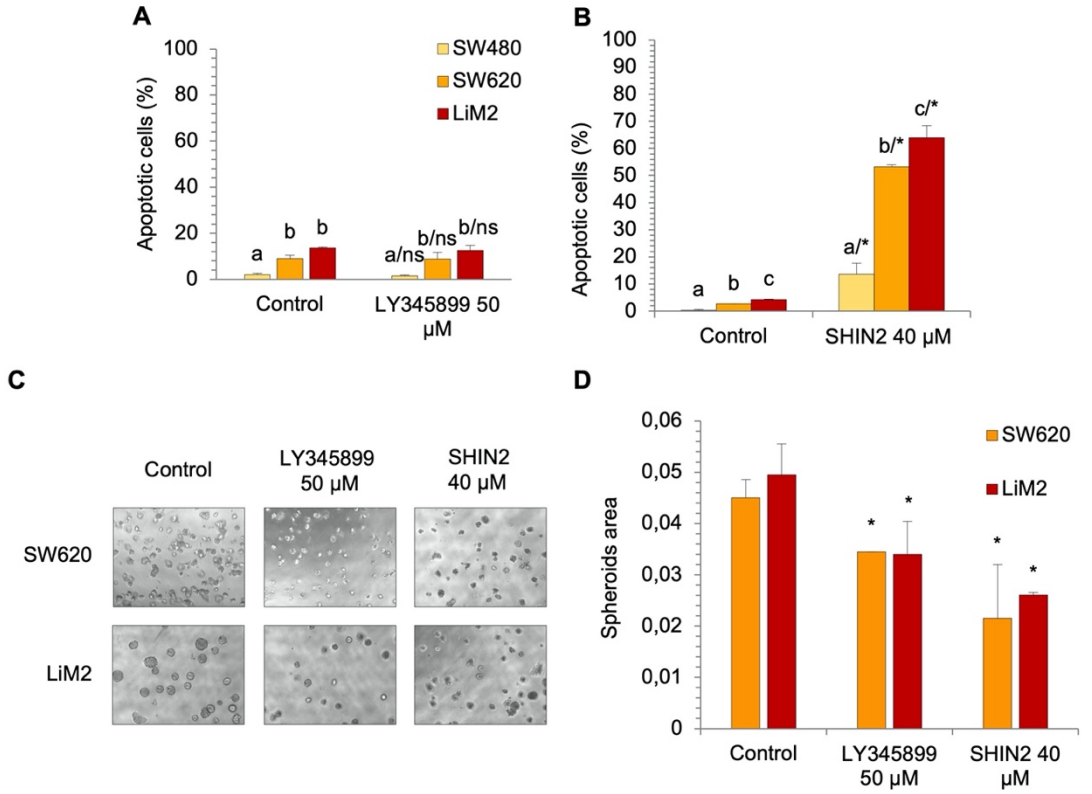

Figure 5.2.13. MTHFD1/2 and SHMT1/2 inhibition effect on apoptosis and 3D growth the primary tumour colon cancer cell line SW480, and metastatic derivatives SW620 and LiM2. A. and **B.** Percentage of early apoptotic cells measured by flow cytometry using Annexin V-PI under a concentration of 50 µM of LY345899 (A) or 40 µM of SHIN2 (B) after 72h incubation. **C.** and **D.** Spheroid formation assay done in the presence of 50% medium (DMEM 12,5 mM Glc and 4 mM Gln, 5% FBS, and 1% S/P) and 50% Matrigel matrix, adding the inhibitors LY345899 (50 µM) and SHIN2 (40 µM) for one week. Images of a contrast-phase microscope (40X) (C) and quantification of the spheroid area using ImageJ software from scanner images below (D). * *t* Student test for LY345899 or SHIN2 vs control conditions, $p<0.05$. [a,b,c] A one-way ANOVA and Scheffe's test for multiple comparisons was performed for the factor "cell line". Groups with different letter show significant differences with $\alpha=0.05$.

3D growth capacity, which would be the desired effect, suggesting that when it comes to the spheroid formation capacity, inhibition of either MTHFD1 or SHMT1/2 is not enough to disrupt the stemness phenotype that allows metastatic cells to start the formation of spheroids.

Afterwards, we aim to further explore the inhibition of folate metabolism in the colon metastatic cells, as well as the putative dependence on the cytosolic folate branch. For that purpose, the therapeutic effectivity of the antifolates methotrexate and pemetrexed was also evaluated, as they are drugs approved for clinical use against cancer and autoimmune diseases (see section 2.3.2.2). Methotrexate inhibits the cytosolic activity of dihydrofolate reductase (DHFR) while pemetrexed inhibits DHFR and also thymidylate synthetase (TYMS) and trifunctional purine biosynthetic protein adenosine-3 (GART) (Wright and Anderson, 2011). Both antimetabolites showed to have greater growth inhibitory effects in the metastatic cell lines than in the primary cell line or healthy colon epithelial cell line, and with high potency at nanomolar ranges (Figure 5.2.14A and B, and Table 5.2.3). The fact that the inhibition of the cytosolic enzyme of the folate pathway DHFR is having greater effects on the metastatic cell lines further confirm that metastatic cell lines are dependent on the cytosolic branch of folate pathway. However, pemetrexed, which inhibits also other enzymes such as TYMS and GART that are both cytosolic and mitochondrial, is also selective for the metastatic cell lines. It is worth mentioning that the three enzymes, DHFR, TYMS, and GART are not enzymes of the core folate cycle (Figure 5.2.10). DHFR recovers THF from dihydrofolate (DHF), and both TYMS and GART are involved in the synthesis of thymidine and purines, respectively. According to the results, it all these activities are also selectively essential for the metastatic cell lines.

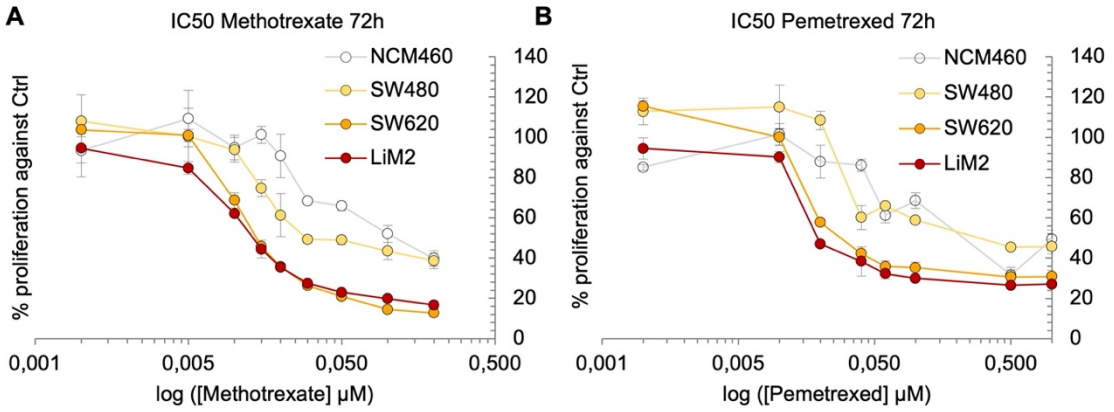

Figure 5.2.14. Folate metabolism inhibition in the healthy colon NCM460, primary tumour colon cancer cell line SW480, and metastatic derivatives SW620 and LiM2. A. IC_{50} curve of the DHFR inhibitor methotrexate measured by DNA content using HO33342 after 72h incubation. **B.** IC_{50} curve of the DHFR, TYMS and GART inhibitor pemetrexed measured by DNA content using HO33342 after 72h incubation.

The results on cell death by apoptosis showed that methotrexate and pemetrexed also caused almost no apoptosis, only few metastatic cell lines undergo apoptosis (Figure 5.2.15A).

This is consistent with the results of the MTHFD1 inhibitor LY345899 that also impaired selectively the metastatic cell lines proliferation but did not cause apoptosis. A deeper look into the IC_{50} curve of methotrexate and pemetrexed allows seeing that there is a point in which even if the concentration of the drug is increased, the curve is stable, indicating that the cells at that point are not dying but also not proliferating. In fact, it was previously observed in the literature that lung cancer cells stop their cell cycle at G1 and reduction of MYC levels under methotrexate treatment (Serra et al., 2008), and also that methotrexate induces differentiation in colon cancer cells (Singh et al., 2006). Interestingly, the images of a contrast-phase microscope under methotrexate treatment revealed that the morphology of both the primary tumour and the metastatic cells change and they appear to be more elongated (Figure 5.2.15B).

Remarkably, both inhibitors were able to dramatically decrease the spheroid formation capacity. This suggests that DHFR, TYMS, and GART activities are not only crucial for cell proliferation of the metastatic cell lines but also for metastatic colonisation, as 3D growth was

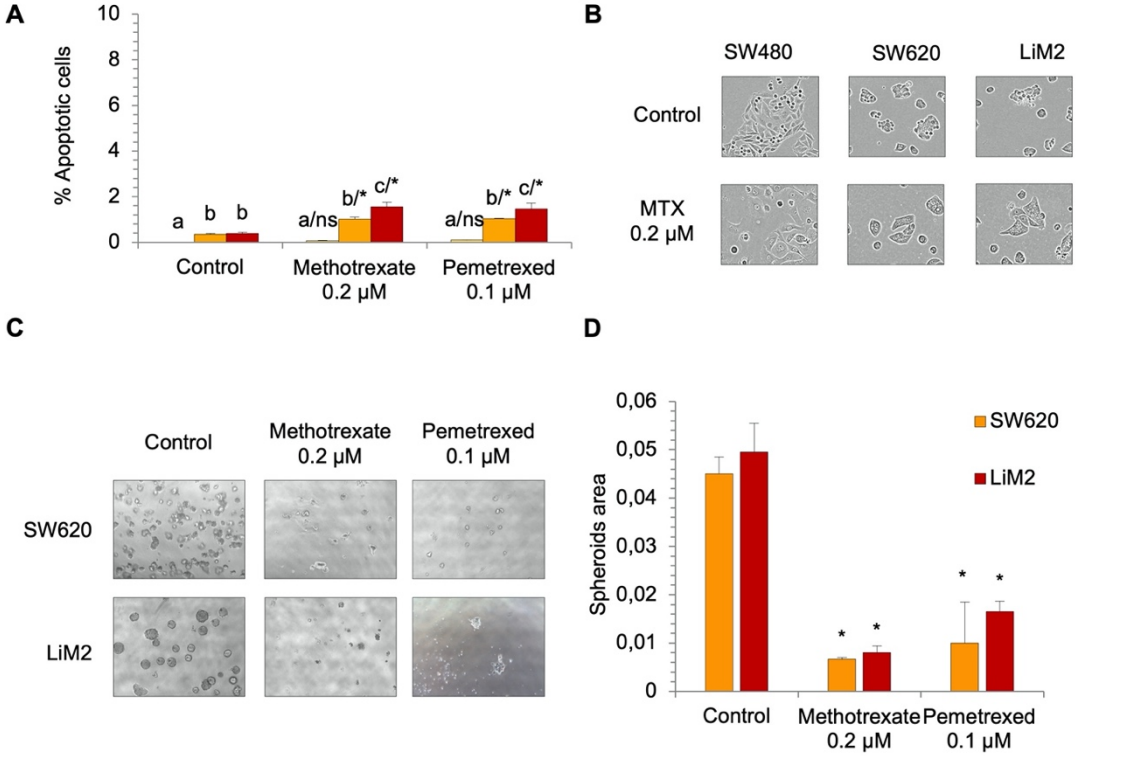

Figure 5.2.15. Folate inhibition effect on apoptosis and 3D growth of the primary tumour colon cancer cell line SW480, and metastatic derivatives SW620 and LiM2. A. Percentage of early apoptotic cells measured by flow cytometry using Annexin V-PI under a concentration of 0.2 µM of methotrexate and 0.1 µM of pemetrexed after 72h incubation. **B.** Images of 2D growth of a contrast-phase microscope under MTX (methotrexate) (0.2 µM) or control conditions. **C.** and **D.** Spheroid formation assay done in the presence of 50% medium (DMEM 12,5 mM Glc and 4 mM Gln, 5% FBS, and 1% S/P) and 50% Matrigel matrix, adding the inhibitors methotrexate (0.2 µM) and pemetrexed (0.1 µM) for one week. Images of a contrast-phase microscope (40X) (C) and quantification of the spheroid area using ImageJ software from scanner images below (D). * *t* Student test for methotrexate or pemetrexed vs control conditions, $p<0.05$. ^{a,b,c} A one-way ANOVA and Scheffe's test for multiple comparisons was performed for the factor "cell line". Groups with different letter show significant differences with $\alpha=0.05$.

impaired, and very few and small spheroids were detected under both methotrexate and pemetrexed treatment.

5.2.2.4 Synergistic effect of the simultaneous inhibition of cysteine uptake and folate metabolism

After having explored the inhibition of two major vulnerabilities of the metastatic cell lines predicted by the computational model, cysteine uptake and folate metabolism, we evaluate if these pathways are interconnected and therefore could be simultaneously inhibited in order to increase the disruption of metastatic populations without affecting non-tumoral cells. As cysteine is the limiting substrate of *de novo* glutathione synthesis (Estrela et al., 2016), cysteine uptake inhibition could impair this process, causing a possible depletion in the levels of NADPH and therefore diminishing the antioxidant defences. Precisely, one of the sources of NADPH is folate metabolism, and its inhibition could impair antioxidant defences as well as *de novo* nucleotide synthesis (Yang and Vousden, 2016). In our case, metastatic cells present a metabolic reprogramming with enhanced cellular respiration that implies higher oxidative stress in the mitochondria. In fact, Piskounova et al. postulated that during metastasis formation there is a need for antioxidant capacity due to higher ROS levels and that precisely MTHDF1 confers the antioxidant capacity being one of the contributors to metastasis (Piskounova et al., 2015). Therefore, we hypothesised that the combination of the inhibition of the two pathways using erastin (system Xc- inhibition) and LY345899 (MTHFD1/2 inhibition) could be synergic, as it would target two main players that sustain redox homeostasis, glutathione and NADPH.

The results showed that the combination was clearly selective for the metastatic cell lines (Figure 5.2.16A and B), as it happened with the inhibitors individually. Furthermore, if we compare the different treatments in the metastatic cell lines SW620 and LiM2, there can be observed that the combination was synergetic from concentrations of 0.5 μM of erastin and 20 μM of LY345899 (Figure 5.2.16D and E and Table 5.2.4).

Regarding cell death, the metastatic cell lines present higher fractions of late apoptosis and necrosis with the combined drug treatment, but lower early apoptosis in comparison with erastin alone (Figure 5.2.17). These results could be explained by the fact that the combination treatment is causing apoptosis faster than erastin alone, or else that as cells proliferate less, they are less exposed to apoptosis death. If both early and late apoptosis or necrosis are taken into account, it is increased under the drug combination in the metastatic cell lines, which confirms an advantage of the drug combination upon the individual targets. Remarkably, neither the individual treatments nor the combination caused any significant increase in apoptosis in the healthy colon (NCM460) or primary tumour (SW480) cell lines, indicating that the drug combination would have no side effects and is specific for metastatic cells.

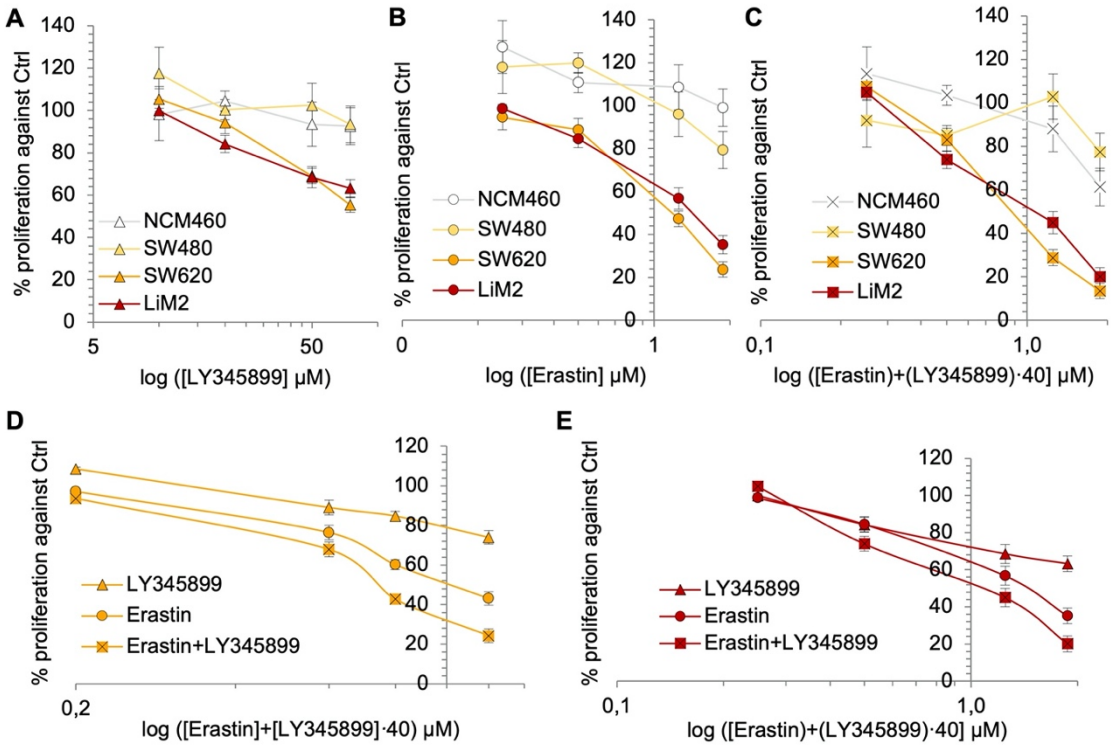

Figure 5.2.16. Simultaneous inhibition of cysteine and folate metabolism in the primary tumour colon cancer cell line SW480, and metastatic derivatives SW620 and LiM2. A. – **C.** IC_{50} curve of LY345899 (A), erastin (B) individually and the combination of both inhibitors (C) determined by cell proliferation measured by DNA content using HO33342. **D.** and **E.** Same experiment in A – C comparing between the three treatments (erastin or LY345899 individually and the combination of both inhibitors) for SW620 (D) and LiM2 (E).

Combinations (CI values)	**[Erastin] + [LY345899]**			
Dose (µM)	**0.25 + 10**	**0.5 + 20**	**1.25 + 50**	**1.88 + 75**
NCM460	1.21	1.42	1.07	1.14
SW480	1.18	1.93	1.46	1.27
SW620	1.35	1.19	0.43	0.31
LiM2	1.41	0.63	0.45	0.22

Table 5.2.4. Combination index values for the combination of erastin and LY345899. Combination index (CI) values calculated with CompuSyn, Inc, software (Chou-Talalay's CI method) of the combinations Erastin + LY345899 at 72 hours of treatment. CI<1, CI=1 and CI>1 indicates synergy, additive effect and antagonism, respectively.

In line with that, 3D growth of the SW620 cell line was significantly more impaired for the combination of both drugs than for the drugs alone. However, in LiM2 we cannot distinguish between the combination and erastin alone due to the pronounced effect of the individual erastin treatment (Figure 5.2.18A and B). That results confirm that the drug combination would be a very

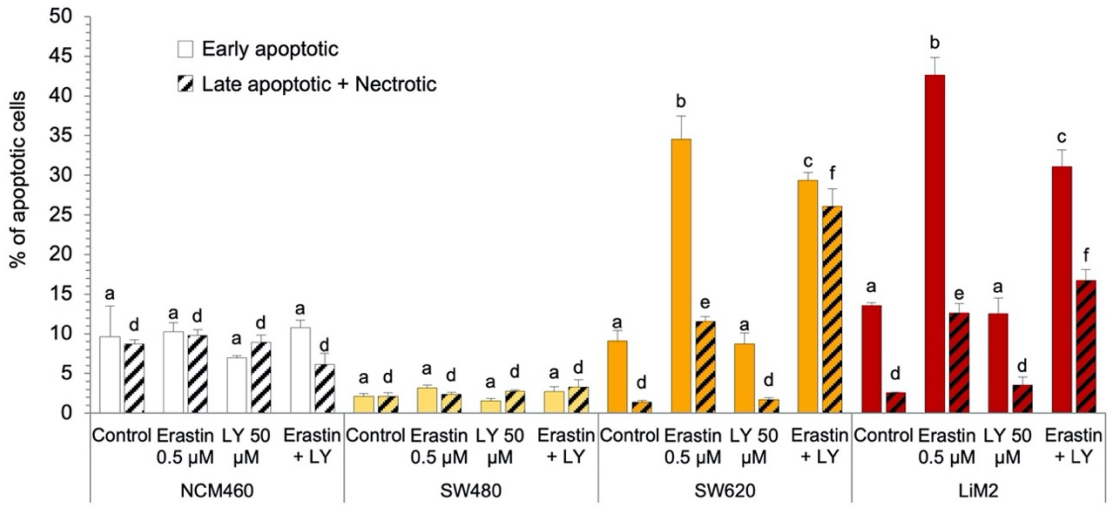

Figure 5.2.17. Simultaneous inhibition of cysteine and folate metabolism effect on apoptosis in the primary tumour colon cancer cell line SW480, and metastatic derivatives SW620 and LiM2. Percentage of early apoptotic cells and late apoptotic + necrotic cells measured by flow cytometry using Annexin V-PI under a concentration of 0.5 µM of erastin, 50 µM of LY345899 or the combination of both treatments after 72h incubation. [a-c and d-f] A one-way ANOVA and Scheffe's test for multiple comparisons was performed for the factor "drug treatment". Groups with different letter show significant difference with α=0.05.

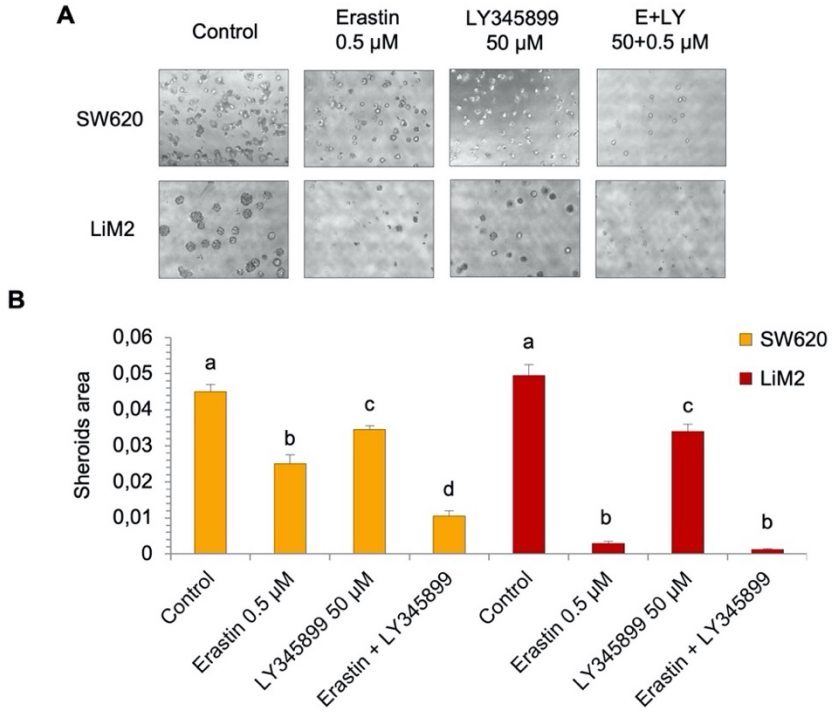

Figure 5.2.18. Simultaneous inhibition of cysteine and folate metabolism effect on 3D growth in the metastatic colon cancer cell lines SW620 and LiM2. A. Spheroid formation assay done in the presence of 50% medium (DMEM 12,5 mM Glc, 4 mM Gln, 5% FBS, and 1% S/P) and 50% Matrigel matrix, adding the inhibitors erastin alone (0.5 µM), LY345899 alone (50 µM) and the combinations of both drugs for one week. Images of a contrast-phase microscope (40X). **B.** Quantification of the spheroid area using ImageJ software from scanner images below. [a-d] A one-way ANOVA and Scheffe's test for multiple comparisons was performed for the factor "drug treatment". Groups with different letter show significant difference with α=0.05.

good option for treatment against metastatic cells, as it also affects the capacity of metastatic cancer stem cells to initiate and form spheroids, as almost any spheroid was detected in the combination treatment.

Nevertheless, it is interesting to observe that taking into account the three experiments (proliferation in 2D, apoptosis and spheroid formation), the drug combination worked better for SW620 than for the LiM2 cell line. In the IC_{50} curves, it can be appreciated that SW620 with the double treatment gets a better inhibition and differentiates more from the individual drugs than LiM2. Then, in both the apoptosis and spheroid formation experiments, as erastin had greater effects on LiM2, it is difficult to observe an improvement with the drug combination. It is possible that LiM2, being the highest metastatic cell line with higher expression of some mesenchymal and cancer stem cell markers could be able to survive and metabolically adapt to the double treatment. However, in terms of spheroid formation, erastin alone is able to reduce the size and quantity of spheroids much more in LiM2 than in SW620, indicating that probably LiM2 is more sensible than SW620 to cysteine depletion and impairment of antioxidant defences.

Finally, we also tried to combine the system xCT inhibition with other folate metabolism targets that were previously tested: SHMT1 (using SHIN2), DHFR, TYMS, and GART (using methotrexate and pemetrexed). These combinations did not show any synergistic effects (Figure 5.2.19A-F and Table 5.2.5), only additive effect at some points, suggesting that among the folate

Combinations (CI values)	**[Erastin] + [SHIN2]**			
Dose (μM)	**0.5 + 5**	**1 + 10**	**2 + 20**	**4 + 40**
SW620	1.16	0.76	0.92	0.32
LiM2	1.20	0.98	1.20	0.25
	[Erastin] + [Methotrexate]			
Dose (μM)	**0.3 + 0.003**	**0.5 + 0.05**	**1 + 0.1**	**2 + 0.2**
SW620	1.58	1.41	1.62	1.26
LiM2	1.6	1.38	1.31	1.59
	[Erastin] + [Pemetrexed]			
Dose (μM)	**0.06 + 1.2**	**0.075 + 1.5**	**0.09 + 1.8**	**0.1 + 2**
SW620	1.27	1.59	1.64	0.93
LiM2	1.37	0.87	0.79	0.82

Table 5.2.5. Combination index values for the combination of erastin and inhibitors of folate metabolism. Combination index (CI) values calculated with CompuSyn, Inc, software (Chou-Talalay's CI method) of the combinations of erastin with other inhibitors at 72 hours of treatment. CI<1, CI=1 and CI>1 indicates synergy, additive effect and antagonism, respectively.

metabolism enzymes we focused on, only MTHFD1 inhibition impairs antioxidant capacity through contribution to increasing the NADPH/$NADP^+$ ratio and therefore synergies with glutathione depletion by system xCT and GSR inhibition.

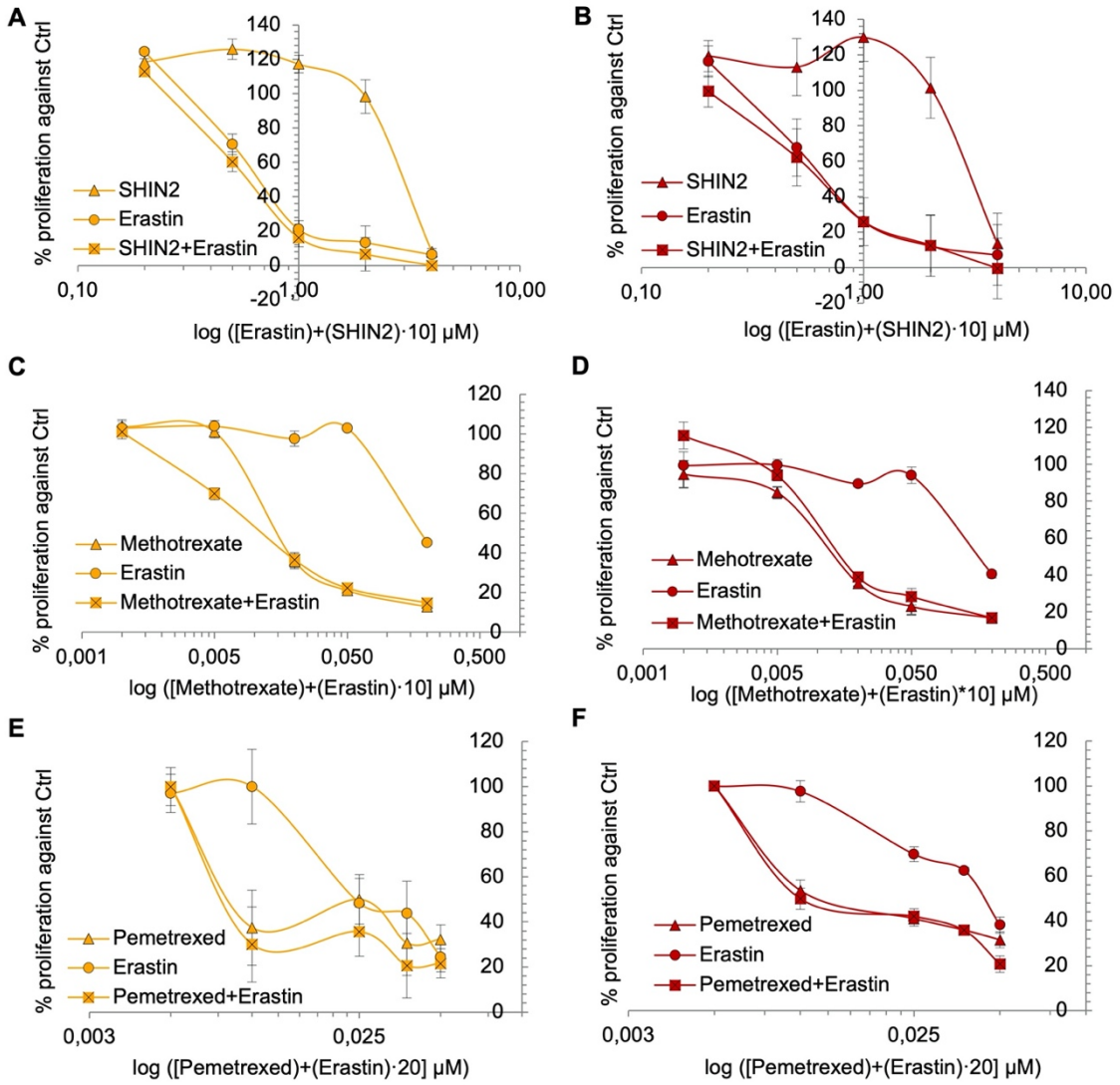

Figure 5.2.19. Simultaneous inhibition of cysteine and folate metabolism in the primary tumour colon cancer cell line SW480, and metastatic derivatives SW620 and LiM2. A. and **B.** IC_{50} curve of erastin, SHIN2 individually and the combination of both inhibitors determined by cell proliferation measured by DNA content using HO33342 for SW620 (A) and LiM2 (B). **C.** and **D.** IC_{50} curve of erastin, methotrexate individually and the combination of both inhibitors determined by cell proliferation measured by DNA content using HO33342 for SW620 (C) and LiM2 (D) **E.** and **F.** IC_{50} curve of erastin, pemetrexed individually and the combination of both inhibitors determined by cell proliferation measured by DNA content using HO33342 for SW620 (E) and LiM2 (F).

5.2.2.5 Other inhibitions

In order to give more value to the model and explore other possible vulnerabilities of metastatic colon cancer, we tested other inhibitors of the predicted targets. We chose the target stearoyl-CoA desaturase (SCD) as it was the next to be more selective for the metastatic cell lines, although it was predicted that the proliferation of SW480 is reduced to 25% (Table A.V.5).

Stearoyl-CoA desaturase is an enzyme responsible for the synthesis of unsaturated fatty acids from saturated fatty acids, a crucial step in the formation of phospholipids that will take part of plasmatic membranes, and therefore important for cell proliferation. SCD1 has been established as a possible therapeutic target for cancer and SCD1 have been proven to cause cancer cell apoptosis (von Roemeling et al., 2013) and impairment of tumour growth, migration, invasion, metastasis and maintenance of cancer cell stemness (Tracz-Gaszewska and Dobrzyn, 2019). We tried the inhibitors A939572 (Xin et al., 2008), which is being broadly used to inhibit SCD1 in preclinical models and MK-8245, which is being explored in the treatment of diabetes and dyslipidaemia (Oballa et al., 2011).

The results were promising, as both drugs were selective for the metastatic cell lines at very low micromolar or even nanomolar ranges (Figure 5.2.20 and Table 5.2.6). A939572 was

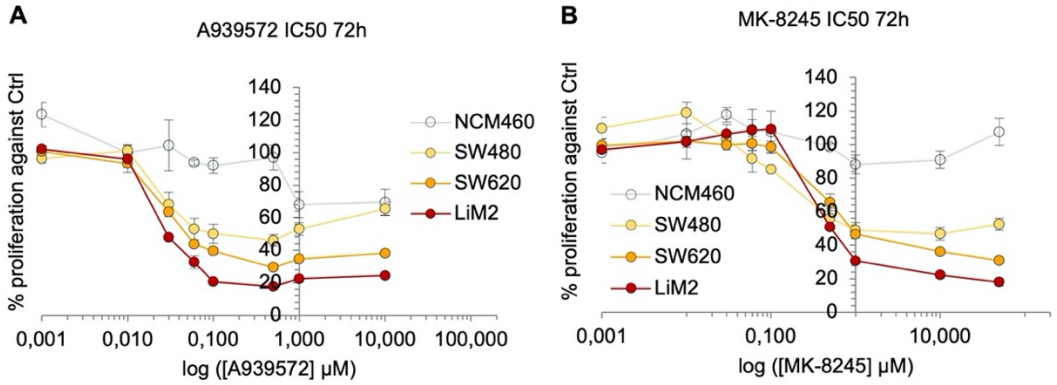

Figure 5.2.20. Stearoyl-CoA desaturase 1 inhibition in the healthy colon cell line NCM460, the primary tumour colon cancer cell line SW480, and metastatic derivatives SW620 and LiM2. A. and **B.** IC_{50} curve of the SCD1 inhibitor A939572 (A) and MK-8245 (B) measured by DNA content using HO33342 after 72h incubation.

Inhibitor	IC_{50} values			
	NCM460	SW480	SW620	LiM2
A939572 (µM)	229 ± 82	11 ± 0.23	0.29 ± 0.05	0.08 ± 0.01
MK-8245 (µM)	1025 ± 35	9.6 ± 2	4.3 ± 1.4	1.6 ± 0.7
Clofarabine (nM)	703 ± 251	123 ± 27	80 ± 16	75 ± 21
Shikonin (µM)	1.07 ± 0.4	0.65 ± 0.1	0.25 ± 0.02	0.29 ± 0.05

Table 5.2.6. IC_{50} values of different inhibitors against predicted targets for NCM460, SW480, SW620 and LiM2 cell lines. A939572 and MK-8245 are specific inhibitors of SCD-1 (stearoyl-CoA desaturase 1), clofarabine is a specific inhibitor of RRM1 (Ribonucleotide reductase catalytic subunit M1) and shikonin is a specific inhibitor of PKM (pyruvate kinase M).

more selective for the metastatic cell lines and more potent, while MK-8245 also inhibited SW480 while having no effect on the healthy colon cell line NCM460. In both cases, the observed effect is in agreement with the model prediction that SW480 proliferation would be affected to 25%. A clear distance between the cancer cells and the healthy cell line is observed, in comparison with the IC50 curves of previous experiments that were specific for the metastatic cell lines (Figures 5.2.5D and 5.2.12A).

Furthermore, both inhibitors also disrupt significantly the capacity to grow in 3D to the same extend (Figure 5.2.21), as the spheroids resulted to be much smaller and in less quantity. Interestingly, there are subtle differences that can be observed through the contrast-phase microscope images between the two cell lines. While SW620 seem to form smaller spheroids, in the case of LiM2 cells, they are not forming proper spheroids but a different type of structure that is more disorganised, suggesting that the metastatic and colonisation capacities are further impaired as the metastatic potential increases with SCD-1 inhibitors, making them a good therapeutic option for metastatic colorectal cancer.

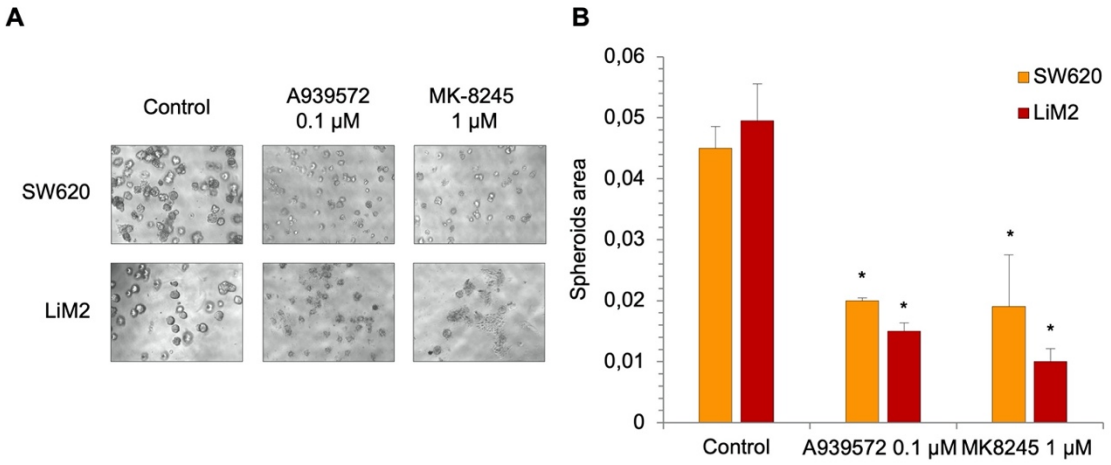

Figure 5.2.21. Stearoyl-CoA desaturase 1 inhibition effect on 3D growth of the colon cancer metastatic derivatives SW620 and LiM2. A. and **B.** Spheroid formation assay done in the presence of 50% medium (DMEM 12,5 mM Glc, 4 mM Gln, 5% FBS, and 1% S/P) and 50% Matrigel matrix, adding the inhibitors A939572 (0.1 µM) and MK-8245 (1 µM) for one week. Images of a contrast-phase microscope (40X) (A) and quantification of the spheroid area using ImageJ software from scanner images below (B). * *t* Student test for A939572 or MK-8245 vs control conditions, $p<0.05$.

Finally, we also tested two other inhibitors whose targets were predicted to inhibit the growth of the three cell lines, SW480, SW620, and LiM2. The targets selected were RRM1 (ribonucleotide reductase catalytic subunit M1) and PKM (pyruvate kinase M).

We chose to inhibit RRM1 as its inhibitor clofarabine (Bonate et al., 2006) is approved for acute lymphoblastic leukaemia (Ho et al., 2015), and therefore it represents an enzyme among all the predicted targets that are currently being inhibited in cancer therapy. Ribonucleotide reductase takes part in the process of formation of deoxyribonucleotides from ribonucleotides, to

form DNA, and therefore represents an important step for cell proliferation. The results showed that clofarabine was effective for the three cell lines and not for NCM460 (Figure 5.2.22A and Table 5.2.6), Additionally, clofarabine completely impaired spheroid formation in both metastatic cell lines, with almost any spheroid observed after one week (Figure 5.2.23).

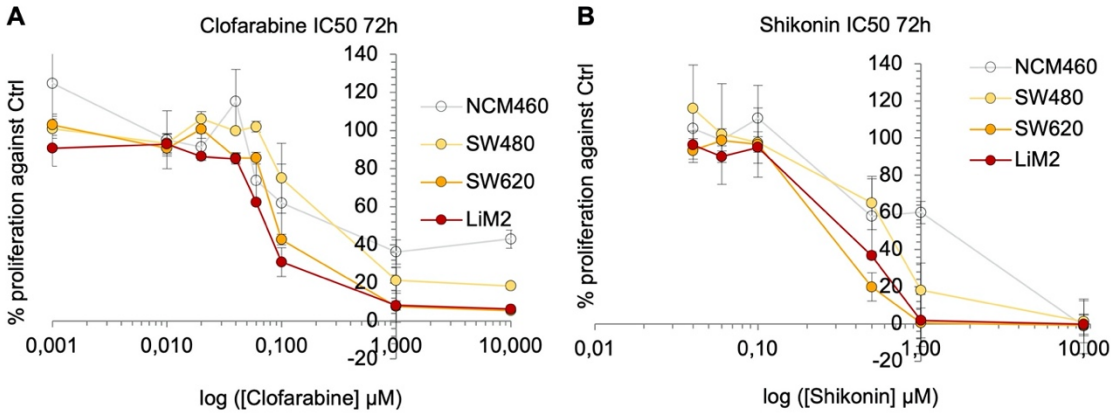

Figure 5.2.22. RRM1 and PKM2 inhibition in the healthy colon cell line NCM460, the primary tumour colon cancer cell line SW480, and metastatic derivatives SW620 and LiM2. A. and **B.** IC_{50} curve of the ribonucleotide reductase catalytic subunit M1 inhibitor clofarabine (A) and the pyruvate kinase M2 inhibitor shikonin (B) measured by DNA content using HO33342 after 72h incubation.

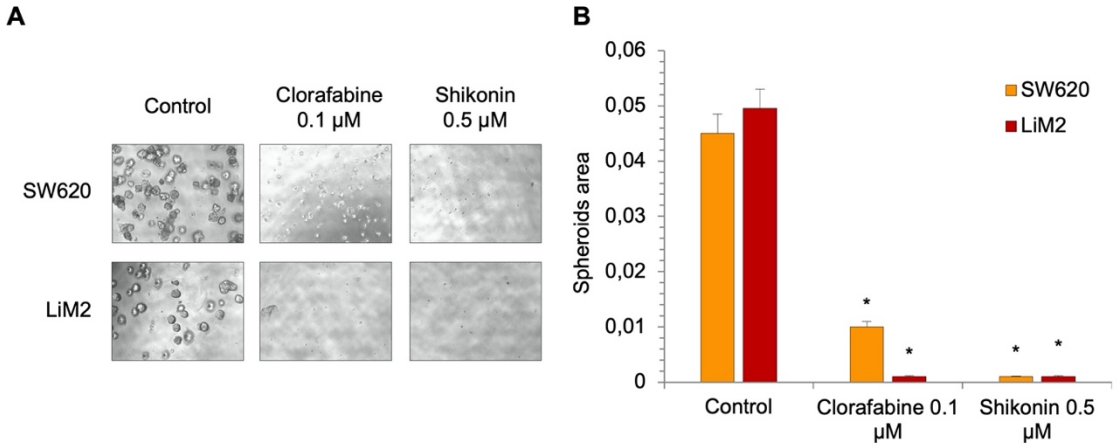

Figure 5.2.23. RRM1 and PKM inhibition effect on 3D growth of the colon cancer metastatic derivatives SW620 and LiM2. A. and **B.** Spheroid formation assay done in the presence of 50% medium (DMEM 12,5 mM Glc, 4 mM Gln, 5%, FBS, and 1% S/P) and 50% Matrigel matrix, adding the inhibitors clofarabine (0.1 µM) and shikonin (0.5 µM) for one week. Images of a contrast-phase microscope (40X) (A) and quantification of the spheroid area using ImageJ software from scanner images below (B). * *t* Student test for clofarabine or shikonin vs control conditions, $p<0.05$.

The other inhibitor that we chose was shikonin, an inhibitor of PKM2. The dependence of the metastatic cells to PKM is probably due to the enhanced pyruvate metabolism observed in the experiments in sections 5.1.2.3. However, the model predicted that this target would not be exclusive for SW620 and LiM2 but also affect SW480 (Table A.V.5). Pyruvate Kinase M is an isoform of the enzyme that catalyses de last step of glycolysis, the conversion from

phosphoenolpyruvate to pyruvate, therefore being determinant for the pyruvate concentration in the cell. PK isoform M2 is characterised for being expressed in early foetal tissues and in most cancer cells, and it presents a lower activity with respect to other isoforms that allow driving the intermediaries of glycolysis to other biosynthetic pathways such as pentose phosphate pathway or serine biosynthesis. Furthermore, PKM2 is implicated in transcriptional regulation of cytokinesis, proliferation, angiogenesis, and MYC expression (Hsu and Hung, 2018), being an attractive target for cancer cells and especially metastatic populations.

Shikonin is an active substance found in the root of *Lithospermum erythrorhizon*, a plant that is used in Chinese medicine (Wiench et al., 2012). It has been demonstrated in clinical trials that shikonin is safe and effective for the treatment of late-stage lung cancer, although to date it has not been approved. Recently, it has been discovered that shikonin inhibits pyruvate kinase M2 (Chen et al., 2011; Zhao et al., 2018). The results are promising, as shikonin is able to completely inhibit the proliferation of the metastatic cell lines at 1 μM, and SW480 cells were also greatly affected by shikonin, as the model predicted, while mild effects have been observed in the NCM460 cell line in the range of concentrations at which the cancer cell lines were affected (Figure 5.2.22B and Table 5.2.6). Additionally, spheroid capacity was also completely impaired at 0.5 μM, which is indicative once more of a good inhibitor for metastatic cells of colon cancer (Figure 5.2.23).

According to our *in vitro* analysis, the targets validated in this section, SCD-1, RRM1 and PKM inhibitors are promising targets for metastatic colorectal cancer. Therefore, the results obtained further confirmed the value of the GSMM model created from the experimental data in chapter 1.

6. General discussion

6 GENERAL DISCUSSION

In the field of cancer research, targeting the cancer cells that acquire the capacity to migrate, survive in the bloodstream and colonise a new organ is still an enormous challenge. Nowadays, it is considered that metastatic programs are closely associated to a cancer stem cell phenotype, and specifically targeting the CSC-associated signalling pathways is being explored as an approach for successful cancer therapy (Shibata and Hoque, 2019; Yang et al., 2020). One of the hallmarks of cancer that is considered to be relevant in cancer progression and metastasis is the metabolic adaptation (Chae and Kim, 2018). Greater knowledge about the metabolic features of metastatic cancer cells represents an opportunity to specifically disrupt the aggressive cancer cells and tackle metastasis, as other researches have also explored (Morandi et al., 2017). In the case of colorectal cancer, which accounts for 1.8 million new cases and 881000 deaths per year (Bray et al., 2018), patients diagnosed at advanced stages cannot be generally treated by surgery and, with current therapies, the 5-year survival rate is less than 10% (Matsuda et al., 2018), being an urgent need to develop effective therapeutic strategies against metastatic colorectal cancer.

Therefore, as part of our effort to identify the metabolic reprogramming in colorectal cancer metastasis, we used the isogenic same patient-derived cell lines SW480, SW620, and LiM2 that represents progressive steps of metastasis and is a valuable model for such study. In order to establish a link between the metabolic and metastatic features, it was necessary to first elucidate the metastatic phenotype of the cell lines. The primary tumour cell line SW480 have lower levels of EMT markers and EMT related transcription factors than the metastatic SW620 and LiM2 cells, except for E-cadherin, which is not found in SW480 and re-expressed in the metastatic cell lines. At the same time, the SW480 cells have the ability to migrate while SW620 and especially LiM2 were endowed with enhanced proliferative and spheroid formation capacity, characteristics that are commonly related to a cancer stem cell phenotype and colonisation capacities.

Remarkably, there are some examples in the literature with a similar pattern (Feng et al., 2014; Park et al., 2016). E-cadherin itself is emerging as a driver of metastatic spread, endowing cells with higher capacity to adhere between themselves and to new tissues (Gunasinghe et al., 2012; Hugo et al., 2017; Reichert et al., 2018). While EMT induction and the loss of E-cadherin could be advantageous at the primary tumour site to initiate metastasis and invasion, CSCs in the metastatic site re-express E-cadherin, which is observed to be mediated by TGFβ and ID1 and linked to β-catenin sequestering in a model of breast cancer metastasis (Stankic et al., 2013). In fact, we observed significantly diminished levels of β-catenin with respect to SW480. It is also described that not always the EMT program is necessary for metastasis (Ye et al., 2015) or else that the metastatic phenotype could be accompanied by multiple intermediate states or mixed EMT traits (Li and Kang, 2016; Nieto et al., 2016) where both mesenchymal and epithelial

features coexist (Beerling et al., 2016; Lo and Zhang, 2018; Pastushenko and Blanpain, 2019; Saitoh, 2018; Shibue and Weinberg, 2017).

Other researchers found that cells continue to express E-cadherin to maintain the cell cohorts (Chung et al., 2016) for collective migration to form CTCs clusters. Correspondingly, it has been observed in colorectal cancer that while single CTCs have completed the full EMT program, CTCs clusters are formed by cells that present a partial EMT with mixed EMT markers and characteristics (Aiello et al., 2018; Cima et al., 2016). Furthermore, collective migration is also guided by mesenchymal marchers such as fibronectin, vimentin, or γ-catenin (Gopal et al., 2017). We discovered that such mesenchymal markers are expressed in the metastatic colorectal cell lines SW620 and LiM2, at the same time as E-cadherin. Interestingly, γ-catenin is also observed to be expressed by breast cancer cells that form multicellular clusters in circulation and such γ-catenin expression helps to trap the metastatic cells in small capillaries that allow extravasation in distant organs (Aceto et al., 2014). Additionally, in leukaemia, γ-catenin has been found the be related to MYC expression (Luong-Gardiol et al., 2019), something that also corresponds with our cell model. Interestingly, we found γ-catenin especially increased in the highest metastatic cell line, the liver metastatic LiM2. In turn, the migratory capacity and loss of E-cadherin displayed by SW480 could have been induced by the transcription factor ZEB1/2, whose levels were higher in SW480 than in the metastatic cell lines (Wellner et al., 2009). Overexpression of EGFR present in SW480 could have been induced both β-catenin activation and mesenchymal initiation (Knight et al., 2019).

Overall, the results on EMT and CSC phenotypes in our cell lines revealed that SW480 is an example of metastatic initiating cells that allow the invasion of surrounding tissues but will not survive in circulation and colonise a new organ, while SW620 and LiM2 represent those mesenchymal cancer stem cells with re-acquired epithelial characteristics that allow them to successfully form a metastasis, probably by forming CTCs clusters.

At the metabolic level, we determined that the metastatic cell lines displayed a significantly more active Warburg effect than the primary cell line, as well as an increased flux of both pentose phosphate pathway branches. In this regard, the Warburg effect is described to support fast proliferation rates by allowing both fast ATP production and redirection of glycolytic intermediates towards the synthesis of biomass components (Vander Heiden et al., 2009; Locasale and Cantley, 2011; Shlomi et al., 2011). Additionally, acidification of the tumour microenvironment as a result of lactate secretion can also promote a gene expression program associated with invasiveness and metastasis in cancer cells (Rohani et al., 2019; Rozhin et al., 1994). Hence, the overactivated Warburg effect is poised to play a key role in enabling metastatic spread and, therefore, targeting it has proven to be an effective strategy to reduce the formation of metastasis in several cancer models (Du et al., 2016; Kolesnik et al., 2015; Sheng et al., 2012; Sottnik et al., 2011; Sun et al., 2010).

Despite the clear advantages of a glycolytic phenotype, the role of oxidative phosphorylation and mitochondrial respiration in metastasis formation has gained prominence in the last years, mainly in breast cancer metastasis (Davis et al., 2020; LeBleu et al., 2014; Porporato et al., 2014; Rodrigues et al., 2016). However, there are also some contradictory results regarding the mitochondrial phenotype accompanying metastasis (Morandi et al., 2017). In our case, a higher Warburg effect coexists with higher oxidative phosphorylation, as the metastatic cells also present an increased activity of PDH (decreased phosphorylation), incorporation of glucose to Krebs cycle and respiration capacity. However, the higher activity of PDH in liver metastasis from colon cancer is not in agreement with the pattern found for liver metastasis from breast cancer, where PDK1 (and therefore phosphorylation and inactivation of PDH) was observed to be upregulated by HIF1α (Dupuy et al., 2015). On the other hand, the observed enhanced pyruvate metabolism and PC overexpression in LiM2 cells are in concordance with the observed role that pyruvate and PC have for metastatic progression of breast cancer metastasis to the lung (Christen et al., 2016). A possible explanation of our metabolic pattern in terms of PDH activity is that a previous inactivation of PDH and decrease in mitochondrial respiration could have occurred in the first steps of metabolic reprogramming in the primary tumour (SW480) and then the metastatic cells (SW620 and LiM2) have reversed this phenotype. In fact, SW480 present higher levels of β-catenin, and Wnt/β-catenin signalling has been related with the inactivation of PDH through PPARγ (Lecarpentier et al., 2017) and PDK1 (Pate et al., 2014). However, it is also possible that phosphorylated PDH and deficient mitochondrial respiration was already present in the healthy colonocytes due to the use butyrate coming from the microbiota as a primary energy source (Donohoe et al., 2011, 2012).

The metastatic cell lines also presented a higher glutamine uptake and glutaminolysis than SW480. In this context, glutamine can support proliferation being both a carbon and nitrogen donor and its metabolism as well as GLS1 overexpression have been reported to enhance invasion and colonisation capacities in many cancer models (Dornier et al., 2017; Jin et al., 2018; Rodrigues et al., 2016; Shelton et al., 2010; Yang et al., 2014) including colorectal cancer (Xiang et al., 2019). Even more, the experiments on substrate availability indicated that the metastatic cells were highly flexible and could easily adapt and grow in various substrates or deprivations scenarios, and therefore survive in any environment such as blood or hypoxic tissue. Hence, increased mitochondrial function, supported by the data from mitochondrial fuel tests, might endow the metastatic cell lines with enhanced capacity to maintain a constant supply of ATP under any metabolic environments (Cannino et al., 2018). Such flexibility is also evident in the amino acid profile and nitrogen metabolism, which was already defined with transcriptomics (Urosevic et al., 2014). The higher serine consumption was also observed by other researchers to be a characteristic of metastatic cells and is indicative of higher one-carbon metabolism (Mattaini et al., 2016). In turn, proline production would be related to a need of extracellular matrix

formation (Phang et al., 2015), although other studies suggested proline catabolism to be an advantage for metastatic cells (Elia et al., 2017).

Overall, increased Warburg effect, glutaminolysis, TCA cycle activity and respiration capacity are consistent with the known effects of MYC (Bhutia et al., 2015; Koufaris et al., 2016; Méndez-Lucas et al., 2020; Satoh et al., 2017) suggesting that this oncogene, found to be overexpressed in the metastatic cell lines, might be the driver of the metabolic changes in the metastatic phenotype (Figure 6.1.1). Furthermore, recent results demonstrate that E-cadherin is also a promoter of mitochondrial metabolism (Padmanaban et al., 2019; Park et al., 2017).

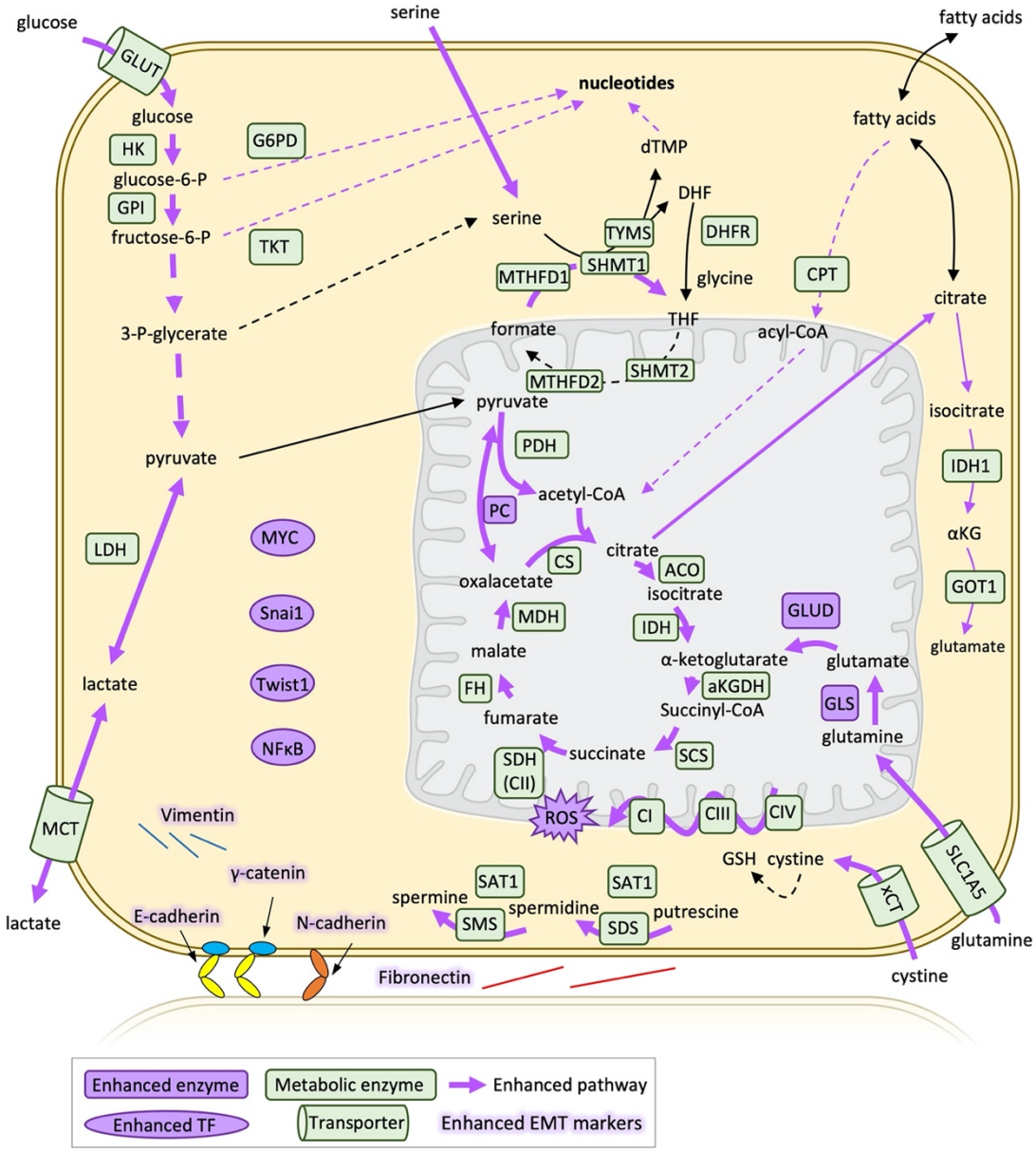

Figure 6.1.1. Metabolic adaptations of metastatic colon cancer cells. The main metabolic alterations observed in the metastatic cell lines (SW620 and LiM2) in comparison with SW480, including enhanced pathways observed experimentally and predicted by the genome-scale metabolic model, observed overexpressed enzymes, transcription factors and EMT markers. All abbreviations are listed in section 1.

In our experiments *in vivo*, we confirmed both the metastatic and metabolic phenotype of the cell lines. After subcutaneous injection, SW480 cells presented the lowest capacity to adhere to the mice tissue, form a tumour and proliferate, while both SW620 and LiM2 rapidly generated tumours. Furthermore, the phosphorylation status of PDH and the enhanced metabolism of glucose and glutamine observed *in vitro* were conserved in an *in vivo* scenario, where there are many different factors such as the concentration of substrates and oxygen or the presence of a tumour stroma (Davidson et al., 2016). Such results give more confidence to the genomic-scale metabolic model that was performed from *in vitro* data, which predicted a series of metabolic vulnerabilities of the metastatic cell lines that we expect that would be valid in an *in vivo* environment.

Having the essentiality of glutaminolysis and oxidative phosphorylation as one of the hallmarks of metabolic phenotype of metastasis, enhanced ROS levels are expected and ROS homeostasis would be one of the major challenges for metastatic cells, although a minimum level of ROS is considered to be necessary for malignancy (Panieri and Santoro, 2016; Porporato and Sonveaux, 2015; Raimondi et al., 2019; Weinberg et al., 2010). ROS scavenging is largely dependent on glutathione (Bansal and Simon, 2018; Traverso et al., 2013). Indeed, glutathione levels tend to be higher in cancer cells than in healthy tissue and glutathione synthesis has been found to support metastasis in several cancer types (Le Gal et al., 2015; Ortega et al., 2003). Glutathione is a tripeptide synthesised from glutamate, cysteine, and glycine. In this context, increased glutathione synthesis is likely supported by the increased concentrations of glutamate and glycine found in metastatic cell lines by us and other authors as a result of the increased glutaminase and serine hydroxymethyltransferase activities (Boysen et al., 2019; Sappington et al., 2016). However, the limited substrate for glutathione synthesis is generally assumed to be cysteine (Estrela et al., 2016).

Precisely, the cell line-specific GSMM predicted that the metastatic cell lines were dependent on cystine uptake from the extracellular media. Indeed, we determined that inhibition of the cystine transporter system xCT with sulfasalazine or erastin was highly specific for the metastatic cell lines. We also validated the inhibitions in 3D cultures, which are a good intermediate step from 2D culture to *in vivo* studies, representing better drug sensitivity and colonisation capacity (Kapałczyńska et al., 2018). This makes system xCT inhibition a potentially effective therapeutic strategy against metastasis in colorectal cancer. Furthermore, the system xCT is overexpressed in several cancer types including colorectal tumours with mutant KRAS (Lim et al., 2019; Shin et al., 2018). The system xCT plays a key role in supplying the cystine for glutathione synthesis (Lewerenz et al., 2013) and, in this regard, GSR, the enzyme that recovers reduced glutathione from the oxidised form, was also predicted to be a putative target. The fact that GSR inhibition with 2-AAPA was also selective for the metastatic cells validated the model predictions. In addition, we found a synergetic response when both *de novo* synthesis and

recycling of glutathione were impaired by combining 2-AAPA and erastin treatments. Remarkably, in other cancer types, both system xCT and 2-AAPA inhibitors individually have already been proven to be successful in combination with cisplatin (Ma et al., 2015; Sato et al., 2018) or radiotherapy (Cobler et al., 2018; Nagane et al., 2018; Pan et al., 2019; Sleire et al., 2015; Zhao et al., 2009), as depleting glutathione and antioxidant defences make cells more sensitive to drug or X-ray irradiation. Thus, we posit that the combination of 2-AAPA and erastin could be used in conjunction with chemotherapy or radiotherapy to effectively tackle metastatic colon cancer without affecting the NCM460 healthy colon cell line.

From genome-scale simulations, cytosolic folate metabolism was also identified as a pathway upregulated in the metastatic cell lines compared to the primary colon cell line SW480. Indeed, because of its role in nucleotide synthesis, epigenetic regulation and redox balance, folate metabolism is often overactivated as part of cancer progression (Locasale, 2013; Maddocks et al., 2017; Meiser et al., 2016). Notably, while the inhibition of both cytosolic and mitochondrial SHMT isoforms was effective for both primary and metastatic cancer cell lines, targeting only cytosolic activities by inhibition of DHFR or MTHFD1, inhibited proliferation only in the metastatic cell lines. This suggests that the metastatic cell lines could be selectively dependent on the cytosolic folate metabolism. In fact, MTHFD1 has been shown to interact with BRD4, linking folate metabolism to transcriptional regulation (Sdelci et al., 2019), something that could explain the specific dependency on the cytosolic isoform upon the mitochondrial. Additionally, both DHFR and MTHFD1 have been found to be overexpressed in colorectal cancer tumours compared to healthy tumour epithelia (Sanz-Pamplona et al., 2014), which makes our results more consistent and clinically reliable for future research.

Furthermore, it has also been postulated that MTHFD1 enhances antioxidant capacity (Piskounova et al., 2015), and the predicted compartmentalisation could reflect the demand of NADPH in the cytosol, which cannot be compensated by the mitochondrial branch of folate metabolism. Folate metabolism also acts as a one-carbon donor in the methionine cycle which regulates both cysteine levels and contributes to the epigenetic modulation that is required to maintain the phenotype of metastatic cells (Wong et al., 2017). For this reason, we hypothesised that the combination of cystine uptake and folate metabolism inhibition could seriously impair the antioxidant capacity of the metastatic cells. We found erastin and LY345899 to be a good combination synergistically impairing cell proliferation as well as 3D growth in the metastatic cell lines. We consider, therefore, that metastatic colon cancer cells rely on antioxidant defence to grow due to its enhanced oxidative metabolism, and impairing both *de novo* glutathione synthesis by system xCT inhibition and MTHFD1 (but not other enzymes of folate metabolism) could be a manner of significantly reducing its aggressivity that does not affect the NCM460 cell line.

Finally, SCD1, RRM1, and PKM2, other targets predicted by the model, were also validated *in vitro*. Inhibitors of such targets successfully impaired metastatic cell lines proliferation. The inhibitors targeting those enzymes were also more effective for SW480 than the previous inhibitors of cysteine and folate metabolism, which concordats with the model predictions. In fact, SCD1 inhibitors have been described to impair tumour migration (Tracz-Gaszewska and Dobrzyn, 2019), which we observed to be a characteristic of SW480. Subsequently, PKM2 has been observed to translocate into the nucleus and induce EMT through the upregulation of ZEB2 and Snai1 (Hamabe et al., 2014), which makes a suitable target for both the metastatic initiating cell lines that have invasive properties (in our case SW480) and the ones that have colonisation capacity (SW620 and LiM2).

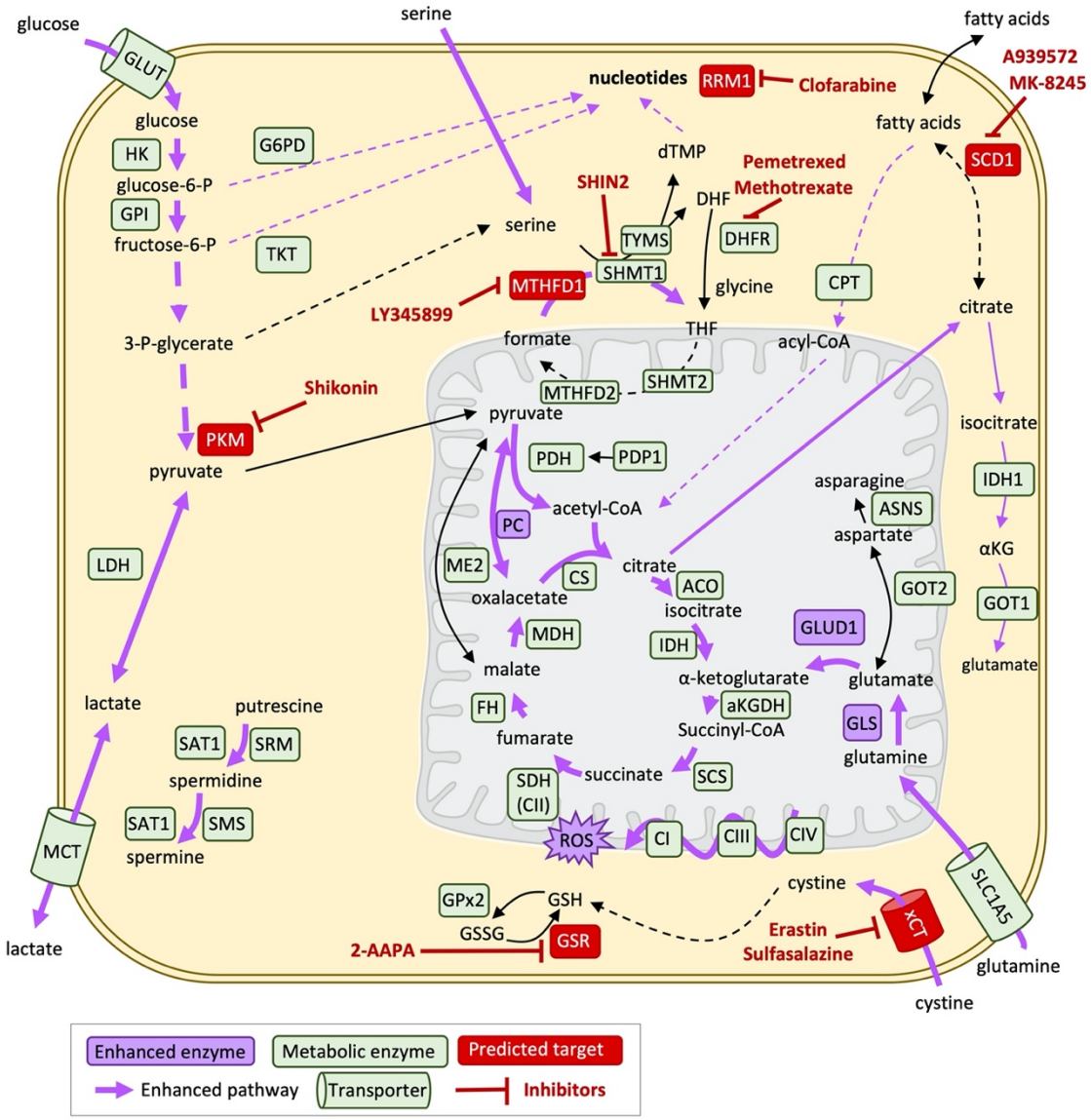

Figure 6.1.2. Metabolic vulnerabilities of metastatic colon cancer cells. The main metabolic alterations observed in the metastatic cell lines (SW620 and LiM2) in comparison with SW480 and metabolic vulnerabilities predicted by the genome-scale metabolic model and the inhibitors used in the present work to tackle metastatic colon cancer cells. All abbreviations are listed in section 1.

To summarise, the work presented here provide an insight into the metabolic reprogramming supporting metastasis. We also revealed and validated the metabolic vulnerabilities that emerge during the transition between primary to metastatic states primary tumour, lymph node and distant metastasis represented by the same patient-derived cellular models SW480, SW620, and LiM2 (Figure 6.1.2). We discovered that metastatic cells with a mesenchymal and stem cell phenotype and re-expression of E-cadherin present an overactivated metabolism of glucose, glutamine and amino acids and have cystine and folate metabolism as the main vulnerabilities, confirming the hypothesis that metabolic reprogramming plays a crucial role in the metastatic progression of colorectal cancer. Regarding the differences between SW620 and LiM2, it is interesting to observe that they are very similar and LiM2 had only some enhanced features with respect to SW620, such as higher levels of specific mesenchymal markers or metabolic enzymes such as Snai1 or PC. This suggests that the cancer stem cell metabolic phenotype of lymph node metastatic cells is already adapted to any environment for metastasis. Indeed, this similarity can be therapeutically exploited as both populations were shown to share the same metabolic dependency on cystine uptake and folate metabolism among other vulnerabilities and hence could be targeted by the same drugs. Such dependencies could be further exploited for therapeutic interventions that would be selective against metastatic cells in colorectal cancer in order to improve colorectal cancer therapies.

7. Conclusions

7 CONCLUSIONS

1. The cell lines SW480, SW620, and LiM2 are a good model to study the metabolic adaptation during metastatic progression in colon cancer.

2. Primary tumour colon cancer cells SW480 display a mesenchymal phenotype and are characterised by loss of E-cadherin, increased levels of EGFR and β-catenin and impaired activity of PDH and mitochondrial metabolism.

3. Cells from metastatic sites SW620 and LiM2 display an enhanced stem cell phenotype and increased levels of mesenchymal markers and transcription factors, E-cadherin re-expression, as well as MYC levels that drive enhanced Warburg effect, pyruvate metabolism and PDH activity, glutaminolysis, amino acid metabolism, TCA and mitochondrial activity as well as higher metabolic flexibility to different substrate availability.

4. The metastatic and metabolic characteristics observed in SW480, SW620, and LiM2 cell lines *in vitro* are maintained in an *in vivo* scenario, which gives more clinical value to such findings.

5. Integration of metabolic and transcriptomic data in cell line-specific GSMM (for SW480, SW620, and LiM2 cell lines) has been proven as a successful strategy to predict folate metabolism and cystine import as main metabolic vulnerabilities specific for metastatic cell lines.

6. Inhibitors of the system xCT and MTHFD1, that are key proteins in cysteine transport and folate metabolism, respectively, have been experimentally validated as effective for impairing metastatic cells proliferation, spheroid formation and causing apoptosis. Furthermore, the combination of both inhibitors is synergetic for the metastatic colon cancer cell lines.

8. Bibliography

8 BIBLIOGRAPHY

Abbasi, M., Mousavi, M.J., Jamalzehi, S., Alimohammadi, R., Bezvan, M.H., Mohammadi, H., and Aslani, S. (2018). Strategies toward rheumatoid arthritis therapy; the old and the new. J. Cell. Physiol. jcp.27860.

Abdalkader, M., Lampinen, R., Kanninen, K.M., Malm, T.M., and Liddell, J.R. (2018). Targeting Nrf2 to Suppress Ferroptosis and Mitochondrial Dysfunction in Neurodegeneration. Front. Neurosci. *12*, 466.

Aceto, N., Bardia, A., Miyamoto, D.T., Donaldson, M.C., Wittner, B.S., Spencer, J.A., Yu, M., Pely, A., Engstrom, A., Zhu, H., et al. (2014). Circulating tumor cell clusters are oligoclonal precursors of breast cancer metastasis. Cell *158*, 1110–1122.

Aguilar, E., Marin de Mas, I., Zodda, E., Marin, S., Morrish, F., Selivanov, V., Meca-Cortés, Ó., Delowar, H., Pons, M., Izquierdo, I., et al. (2016). Metabolic Reprogramming and Dependencies Associated with Epithelial Cancer Stem Cells Independent of the Epithelial-Mesenchymal Transition Program. Stem Cells *34*, 1163–1176.

Aiello, N.M., Maddipati, R., Norgard, R.J., Balli, D., Li, J., Yuan, S., Yamazoe, T., Black, T., Sahmoud, A., Furth, E.E., et al. (2018). EMT Subtype Influences Epithelial Plasticity and Mode of Cell Migration. Dev. Cell *45*, 681-695.e4.

Alamo, P., Gallardo, A., Di Nicolantonio, F., Pavón, M.A., Casanova, I., Trias, M., Mangues, M.A., Lopez-Pousa, A., Villaverde, A., Vázquez, E., et al. (2015). Higher metastatic efficiency of KRas G12V than KRas G13D in a colorectal cancer model. FASEB J. *29*, 464–476.

Alcarraz-Vizán, G., Sánchez-Tena, S., Moyer, M.P., and Cascante, M. (2014). Validation of NCM460 cell model as control in antitumor strategies targeting colon adenocarcinoma metabolic reprogramming: Trichostatin A as a case study. Biochim. Biophys. Acta - Gen. Subj. *1840*, 1634–1639.

Amin, M.B., Greene, F.L., Edge, S.B., Compton, C.C., Gershenwald, J.E., Brookland, R.K., Meyer, L., Gress, D.M., Byrd, D.R., and Winchester, D.P. (2017). The Eighth Edition AJCC Cancer Staging Manual: Continuing to build a bridge from a population-based to a more "personalized" approach to cancer staging. CA. Cancer J. Clin. *67*, 93–99.

Anand, P., Kunnumakkara, A.B., Kunnumakara, A.B., Sundaram, C., Harikumar, K.B., Tharakan, S.T., Lai, O.S., Sung, B., and Aggarwal, B.B. (2008). Cancer is a preventable disease that requires major lifestyle changes. Pharm. Res. *25*, 2097–2116.

Anderson, D.D., and Stover, P.J. (2009). SHMT1 and SHMT2 are functionally redundant in nuclear de novo thymidylate biosynthesis. PLoS One *4*, e5839.

Andrzejewski, S., Klimcakova, E., Johnson, R.M., Tabariès, S., Annis, M.G., McGuirk, S., Northey, J.J., Chénard, V., Sriram, U., Papadopoli, D.J., et al. (2017). PGC-1α Promotes Breast Cancer Metastasis and Confers Bioenergetic Flexibility against Metabolic Drugs. Cell Metab. *26*, 778-787.e5.

Antoniewicz, M.R. (2018). A guide to 13C metabolic flux analysis for the cancer biologist. Exp. Mol. Med. *50*, 19.

Apaolaza, I., San José-Eneriz, E., Tobalina, L., Miranda, E., Garate, L., Agirre, X., Prósper, F., and Planes, F.J. (2017). An in-silico approach to predict and exploit synthetic lethality in cancer

metabolism. Nat. Commun. *8*, 459.

Apaolaza, I., Valcarcel, L.V., and Planes, F.J. (2019). gMCS: fast computation of genetic minimal cut sets in large networks. Bioinformatics *35*, 535–537.

Arnold, M., Sierra, M.S., Laversanne, M., Soerjomataram, I., Jemal, A., and Bray, F. (2017). Global patterns and trends in colorectal cancer incidence and mortality. Gut *66*, 683–691.

Arruebo, M., Vilaboa, N., Sáez-Gutierrez, B., Lambea, J., Tres, A., Valladares, M., and González-Fernández, A. (2011). Assessment of the evolution of cancer treatment therapies. Cancers (Basel). *3*, 3279–3330.

Attanasio, F., Caldieri, G., Giacchetti, G., van Horssen, R., Wieringa, B., and Buccione, R. (2011). Novel invadopodia components revealed by differential proteomic analysis. Eur. J. Cell Biol. *90*, 115–127.

Audia, J.E., and Campbell, R.M. (2016). Histone Modifications and Cancer. Cold Spring Harb. Perspect. Biol. *8*, a019521.

Auslander, N., Cunningham, C.E., Toosi, B.M., McEwen, E.J., Yizhak, K., Vizeacoumar, F.S., Parameswaran, S., Gonen, N., Freywald, T., Bhanumathy, K.K., et al. (2017). An integrated computational and experimental study uncovers FUT9 as a metabolic driver of colorectal cancer. Mol. Syst. Biol. *13*, 956.

Ayob, A.Z., and Ramasamy, T.S. (2018). Cancer stem cells as key drivers of tumour progression. J. Biomed. Sci. *25*, 20.

Balcells, C., Foguet, C., Tarragó-Celada, J., de Atauri, P., Marin, S., and Cascante, M. (2019). Tracing metabolic fluxes using mass spectrometry: Stable isotope-resolved metabolomics in health and disease. TrAC - Trends Anal. Chem. *120*, 115371.

Bansal, A., and Simon, M.C. (2018). Glutathione metabolism in cancer progression and treatment resistance. J. Cell Biol. *217*, 2291–2298.

Barrett, T., Wilhite, S.E., Ledoux, P., Evangelista, C., Kim, I.F., Tomashevsky, M., Marshall, K.A., Phillippy, K.H., Sherman, P.M., Holko, M., et al. (2013). NCBI GEO: archive for functional genomics data sets--update. Nucleic Acids Res. *41*, D991-5.

Baysal, B.E., Ferrell, R.E., Willett-Brozick, J.E., Lawrence, E.C., Myssiorek, D., Bosch, A., van der Mey, A., Taschner, P.E.M., Rubinstein, W.S., Myers, E.N., et al. (2000). Mutations in SDHD, a mitochondrial complex II gene, in hereditary paraganglioma. Science *287*, 848–851.

Becker, S.A., and Palsson, B.O. (2008). Context-specific metabolic networks are consistent with experiments. PLoS Comput. Biol. *4*, e1000082.

Beerling, E., Seinstra, D., de Wit, E., Kester, L., van der Velden, D., Maynard, C., Schäfer, R., van Diest, P., Voest, E., van Oudenaarden, A., et al. (2016). Plasticity between Epithelial and Mesenchymal States Unlinks EMT from Metastasis-Enhancing Stem Cell Capacity. Cell Rep. *14*, 2281–2288.

Beloribi-Djefaflia, S., Vasseur, S., and Guillaumond, F. (2016). Lipid metabolic reprogramming in cancer cells. Oncogenesis *5*, e189.

Beloueche-Babari, M., Wantuch, S., Casals Galobart, T., Koniordou, M., Parkes, H.G., Arunan, V., Chung, Y.-L., Eykyn, T.R., Smith, P.D., and Leach, M.O. (2017). MCT1 Inhibitor AZD3965

Increases Mitochondrial Metabolism, Facilitating Combination Therapy and Noninvasive Magnetic Resonance Spectroscopy. Cancer Res. *77*, 5913–5924.

Beloueche-Babari, M., Casals Galobart, T., Delgado-Goni, T., Wantuch, S., Parkes, H.G., Tandy, D., Harker, J.A., and Leach, M.O. (2020). Monocarboxylate transporter 1 blockade with AZD3965 inhibits lipid biosynthesis and increases tumour immune cell infiltration. Br. J. Cancer *122*, 895–903.

Ben, Q., Sun, Y., Chai, R., Qian, A., Xu, B., and Yuan, Y. (2014). Dietary fiber intake reduces risk for colorectal adenoma: a meta-analysis. Gastroenterology *146*, 689-699.e6.

Bender, U., Rho, Y.S., Barrera, I., Aghajanyan, S., Acoba, J., and Kavan, P. (2019). Adjuvant therapy for stages II and III colon cancer: risk stratification, treatment duration, and future directions. Curr. Oncol. *26*, S43–S52.

Benito, A., Polat, I.H., Noé, V., Ciudad, C.J., Marin, S., and Cascante, M. (2017). Glucose-6-phosphate dehydrogenase and transketolase modulate breast cancer cell metabolic reprogramming and correlate with poor patient outcome. Oncotarget *8*, 106693–106706.

Bernfeld, E., and Foster, D.A. (2019). Glutamine as an Essential Amino Acid for KRas-Driven Cancer Cells. Trends Endocrinol. Metab. *30*, 357–368.

Bernstein, I.D., Tam, M.R., and Nowinski, R.C. (1980). Mouse leukemia: therapy with monoclonal antibodies against a thymus differentiation antigen. Science *207*, 68–71.

Bhutia, Y.D., Babu, E., Ramachandran, S., and Ganapathy, V. (2015). Amino Acid transporters in cancer and their relevance to “glutamine addiction”: novel targets for the design of a new class of anticancer drugs. Cancer Res. *75*, 1782–1788.

Bie, Y., Ge, W., Yang, Z., Cheng, X., Zhao, Z., Li, S., Wang, W., Wang, Y., Zhao, X., Yin, Z., et al. (2019). The Crucial Role of CXCL8 and Its Receptors in Colorectal Liver Metastasis. Dis. Markers *2019*, 8023460.

Bonate, P.L., Arthaud, L., Cantrell, W.R., Stephenson, K., Secrist, J.A., and Weitman, S. (2006). Discovery and development of clofarabine: a nucleoside analogue for treating cancer. Nat. Rev. Drug Discov. *5*, 855–863.

Bonovas, S., Fiorino, G., Lytras, T., Malesci, A., and Danese, S. (2016). Calcium supplementation for the prevention of colorectal adenomas: A systematic review and meta-analysis of randomized controlled trials. World J. Gastroenterol. *22*, 4594–4603.

Bost, F., and Kaminski, L. (2019). The metabolic modulator PGC-1α in cancer. Am. J. Cancer Res. *9*, 198–211.

Boysen, G., Jamshidi-Parsian, A., Davis, M.A., Siegel, E.R., Simecka, C.M., Kore, R.A., Dings, R.P.M., and Griffin, R.J. (2019). Glutaminase inhibitor CB-839 increases radiation sensitivity of lung tumor cells and human lung tumor xenografts in mice. Int. J. Radiat. Biol. *95*, 436–442.

Bray, F., Ferlay, J., Soerjomataram, I., Siegel, R.L., Torre, L.A., and Jemal, A. (2018). Global cancer statistics 2018: GLOBOCAN estimates of incidence and mortality worldwide for 36 cancers in 185 countries. CA. Cancer J. Clin. *68*, 394–424.

Brown, R.E., Short, S.P., and Williams, C.S. (2018). Colorectal Cancer and Metabolism. Curr. Colorectal Cancer Rep. *14*, 226–241.

Brumano, L.P., da Silva, F.V.S., Costa-Silva, T.A., Apolinário, A.C., Santos, J.H.P.M., Kleingesinds, E.K., Monteiro, G., Rangel-Yagui, C. de O., Benyahia, B., and Junior, A.P. (2018). Development of L-Asparaginase Biobetters: Current Research Status and Review of the Desirable Quality Profiles. Front. Bioeng. Biotechnol. *6*, 212.

Bu, P., Chen, K.-Y., Xiang, K., Johnson, C., Crown, S.B., Rakhilin, N., Ai, Y., Wang, L., Xi, R., Astapova, I., et al. (2018). Aldolase B-Mediated Fructose Metabolism Drives Metabolic Reprogramming of Colon Cancer Liver Metastasis. Cell Metab. *27*, 1249-1262.e4.

Burgos-Panadero, R., Lucantoni, F., Gamero-Sandemetrio, E., Cruz-Merino, L. de la, Álvaro, T., and Noguera, R. (2019). The tumour microenvironment as an integrated framework to understand cancer biology. Cancer Lett. *461*, 112–122.

Cannino, G., Ciscato, F., Masgras, I., Sánchez-Martín, C., and Rasola, A. (2018). Metabolic Plasticity of Tumor Cell Mitochondria. Front. Oncol. *8*, 333.

Capello, M., Ferri-Borgogno, S., Riganti, C., Chattaragada, M.S., Principe, M., Roux, C., Zhou, W., Petricoin, E.F., Cappello, P., and Novelli, F. (2016). Targeting the Warburg effect in cancer cells through ENO1 knockdown rescues oxidative phosphorylation and induces growth arrest. Oncotarget *7*, 5598–5612.

Capp, J.-P. (2019). Cancer Stem Cells: From Historical Roots to a New Perspective. J. Oncol. *2019*, 5189232.

Carrer, A., Trefely, S., Zhao, S., Campbell, S.L., Norgard, R.J., Schultz, K.C., Sidoli, S., Parris, J.L.D., Affronti, H.C., Sivanand, S., et al. (2019). Acetyl-CoA Metabolism Supports Multistep Pancreatic Tumorigenesis. Cancer Discov. *9*, 416–435.

Casero, R.A., Murray Stewart, T., and Pegg, A.E. (2018). Polyamine metabolism and cancer: treatments, challenges and opportunities. Nat. Rev. Cancer *18*, 681–695.

Cha, Y.J., Jung, W.H., and Koo, J.S. (2017). Differential Site-Based Expression of Pentose Phosphate Pathway-Related Proteins among Breast Cancer Metastases. Dis. Markers *2017*, 7062517.

Chabner, B.A., and Roberts, T.G. (2005). Timeline: Chemotherapy and the war on cancer. Nat. Rev. Cancer *5*, 65–72.

Chae, Y.C., and Kim, J.H. (2018). Cancer stem cell metabolism: target for cancer therapy. BMB Rep. *51*, 319–326.

Chae, Y.K., Anker, J.F., Oh, M.S., Bais, P., Namburi, S., Agte, S., Giles, F.J., and Chuang, J.H. (2019). Mutations in DNA repair genes are associated with increased neoantigen burden and a distinct immunophenotype in lung squamous cell carcinoma. Sci. Rep. *9*, 3235.

Chaicharoenaudomrung, N., Kunhorm, P., and Noisa, P. (2019). Three-dimensional cell culture systems as an in vitro platform for cancer and stem cell modeling. World J. Stem Cells *11*, 1065–1083.

Chaiyawat, P., Chokchaichamnankit, D., Lirdprapamongkol, K., Srisomsap, C., Svasti, J., and Champattanachai, V. (2015). Alteration of O-GlcNAcylation affects serine phosphorylation and regulates gene expression and activity of pyruvate kinase M2 in colorectal cancer cells. Oncol. Rep. *34*, 1933–1942.

Chawla, R.K., Lewis, F.W., Kutner, M.H., Bate, D.M., Roy, R.G.B., and Rudman, D. (1984).

Plasma cysteine, cystine, and glutathione in cirrhosis. Gastroenterology *87*, 770–776.

Chen, H., Liu, H., and Qing, G. (2018). Targeting oncogenic Myc as a strategy for cancer treatment. Signal Transduct. Target. Ther. *3*, 5.

Chen, J., Xie, J., Jiang, Z., Wang, B., Wang, Y., and Hu, X. (2011). Shikonin and its analogs inhibit cancer cell glycolysis by targeting tumor pyruvate kinase-M2. Oncogene *30*, 4297–4306.

Chen, J., Lee, H.-J., Wu, X., Huo, L., Kim, S.-J., Xu, L., Wang, Y., He, J., Bollu, L.R., Gao, G., et al. (2015). Gain of glucose-independent growth upon metastasis of breast cancer cells to the brain. Cancer Res. *75*, 554–565.

Chen, K.-Y., Liu, X., Bu, P., Lin, C.-S., Rakhilin, N., Locasale, J.W., and Shen, X. (2014). A metabolic signature of colon cancer initiating cells. IEEE Eng. Med. Biol. Soc. Annu. Conf. *2014*, 4759–4762.

Chen, W., Seefeldt, T., Young, A., Zhang, X., Zhao, Y., Ruffolo, J., Kaushik, R.S., and Guan, X. (2012). Microtubule S-glutathionylation as a potential approach for antimitotic agents. BMC Cancer *12*, 245.

Choi, Y.J., Kim, Y.H., Cho, C.H., Kim, S.H., and Lee, J.E. (2015). Circulating levels of vitamin D and colorectal adenoma: A case-control study and a meta-analysis. World J. Gastroenterol. *21*, 8868–8877.

Chong, J., Yamamoto, M., and Xia, J. (2019). MetaboAnalystR 2.0: From Raw Spectra to Biological Insights. Metabolites *9*, 57.

Chou, T.-C. (2010). Drug combination studies and their synergy quantification using the Chou-Talalay method. Cancer Res. *70*, 440–446.

Christen, S., Lorendeau, D., Schmieder, R., Broekaert, D., Metzger, K., Veys, K., Elia, I., Buescher, J.M., Orth, M.F., Davidson, S.M., et al. (2016). Breast Cancer-Derived Lung Metastases Show Increased Pyruvate Carboxylase-Dependent Anaplerosis. Cell Rep. *17*, 837–848.

Chung, Y.-C., Wei, W.-C., Hung, C.-N., Kuo, J.-F., Hsu, C.-P., Chang, K.-J., and Chao, W.-T. (2016). Rab11 collaborates E-cadherin to promote collective cell migration and indicates a poor prognosis in colorectal carcinoma. Eur. J. Clin. Invest. *46*, 1002–1011.

Cima, I., Kong, S.L., Sengupta, D., Tan, I.B., Phyo, W.M., Lee, D., Hu, M., Iliescu, C., Alexander, I., Goh, W.L., et al. (2016). Tumor-derived circulating endothelial cell clusters in colorectal cancer. Sci. Transl. Med. *8*, 345ra89.

Ciudad, C.J., Rodríguez, L., Villalobos, X., Félix, A.J., and Noé, V. (2017). Polypurine Reverse Hoogsteen Hairpins as a Gene Silencing Tool for Cancer. Curr. Med. Chem. *24*, 2809–2826.

Cobler, L., Zhang, H., Suri, P., Park, C., and Timmerman, L.A. (2018). xCT inhibition sensitizes tumors to γ-radiation via glutathione reduction. Oncotarget *9*, 32280–32297.

Combs, J.A., and DeNicola, G.M. (2019). The Non-Essential Amino Acid Cysteine Becomes Essential for Tumor Proliferation and Survival. Cancers (Basel). *11*.

Commander, R., Wei, C., Sharma, A., Mouw, J.K., Burton, L.J., Summerbell, E., Mahboubi, D., Peterson, R.J., Konen, J., Zhou, W., et al. (2020). Subpopulation targeting of pyruvate dehydrogenase and GLUT1 decouples metabolic heterogeneity during collective cancer cell

invasion. Nat. Commun. *11*, 1533.

Crabtree, H.G. (1929). Observations on the carbohydrate metabolism of tumours. Biochem. J. *23*, 536–545.

Curtis, M., Kenny, H.A., Ashcroft, B., Mukherjee, A., Johnson, A., Zhang, Y., Helou, Y., Batlle, R., Liu, X., Gutierrez, N., et al. (2019). Fibroblasts Mobilize Tumor Cell Glycogen to Promote Proliferation and Metastasis. Cell Metab. *29*, 141-155.e9.

Van Cutsem, E., Cervantes, A., Adam, R., Sobrero, A., Van Krieken, J.H., Aderka, D., Aranda Aguilar, E., Bardelli, A., Benson, A., Bodoky, G., et al. (2016). ESMO consensus guidelines for the management of patients with metastatic colorectal cancer. Ann. Oncol. Off. J. Eur. Soc. Med. Oncol. *27*, 1386–1422.

D'Souza, M.M., Sharma, R., Jaimini, A., Panwar, P., Saw, S., Kaur, P., Mondal, A., Mishra, A., and Tripathi, R.P. (2014). 11C-MET PET/CT and advanced MRI in the evaluation of tumor recurrence in high-grade gliomas. Clin. Nucl. Med. *39*, 791–798.

Dang, L., White, D.W., Gross, S., Bennett, B.D., Bittinger, M.A., Driggers, E.M., Fantin, V.R., Jang, H.G., Jin, S., Keenan, M.C., et al. (2009). Cancer-associated IDH1 mutations produce 2-hydroxyglutarate. Nature *462*, 739–744.

Davidson, S.M., Papagiannakopoulos, T., Olenchock, B.A., Heyman, J.E., Keibler, M.A., Luengo, A., Bauer, M.R., Jha, A.K., O'Brien, J.P., Pierce, K.A., et al. (2016). Environment Impacts the Metabolic Dependencies of Ras-Driven Non-Small Cell Lung Cancer. Cell Metab. *23*, 517–528.

Davis, R.T., Blake, K., Ma, D., Gabra, M.B.I., Hernandez, G.A., Phung, A.T., Yang, Y., Maurer, D., Lefebvre, A.E.Y.T., Alshetaiwi, H., et al. (2020). Transcriptional diversity and bioenergetic shift in human breast cancer metastasis revealed by single-cell RNA sequencing. Nat. Cell Biol. *22*, 310–320.

Dedhia, P.H., Bertaux-Skeirik, N., Zavros, Y., and Spence, J.R. (2016). Organoid Models of Human Gastrointestinal Development and Disease. Gastroenterology *150*, 1098–1112.

Dey, S., Sayers, C.M., Verginadis, I.I., Lehman, S.L., Cheng, Y., Cerniglia, G.J., Tuttle, S.W., Feldman, M.D., Zhang, P.J.L., Fuchs, S.Y., et al. (2015). ATF4-dependent induction of heme oxygenase 1 prevents anoikis and promotes metastasis. J. Clin. Invest. *125*, 2592–2608.

Díaz-Rubio, E., Tabernero-Caturla, J., and Capdevila-Castillón, J. (2012). Atlas integral del cáncer colorrectal (Madrid).

Ding, K., Jiang, J., Chen, L., and Xu, X. (2018). Methylenetetrahydrofolate Dehydrogenase 1 Silencing Expedites the Apoptosis of Non-Small Cell Lung Cancer Cells via Modulating DNA Methylation. Med. Sci. Monit. *24*, 7499–7507.

Dixon, S.J., Lemberg, K.M., Lamprecht, M.R., Skouta, R., Zaitsev, E.M., Gleason, C.E., Patel, D.N., Bauer, A.J., Cantley, A.M., Yang, W.S., et al. (2012). Ferroptosis: an iron-dependent form of nonapoptotic cell death. Cell *149*, 1060–1072.

Dixon, S.J., Patel, D.N., Welsch, M., Skouta, R., Lee, E.D., Hayano, M., Thomas, A.G., Gleason, C.E., Tatonetti, N.P., Slusher, B.S., et al. (2014). Pharmacological inhibition of cystine-glutamate exchange induces endoplasmic reticulum stress and ferroptosis. Elife *3*, e02523.

Doglioni, G., Parik, S., and Fendt, S.-M. (2019). Interactions in the (Pre)metastatic Niche Support

Metastasis Formation. Front. Oncol. *9*, 219.

Dolfi, S.C., Chan, L.L.-Y., Qiu, J., Tedeschi, P.M., Bertino, J.R., Hirshfield, K.M., Oltvai, Z.N., and Vazquez, A. (2013). The metabolic demands of cancer cells are coupled to their size and protein synthesis rates. Cancer Metab. *1*, 20.

Dolma, S., Lessnick, S.L., Hahn, W.C., and Stockwell, B.R. (2003). Identification of genotype-selective antitumor agents using synthetic lethal chemical screening in engineered human tumor cells. Cancer Cell *3*, 285–296.

Dong, C., Yuan, T., Wu, Y., Wang, Y., Fan, T.W.M., Miriyala, S., Lin, Y., Yao, J., Shi, J., Kang, T., et al. (2013). Loss of FBP1 by Snail-mediated repression provides metabolic advantages in basal-like breast cancer. Cancer Cell *23*, 316–331.

Dong, Y., Zhou, J., Zhu, Y., Luo, L., He, T., Hu, H., Liu, H., Zhang, Y., Luo, D., Xu, S., et al. (2017). Abdominal obesity and colorectal cancer risk: systematic review and meta-analysis of prospective studies. Biosci. Rep. *37*, 1–12.

Dongre, A., and Weinberg, R.A. (2019). New insights into the mechanisms of epithelial-mesenchymal transition and implications for cancer. Nat. Rev. Mol. Cell Biol. *20*, 69–84.

Donohoe, D.R., Garge, N., Zhang, X., Sun, W., O'Connell, T.M., Bunger, M.K., and Bultman, S.J. (2011). The microbiome and butyrate regulate energy metabolism and autophagy in the mammalian colon. Cell Metab. *13*, 517–526.

Donohoe, D.R., Wali, A., Brylawski, B.P., and Bultman, S.J. (2012). Microbial regulation of glucose metabolism and cell-cycle progression in mammalian colonocytes. PLoS One *7*, e46589.

Dornier, E., Rabas, N., Mitchell, L., Novo, D., Dhayade, S., Marco, S., Mackay, G., Sumpton, D., Pallares, M., Nixon, C., et al. (2017). Glutaminolysis drives membrane trafficking to promote invasiveness of breast cancer cells. Nat. Commun. *8*, 2255.

Druker, B.J., Tamura, S., Buchdunger, E., Ohno, S., Segal, G.M., Fanning, S., Zimmermann, J., and Lydon, N.B. (1996). Effects of a selective inhibitor of the Abl tyrosine kinase on the growth of Bcr-Abl positive cells. Nat. Med. *2*, 561–566.

Du, J., Yang, M., Chen, S., Li, D., Chang, Z., and Dong, Z. (2016). PDK1 promotes tumor growth and metastasis in a spontaneous breast cancer model. Oncogene *35*, 3314–3323.

Ducker, G.S., and Rabinowitz, J.D. (2017). One-Carbon Metabolism in Health and Disease. Cell Metab. *25*, 27–42.

Ducker, G.S., Ghergurovich, J.M., Mainolfi, N., Suri, V., Jeong, S.K., Hsin-Jung Li, S., Friedman, A., Manfredi, M.G., Gitai, Z., Kim, H., et al. (2017). Human SHMT inhibitors reveal defective glycine import as a targetable metabolic vulnerability of diffuse large B-cell lymphoma. Proc. Natl. Acad. Sci. U. S. A. *114*, 11404–11409.

Dupuy, F., Tabariès, S., Andrzejewski, S., Dong, Z., Blagih, J., Annis, M.G., Omeroglu, A., Gao, D., Leung, S., Amir, E., et al. (2015). PDK1-Dependent Metabolic Reprogramming Dictates Metastatic Potential in Breast Cancer. Cell Metab. *22*, 577–589.

Duranton, B., Holl, V., Schneider, Y., Carnesecchi, S., Gossé, F., Raul, F., and Seiler, N. (2003). Polyamine metabolism in primary human colon adenocarcinoma cells (SW480) and their lymph node metastatic derivatives (SW620). Amino Acids *24*, 63–72.

Duraturo, F., Liccardo, R., De Rosa, M., and Izzo, P. (2019). Genetics, diagnosis and treatment of Lynch syndrome: Old lessons and current challenges. Oncol. Lett. *17*, 3048–3054.

Eagle, H., Oyama, V.I., Levy, M., Horton, C.L., and Fleischman, R. (1956). The growth response of mammalian cells in tissue culture to L-glutamine and L-glutamic acid. J. Biol. Chem. *218*, 607–616.

Ebrahim, A., Lerman, J.A., Palsson, B.O., and Hyduke, D.R. (2013). COBRApy: COnstraints-Based Reconstruction and Analysis for Python. BMC Syst. Biol. *7*, 74.

Elia, I., Broekaert, D., Christen, S., Boon, R., Radaelli, E., Orth, M.F., Verfaillie, C., Grünewald, T.G.P., and Fendt, S.-M. (2017). Proline metabolism supports metastasis formation and could be inhibited to selectively target metastasizing cancer cells. Nat. Commun. *8*, 15267.

Elia, I., Rossi, M., Stegen, S., Broekaert, D., Doglioni, G., van Gorsel, M., Boon, R., Escalona-Noguero, C., Torrekens, S., Verfaillie, C., et al. (2019). Breast cancer cells rely on environmental pyruvate to shape the metastatic niche. Nature.

Erben, V., Bhardwaj, M., Schrotz-King, P., and Brenner, H. (2018). Metabolomics Biomarkers for Detection of Colorectal Neoplasms: A Systematic Review. Cancers (Basel). *10*.

Estrela, J.M., Ortega, A., Mena, S., Sirerol, J.A., and Obrador, E. (2016). Glutathione in metastases: From mechanisms to clinical applications. Crit. Rev. Clin. Lab. Sci. *53*, 253–267.

Falzone, L., Salomone, S., and Libra, M. (2018). Evolution of Cancer Pharmacological Treatments at the Turn of the Third Millennium. Front. Pharmacol. *9*, 1300.

Fan, J., Ye, J., Kamphorst, J.J., Shlomi, T., Thompson, C.B., and Rabinowitz, J.D. (2014). Quantitative flux analysis reveals folate-dependent NADPH production. Nature *510*, 298–302.

Farber, S., and Diamond, L.K. (1948). Temporary remissions in acute leukemia in children produced by folic acid antagonist, 4-aminopteroyl-glutamic acid. N. Engl. J. Med. *238*, 787–793.

Fares, J., Fares, M.Y., Khachfe, H.H., Salhab, H.A., and Fares, Y. (2020). Molecular principles of metastasis: a hallmark of cancer revisited. Signal Transduct. Target. Ther. *5*, 28.

Farshidfar, F., Weljie, A.M., Kopciuk, K.A., Hilsden, R., McGregor, S.E., Buie, W.D., MacLean, A., Vogel, H.J., and Bathe, O.F. (2016). A validated metabolomic signature for colorectal cancer: exploration of the clinical value of metabolomics. Br. J. Cancer *115*, 848–857.

Feng, J., Fu, Z., Guo, J., Lu, W., Wen, K., Chen, W., Wang, H., Wei, J., and Zhang, S. (2014). Overexpression of peroxiredoxin 2 inhibits TGF-β1-induced epithelial-mesenchymal transition and cell migration in colorectal cancer. Mol. Med. Rep. *10*, 867–873.

Ferlay, J., Ervik, M., Lam, F., Colombet, M., Mery, L., Piñeros, M., Znaor, A., Soerjomataram, I., and Bray, F. (2019). Global Cancer Observatory: Cancer Tomorrow.

Ferro, S., Azevedo-Silva, J., Casal, M., Côrte-Real, M., Baltazar, F., and Preto, A. (2016). Characterization of acetate transport in colorectal cancer cells and potential therapeutic implications. Oncotarget *7*, 70639–70653.

Fidler, I.J., and Poste, G. (2008). The “seed and soil” hypothesis revisited. Lancet. Oncol. *9*, 808.
Fidler, M.M., Soerjomataram, I., and Bray, F. (2016). A global view on cancer incidence and national levels of the human development index. Int. J. Cancer *139*, 2436–2446.

Finci, L., Zhang, Y., Meijers, R., and Wang, J.-H. (2015). Signaling mechanism of the netrin-1 receptor DCC in axon guidance. Prog. Biophys. Mol. Biol. *118*, 153–160.

Fodde, R., and Brabletz, T. (2007). Wnt/beta-catenin signaling in cancer stemness and malignant behavior. Curr. Opin. Cell Biol. *19*, 150–158.

Foguet, C., Marin, S., Selivanov, V.A., Fanchon, E., Lee, W.-N.P., Guinovart, J.J., de Atauri, P., and Cascante, M. (2016). HepatoDyn: A Dynamic Model of Hepatocyte Metabolism That Integrates 13C Isotopomer Data. PLOS Comput. Biol. *12*, e1004899.

Fong, M.Y., Zhou, W., Liu, L., Alontaga, A.Y., Chandra, M., Ashby, J., Chow, A., O'Connor, S.T.F., Li, S., Chin, A.R., et al. (2015). Breast-cancer-secreted miR-122 reprograms glucose metabolism in premetastatic niche to promote metastasis. Nat. Cell Biol. *17*, 183–194.

Fontana, E., Eason, K., Cervantes, A., Salazar, R., and Sadanandam, A. (2019). Context matters-consensus molecular subtypes of colorectal cancer as biomarkers for clinical trials. Ann. Oncol. Off. J. Eur. Soc. Med. Oncol. *30*, 520–527.

Frezza, C. (2020). Metabolism and cancer: the future is now. Br. J. Cancer *122*, 133–135.
Le Gal, K., Ibrahim, M.X., Wiel, C., Sayin, V.I., Akula, M.K., Karlsson, C., Dalin, M.G., Akyürek, L.M., Lindahl, P., Nilsson, J., et al. (2015). Antioxidants can increase melanoma metastasis in mice. Sci. Transl. Med. *7*, 308re8.

Garcia, M., Domènech, X., Vidal, C., Torné, E., Milà, N., Binefa, G., Benito, L., and Moreno, V. (2015). Interval cancers in a population-based screening program for colorectal cancer in catalonia, Spain. Gastroenterol. Res. Pract. *2015*, 672410.

Garibaldi, C., Jereczek-Fossa, B.A., Marvaso, G., Dicuonzo, S., Rojas, D.P., Cattani, F., Starzyńska, A., Ciardo, D., Surgo, A., Leonardi, M.C., et al. (2017). Recent advances in radiation oncology. Ecancermedicalscience *11*, 785.

Garza, D.R., Taddese, R., Wirbel, J., Zeller, G., Boleij, A., Huynen, M.A., and Dutilh, B.E. (2020). Metabolic models predict bacterial passengers in colorectal cancer. Cancer Metab. *8*, 3.

Gaude, E., and Frezza, C. (2016). Tissue-specific and convergent metabolic transformation of cancer correlates with metastatic potential and patient survival. Nat. Commun. *7*, 13041.

Ghosh, D., Yu, H., Tan, X.F., Lim, T.K., Zubaidah, R.M., Tan, H.T., Chung, M.C.M., and Lin, Q. (2011). Identification of key players for colorectal cancer metastasis by iTRAQ quantitative proteomics profiling of isogenic SW480 and SW620 cell lines. J. Proteome Res. *10*, 4373–4387.

Giannoni, E., Taddei, M.L., Morandi, A., Comito, G., Calvani, M., Bianchini, F., Richichi, B., Raugei, G., Wong, N., Tang, D., et al. (2015). Targeting stromal-induced pyruvate kinase M2 nuclear translocation impairs oxphos and prostate cancer metastatic spread. Oncotarget *6*, 24061–24074.

Gilman, A. (1946). Therapeutic applications of chemical warfare agents. Fed. Proc. *5*, 285–292.
Goetzman, E.S., and Prochownik, E. V. (2018). The Role for Myc in Coordinating Glycolysis, Oxidative Phosphorylation, Glutaminolysis, and Fatty Acid Metabolism in Normal and Neoplastic Tissues. Front. Endocrinol. (Lausanne). *9*, 129.

Golub, D., Iyengar, N., Dogra, S., Wong, T., Bready, D., Tang, K., Modrek, A.S., and Placantonakis, D.G. (2019). Mutant Isocitrate Dehydrogenase Inhibitors as Targeted Cancer Therapeutics. Front. Oncol. *9*, 417.

Gopal, S., Veracini, L., Grall, D., Butori, C., Schaub, S., Audebert, S., Camoin, L., Baudelet, E., Radwanska, A., Beghelli-de la Forest Divonne, S., et al. (2017). Fibronectin-guided migration of carcinoma collectives. Nat. Commun. *8*, 14105.

Gout, P.W., Kang, Y.J., Buckley, D.J., Bruchovsky, N., and Buckley, A.R. (1997). Increased cystine uptake capability associated with malignant progression of Nb2 lymphoma cells. Leukemia *11*, 1329–1337.

Gout, P.W., Buckley, A.R., Simms, C.R., and Bruchovsky, N. (2001). Sulfasalazine, a potent suppressor of lymphoma growth by inhibition of the x(c)- cystine transporter: a new action for an old drug. Leukemia *15*, 1633–1640.

Grassian, A.R., Metallo, C.M., Coloff, J.L., Stephanopoulos, G., and Brugge, J.S. (2011). Erk regulation of pyruvate dehydrogenase flux through PDK4 modulates cell proliferation. Genes Dev. *25*, 1716–1733.

Grassian, A.R., Lin, F., Barrett, R., Liu, Y., Jiang, W., Korpal, M., Astley, H., Gitterman, D., Henley, T., Howes, R., et al. (2012). Isocitrate dehydrogenase (IDH) mutations promote a reversible ZEB1/microRNA (miR)-200-dependent epithelial-mesenchymal transition (EMT). J. Biol. Chem. *287*, 42180–42194.

Gudmundsson, S., and Thiele, I. (2010). Computationally efficient flux variability analysis. BMC Bioinformatics *11*, 489.

Guerra, F., Guaragnella, N., Arbini, A.A., Bucci, C., Giannattasio, S., and Moro, L. (2017). Mitochondrial Dysfunction: A Novel Potential Driver of Epithelial-to-Mesenchymal Transition in Cancer. Front. Oncol. *7*, 295.

Guinney, J., Dienstmann, R., Wang, X., de Reyniès, A., Schlicker, A., Soneson, C., Marisa, L., Roepman, P., Nyamundanda, G., Angelino, P., et al. (2015). The consensus molecular subtypes of colorectal cancer. Nat. Med. *21*, 1350–1356.

Gunasinghe, N.P.A.D., Wells, A., Thompson, E.W., and Hugo, H.J. (2012). Mesenchymal-epithelial transition (MET) as a mechanism for metastatic colonisation in breast cancer. Cancer Metastasis Rev. *31*, 469–478.

Guo, J.Y., Teng, X., Laddha, S. V., Ma, S., Van Nostrand, S.C., Yang, Y., Khor, S., Chan, C.S., Rabinowitz, J.D., and White, E. (2016). Autophagy provides metabolic substrates to maintain energy charge and nucleotide pools in Ras-driven lung cancer cells. Genes Dev. *30*, 1704–1717.

Gupta, P.B., Fillmore, C.M., Jiang, G., Shapira, S.D., Tao, K., Kuperwasser, C., and Lander, E.S. (2011). Stochastic state transitions give rise to phenotypic equilibrium in populations of cancer cells. Cell *146*, 633–644.

Gustafsson, R., Jemth, A.-S., Gustafsson, N.M.S., Färnegårdh, K., Loseva, O., Wiita, E., Bonagas, N., Dahllund, L., Llona-Minguez, S., Häggblad, M., et al. (2017). Crystal Structure of the Emerging Cancer Target MTHFD2 in Complex with a Substrate-Based Inhibitor. Cancer Res. *77*, 937–948.

Halama, A., Guerrouahen, B.S., Pasquier, J., Diboun, I., Karoly, E.D., Suhre, K., and Rafii, A. (2015). Metabolic signatures differentiate ovarian from colon cancer cell lines. J. Transl. Med. *13*, 223.

Hamabe, A., Konno, M., Tanuma, N., Shima, H., Tsunekuni, K., Kawamoto, K., Nishida, N., Koseki, J., Mimori, K., Gotoh, N., et al. (2014). Role of pyruvate kinase M2 in transcriptional

regulation leading to epithelial-mesenchymal transition. Proc. Natl. Acad. Sci. U. S. A. *111*, 15526–15531.

Hamzehzadeh, L., Yousefi, M., and Ghaffari, S.-H. (2017). Colorectal Cancer Screening: A Comprehensive Review to Recent Non-Invasive Methods. Int. J. Hematol. Stem Cell Res. *11*, 250–261.

Hanahan, D., and Weinberg, R.A. (2000). The hallmarks of cancer. Cell *100*, 57–70.
Hanahan, D., and Weinberg, R.A. (2011). Hallmarks of cancer: the next generation. Cell *144*, 646–674.

Hausser, J., and Alon, U. (2020). Tumour heterogeneity and the evolutionary trade-offs of cancer. Nat. Rev. Cancer *20*, 247–257.

Hay, E.D. (2005). The mesenchymal cell, its role in the embryo, and the remarkable signaling mechanisms that create it. Dev. Dyn. *233*, 706–720.

Hayama, T., Hashiguchi, Y., Okamoto, K., Okada, Y., Ono, K., Shimada, R., Ozawa, T., Toyoda, T., Tsuchiya, T., Iinuma, H., et al. (2019). G12V and G12C mutations in the gene KRAS are associated with a poorer prognosis in primary colorectal cancer. Int. J. Colorectal Dis. *34*, 1491–1496.

Vander Heiden, M.G., Cantley, L.C., and Thompson, C.B. (2009). Understanding the Warburg effect: the metabolic requirements of cell proliferation. Science *324*, 1029–1033.

Heirendt, L., Arreckx, S., Pfau, T., Mendoza, S.N., Richelle, A., Heinken, A., Haraldsdóttir, H.S., Wachowiak, J., Keating, S.M., Vlasov, V., et al. (2019). Creation and analysis of biochemical constraint-based models using the COBRA Toolbox v.3.0. Nat. Protoc. *14*, 639–702.

Hewitt, R.E., McMarlin, A., Kleiner, D., Wersto, R., Martin, P., Tsokos, M., Stamp, G.W., Stetler-Stevenson, W.G., and Tsoskas, M. (2000). Validation of a model of colon cancer progression. J. Pathol. *192*, 446–454.

Ho, K. V., Solimando, D.A., and Waddell, J.A. (2015). Clofarabine and Cytarabine Regimen for Acute Myeloid Leukemia. Hosp. Pharm. *50*, 969–974.

Hoerner, C.R., Chen, V.J., and Fan, A.C. (2019). The "Achilles Heel" of Metabolism in Renal Cell Carcinoma: Glutaminase Inhibition as a Rational Treatment Strategy. Kidney Cancer (Clifton, Va.) *3*, 15–29.

Holmgren, A. (1977). Bovine thioredoxin system. Purification of thioredoxin reductase from calf liver and thymus and studies of its function in disulfide reduction. J. Biol. Chem. *252*, 4600–4606.
Hornsveld, M., and Dansen, T.B. (2016). The Hallmarks of Cancer from a Redox Perspective. Antioxid. Redox Signal. *25*, 300–325.

Horvay, K., Jardé, T., Casagranda, F., Perreau, V.M., Haigh, K., Nefzger, C.M., Akhtar, R., Gridley, T., Berx, G., Haigh, J.J., et al. (2015). Snai1 regulates cell lineage allocation and stem cell maintenance in the mouse intestinal epithelium. EMBO J. *34*, 1319–1335.

Hoxhaj, G., and Manning, B.D. (2020). The PI3K-AKT network at the interface of oncogenic signalling and cancer metabolism. Nat. Rev. Cancer *20*, 74–88.

Hsu, M.-C., and Hung, W.-C. (2018). Pyruvate kinase M2 fuels multiple aspects of cancer cells: from cellular metabolism, transcriptional regulation to extracellular signaling. Mol. Cancer *17*, 35.

Hsu, C.-C., Tseng, L.-M., and Lee, H.-C. (2016). Role of mitochondrial dysfunction in cancer progression. Exp. Biol. Med. (Maywood). *241*, 1281–1295.

Hugo, H.J., Gunasinghe, N.P.A.D., Hollier, B.G., Tanaka, T., Blick, T., Toh, A., Hill, P., Gilles, C., Waltham, M., and Thompson, E.W. (2017). Epithelial requirement for in vitro proliferation and xenograft growth and metastasis of MDA-MB-468 human breast cancer cells: oncogenic rather than tumor-suppressive role of E-cadherin. Breast Cancer Res. *19*, 86.

Izumi, H., Takahashi, M., Uramoto, H., Nakayama, Y., Oyama, T., Wang, K.-Y., Sasaguri, Y., Nishizawa, S., and Kohno, K. (2011). Monocarboxylate transporters 1 and 4 are involved in the invasion activity of human lung cancer cells. Cancer Sci. *102*, 1007–1013.

Jácome, A.A., and Eng, C. (2019). Role of immune checkpoint inhibitors in the treatment of colorectal cancer: focus on nivolumab. Expert Opin. Biol. Ther. *19*, 1247–1263.

Jain, M., Nilsson, R., Sharma, S., Madhusudhan, N., Kitami, T., Souza, A.L., Kafri, R., Kirschner, M.W., Clish, C.B., and Mootha, V.K. (2012). Metabolite profiling identifies a key role for glycine in rapid cancer cell proliferation. Science *336*, 1040–1044.

Jia, X.-Q., Zhang, S., Zhu, H.-J., Wang, W., Zhu, J.-H., Wang, X.-D., and Qiang, J.-F. (2016). Increased Expression of PHGDH and Prognostic Significance in Colorectal Cancer. Transl. Oncol. *9*, 191–196.

Jiang, L., Shestov, A.A., Swain, P., Yang, C., Parker, S.J., Wang, Q.A., Terada, L.S., Adams, N.D., McCabe, M.T., Pietrak, B., et al. (2016a). Reductive carboxylation supports redox homeostasis during anchorage-independent growth. Nature *532*, 255–258.

Jiang, L., Shestov, A.A., Swain, P., Yang, C., Parker, S.J., Wang, Q.A., Terada, L.S., Adams, N.D., McCabe, M.T., Pietrak, B., et al. (2016b). Reductive carboxylation supports redox homeostasis during anchorage-independent growth. Nature *532*, 255–258.

Jiang, P., Du, W., Mancuso, A., Wellen, K.E., and Yang, X. (2013). Reciprocal regulation of p53 and malic enzymes modulates metabolism and senescence. Nature *493*, 689–693.

Jiang, Y., Cao, Y., Wang, Y., Li, W., Liu, X., Lv, Y., Li, X., and Mi, J. (2017). Cysteine transporter SLC3A1 promotes breast cancer tumorigenesis. Theranostics *7*, 1036–1046.

Jin, L., Chun, J., Pan, C., Kumar, A., Zhang, G., Ha, Y., Li, D., Alesi, G.N., Kang, Y., Zhou, L., et al. (2018). The PLAG1-GDH1 Axis Promotes Anoikis Resistance and Tumor Metastasis through CamKK2-AMPK Signaling in LKB1-Deficient Lung Cancer. Mol. Cell *69*, 87-99.e7.

Jolly, M.K., Ware, K.E., Gilja, S., Somarelli, J.A., and Levine, H. (2017). EMT and MET: necessary or permissive for metastasis? Mol. Oncol. *11*, 755–769.

Joshi, S., Tolkunov, D., Aviv, H., Hakimi, A.A., Yao, M., Hsieh, J.J., Ganesan, S., Chan, C.S., and White, E. (2015). The Genomic Landscape of Renal Oncocytoma Identifies a Metabolic Barrier to Tumorigenesis. Cell Rep. *13*, 1895–1908.

Ju, H.-Q., Lu, Y.-X., Chen, D.-L., Zuo, Z.-X., Liu, Z.-X., Wu, Q.-N., Mo, H.-Y., Wang, Z.-X., Wang, D.-S., Pu, H.-Y., et al. (2018). Modulation of Redox Homeostasis by Inhibition of MTHFD2 in Colorectal Cancer: Mechanisms and Therapeutic Implications. J. Natl. Cancer Inst. *111*, 1–13.

Jung, B., Staudacher, J.J., and Beauchamp, D. (2017). Transforming Growth Factor β Superfamily

Signaling in Development of Colorectal Cancer. Gastroenterology *152*, 36–52.

Kamarajugadda, S., Stemboroski, L., Cai, Q., Simpson, N.E., Nayak, S., Tan, M., and Lu, J. (2012). Glucose oxidation modulates anoikis and tumor metastasis. Mol. Cell. Biol. *32*, 1893–1907.

Kamarudin, M.N.A., Sarker, M.M.R., Zhou, J.-R., and Parhar, I. (2019). Metformin in colorectal cancer: molecular mechanism, preclinical and clinical aspects. J. Exp. Clin. Cancer Res. *38*, 491.

Kamphorst, J.J., Cross, J.R., Fan, J., de Stanchina, E., Mathew, R., White, E.P., Thompson, C.B., and Rabinowitz, J.D. (2013). Hypoxic and Ras-transformed cells support growth by scavenging unsaturated fatty acids from lysophospholipids. Proc. Natl. Acad. Sci. U. S. A. *110*, 8882–8887.

Kapałczyńska, M., Kolenda, T., Przybyła, W., Zajączkowska, M., Teresiak, A., Filas, V., Ibbs, M., Bliźniak, R., Łuczewski, Ł., and Lamperska, K. (2018). 2D and 3D cell cultures - a comparison of different types of cancer cell cultures. Arch. Med. Sci. *14*, 910–919.

Kato, Y., Ozawa, S., Tsukuda, M., Kubota, E., Miyazaki, K., St-Pierre, Y., and Hata, R.-I. (2007). Acidic extracellular pH increases calcium influx-triggered phospholipase D activity along with acidic sphingomyelinase activation to induce matrix metalloproteinase-9 expression in mouse metastatic melanoma. FEBS J. *274*, 3171–3183.

Katzir, R., Polat, I.H., Harel, M., Katz, S., Foguet, C., Selivanov, V.A., Sabatier, P., Cascante, M., Geiger, T., and Ruppin, E. (2019). The landscape of tiered regulation of breast cancer cell metabolism. Sci. Rep. *9*, 17760.

Keum, N., and Giovannucci, E. (2019). Global burden of colorectal cancer: emerging trends, risk factors and prevention strategies. Nat. Rev. Gastroenterol. Hepatol. *16*, 713–732.

Khwairakpam, A.D., Shyamananda, M.S., Sailo, B.L., Rathnakaram, S.R., Padmavathi, G., Kotoky, J., and Kunnumakkara, A.B. (2015). ATP citrate lyase (ACLY): a promising target for cancer prevention and treatment. Curr. Drug Targets *16*, 156–163.

Kim, H.M., Jung, W.H., and Koo, J.S. (2014). Site-specific metabolic phenotypes in metastatic breast cancer. J. Transl. Med. *12*, 354.

Kim, J., Tchernyshyov, I., Semenza, G.L., and Dang, C. V. (2006). HIF-1-mediated expression of pyruvate dehydrogenase kinase: a metabolic switch required for cellular adaptation to hypoxia. Cell Metab. *3*, 177–185.

Kimmelman, A.C. (2015). Metabolic Dependencies in RAS-Driven Cancers. Clin. Cancer Res. *21*, 1828–1834.

Kinugasa, H., Whelan, K.A., Tanaka, K., Natsuizaka, M., Long, A., Guo, A., Chang, S., Kagawa, S., Srinivasan, S., Guha, M., et al. (2015). Mitochondrial SOD2 regulates epithelial-mesenchymal transition and cell populations defined by differential CD44 expression. Oncogene *34*, 5229–5239.

Knight, C., James, S., Kuntin, D., Fox, J., Newling, K., Hollings, S., Pennock, R., and Genever, P. (2019). Epidermal growth factor can signal via β-catenin to control proliferation of mesenchymal stem cells independently of canonical Wnt signalling. Cell. Signal. *53*, 256–268.

Knott, S.R. V, Wagenblast, E., Khan, S., Kim, S.Y., Soto, M., Wagner, M., Turgeon, M.-O., Fish, L., Erard, N., Gable, A.L., et al. (2018). Asparagine bioavailability governs metastasis in a model of breast cancer. Nature *554*, 378–381.

Koch, L. (2014). Cancer classification within tissues and beyond. Nat. Rev. Genet. *15*, 645–645.

Kolesnik, D.L., Pyaskovskaya, O.N., Boychuk, I. V, Dasyukevich, O.I., Melnikov, O.R., Tarasov, A.S., and Solyanik, G.I. (2015). Effect of dichloroacetate on Lewis lung carcinoma growth and metastasis. Exp. Oncol. *37*, 126–129.

Kong, D., Ahmad, A., Bao, B., Li, Y., Banerjee, S., and Sarkar, F.H. (2012). Histone deacetylase inhibitors induce epithelial-to-mesenchymal transition in prostate cancer cells. PLoS One *7*, e45045.

König, R., Chiang, C., Tu, B.P., Yan, S.F., DeJesus, P.D., Romero, A., Bergauer, T., Orth, A., Krueger, U., Zhou, Y., et al. (2007). A probability-based approach for the analysis of large-scale RNAi screens. Nat. Methods *4*, 847–849.

Kordes, S., Pollak, M.N., Zwinderman, A.H., Mathôt, R.A., Weterman, M.J., Beeker, A., Punt, C.J., Richel, D.J., and Wilmink, J.W. (2015). Metformin in patients with advanced pancreatic cancer: a double-blind, randomised, placebo-controlled phase 2 trial. Lancet. Oncol. *16*, 839–847.

Koufaris, C., Valbuena, G.N., Pomyen, Y., Tredwell, G.D., Nevedomskaya, E., Lau, C.-H., Yang, T., Benito, A., Ellis, J.K., and Keun, H.C. (2016). Systematic integration of molecular profiles identifies miR-22 as a regulator of lipid and folate metabolism in breast cancer cells. Oncogene *35*, 2766–2776.

Koundouros, N., and Poulogiannis, G. (2020). Reprogramming of fatty acid metabolism in cancer. Br. J. Cancer *122*, 4–22.

Koveitypour, Z., Panahi, F., Vakilian, M., Peymani, M., Seyed Forootan, F., Nasr Esfahani, M.H., and Ghaedi, K. (2019). Signaling pathways involved in colorectal cancer progression. Cell Biosci. *9*, 97.

Kreuzaler, P., Panina, Y., Segal, J., and Yuneva, M. (2019). Adapt and conquer: Metabolic flexibility in cancer growth, invasion and evasion. Mol. Metab. 1–19.

Kuo, C.-C., Ling, H.-H., Chiang, M.-C., Chung, C.-H., Lee, W.-Y., Chu, C.-Y., Wu, Y.-C., Chen, C.-H., Lai, Y.-W., Tsai, I.-L., et al. (2019). Metastatic Colorectal Cancer Rewrites Metabolic Program Through a Glut3-YAP-dependent Signaling Circuit. Theranostics *9*, 2526–2540.

Lacina, L., Čoma, M., Dvořánková, B., Kodet, O., Melegová, N., Gál, P., and Smetana, K. (2019). Evolution of Cancer Progression in the Context of Darwinism. Anticancer Res. *39*, 1–16.

Ladanyi, A., Mukherjee, A., Kenny, H.A., Johnson, A., Mitra, A.K., Sundaresan, S., Nieman, K.M., Pascual, G., Benitah, S.A., Montag, A., et al. (2018). Adipocyte-induced CD36 expression drives ovarian cancer progression and metastasis. Oncogene *37*, 2285–2301.

Lawson, D.A., Bhakta, N.R., Kessenbrock, K., Prummel, K.D., Yu, Y., Takai, K., Zhou, A., Eyob, H., Balakrishnan, S., Wang, C.-Y., et al. (2015). Single-cell analysis reveals a stem-cell program in human metastatic breast cancer cells. Nature *526*, 131–135.

LeBleu, V.S., O'Connell, J.T., Gonzalez Herrera, K.N., Wikman, H., Pantel, K., Haigis, M.C., de Carvalho, F.M., Damascena, A., Domingos Chinen, L.T., Rocha, R.M., et al. (2014). PGC-1α mediates mitochondrial biogenesis and oxidative phosphorylation in cancer cells to promote metastasis. Nat. Cell Biol. *16*, 992–1003, 1–15.

Lecarpentier, Y., Claes, V., Vallée, A., and Hébert, J.-L. (2017). Interactions between PPAR

Gamma and the Canonical Wnt/Beta-Catenin Pathway in Type 2 Diabetes and Colon Cancer. PPAR Res. *2017*, 5879090.

Lee, J.J., and Chu, E. (2018). The Adjuvant Treatment of Stage III Colon Cancer: Might Less Be More? Oncology (Williston Park). *32*.

Lee, C.-K., Jeong, S.-H., Jang, C., Bae, H., Kim, Y.H., Park, I., Kim, S.K., and Koh, G.Y. (2019). Tumor metastasis to lymph nodes requires YAP-dependent metabolic adaptation. Science *363*, 644–649.

Lee, J.-G., McKinney, K.Q., Pavlopoulos, A.J., Park, J.-H., and Hwang, S. (2015). Identification of anti-metastatic drug and natural compound targets in isogenic colorectal cancer cells. J. Proteomics *113*, 326–336.

Lee, S.Y., Jeon, H.M., Ju, M.K., Jeong, E.K., Kim, C.H., Park, H.G., Han, S.I., and Kang, H.S. (2016). Dlx-2 and glutaminase upregulate epithelial-mesenchymal transition and glycolytic switch. Oncotarget *7*, 7925–7939.

Leek, J.T., Johnson, W.E., Parker, H.S., Jaffe, A.E., and Storey, J.D. (2012). The sva package for removing batch effects and other unwanted variation in high-throughput experiments. Bioinformatics *28*, 882–883.

Lehuédé, C., Dupuy, F., Rabinovitch, R., Jones, R.G., and Siegel, P.M. (2016). Metabolic Plasticity as a Determinant of Tumor Growth and Metastasis. Cancer Res. *76*, 5201–5208.

Leibovitz, A., Stinson, J.C., McCombs, W.B., McCoy, C.E., Mazur, K.C., and Mabry, N.D. (1976). Classification of human colorectal adenocarcinoma cell lines. Cancer Res. *36*, 4562–4569.

Lemma, S., Di Pompo, G., Porporato, P.E., Sboarina, M., Russell, S., Gillies, R.J., Baldini, N., Sonveaux, P., and Avnet, S. (2017). MDA-MB-231 breast cancer cells fuel osteoclast metabolism and activity: A new rationale for the pathogenesis of osteolytic bone metastases. Biochim. Biophys. Acta. Mol. Basis Dis. *1863*, 3254–3264.

Lewerenz, J., Hewett, S.J., Huang, Y., Lambros, M., Gout, P.W., Kalivas, P.W., Massie, A., Smolders, I., Methner, A., Pergande, M., et al. (2013). The cystine/glutamate antiporter system x(c)(-) in health and disease: from molecular mechanisms to novel therapeutic opportunities. Antioxid. Redox Signal. *18*, 522–555.

Li, W., and Kang, Y. (2016). Probing the Fifty Shades of EMT in Metastasis. Trends in Cancer *2*, 65–67.

Li, C.-F., Fang, F.-M., Chen, Y.-Y., Liu, T.-T., Chan, T.-C., Yu, S.-C., Chen, L.-T., and Huang, H.-Y. (2017a). Overexpressed Fatty Acid Synthase in Gastrointestinal Stromal Tumors: Targeting a Progression-Associated Metabolic Driver Enhances the Antitumor Effect of Imatinib. Clin. Cancer Res. *23*, 4908–4918.

Li, E.-Q., Zhao, W., Zhang, C., Qin, L.-Z., Liu, S.-J., Feng, Z.-Q., Wen, X., and Chen, C.-P. (2019a). Synthesis and anti-cancer activity of ND-646 and its derivatives as acetyl-CoA carboxylase 1 inhibitors. Eur. J. Pharm. Sci. *137*, 105010.

Li, H., Zhang, X., Jin, Z., Yin, T., Duan, C., Sun, J., Xiong, R., and Li, Z. (2019b). MiR-122 Promotes the Development of Colon Cancer by Targeting ALDOA In Vitro. Technol. Cancer Res. Treat. *18*.

Li, X., Jiang, Z., Feng, J., Zhang, X., Wu, J., and Chen, W. (2017b). 2-Acetylamino-3-[4-(2-acetylamino-2-carboxyethylsulfanylcarbonylamino) phenyl carbamoylsulfanyl] propionic acid, a glutathione reductase inhibitor, induces G2/M cell cycle arrest through generation of thiol oxidative stress in human esophageal cancer cell. Oncotarget *8*, 61846–61860.

Liberti, M. V., and Locasale, J.W. (2016). The Warburg Effect: How Does it Benefit Cancer Cells? Trends Biochem. Sci. *41*, 211–218.

Lim, J.K.M., Delaidelli, A., Minaker, S.W., Zhang, H.-F., Colovic, M., Yang, H., Negri, G.L., von Karstedt, S., Lockwood, W.W., Schaffer, P., et al. (2019). Cystine/glutamate antiporter xCT (SLC7A11) facilitates oncogenic RAS transformation by preserving intracellular redox balance. Proc. Natl. Acad. Sci. U. S. A. *116*, 9433–9442.

Liu, G., Zhu, J., Yu, M., Cai, C., Zhou, Y., Yu, M., Fu, Z., Gong, Y., Yang, B., Li, Y., et al. (2015). Glutamate dehydrogenase is a novel prognostic marker and predicts metastases in colorectal cancer patients. J. Transl. Med. *13*, 144.

Liu, J., Gao, L., Zhang, H., Wang, D., Wang, M., Zhu, J., Pang, C., and Wang, C. (2013). Succinate dehydrogenase 5 (SDH5) regulates glycogen synthase kinase 3β-β-catenin-mediated lung cancer metastasis. J. Biol. Chem. *288*, 29965–29973.

Liu, N., Lin, X., and Huang, C. (2019). Activation of the reverse transsulfuration pathway through NRF2/CBS confers erastin-induced ferroptosis resistance. Br. J. Cancer.

Liu, W., Fang, Y., Wang, X.-T., Liu, J., Dan, X., and Sun, L.-L. (2014). Overcoming 5-Fu resistance of colon cells through inhibition of Glut1 by the specific inhibitor WZB117. Asian Pac. J. Cancer Prev. *15*, 7037–7041.

Lo, H.C., and Zhang, X.H.-F. (2018). EMT in Metastasis: Finding the Right Balance. Dev. Cell *45*, 663–665.

Lo, M., Ling, V., Wang, Y.Z., and Gout, P.W. (2008). The xc- cystine/glutamate antiporter: a mediator of pancreatic cancer growth with a role in drug resistance. Br. J. Cancer *99*, 464–472.

Lo, M., Ling, V., Low, C., Wang, Y.Z., and Gout, P.W. (2010). Potential use of the anti-inflammatory drug, sulfasalazine, for targeted therapy of pancreatic cancer. Curr. Oncol. *17*, 9–16.

Locasale, J.W. (2013). Serine, glycine and one-carbon units: cancer metabolism in full circle. Nat. Rev. Cancer *13*, 572–583.

Locasale, J.W., and Cantley, L.C. (2011). Metabolic flux and the regulation of mammalian cell growth. Cell Metab. *14*, 443–451.

Locasale, J.W., Grassian, A.R., Melman, T., Lyssiotis, C.A., Mattaini, K.R., Bass, A.J., Heffron, G., Metallo, C.M., Muranen, T., Sharfi, H., et al. (2011). Phosphoglycerate dehydrogenase diverts glycolytic flux and contributes to oncogenesis. Nat. Genet. *43*, 869–874.

Loo, J.M., Scherl, A., Nguyen, A., Man, F.Y., Weinberg, E., Zeng, Z., Saltz, L., Paty, P.B., and Tavazoie, S.F. (2015). Extracellular metabolic energetics can promote cancer progression. Cell *160*, 393–406.

López-López, Á., López-Gonzálvez, Á., Barker-Tejeda, T.C., and Barbas, C. (2018). A review of validated biomarkers obtained through metabolomics. Expert Rev. Mol. Diagn. *18*, 557–575.

López-Luque, J., Bertran, E., Crosas-Molist, E., Maiques, O., Malfettone, A., Caja, L., Serrano, T., Ramos, E., Sanz-Moreno, V., and Fabregat, I. (2019). Downregulation of Epidermal Growth Factor Receptor in hepatocellular carcinoma facilitates Transforming Growth Factor-β-induced epithelial to amoeboid transition. Cancer Lett. *464*, 15–24.

Lu, C., Ward, P.S., Kapoor, G.S., Rohle, D., Turcan, S., Abdel-Wahab, O., Edwards, C.R., Khanin, R., Figueroa, M.E., Melnick, A., et al. (2012). IDH mutation impairs histone demethylation and results in a block to cell differentiation. Nature *483*, 474–478.

Luengo, A., Gui, D.Y., and Vander Heiden, M.G. (2017). Targeting Metabolism for Cancer Therapy. Cell Chem. Biol. *24*, 1161–1180.

Luo, C., Lim, J.-H., Lee, Y., Granter, S.R., Thomas, A., Vazquez, F., Widlund, H.R., and Puigserver, P. (2016). A PGC1α-mediated transcriptional axis suppresses melanoma metastasis. Nature *537*, 422–426.

Luo, X., Cheng, C., Tan, Z., Li, N., Tang, M., Yang, L., and Cao, Y. (2017). Emerging roles of lipid metabolism in cancer metastasis. Mol. Cancer *16*, 76.

Luong-Gardiol, N., Siddiqui, I., Pizzitola, I., Jeevan-Raj, B., Charmoy, M., Huang, Y., Irmisch, A., Curtet, S., Angelov, G.S., Danilo, M., et al. (2019). γ-Catenin-Dependent Signals Maintain BCR-ABL1+ B Cell Acute Lymphoblastic Leukemia. Cancer Cell *35*, 649-663.e10.

Lv, L., Li, D., Zhao, D., Lin, R., Chu, Y., Zhang, H., Zha, Z., Liu, Y., Li, Z., Xu, Y., et al. (2011). Acetylation Targets the M2 Isoform of Pyruvate Kinase for Degradation through Chaperone-Mediated Autophagy and Promotes Tumor Growth. Mol. Cell *42*, 719–730.

Lyssiotis, C.A., and Kimmelman, A.C. (2017). Metabolic Interactions in the Tumor Microenvironment. Trends Cell Biol. *27*, 863–875.

Ma, M.-Z., Chen, G., Wang, P., Lu, W., Zhu, C., Song, M., Yang, J., Wen, S., Xu, R.-H., Hu, Y., et al. (2015). Xc- inhibitor sulfasalazine sensitizes colorectal cancer to cisplatin by a GSH-dependent mechanism. Cancer Lett. *368*, 88–96.

Maamer-Azzabi, a, Ndozangue-Touriguine, O., and Bréard, J. (2013). Metastatic SW620 colon cancer cells are primed for death when detached and can be sensitized to anoikis by the BH3-mimetic ABT-737. Cell Death Dis. *4*, e801.

Macrae, F.A., and Bendell, J. (2020). Clinical manifestations, diagnosis, and staging of colorectal cancer. UpToDate 1–10.

Maddocks, O.D.K., Berkers, C.R., Mason, S.M., Zheng, L., Blyth, K., Gottlieb, E., and Vousden, K.H. (2013). Serine starvation induces stress and p53-dependent metabolic remodelling in cancer cells. Nature *493*, 542–546.

Maddocks, O.D.K., Athineos, D., Cheung, E.C., Lee, P., Zhang, T., van den Broek, N.J.F., Mackay, G.M., Labuschagne, C.F., Gay, D., Kruiswijk, F., et al. (2017). Modulating the therapeutic response of tumours to dietary serine and glycine starvation. Nature *544*, 372–376.

Martínez-Reyes, I., and Chandel, N.S. (2020). Mitochondrial TCA cycle metabolites control physiology and disease. Nat. Commun. *11*, 102.

Mashimo, T., Pichumani, K., Vemireddy, V., Hatanpaa, K.J., Singh, D.K., Sirasanagandla, S., Nannepaga, S., Piccirillo, S.G., Kovacs, Z., Foong, C., et al. (2014). Acetate is a bioenergetic substrate for human glioblastoma and brain metastases. Cell *159*, 1603–1614.

Masoud, G.N., and Li, W. (2015). HIF-1α pathway: role, regulation and intervention for cancer therapy. Acta Pharm. Sin. B *5*, 378–389.

Matsuda, T., Yamashita, K., Hasegawa, H., Oshikiri, T., Hosono, M., Higashino, N., Yamamoto, M., Matsuda, Y., Kanaji, S., Nakamura, T., et al. (2018). Recent updates in the surgical treatment of colorectal cancer. Ann. Gastroenterol. Surg. *2*, 129–136.

Mattaini, K.R., Sullivan, M.R., and Vander Heiden, M.G. (2016). The importance of serine metabolism in cancer. J. Cell Biol. *214*, 249–257.

McDonald, E.R., de Weck, A., Schlabach, M.R., Billy, E., Mavrakis, K.J., Hoffman, G.R., Belur, D., Castelletti, D., Frias, E., Gampa, K., et al. (2017a). Project DRIVE: A Compendium of Cancer Dependencies and Synthetic Lethal Relationships Uncovered by Large-Scale, Deep RNAi Screening. Cell *170*, 577-592.e10.

McDonald, O.G., Li, X., Saunders, T., Tryggvadottir, R., Mentch, S.J., Warmoes, M.O., Word, A.E., Carrer, A., Salz, T.H., Natsume, S., et al. (2017b). Epigenomic reprogramming during pancreatic cancer progression links anabolic glucose metabolism to distant metastasis. Nat. Genet. *49*, 367–376.

McFate, T., Mohyeldin, A., Lu, H., Thakar, J., Henriques, J., Halim, N.D., Wu, H., Schell, M.J., Tsang, T.M., Teahan, O., et al. (2008). Pyruvate dehydrogenase complex activity controls metabolic and malignant phenotype in cancer cells. J. Biol. Chem. *283*, 22700–22708.

Meiser, J., Tumanov, S., Maddocks, O., Labuschagne, C.F., Athineos, D., Van Den Broek, N., Mackay, G.M., Gottlieb, E., Blyth, K., Vousden, K., et al. (2016). Serine one-carbon catabolism with formate overflow. Sci. Adv. *2*, e1601273.

Méndez-Lucas, A., Lin, W., Driscoll, P.C., Legrave, N., Novellasdemunt, L., Xie, C., Charles, M., Wilson, Z., Jones, N.P., Rayport, S., et al. (2020). Identifying strategies to target the metabolic flexibility of tumours. Nat. Metab. *2*, 335–350.

Meric-Bernstam, F., Lee, R.J., Carthon, B.C., Iliopoulos, O., Mier, J.W., Patel, M.R., Tannir, N.M., Owonikoko, T.K., Haas, N.B., Voss, M.H., et al. (2019). CB-839, a glutaminase inhibitor, in combination with cabozantinib in patients with clear cell and papillary metastatic renal cell cancer (mRCC): Results of a phase I study. J. Clin. Oncol. *37*, 549–549.

Mielgo, A., and Schmid, M.C. (2020). Liver Tropism in Cancer: The Hepatic Metastatic Niche. Cold Spring Harb. Perspect. Med. *10*.

Mittal, V. (2018). Epithelial Mesenchymal Transition in Tumor Metastasis. Annu. Rev. Pathol. *13*, 395–412.

Miyo, M., Konno, M., Nishida, N., Sueda, T., Noguchi, K., Matsui, H., Colvin, H., Kawamoto, K., Koseki, J., Haraguchi, N., et al. (2016). Metabolic Adaptation to Nutritional Stress in Human Colorectal Cancer. Sci. Rep. *6*, 38415.

Mizukami, T., Izawa, N., Nakajima, T.E., and Sunakawa, Y. (2019). Targeting EGFR and RAS/RAF Signaling in the Treatment of Metastatic Colorectal Cancer: From Current Treatment Strategies to Future Perspectives. Drugs *79*, 633–645.

Morandi, A., Taddei, M.L., Chiarugi, P., and Giannoni, E. (2017). Targeting the Metabolic Reprogramming That Controls Epithelial-to-Mesenchymal Transition in Aggressive Tumors. Front. Oncol. *7*, 40.

Moss, S., Mathews, C., Day, T.J., Smith, S., Seaman, H.E., Snowball, J., and Halloran, S.P. (2017). Increased uptake and improved outcomes of bowel cancer screening with a faecal immunochemical test: results from a pilot study within the national screening programme in England. Gut *66*, 1631–1644.

Moyer, M.P., Manzano, L.A., Merriman, R.L., Stauffer, J.S., and Tanzer, L.R. (1996). NCM460, a normal human colon mucosal epithelial cell line. In Vitro Cell. Dev. Biol. Anim. *32*, 315–317.

Muir, B., and Nunney, L. (2015). The expression of tumour suppressors and proto-oncogenes in tissues susceptible to their hereditary cancers. Br. J. Cancer *113*, 345–353.

Mullen, A.R., Wheaton, W.W., Jin, E.S., Chen, P.-H., Sullivan, L.B., Cheng, T., Yang, Y., Linehan, W.M., Chandel, N.S., and DeBerardinis, R.J. (2011). Reductive carboxylation supports growth in tumour cells with defective mitochondria. Nature *481*, 385–388.

Munir, R., Lisec, J., Swinnen, J. V, and Zaidi, N. (2019). Lipid metabolism in cancer cells under metabolic stress. Br. J. Cancer *120*, 1090–1098.

Murai, S., Ando, A., Ebara, S., Hirayama, M., Satomi, Y., and Hara, T. (2017). Inhibition of malic enzyme 1 disrupts cellular metabolism and leads to vulnerability in cancer cells in glucose-restricted conditions. Oncogenesis *6*, e329.

Muthu, M., and Nordström, A. (2019). Current Status and Future Prospects of Clinically Exploiting Cancer-specific Metabolism-Why Is Tumor Metabolism Not More Extensively Translated into Clinical Targets and Biomarkers? Int. J. Mol. Sci. *20*, 1385.

Nagane, M., Kanai, E., Shibata, Y., Shimizu, T., Yoshioka, C., Maruo, T., and Yamashita, T. (2018). Sulfasalazine, an inhibitor of the cystine-glutamate antiporter, reduces DNA damage repair and enhances radiosensitivity in murine B16F10 melanoma. PLoS One *13*, e0195151.

Naik, E., and Dixit, V.M. (2011). Mitochondrial reactive oxygen species drive proinflammatory cytokine production. J. Exp. Med. *208*, 417–420.

Nath, A., and Chan, C. (2016). Genetic alterations in fatty acid transport and metabolism genes are associated with metastatic progression and poor prognosis of human cancers. Sci. Rep. *6*, 18669.

Naxerova, K., Reiter, J.G., Brachtel, E., Lennerz, J.K., van de Wetering, M., Rowan, A., Cai, T., Clevers, H., Swanton, C., Nowak, M.A., et al. (2017). Origins of lymphatic and distant metastases in human colorectal cancer. Science (80-.). *357*, 55–60.

Neman, J., Termini, J., Wilczynski, S., Vaidehi, N., Choy, C., Kowolik, C.M., Li, H., Hambrecht, A.C., Roberts, E., and Jandial, R. (2014). Human breast cancer metastases to the brain display GABAergic properties in the neural niche. Proc. Natl. Acad. Sci. U. S. A. *111*, 984–989.

Nguyen, H.T., and Duong, H.-Q. (2018). The molecular characteristics of colorectal cancer: Implications for diagnosis and therapy. Oncol. Lett. *16*, 9–18.

Nieto, M.A., Huang, R.Y.-J., Jackson, R.A., and Thiery, J.P. (2016). EMT: 2016. Cell *166*, 21–45.

Nilsson, A., and Nielsen, J. (2017). Genome scale metabolic modeling of cancer. Metab. Eng. *43*, 103–112.

Nilsson, R., Jain, M., Madhusudhan, N., Sheppard, N.G., Strittmatter, L., Kampf, C., Huang, J.,

Asplund, A., and Mootha, V.K. (2014). Metabolic enzyme expression highlights a key role for MTHFD2 and the mitochondrial folate pathway in cancer. Nat. Commun. *5*, 3128.

Ning, S., Ma, S., Saleh, A.Q., Guo, L., Zhao, Z., and Chen, Y. (2018). SHMT2 Overexpression Predicts Poor Prognosis in Intrahepatic Cholangiocarcinoma. Gastroenterol. Res. Pract. *2018*, 1–6.

Nishimura, T., Nakata, A., Chen, X., Nishi, K., Meguro-Horike, M., Sasaki, S., Kita, K., Horike, S.-I., Saitoh, K., Kato, K., et al. (2019). Cancer stem-like properties and gefitinib resistance are dependent on purine synthetic metabolism mediated by the mitochondrial enzyme MTHFD2. Oncogene *38*, 2464–2481.

Noack, S., Nöh, K., Moch, M., Oldiges, M., and Wiechert, W. (2011). Stationary versus non-stationary (13)C-MFA: a comparison using a consistent dataset. J. Biotechnol. *154*, 179–190.

Novellasdemunt, L., Antas, P., and Li, V.S.W. (2015). Targeting Wnt signaling in colorectal cancer. A Review in the Theme: Cell Signaling: Proteins, Pathways and Mechanisms. Am. J. Physiol. - Cell Physiol. *309*, C511–C521.

Nunes, A.S., Barros, A.S., Costa, E.C., Moreira, A.F., and Correia, I.J. (2019). 3D tumor spheroids as in vitro models to mimic in vivo human solid tumors resistance to therapeutic drugs. Biotechnol. Bioeng. *116*, 206–226.

Oballa, R.M., Belair, L., Black, W.C., Bleasby, K., Chan, C.C., Desroches, C., Du, X., Gordon, R., Guay, J., Guiral, S., et al. (2011). Development of a liver-targeted stearoyl-CoA desaturase (SCD) inhibitor (MK-8245) to establish a therapeutic window for the treatment of diabetes and dyslipidemia. J. Med. Chem. *54*, 5082–5096.

Obenauf, A.C., and Massagué, J. (2015). Surviving at a Distance: Organ-Specific Metastasis. Trends in Cancer *1*, 76–91.

Oki, E., Ando, K., Nakanishi, R., Sugiyama, M., Nakashima, Y., Kubo, N., Kudou, K., Saeki, H., Nozoe, T., Emi, Y., et al. (2018). Recent advances in treatment for colorectal liver metastasis. Ann. Gastroenterol. Surg. *2*, 167–175.

Olivares, O., Mayers, J.R., Gouirand, V., Torrence, M.E., Gicquel, T., Borge, L., Lac, S., Roques, J., Lavaut, M.-N., Berthezène, P., et al. (2017). Collagen-derived proline promotes pancreatic ductal adenocarcinoma cell survival under nutrient limited conditions. Nat. Commun. *8*, 16031.

Orhan, H., and Aktaş Uygun, D. (2020). Immobilization of L-Asparaginase on Magnetic Nanoparticles for Cancer Treatment. Appl. Biochem. Biotechnol.

Ortega, A.L., Carretero, J., Obrador, E., Gambini, J., Asensi, M., Rodilla, V., and Estrela, J.M. (2003). Tumor cytotoxicity by endothelial cells. Impairment of the mitochondrial system for glutathione uptake in mouse B16 melanoma cells that survive after in vitro interaction with the hepatic sinusoidal endothelium. J. Biol. Chem. *278*, 13888–13897.

Orth, J.D., Thiele, I., and Palsson, B.Ø. (2010). What is flux balance analysis? Nat. Biotechnol. *28*, 245–248.

Oskarsson, T., Batlle, E., and Massagué, J. (2014). Metastatic stem cells: sources, niches, and vital pathways. Cell Stem Cell *14*, 306–321.

Padmanaban, V., Krol, I., Suhail, Y., Szczerba, B.M., Aceto, N., Bader, J.S., and Ewald, A.J. (2019). E-cadherin is required for metastasis in multiple models of breast cancer. Nature *324*,

297–314.

Pakiet, A., Kobiela, J., Stepnowski, P., Sledzinski, T., and Mika, A. (2019). Changes in lipids composition and metabolism in colorectal cancer: a review. Lipids Health Dis. *18*, 29.

Palen, K., Weber, J., Dwinell, M.B., Johnson, B.D., Ramchandran, R., and Gershan, J.A. (2016). E-cadherin re-expression shows in vivo evidence for mesenchymal to epithelial transition in clonal metastatic breast tumor cells. Oncotarget *7*, 43363–43375.

Pan, X., Lin, Z., Jiang, D., Yu, Y., Yang, D., Zhou, H., Zhan, D., Liu, S., Peng, G., Chen, Z., et al. (2019). Erastin decreases radioresistance of NSCLC cells partially by inducing GPX4-mediated ferroptosis. Oncol. Lett. *17*, 3001–3008.

Panieri, E., and Santoro, M.M. (2016). ROS homeostasis and metabolism: a dangerous liason in cancer cells. Cell Death Dis. *7*, e2253.

Paoli, P., Giannoni, E., and Chiarugi, P. (2013). Anoikis molecular pathways and its role in cancer progression. Biochim. Biophys. Acta *1833*, 3481–3498.

Paone, A., Marani, M., Fiascarelli, A., Rinaldo, S., Giardina, G., Contestabile, R., Paiardini, A., and Cutruzzolà, F. (2014). SHMT1 knockdown induces apoptosis in lung cancer cells by causing uracil misincorporation. Cell Death Dis. *5*, e1525.

Papadatos-Pastos, D., Rabbie, R., Ross, P., and Sarker, D. (2015). The role of the PI3K pathway in colorectal cancer. Crit. Rev. Oncol. Hematol. *94*, 18–30.

Papandreou, I., Cairns, R.A., Fontana, L., Lim, A.L., and Denko, N.C. (2006). HIF-1 mediates adaptation to hypoxia by actively downregulating mitochondrial oxygen consumption. Cell Metab. *3*, 187–197.

Park, S.Y., Lee, S.-J., Cho, H.J., Kim, T.W., Kim, J.-T., Kim, J.W., Lee, C.-H., Kim, B.-Y., Yeom, Y. Il, Lim, J.-S., et al. (2016). Dehydropeptidase 1 promotes metastasis through regulation of E-cadherin expression in colon cancer. Oncotarget *7*, 9501–9512.

Park, S.Y., Shin, J.-H., and Kee, S.-H. (2017). E-cadherin expression increases cell proliferation by regulating energy metabolism through nuclear factor-κB in AGS cells. Cancer Sci. *108*, 1769–1777.

Pascual, G., Avgustinova, A., Mejetta, S., Martín, M., Castellanos, A., Attolini, C.S.-O., Berenguer, A., Prats, N., Toll, A., Hueto, J.A., et al. (2017). Targeting metastasis-initiating cells through the fatty acid receptor CD36. Nature *541*, 41–45.

Pastushenko, I., and Blanpain, C. (2019). EMT Transition States during Tumor Progression and Metastasis. Trends Cell Biol. *29*, 212–226.

Pate, K.T., Stringari, C., Sprowl-Tanio, S., Wang, K., TeSlaa, T., Hoverter, N.P., McQuade, M.M., Garner, C., Digman, M.A., Teitell, M.A., et al. (2014). Wnt signaling directs a metabolic program of glycolysis and angiogenesis in colon cancer. EMBO J. *33*, 1454–1473.

Patel, S.G., and Ahnen, D.J. (2012). Familial colon cancer syndromes: an update of a rapidly evolving field. Curr. Gastroenterol. Rep. *14*, 428–438.

Patel, M.S., Nemeria, N.S., Furey, W., and Jordan, F. (2014). The pyruvate dehydrogenase complexes: structure-based function and regulation. J. Biol. Chem. *289*, 16615–16623.

Pattabiraman, D.R., and Weinberg, R.A. (2014). Tackling the cancer stem cells - what challenges do they pose? Nat. Rev. Drug Discov. *13*, 497–512.

Pavlova, N.N., and Thompson, C.B. (2016). The Emerging Hallmarks of Cancer Metabolism. Cell Metab. *23*, 27–47.

Pavlova, N.N., Hui, S., Ghergurovich, J.M., Fan, J., Intlekofer, A.M., White, R.M., Rabinowitz, J.D., Thompson, C.B., and Zhang, J. (2018). As Extracellular Glutamine Levels Decline, Asparagine Becomes an Essential Amino Acid. Cell Metab. *27*, 428-438.e5.

Pena-Couso, L., Perea, J., Melo, S., Mercadillo, F., Figueiredo, J., Sanches, J.M., Sánchez-Ruiz, A., Robles, L., Seruca, R., and Urioste, M. (2018). Clinical and functional characterization of the CDH1 germline variant c.1679C>G in three unrelated families with hereditary diffuse gastric cancer. Eur. J. Hum. Genet. *26*, 1348–1353.

Pento, J.T. (2017). Monoclonal Antibodies for the Treatment of Cancer. Anticancer Res. *37*, 5935–5939.

Phang, J.M., Liu, W., Hancock, C.N., and Fischer, J.W. (2015). Proline metabolism and cancer: emerging links to glutamine and collagen. Curr. Opin. Clin. Nutr. Metab. Care *18*, 71–77.

Pikman, Y., Puissant, A., Alexe, G., Furman, A., Chen, L.M., Frumm, S.M., Ross, L., Fenouille, N., Bassil, C.F., Lewis, C.A., et al. (2016). Targeting MTHFD2 in acute myeloid leukemia. J. Exp. Med. *213*, 1285–1306.

Piskounova, E., Agathocleous, M., Murphy, M.M., Hu, Z., Huddlestun, S.E., Zhao, Z., Leitch, A.M., Johnson, T.M., DeBerardinis, R.J., and Morrison, S.J. (2015). Oxidative stress inhibits distant metastasis by human melanoma cells. Nature *527*, 186–191.

Plawski, A., Banasiewicz, T., Borun, P., Kubaszewski, L., Krokowicz, P., Skrzypczak-Zielinska, M., and Lubinski, J. (2013). Familial adenomatous polyposis of the colon. Hered. Cancer Clin. Pract. *11*, 15.

Pollari, S., Käkönen, S.-M., Edgren, H., Wolf, M., Kohonen, P., Sara, H., Guise, T., Nees, M., and Kallioniemi, O. (2011). Enhanced serine production by bone metastatic breast cancer cells stimulates osteoclastogenesis. Breast Cancer Res. Treat. *125*, 421–430.

Porporato, P.E., and Sonveaux, P. (2015). Paving the way for therapeutic prevention of tumor metastasis with agents targeting mitochondrial superoxide. Mol. Cell. Oncol. *2*, e968043.

Porporato, P.E., Payen, V.L., Pérez-Escuredo, J., De Saedeleer, C.J., Danhier, P., Copetti, T., Dhup, S., Tardy, M., Vazeille, T., Bouzin, C., et al. (2014). A mitochondrial switch promotes tumor metastasis. Cell Rep. *8*, 754–766.

Porru, M., Pompili, L., Caruso, C., Biroccio, A., and Leonetti, C. (2018). Targeting KRAS in metastatic colorectal cancer: current strategies and emerging opportunities. J. Exp. Clin. Cancer Res. *37*, 57.

Prabhu, A., Sarcar, B., Kahali, S., Yuan, Z., Johnson, J.J., Adam, K.P., Kensicki, E., and Chinnaiyan, P. (2014). Cysteine catabolism: A novel metabolic pathway contributing to glioblastoma growth. Cancer Res. *74*, 787–796.

Prager, B.C., Xie, Q., Bao, S., and Rich, J.N. (2019). Cancer Stem Cells: The Architects of the Tumor Ecosystem. Cell Stem Cell *24*, 41–53.

Pratapa, A., Balachandran, S., and Raman, K. (2015). Fast-SL: an efficient algorithm to identify synthetic lethal sets in metabolic networks. Bioinformatics *31*, 3299–3305.

Pretzsch, E., Bösch, F., Neumann, J., Ganschow, P., Bazhin, A., Guba, M., Werner, J., and Angele, M. (2019). Mechanisms of Metastasis in Colorectal Cancer and Metastatic Organotropism: Hematogenous versus Peritoneal Spread. J. Oncol. *2019*, 7407190.

Primo, L.M.F., and Teixeira, L.K. (2019). DNA replication stress: oncogenes in the spotlight. Genet. Mol. Biol. *43*, e20190138.

Provenzani, A., Fronza, R., Loreni, F., Pascale, A., Amadio, M., and Quattrone, A. (2006). Global alterations in mRNA polysomal recruitment in a cell model of colorectal cancer progression to metastasis. Carcinogenesis *27*, 1323–1333.

Puppa, G., Sonzogni, A., Colombari, R., and Pelosi, G. (2010). TNM staging system of colorectal carcinoma: a critical appraisal of challenging issues. Arch. Pathol. Lab. Med. *134*, 837–852.

Qi, L., Sun, B., Liu, Z., Cheng, R., Li, Y., and Zhao, X. (2014). Wnt3a expression is associated with epithelial-mesenchymal transition and promotes colon cancer progression. J. Exp. Clin. Cancer Res. *33*, 107.

Qie, S., Yoshida, A., Parnham, S., Oleinik, N., Beeson, G.C., Beeson, C.C., Ogretmen, B., Bass, A.J., Wong, K.-K., Rustgi, A.K., et al. (2019). Targeting glutamine-addiction and overcoming CDK4/6 inhibitor resistance in human esophageal squamous cell carcinoma. Nat. Commun. *10*, 1296.

de Queiroz, R.M., Oliveira, I.A., Piva, B., Bouchuid Catão, F., da Costa Rodrigues, B., da Costa Pascoal, A., Diaz, B.L., Todeschini, A.R., Caarls, M.B., and Dias, W.B. (2019). Hexosamine Biosynthetic Pathway and Glycosylation Regulate Cell Migration in Melanoma Cells. Front. Oncol. *9*, 116.

Radomski, M.W., Jenkins, D.C., Holmes, L., and Moncada, S. (1991). Human colorectal adenocarcinoma cells: differential nitric oxide synthesis determines their ability to aggregate platelets. Cancer Res. *51*, 6073–6078.

Rahmathulla, G., Toms, S.A., and Weil, R.J. (2012). The molecular biology of brain metastasis. J. Oncol. *2012*, 723541.

Raimondi, V., Ciccarese, F., and Ciminale, V. (2019). Oncogenic pathways and the electron transport chain: a dangeROS liaison. Br. J. Cancer.

Ray, A., Song, Y., Du, T., Chauhan, D., and Anderson, K.C. (2020). Preclinical validation of Alpha-Enolase (ENO1) as a novel immunometabolic target in multiple myeloma. Oncogene *39*, 2786–2796.

Reichert, M., Bakir, B., Moreira, L., Pitarresi, J.R., Feldmann, K., Simon, L., Suzuki, K., Maddipati, R., Rhim, A.D., Schlitter, A.M., et al. (2018). Regulation of Epithelial Plasticity Determines Metastatic Organotropism in Pancreatic Cancer. Dev. Cell *45*, 696-711.e8.

Reimers, A.-M., and Reimers, A.C. (2016). The steady-state assumption in oscillating and growing systems. J. Theor. Biol. *406*, 176–186.

Riester, M., Wu, H.-J., Zehir, A., Gönen, M., Moreira, A.L., Downey, R.J., and Michor, F. (2017). Distance in cancer gene expression from stem cells predicts patient survival. PLoS One *12*, e0173589.

Riihimäki, M., Hemminki, A., Sundquist, J., and Hemminki, K. (2016). Patterns of metastasis in colon and rectal cancer. Sci. Rep. *6*, 29765.

Rodrigues, M.F., Obre, E., de Melo, F.H.M., Santos, G.C., Galina, A., Jasiulionis, M.G., Rossignol, R., Rumjanek, F.D., and Amoêdo, N.D. (2016). Enhanced OXPHOS, glutaminolysis and β-oxidation constitute the metastatic phenotype of melanoma cells. Biochem. J. *473*, 703–715.

von Roemeling, C.A., Marlow, L.A., Wei, J.J., Cooper, S.J., Caulfield, T.R., Wu, K., Tan, W.W., Tun, H.W., and Copland, J.A. (2013). Stearoyl-CoA desaturase 1 is a novel molecular therapeutic target for clear cell renal cell carcinoma. Clin. Cancer Res. *19*, 2368–2380.

Rohani, N., Hao, L., Alexis, M.S., Joughin, B.A., Krismer, K., Moufarrej, M.N., Soltis, A.R., Lauffenburger, D.A., Yaffe, M.B., Burge, C.B., et al. (2019). Acidification of Tumor at Stromal Boundaries Drives Transcriptome Alterations Associated with Aggressive Phenotypes. Cancer Res. *79*, 1952–1966.

Rossi, M., Jahanzaib Anwar, M., Usman, A., Keshavarzian, A., and Bishehsari, F. (2018). Colorectal Cancer and Alcohol Consumption-Populations to Molecules. Cancers (Basel). *10*.

Rozhin, J., Sameni, M., Ziegler, G., and Sloane, B.F. (1994). Pericellular pH affects distribution and secretion of cathepsin B in malignant cells. Cancer Res. *54*, 6517–6525.

Sabnis, A.J., and Bivona, T.G. (2019). Principles of Resistance to Targeted Cancer Therapy: Lessons from Basic and Translational Cancer Biology. Trends Mol. Med. *25*, 185–197.

Saitoh, M. (2018). Involvement of partial EMT in cancer progression. J. Biochem. *164*, 257–264.

Salem, A.F., Whitaker-Menezes, D., Howell, A., Sotgia, F., and Lisanti, M.P. (2012). Mitochondrial biogenesis in epithelial cancer cells promotes breast cancer tumor growth and confers autophagy resistance. Cell Cycle *11*, 4174–4180.

Sánchez-Martínez, R., Cruz-Gil, S., Gómez de Cedrón, M., Álvarez-Fernández, M., Vargas, T., Molina, S., García, B., Herranz, J., Moreno-Rubio, J., Reglero, G., et al. (2015). A link between lipid metabolism and epithelial-mesenchymal transition provides a target for colon cancer therapy. Oncotarget *6*, 38719–38736.

Sandberg, T.P., Stuart, M.P.M.E., Oosting, J., Tollenaar, R.A.E.M., Sier, C.F.M., and Mesker, W.E. (2019). Increased expression of cancer-associated fibroblast markers at the invasive front and its association with tumor-stroma ratio in colorectal cancer. BMC Cancer *19*, 284.

Sanderson, S.M., Gao, X., Dai, Z., and Locasale, J.W. (2019). Methionine metabolism in health and cancer: a nexus of diet and precision medicine. Nat. Rev. Cancer *19*, 625–637.

De Santo, C., Cheng, P., Beggs, A., Egan, S., Bessudo, A., and Mussai, F. (2018). Metabolic therapy with PEG-arginase induces a sustained complete remission in immunotherapy-resistant melanoma. J. Hematol. Oncol. *11*, 68.

Sanz-Pamplona, R., Berenguer, A., Cordero, D., Molleví, D.G., Crous-Bou, M., Sole, X., Paré-Brunet, L., Guino, E., Salazar, R., Santos, C., et al. (2014). Aberrant gene expression in mucosa adjacent to tumor reveals a molecular crosstalk in colon cancer. Mol. Cancer *13*, 46.

Sappington, D.R., Siegel, E.R., Hiatt, G., Desai, A., Penney, R.B., Jamshidi-Parsian, A., Griffin, R.J., and Boysen, G. (2016). Glutamine drives glutathione synthesis and contributes to radiation

sensitivity of A549 and H460 lung cancer cell lines. Biochim. Biophys. Acta *1860*, 836–843.

Saraei, P., Asadi, I., Kakar, M.A., and Moradi-Kor, N. (2019). The beneficial effects of metformin on cancer prevention and therapy: a comprehensive review of recent advances. Cancer Manag. Res. *11*, 3295–3313.

Sato, M., Kusumi, R., Hamashima, S., Kobayashi, S., Sasaki, S., Komiyama, Y., Izumikawa, T., Conrad, M., Bannai, S., and Sato, H. (2018). The ferroptosis inducer erastin irreversibly inhibits system xc- and synergizes with cisplatin to increase cisplatin's cytotoxicity in cancer cells. Sci. Rep. *8*, 968.

Satoh, K., Yachida, S., Sugimoto, M., Oshima, M., Nakagawa, T., Akamoto, S., Tabata, S., Saitoh, K., Kato, K., Sato, S., et al. (2017). Global metabolic reprogramming of colorectal cancer occurs at adenoma stage and is induced by MYC. Proc. Natl. Acad. Sci. U. S. A. *114*, E7697–E7706.

Savaskan, N.E., Heckel, A., Hahnen, E., Engelhorn, T., Doerfler, A., Ganslandt, O., Nimsky, C., Buchfelder, M., and Eyüpoglu, I.Y. (2008). Small interfering RNA-mediated xCT silencing in gliomas inhibits neurodegeneration and alleviates brain edema. Nat. Med. *14*, 629–632.

Saxton, R.A., and Sabatini, D.M. (2017). mTOR Signaling in Growth, Metabolism, and Disease. Cell *168*, 960–976.

Sayin, V.I., LeBoeuf, S.E., Singh, S.X., Davidson, S.M., Biancur, D., Guzelhan, B.S., Alvarez, S.W., Wu, W.L., Karakousi, T.R., Zavitsanou, A.M., et al. (2017). Activation of the NRF2 antioxidant program generates an imbalance in central carbon metabolism in cancer. Elife *6*, 1–23.

Sbodio, J.I., Snyder, S.H., and Paul, B.D. (2019). Regulators of the transsulfuration pathway. Br. J. Pharmacol. *176*, 583–593.

Scalise, M., Pochini, L., Galluccio, M., Console, L., and Indiveri, C. (2017). Glutamine Transport and Mitochondrial Metabolism in Cancer Cell Growth. Front. Oncol. *7*, 306.

Sceneay, J., Smyth, M.J., and Möller, A. (2013). The pre-metastatic niche: finding common ground. Cancer Metastasis Rev. *32*, 449–464.

Schafer, Z.T., Grassian, A.R., Song, L., Jiang, Z., Gerhart-Hines, Z., Irie, H.Y., Gao, S., Puigserver, P., and Brugge, J.S. (2009). Antioxidant and oncogene rescue of metabolic defects caused by loss of matrix attachment. Nature *461*, 109–113.

Schmidt, A., Wu, H., MacKenzie, R.E., Chen, V.J., Bewly, J.R., Ray, J.E., Toth, J.E., and Cygler, M. (2000). Structures of three inhibitor complexes provide insight into the reaction mechanism of the human methylenetetrahydrofolate dehydrogenase/cyclohydrolase. Biochemistry *39*, 6325–6335.

Schmidt, B.J., Ebrahim, A., Metz, T.O., Adkins, J.N., Palsson, B.Ø., and Hyduke, D.R. (2013). GIM3E: condition-specific models of cellular metabolism developed from metabolomics and expression data. Bioinformatics *29*, 2900–2908.

Schmukler, E., Kloog, Y., and Pinkas-Kramarski, R. (2014). Ras and autophagy in cancer development and therapy. Oncotarget *5*, 577–586.

Schneider, G., Schmidt-Supprian, M., Rad, R., and Saur, D. (2017). Tissue-specific tumorigenesis: context matters. Nat. Rev. Cancer *17*, 239–253.

Sdelci, S., Rendeiro, A.F., Rathert, P., You, W., Lin, J.-M.G., Ringler, A., Hofstätter, G., Moll, H.P., Gürtl, B., Farlik, M., et al. (2019). MTHFD1 interaction with BRD4 links folate metabolism to transcriptional regulation. Nat. Genet. *51*, 990–998.

Seefeldt, T., Zhao, Y., Chen, W., Raza, A.S., Carlson, L., Herman, J., Stoebner, A., Hanson, S., Foll, R., and Guan, X. (2009). Characterization of a novel dithiocarbamate glutathione reductase inhibitor and its use as a tool to modulate intracellular glutathione. J. Biol. Chem. *284*, 2729–2737.

Segrè, D., Vitkup, D., and Church, G.M. (2002). Analysis of optimality in natural and perturbed metabolic networks. Proc. Natl. Acad. Sci. U. S. A. *99*, 15112–15117.

Seidel, J.A., Otsuka, A., and Kabashima, K. (2018). Anti-PD-1 and Anti-CTLA-4 Therapies in Cancer: Mechanisms of Action, Efficacy, and Limitations. Front. Oncol. *8*, 86.

Selivanov, V.A., Benito, A., Miranda, A., Aguilar, E., Polat, I.H., Centelles, J.J., Jayaraman, A., Lee, P.W.N.N., Marin, S., and Cascante, M. (2017). MIDcor, an R-program for deciphering mass interferences in mass spectra of metabolites enriched in stable isotopes. BMC Bioinformatics *18*, 88.

Selivanov, V.A., Marin, S., Tarragó-Celada, J., Lane, A.N., Higashi, R.M., Fan, T.W.M., de Atauri, P., and Cascante, M. (2020). Software supporting a workflow of quantitative dynamic flux maps estimation in central metabolism from SIRM experimental data. In Methods in Molecular Biology, (Humana Press Inc.), pp. 271–298.

Semenza, G.L. (2013). HIF-1 mediates metabolic responses to intratumoral hypoxia and oncogenic mutations. J. Clin. Invest. *123*, 3664–3671.

Serra, J.M., Gutiérrez, A., Alemany, R., Navarro, M., Ros, T., Saus, C., Ginés, J., Sampol, A., Amat, J.C., Serra-Moisés, L., et al. (2008). Inhibition of c-Myc down-regulation by sustained extracellular signal-regulated kinase activation prevents the antimetabolite methotrexate- and gemcitabine-induced differentiation in non-small-cell lung cancer cells. Mol. Pharmacol. *73*, 1679–1687.

Seth Nanda, C., Venkateswaran, S.V., Patani, N., and Yuneva, M. (2019). Defining a metabolic landscape of tumours: genome meets metabolism. Br. J. Cancer.

Seward, E. (2019). Recent advances in colonoscopy. F1000Research *8*, 1028.

Shaw, E., Farris, M.S., Stone, C.R., Derksen, J.W.G., Johnson, R., Hilsden, R.J., Friedenreich, C.M., and Brenner, D.R. (2018). Effects of physical activity on colorectal cancer risk among family history and body mass index subgroups: a systematic review and meta-analysis. BMC Cancer *18*, 71.

Sheikh, K., Förster, J., and Nielsen, L.K. (2005). Modeling hybridoma cell metabolism using a generic genome-scale metabolic model of Mus musculus. Biotechnol. Prog. *21*, 112–121.

Shelton, L.M., Huysentruyt, L.C., and Seyfried, T.N. (2010). Glutamine targeting inhibits systemic metastasis in the VM-M3 murine tumor model. Int. J. Cancer *127*, 2478–2485.

Sheng, S.L., Liu, J.J., Dai, Y.H., Sun, X.G., Xiong, X.P., and Huang, G. (2012). Knockdown of lactate dehydrogenase A suppresses tumor growth and metastasis of human hepatocellular carcinoma. FEBS J. *279*, 3898–3910.

Shibata, M., and Hoque, M.O. (2019). Targeting Cancer Stem Cells: A Strategy for Effective Eradication of Cancer. Cancers (Basel). *11*.

Shibue, T., and Weinberg, R.A. (2017). EMT, CSCs, and drug resistance: the mechanistic link and clinical implications. Nat. Rev. Clin. Oncol. *14*, 611–629.

Shim, E.-H., Livi, C.B., Rakheja, D., Tan, J., Benson, D., Parekh, V., Kho, E.-Y., Ghosh, A.P., Kirkman, R., Velu, S., et al. (2014). L-2-Hydroxyglutarate: an epigenetic modifier and putative oncometabolite in renal cancer. Cancer Discov. *4*, 1290–1298.

Shima, H., Matsumoto, M., Ishigami, Y., Ebina, M., Muto, A., Sato, Y., Kumagai, S., Ochiai, K., Suzuki, T., and Igarashi, K. (2017). S-Adenosylmethionine Synthesis Is Regulated by Selective N6-Adenosine Methylation and mRNA Degradation Involving METTL16 and YTHDC1. Cell Rep. *21*, 3354–3363.

Shin, M., Momb, J., and Appling, D.R. (2017). Human mitochondrial MTHFD2 is a dual redox cofactor-specific methylenetetrahydrofolate dehydrogenase/methenyltetrahydrofolate cyclohydrolase. Cancer Metab. *5*, 2–7.

Shin, S.-S., Jeong, B.-S., Wall, B.A., Li, J., Shan, N.L., Wen, Y., Goydos, J.S., and Chen, S. (2018). Participation of xCT in melanoma cell proliferation in vitro and tumorigenesis in vivo. Oncogenesis *7*, 86.

Shinde, A., Wilmanski, T., Chen, H., Teegarden, D., and Wendt, M.K. (2018). Pyruvate carboxylase supports the pulmonary tropism of metastatic breast cancer. Breast Cancer Res. *20*, 76.

Shlomi, T., Benyamini, T., Gottlieb, E., Sharan, R., and Ruppin, E. (2011). Genome-scale metabolic modeling elucidates the role of proliferative adaptation in causing the Warburg effect. PLoS Comput. Biol. *7*, e1002018.

Siegel, R.L., Miller, K.D., Goding Sauer, A., Fedewa, S.A., Butterly, L.F., Anderson, J.C., Cercek, A., Smith, R.A., and Jemal, A. (2020). Colorectal cancer statistics, 2020. CA. Cancer J. Clin.

Singh, R., Fouladi-Nashta, A.A., Li, D., Halliday, N., Barrett, D.A., and Sinclair, K.D. (2006). Methotrexate induced differentiation in colon cancer cells is primarily due to purine deprivation. J. Cell. Biochem. *99*, 146–155.

Siravegna, G., and Bardelli, A. (2016). Blood circulating tumor DNA for non-invasive genotyping of colon cancer patients. Mol. Oncol. *10*, 475–480.

Slavov, N., Budnik, B.A., Schwab, D., Airoldi, E.M., and van Oudenaarden, A. (2014). Constant growth rate can be supported by decreasing energy flux and increasing aerobic glycolysis. Cell Rep. *7*, 705–714.

Sleire, L., Skeie, B.S., Netland, I.A., Førde, H.E., Dodoo, E., Selheim, F., Leiss, L., Heggdal, J.I., Pedersen, P.-H., Wang, J., et al. (2015). Drug repurposing: sulfasalazine sensitizes gliomas to gamma knife radiosurgery by blocking cystine uptake through system Xc-, leading to glutathione depletion. Oncogene *34*, 5951–5959.

De Smedt, L., Lemahieu, J., Palmans, S., Govaere, O., Tousseyn, T., Van Cutsem, E., Prenen, H., Tejpar, S., Spaepen, M., Matthijs, G., et al. (2015). Microsatellite instable vs stable colon carcinomas: analysis of tumour heterogeneity, inflammation and angiogenesis. Br. J. Cancer *113*, 500–509.

Sottnik, J.L., Lori, J.C., Rose, B.J., and Thamm, D.H. (2011). Glycolysis inhibition by 2-deoxy-D-glucose reverts the metastatic phenotype in vitro and in vivo. Clin. Exp. Metastasis *28*, 865–875.

Soussi, T., and Wiman, K.G. (2015). TP53: an oncogene in disguise. Cell Death Differ. *22*, 1239–1249.

de Souza, L.F., Schmitz, A.E., da Silva, L.C.S., de Oliveira, K.A., Nedel, C.B., Tasca, C.I., de Bem, A.F., Farina, M., and Dafre, A.L. (2017). Inhibition of reductase systems by 2-AAPA modulates peroxiredoxin oxidation and mitochondrial function in A172 glioblastoma cells. Toxicol. In Vitro *42*, 273–280.

Sprowl-Tanio, S., Habowski, A.N., Pate, K.T., McQuade, M.M., Wang, K., Edwards, R.A., Grun, F., Lyou, Y., and Waterman, M.L. (2016). Lactate/pyruvate transporter MCT-1 is a direct Wnt target that confers sensitivity to 3-bromopyruvate in colon cancer. Cancer Metab. *4*, 20.

Stankic, M., Pavlovic, S., Chin, Y., Brogi, E., Padua, D., Norton, L., Massagué, J., and Benezra, R. (2013). TGF-β-Id1 signaling opposes Twist1 and promotes metastatic colonization via a mesenchymal-to-epithelial transition. Cell Rep. *5*, 1228–1242.

Still, E.R., and Yuneva, M.O. (2017). Hopefully devoted to Q: targeting glutamine addiction in cancer. Br. J. Cancer *116*, 1375–1381.

Stresing, V., Baltziskueta, E., Rubio, N., Blanco, J., Arriba, M.C., Valls, J., Janier, M., Clézardin, P., Sanz-Pamplona, R., Nieva, C., et al. (2013). Peroxiredoxin 2 specifically regulates the oxidative and metabolic stress response of human metastatic breast cancer cells in lungs. Oncogene *32*, 724–735.

Strilic, B., and Offermanns, S. (2017). Intravascular Survival and Extravasation of Tumor Cells. Cancer Cell *32*, 282–293.

Strul, H., and Arber, N. (2007). Screening techniques for prevention and early detection of colorectal cancer in the average-risk population. Gastrointest. Cancer Res. *1*, 98–106.

Sun, R.C., Fadia, M., Dahlstrom, J.E., Parish, C.R., Board, P.G., and Blackburn, A.C. (2010). Reversal of the glycolytic phenotype by dichloroacetate inhibits metastatic breast cancer cell growth in vitro and in vivo. Breast Cancer Res. Treat. *120*, 253–260.

Sun, Y., Zheng, Y., Wang, C., and Liu, Y. (2018). Glutathione depletion induces ferroptosis, autophagy, and premature cell senescence in retinal pigment epithelial cells. Cell Death Dis. *9*, 753.

Suzuki, A., Maeda, T., Baba, Y., Shimamura, K., and Kato, Y. (2014). Acidic extracellular pH promotes epithelial mesenchymal transition in Lewis lung carcinoma model. Cancer Cell Int. *14*, 129.

Swainston, N., Smallbone, K., Hefzi, H., Dobson, P.D., Brewer, J., Hanscho, M., Zielinski, D.C., Ang, K.S., Gardiner, N.J., Gutierrez, J.M., et al. (2016). Recon 2.2: from reconstruction to model of human metabolism. Metabolomics *12*, 109.

Al Tameemi, W., Dale, T.P., Al-Jumaily, R.M.K., and Forsyth, N.R. (2019). Hypoxia-Modified Cancer Cell Metabolism. Front. Cell Dev. Biol. *7*, 4.

Tanner, J.J., Fendt, S.-M., and Becker, D.F. (2018). The Proline Cycle As a Potential Cancer

Therapy Target. Biochemistry *57*, 3433–3444.

Tarrado-Castellarnau, M., de Atauri, P., Tarragó-Celada, J., Perarnau, J., Yuneva, M., Thomson, T.M., and Cascante, M. (2017). De novo MYC addiction as an adaptive response of cancer cells to CDK4/6 inhibition. Mol. Syst. Biol. *13*, 940.

Teeuwssen, M., and Fodde, R. (2019). Cell Heterogeneity and Phenotypic Plasticity in Metastasis Formation: The Case of Colon Cancer. Cancers (Basel). *11*.

Terunuma, A., Putluri, N., Mishra, P., Mathé, E.A., Dorsey, T.H., Yi, M., Wallace, T.A., Issaq, H.J., Zhou, M., Killian, J.K., et al. (2014). MYC-driven accumulation of 2-hydroxyglutarate is associated with breast cancer prognosis. J. Clin. Invest. *124*, 398–412.

Tichet, M., Prod'Homme, V., Fenouille, N., Ambrosetti, D., Mallavialle, A., Cerezo, M., Ohanna, M., Audebert, S., Rocchi, S., Giacchero, D., et al. (2015). Tumour-derived SPARC drives vascular permeability and extravasation through endothelial VCAM1 signalling to promote metastasis. Nat. Commun. *6*, 6993.

Tietze, F., Bradley, K.H., and Schulman, J.D. (1972). Enzymic reduction of cystine by subcellular fractions of cultured and peripheral leukocytes from normal and cystinotic individuals. Pediatr. Res. *6*, 649–658.

Tomlinson, I.P.M., Alam, N.A., Rowan, A.J., Barclay, E., Jaeger, E.E.M., Kelsell, D., Leigh, I., Gorman, P., Lamlum, H., Rahman, S., et al. (2002). Germline mutations in FH predispose to dominantly inherited uterine fibroids, skin leiomyomata and papillary renal cell cancer. Nat. Genet. *30*, 406–410.

Torrano, V., Valcarcel-Jimenez, L., Cortazar, A.R., Liu, X., Urosevic, J., Castillo-Martin, M., Fernández-Ruiz, S., Morciano, G., Caro-Maldonado, A., Guiu, M., et al. (2016). The metabolic co-regulator PGC1α suppresses prostate cancer metastasis. Nat. Cell Biol. *18*, 645–656.

Tracz-Gaszewska, Z., and Dobrzyn, P. (2019). Stearoyl-CoA Desaturase 1 as a Therapeutic Target for the Treatment of Cancer. Cancers (Basel). *11*.

Traverso, N., Ricciarelli, R., Nitti, M., Marengo, B., Furfaro, A.L., Pronzato, M.A., Marinari, U.M., and Domenicotti, C. (2013). Role of glutathione in cancer progression and chemoresistance. Oxid. Med. Cell. Longev. *2013*, 972913.

Tsai, W.-S., Chen, J.-S., Shao, H.-J., Wu, J.-C., Lai, J.-M., Lu, S.-H., Hung, T.-F., Chiu, Y.-C., You, J.-F., Hsieh, P.-S., et al. (2016). Circulating Tumor Cell Count Correlates with Colorectal Neoplasm Progression and Is a Prognostic Marker for Distant Metastasis in Non-Metastatic Patients. Sci. Rep. *6*, 24517.

Unterrainer, M., Eze, C., Ilhan, H., Marschner, S., Roengvoraphoj, O., Schmidt-Hegemann, N.S., Walter, F., Kunz, W.G., Rosenschöld, P.M. af, Jeraj, R., et al. (2020). Recent advances of PET imaging in clinical radiation oncology. Radiat. Oncol. *15*, 88.

Urosevic, J., Garcia-Albéniz, X., Planet, E., Real, S., Céspedes, M.V., Guiu, M., Fernandez, E., Bellmunt, A., Gawrzak, S., Pavlovic, M., et al. (2014). Colon cancer cells colonize the lung from established liver metastases through p38 MAPK signalling and PTHLH. Nat. Cell Biol. *16*, 685–694.

Vafa, O., Wade, M., Kern, S., Beeche, M., Pandita, T.K., Hampton, G.M., and Wahl, G.M. (2002). c-Myc can induce DNA damage, increase reactive oxygen species, and mitigate p53 function: a mechanism for oncogene-induced genetic instability. Mol. Cell *9*, 1031–1044.

La Vecchia, S., and Sebastián, C. (2020). Metabolic pathways regulating colorectal cancer

initiation and progression. Semin. Cell Dev. Biol. *98*, 63–70.

Vergara, D., Stanca, E., Guerra, F., Priore, P., Gaballo, A., Franck, J., Simeone, P., Trerotola, M., De Domenico, S.D., Fournier, I., et al. (2017). B-Catenin Knockdown Affects Mitochondrial Biogenesis and Lipid Metabolism in Breast Cancer Cells. Front. Physiol. *8*, 1–17.

Vettore, L., Westbrook, R.L., and Tennant, D.A. (2020). New aspects of amino acid metabolism in cancer. Br. J. Cancer *122*, 150–156.

Vinson, K.E., George, D.C., Fender, A.W., Bertrand, F.E., and Sigounas, G. (2016). The Notch pathway in colorectal cancer. Int. J. Cancer *138*, 1835–1842.

Voorhees, P.M., Schlossman, R.L., Gasparetto, C.J., Berdeja, J.G., Morris, J., Jacobstein, D.A., Anderson, K.C., Mitsiades, C.S., Laubach, J.P., and Richardson, P.G. (2014). An Open-Label, Dose Escalation, Multi-Center Phase 1 Study of PRLX 93936, an Agent Synthetically Active Against the Activated Ras Pathway, in the Treatment of Relapsed or Relapsed and Refractory Multiple Myeloma. Blood *124*, 2140–2140.

Vučetić, M., Cormerais, Y., Parks, S.K., and Pouysségur, J. (2017). The Central Role of Amino Acids in Cancer Redox Homeostasis: Vulnerability Points of the Cancer Redox Code. Front. Oncol. *7*, 319.

Walther, J.L., Metallo, C.M., Zhang, J., and Stephanopoulos, G. (2012). Optimization of13C isotopic tracers for metabolic flux analysis in mammalian cells. Metab. Eng. *14*, 162–171.

Wang, H., Yu, C., Gao, X., Welte, T., Muscarella, A.M., Tian, L., Zhao, H., Zhao, Z., Du, S., Tao, J., et al. (2015). The osteogenic niche promotes early-stage bone colonization of disseminated breast cancer cells. Cancer Cell *27*, 193–210.

Wang, L.-H., Wu, C.-F., Rajasekaran, N., and Shin, Y.K. (2018a). Loss of Tumor Suppressor Gene Function in Human Cancer: An Overview. Cell. Physiol. Biochem. *51*, 2647–2693.

Wang, Q., Liberti, M. V., Liu, P., Deng, X., Liu, Y., Locasale, J.W., and Lai, L. (2017a). Rational Design of Selective Allosteric Inhibitors of PHGDH and Serine Synthesis with Anti-tumor Activity. Cell Chem. Biol. *24*, 55–65.

Wang, Y.-N., Zeng, Z.-L., Lu, J., Wang, Y., Liu, Z.-X., He, M.-M., Zhao, Q., Wang, Z.-X., Li, T., Lu, Y.-X., et al. (2018b). CPT1A-mediated fatty acid oxidation promotes colorectal cancer cell metastasis by inhibiting anoikis. Oncogene *37*, 6025–6040.

Wang, Y.-P., Zhou, L.-S., Zhao, Y.-Z., Wang, S.-W., Chen, L.-L., Liu, L.-X., Ling, Z.-Q., Hu, F.-J., Sun, Y.-P., Zhang, J.-Y., et al. (2014). Regulation of G6PD acetylation by SIRT2 and KAT9 modulates NADPH homeostasis and cell survival during oxidative stress. EMBO J. *33*, 1304–1320.

Wang, Y., Sun, Z., and Szyf, M. (2017b). S-adenosyl-methionine (SAM) alters the transcriptome and methylome and specifically blocks growth and invasiveness of liver cancer cells. Oncotarget *8*, 111866–111881.

Warburg, O. (1925). The metabolism of carcinoma cells. J. Cancer Res. *9*, 148–163.

Warburg, O. (1956). On the origin of cancer cells. Science *123*, 309–314.

Watt, M.J., Clark, A.K., Selth, L.A., Haynes, V.R., Lister, N., Rebello, R., Porter, L.H., Niranjan, B., Whitby, S.T., Lo, J., et al. (2019). Suppressing fatty acid uptake has therapeutic effects in

preclinical models of prostate cancer. Sci. Transl. Med. *11*.

Weinberg, F., Hamanaka, R., Wheaton, W.W., Weinberg, S., Joseph, J., Lopez, M., Kalyanaraman, B., Mutlu, G.M., Budinger, G.R.S., and Chandel, N.S. (2010). Mitochondrial metabolism and ROS generation are essential for Kras-mediated tumorigenicity. Proc. Natl. Acad. Sci. U. S. A. *107*, 8788–8793.

Wellner, U., Schubert, J., Burk, U.C., Schmalhofer, O., Zhu, F., Sonntag, A., Waldvogel, B., Vannier, C., Darling, D., zur Hausen, A., et al. (2009). The EMT-activator ZEB1 promotes tumorigenicity by repressing stemness-inhibiting microRNAs. Nat. Cell Biol. *11*, 1487–1495.

Wen, D., Liu, D., Tang, J., Dong, L., Liu, Y., Tao, Z., Wan, J., Gao, D., Wang, L., Sun, H., et al. (2015). Malic enzyme 1 induces epithelial-mesenchymal transition and indicates poor prognosis in hepatocellular carcinoma. Tumour Biol. *36*, 6211–6221.

Wendt, M.K., Williams, W.K., Pascuzzi, P.E., Balanis, N.G., Schiemann, B.J., Carlin, C.R., and Schiemann, W.P. (2015). The antitumorigenic function of EGFR in metastatic breast cancer is regulated by expression of Mig6. Neoplasia *17*, 124–133.

Whillier, S., Raftos, J.E., Chapman, B., and Kuchel, P.W. (2009). Role of N-acetylcysteine and cystine in glutathione synthesis in human erythrocytes. Redox Rep. *14*, 115–124.

Wieland, E., Rodriguez-Vita, J., Liebler, S.S., Mogler, C., Moll, I., Herberich, S.E., Espinet, E., Herpel, E., Menuchin, A., Chang-Claude, J., et al. (2017). Endothelial Notch1 Activity Facilitates Metastasis. Cancer Cell *31*, 355–367.

Wiench, B., Eichhorn, T., Paulsen, M., and Efferth, T. (2012). Shikonin directly targets mitochondria and causes mitochondrial dysfunction in cancer cells. Evid. Based. Complement. Alternat. Med. *2012*, 726025.

Wise, D.R., DeBerardinis, R.J., Mancuso, A., Sayed, N., Zhang, X.-Y., Pfeiffer, H.K., Nissim, I., Daikhin, E., Yudkoff, M., McMahon, S.B., et al. (2008). Myc regulates a transcriptional program that stimulates mitochondrial glutaminolysis and leads to glutamine addiction. Proc. Natl. Acad. Sci. U. S. A. *105*, 18782–18787.

Wise, D.R., Ward, P.S., Shay, J.E.S., Cross, J.R., Gruber, J.J., Sachdeva, U.M., Platt, J.M., DeMatteo, R.G., Simon, M.C., and Thompson, C.B. (2011). Hypoxia promotes isocitrate dehydrogenase-dependent carboxylation of α-ketoglutarate to citrate to support cell growth and viability. Proc. Natl. Acad. Sci. U. S. A. *108*, 19611–19616.

Wong, C.C., Qian, Y., and Yu, J. (2017). Interplay between epigenetics and metabolism in oncogenesis: mechanisms and therapeutic approaches. Oncogene *36*, 3359–3374.

Woo, C.C., Chen, W.C., Teo, X.Q., Radda, G.K., and Lee, P.T.H. (2016). Downregulating serine hydroxymethyltransferase 2 (SHMT2) suppresses tumorigenesis in human hepatocellular carcinoma. Oncotarget *7*, 53005–53017.

Wright, D.L., and Anderson, A.C. (2011). Antifolate agents: a patent review (2006 - 2010). Expert Opin. Ther. Pat. *21*, 1293–1308.

Wu, Z., Wei, D., Gao, W., Xu, Y., Hu, Z., Ma, Z., Gao, C., Zhu, X., and Li, Q. (2015). TPO-Induced Metabolic Reprogramming Drives Liver Metastasis of Colorectal Cancer CD110+ Tumor-Initiating Cells. Cell Stem Cell *17*, 47–59.

Xian, D., Lai, R., Song, J., Xiong, X., and Zhong, J. (2019). Emerging Perspective: Role of

Increased ROS and Redox Imbalance in Skin Carcinogenesis. Oxid. Med. Cell. Longev. *2019*, 8127362.

Xiang, L., Mou, J., Shao, B., Wei, Y., Liang, H., Takano, N., Semenza, G.L., and Xie, G. (2019). Glutaminase 1 expression in colorectal cancer cells is induced by hypoxia and required for tumor growth, invasion, and metastatic colonization. Cell Death Dis. *10*, 40.

Xiao, M., Yang, H., Xu, W., Ma, S., Lin, H., Zhu, H., Liu, L., Liu, Y., Yang, C., Xu, Y., et al. (2012). Inhibition of α-KG-dependent histone and DNA demethylases by fumarate and succinate that are accumulated in mutations of FH and SDH tumor suppressors. Genes Dev. *26*, 1326–1338.

Xie, Y.-H., Chen, Y.-X., and Fang, J.-Y. (2020). Comprehensive review of targeted therapy for colorectal cancer. Signal Transduct. Target. Ther. *5*, 22.

Xin, Z., Zhao, H., Serby, M.D., Liu, B., Liu, M., Szczepankiewicz, B.G., Nelson, L.T.J., Smith, H.T., Suhar, T.S., Janis, R.S., et al. (2008). Discovery of piperidine-aryl urea-based stearoyl-CoA desaturase 1 inhibitors. Bioorg. Med. Chem. Lett. *18*, 4298–4302.

Xu, D., Jin, G., Chai, D., Zhou, X., Gu, W., Chong, Y., Song, J., and Zheng, J. (2018). The development of CAR design for tumor CAR-T cell therapy. Oncotarget *9*, 13991–14004.

Yamamoto, H., Murata, K., Fukunaga, M., Ohnishi, T., Noura, S., Miyake, Y., Kato, T., Ohtsuka, M., Nakamura, Y., Takemasa, I., et al. (2016). Micrometastasis Volume in Lymph Nodes Determines Disease Recurrence Rate of Stage II Colorectal Cancer: A Prospective Multicenter Trial. Clin. Cancer Res. *22*, 3201–3208.

Yang, M., and Vousden, K.H. (2016). Serine and one-carbon metabolism in cancer. Nat. Rev. Cancer *16*, 650–662.

Yang, L., Moss, T., Mangala, L.S., Marini, J., Zhao, H., Wahlig, S., Armaiz-Pena, G., Jiang, D., Achreja, A., Win, J., et al. (2014). Metabolic shifts toward glutamine regulate tumor growth, invasion and bioenergetics in ovarian cancer. Mol. Syst. Biol. *10*, 728.

Yang, L., Shi, P., Zhao, G., Xu, J., Peng, W., Zhang, J., Zhang, G., Wang, X., Dong, Z., Chen, F., et al. (2020). Targeting cancer stem cell pathways for cancer therapy. Signal Transduct. Target. Ther. *5*, 8.

Yang, S.-W., Zhang, Z.-G., Hao, Y.-X., Zhao, Y.-L., Qian, F., Shi, Y., Li, P.-A., Liu, C.-Y., and Yu, P.-W. (2017). HIF-1α induces the epithelial-mesenchymal transition in gastric cancer stem cells through the Snail pathway. Oncotarget *8*, 9535–9545.

Ye, D., Guan, K.-L., and Xiong, Y. (2018). Metabolism, Activity, and Targeting of D- and L-2-Hydroxyglutarates. Trends in Cancer *4*, 151–165.

Ye, J., Mancuso, A., Tong, X., Ward, P.S., Fan, J., Rabinowitz, J.D., and Thompson, C.B. (2012). Pyruvate kinase M2 promotes de novo serine synthesis to sustain mTORC1 activity and cell proliferation. Proc. Natl. Acad. Sci. U. S. A. *109*, 6904–6909.

Ye, J., Wu, D., Wu, P., Chen, Z., and Huang, J. (2014). The cancer stem cell niche: cross talk between cancer stem cells and their microenvironment. Tumour Biol. *35*, 3945–3951.

Ye, X., Tam, W.L., Shibue, T., Kaygusuz, Y., Reinhardt, F., Ng Eaton, E., and Weinberg, R.A. (2015). Distinct EMT programs control normal mammary stem cells and tumour-initiating cells. Nature *525*, 256–260.

Yeung, K.T., and Yang, J. (2017). Epithelial-mesenchymal transition in tumor metastasis. Mol. Oncol. *11*, 28–39.

Yizhak, K., Gaude, E., Le Dévédec, S., Waldman, Y.Y., Stein, G.Y., van de Water, B., Frezza, C., and Ruppin, E. (2014). Phenotype-based cell-specific metabolic modeling reveals metabolic liabilities of cancer. Elife *3*, 1–23.

Yonashiro, R., Eguchi, K., Wake, M., Takeda, N., and Nakayama, K. (2018). Pyruvate Dehydrogenase PDH-E1β Controls Tumor Progression by Altering the Metabolic Status of Cancer Cells. Cancer Res. *78*, 1592–1603.

Young, J.D. (2014). INCA: a computational platform for isotopically non-stationary metabolic flux analysis. Bioinformatics *30*, 1333–1335.

Yu, H., Zhong, X., Gao, P., Shi, J., Wu, Z., Guo, Z., Wang, Z., and Song, Y. (2019). The Potential Effect of Metformin on Cancer: An Umbrella Review. Front. Endocrinol. (Lausanne). *10*, 617.

Yuan, B., Schafferer, S., Tang, Q., Scheffler, M., Nees, J., Heil, J., Schott, S., Golatta, M., Wallwiener, M., Sohn, C., et al. (2019). A plasma metabolite panel as biomarkers for early primary breast cancer detection. Int. J. Cancer *144*, 2833–2842.

Zamboni, N., Saghatelian, A., and Patti, G.J. (2015). Defining the metabolome: size, flux, and regulation. Mol. Cell *58*, 699–706.

Zarour, L.R., Anand, S., Billingsley, K.G., Bisson, W.H., Cercek, A., Clarke, M.F., Coussens, L.M., Gast, C.E., Geltzeiler, C.B., Hansen, L., et al. (2017). Colorectal Cancer Liver Metastasis: Evolving Paradigms and Future Directions. Cell. Mol. Gastroenterol. Hepatol. *3*, 163–173.

Zhan, T., Rindtorff, N., Betge, J., Ebert, M.P., and Boutros, M. (2019). CRISPR/Cas9 for cancer research and therapy. Semin. Cancer Biol. *55*, 106–119.

Zhang, J., Fan, J., Venneti, S., Cross, J.R., Takagi, T., Bhinder, B., Djaballah, H., Kanai, M., Cheng, E.H., Judkins, A.R., et al. (2014). Asparagine plays a critical role in regulating cellular adaptation to glutamine depletion. Mol. Cell *56*, 205–218.

Zhang, L.-X., Lv, Y., Xu, A.-M., and Wang, H.-Z. (2019). The prognostic significance of serum gamma-glutamyltransferase levels and AST/ALT in primary hepatic carcinoma. BMC Cancer *19*, 841.

Zhang, L., Liu, Z., Ma, W., and Wang, B. (2013). The landscape of histone acetylation involved in epithelial-mesenchymal transition in lung cancer. J. Cancer Res. Ther. *9 Suppl 2*, S86-91.

Zhang, L., Chen, Z., Xue, D., Zhang, Q., Liu, X., Luh, F., Hong, L., Zhang, H., Pan, F., Liu, Y., et al. (2016). Prognostic and therapeutic value of mitochondrial serine hydroxyl-methyltransferase 2 as a breast cancer biomarker. Oncol. Rep. *36*, 2489–2500.

Zhang, N., Yang, X., Yuan, F., Zhang, L., Wang, Y., Wang, L., Mao, Z., Luo, J., Zhang, H., Zhu, W.-G., et al. (2018). Increased Amino Acid Uptake Supports Autophagy-Deficient Cell Survival upon Glutamine Deprivation. Cell Rep. *23*, 3006–3020.

Zhang, X., Ai, F., Li, X., Tian, L., Wang, X., Shen, S., and Liu, F. (2017). MicroRNA-34a suppresses colorectal cancer metastasis by regulating Notch signaling. Oncol. Lett. *14*, 2325–2333.

Zhao, D., Zou, S.-W., Liu, Y., Zhou, X., Mo, Y., Wang, P., Xu, Y.-H., Dong, B., Xiong, Y., Lei,

Q.-Y., et al. (2013). Lysine-5 acetylation negatively regulates lactate dehydrogenase A and is decreased in pancreatic cancer. Cancer Cell *23*, 464–476.

Zhao, L., Lee, V.H.F., Ng, M.K., Yan, H., and Bijlsma, M.F. (2019). Molecular subtyping of cancer: current status and moving toward clinical applications. Brief. Bioinform. *20*, 572–584.

Zhao, X., Zhu, Y., Hu, J., Jiang, L., Li, L., Jia, S., and Zen, K. (2018). Shikonin Inhibits Tumor Growth in Mice by Suppressing Pyruvate Kinase M2-mediated Aerobic Glycolysis. Sci. Rep. *8*, 14517.

Zhao, Y., Seefeldt, T., Chen, W., Carlson, L., Stoebner, A., Hanson, S., Foll, R., Matthees, D.P., Palakurthi, S., and Guan, X. (2009). Increase in thiol oxidative stress via glutathione reductase inhibition as a novel approach to enhance cancer sensitivity to X-ray irradiation. Free Radic. Biol. Med. *47*, 176–183.

Zhao, Z., Feng, Q., Yin, Z., Shuang, J., Bai, B., Yu, P., Guo, M., and Zhao, Q. (2017). Red and processed meat consumption and colorectal cancer risk: a systematic review and meta-analysis. Oncotarget *8*, 83306–83314.

Zheng, Y., Lin, T.-Y., Lee, G., Paddock, M.N., Momb, J., Cheng, Z., Li, Q., Fei, D.L., Stein, B.D., Ramsamooj, S., et al. (2018). Mitochondrial One-Carbon Pathway Supports Cytosolic Folate Integrity in Cancer Cells. Cell *175*, 1546-1560.e17.

Zhou, S., Kachhap, S., and Singh, K.K. (2003). Mitochondrial impairment in p53-deficient human cancer cells. Mutagenesis *18*, 287–292.

Zong, W.-X., Rabinowitz, J.D., and White, E. (2016). Mitochondria and Cancer. Mol. Cell *61*, 667–676.

9. Appendix I

9 APPENDIX I

Characterisation of growth, cell volume and metabolite uptake and secretion rates in SW480, SW620, LiM1, and LiM2 cells

The experiments shown on the present appendix were used to optimise the best incubation conditions in terms of incubation time, cell growth and confluence for metabolic measurements, as discussed in section 5.1.2.1 and 5.1.2.2. Furthermore, cell volume determination was necessary for the normalisation of metabolic measurements and the computational model generation.

9.1 MATERIALS AND METHODS

Materials and methods of the present appendix are the ones described in the following sections: Cell resources, culture and maintenance (section 4.2.1), cell doubling time, volume determination and seeding conditions (section 4.2.2), cell cycle analysis (section 4.2.6) and extracellular metabolite measurements by spectrophotometry (section 4.3.1).

9.2 RESULTS

The first growing curves up to 144 hours in order to characterise the relationship between cell growth, cell confluence and volume are shown in Figures A.I.1 – A.I.8, changing the medium every 24 hours. Other growth curves were done at low and high confluence without changing the medium (Figure A.I.9) and cell cycle was analysed in order to know if cells were proliferating or stopped at some incubation point (Figure A.I.10). Then, the extracellular metabolites were measured, and it was determined that even at low confluence, metastatic cells consumed all the glutamine of the medium at 72 hours (Figure A.I.11). Tables A.I.1 – A.I.8 show the results of the glucose, lactate, glutamine and glutamate uptake and secretion rates. The best conditions were established to be incubations of 48 hours at low confluence for exponential growth, specifically seeding: $1{,}5 \cdot 10^5$ cells / p6 plate well for SW480 and $2 \cdot 10^5$ / p6 plate for SW620, LiM1 and LiM2 cells. Then, confluence and incubation time can be adapted for the different experiments that were done.

Taking into account all these experiments, the duplication time and cell volume shown in Figure 5.1.4C and D from section 5.1.2.1 were calculated.

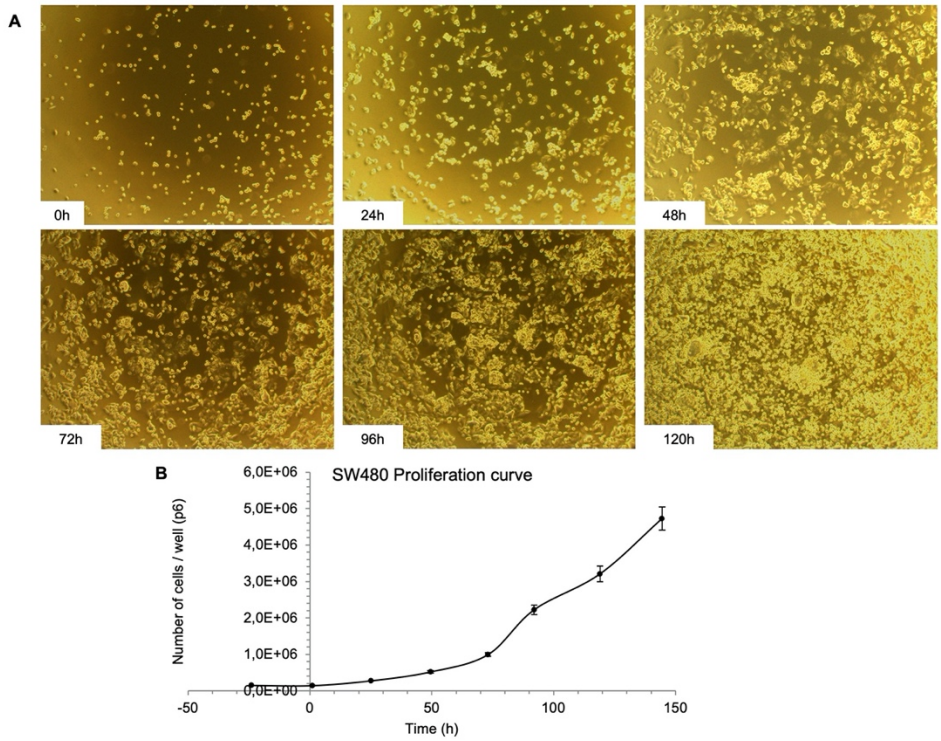

Figure A.I.1. Proliferation curve of SW480 colon cell line from primary tumour. A. Images from contrast-phase microscopy at 10X. **B.** Cell number measured by the automatic cell counter Scepter™ up to 144h, changing the medium (DMEM 25 mM Glc, 4 mM Gln, 5% FBS, and 1% S/P) every 24 hours.

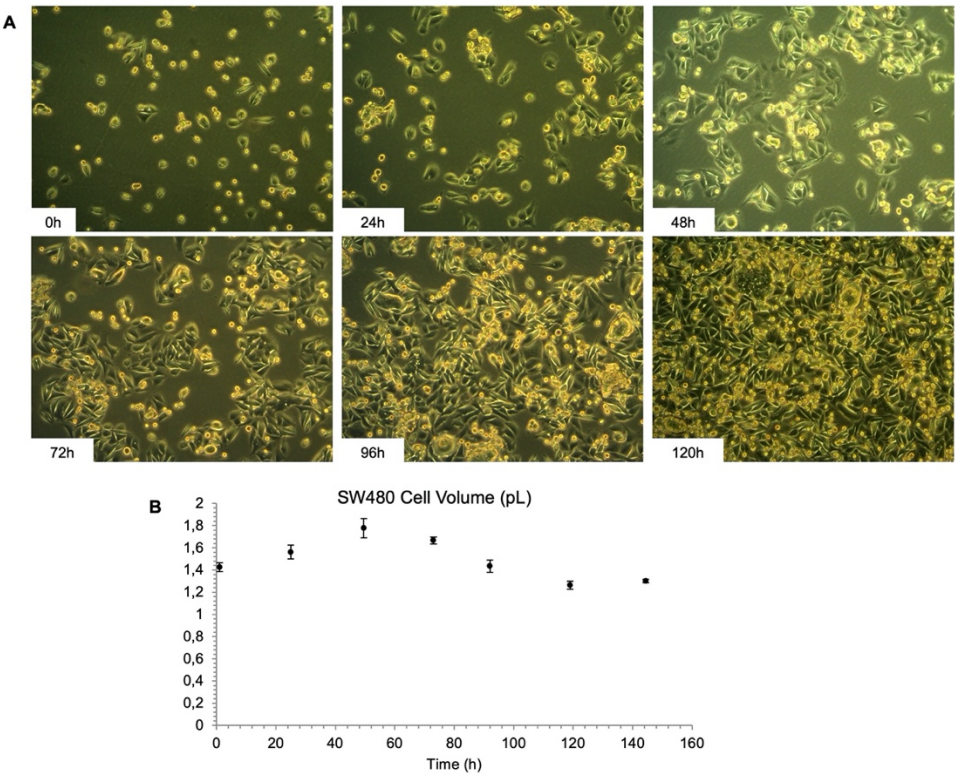

Figure A.I.2. Cell volume of SW480 colon cell line from primary tumour. A. Images from contrast-phase microscopy at 40X. **B.** Cell volume measured by the automatic cell counter Scepter™ at each point of the proliferation curve to 144h, changing the medium (DMEM 25 mM Glc, 4 mM Gln, 5% FBS, and 1% S/P) every 24 hours.

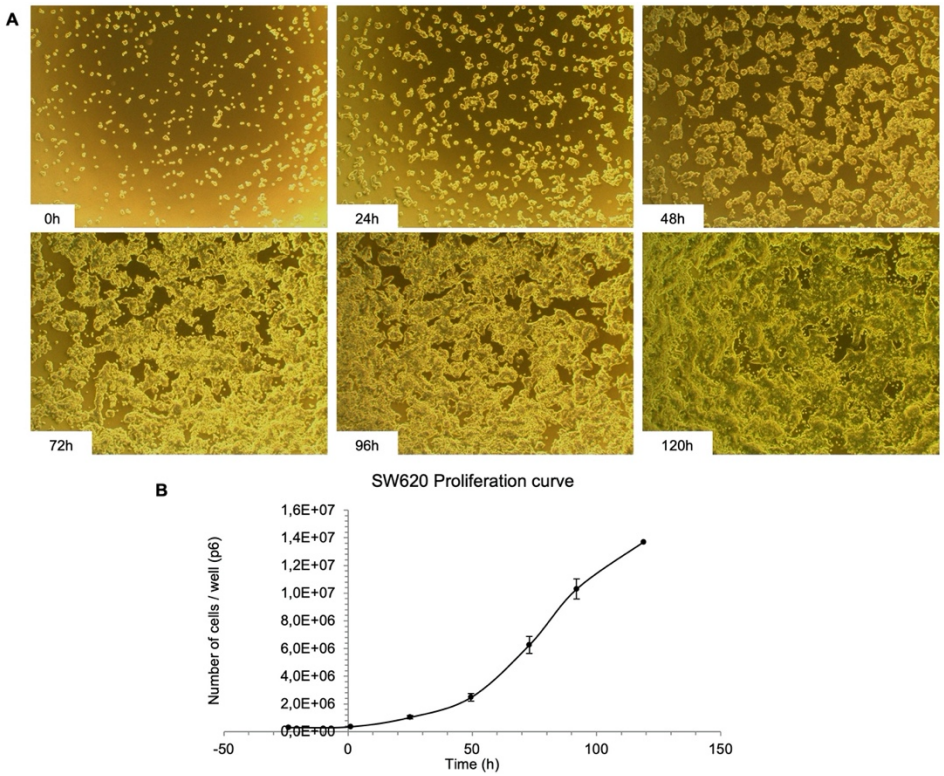

Figure A.I.3. Proliferation curve of SW620 lymph node-derived colon metastatic cell line. A. Images from contrast-phase microscopy at 10X. **B.** Cell number measured by the automatic cell counter Scepter™ up to 144h, changing the medium (DMEM 25 mM Glc, 4 mM Gln, 5% FBS and 1% S/P) every 24 hours.

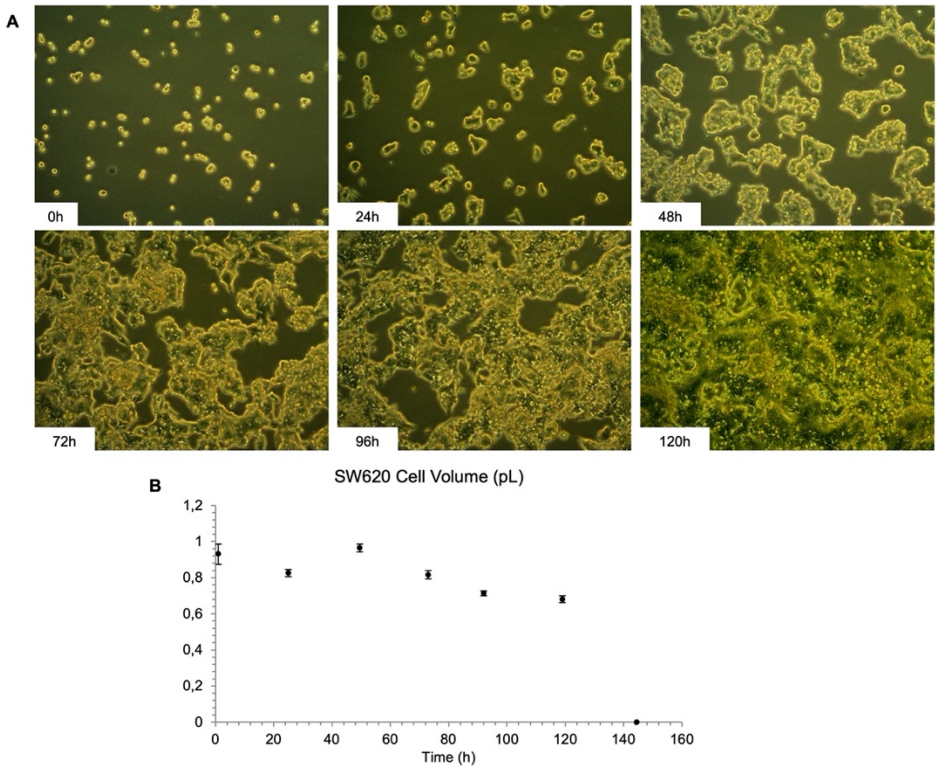

Figure A.I.4. Cell volume of SW620 lymph node-derived colon metastatic cell line. A. Images from contrast-phase microscopy at 40X. **B.** Cell volume measured by the automatic cell counter Scepter™ at each point of the proliferation curve to 144h, changing the medium (DMEM 25 mM Glc, 4 mM Gln, 5% FBS, and 1% S/P) every 24 hours.

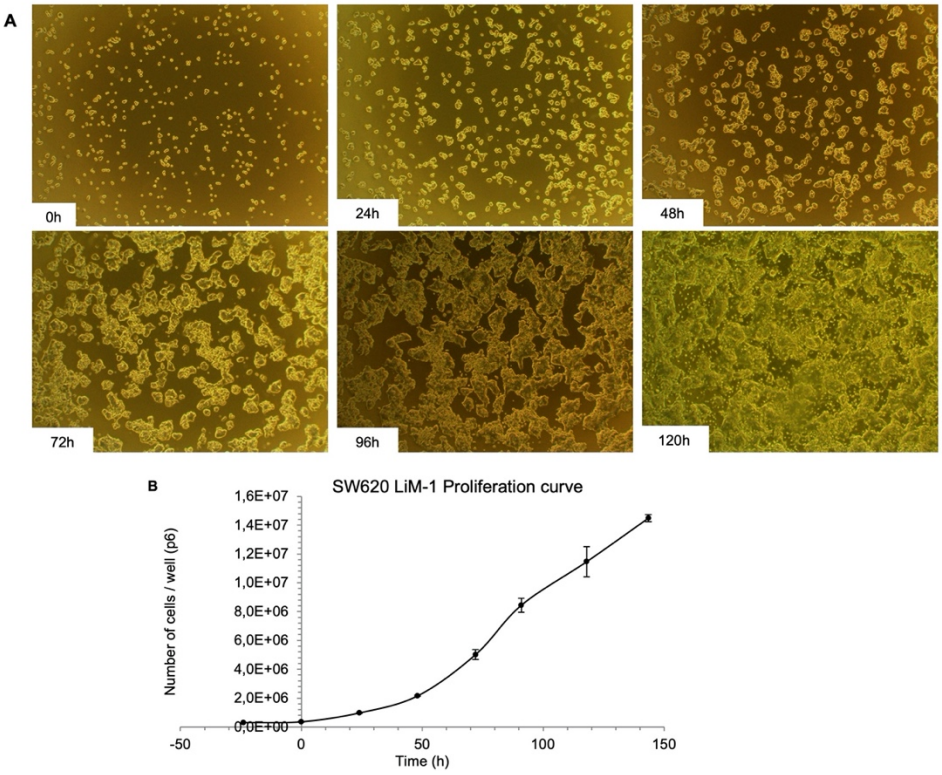

Figure A.I.5. Proliferation curve of LiM1 liver-derived colon metastatic cell line. A. Images from contrast-phase microscopy at 10X. **B.** Cell number measured by the automatic cell counter Scepter™ up to 144h, changing the medium (DMEM 25 mM Glc, 4 mM Gln, 5% FBS, and 1% S/P) every 24 hours.

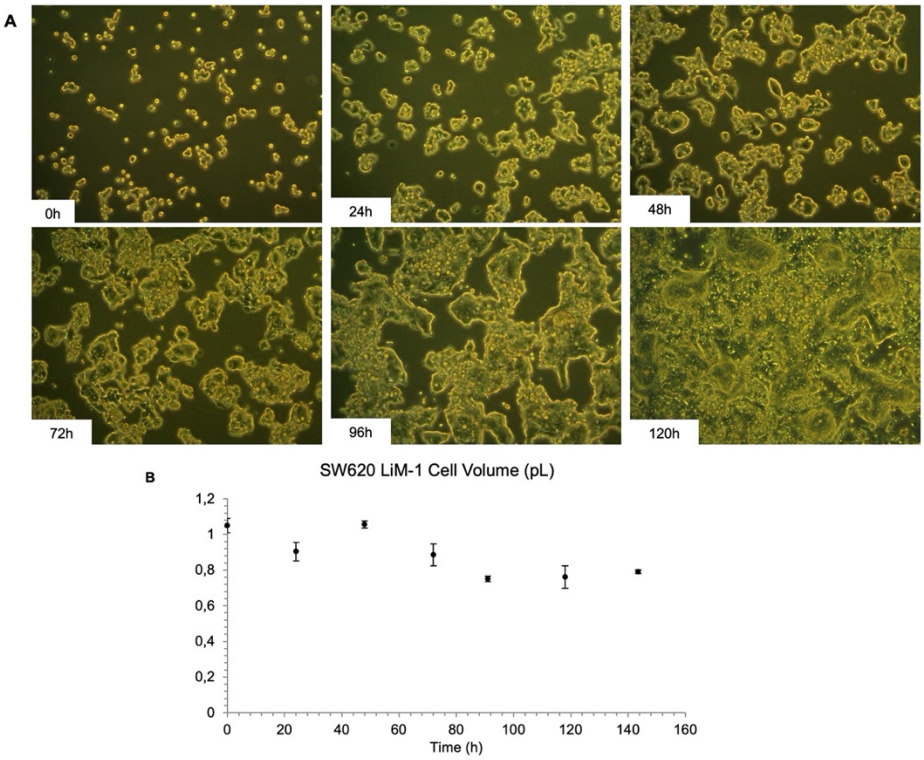

Figure A.I.6. Cell volume of LiM1 liver-derived colon metastatic cell line. A. Images from contrast-phase microscopy at 40X. **B.** Cell volume measured by the automatic cell counter Scepter™ at each point of the proliferation curve to 144h, changing the medium (DMEM 25 mM Glc, 4 mM Gln, 5% FBS, and 1% S/P) every 24 hours.

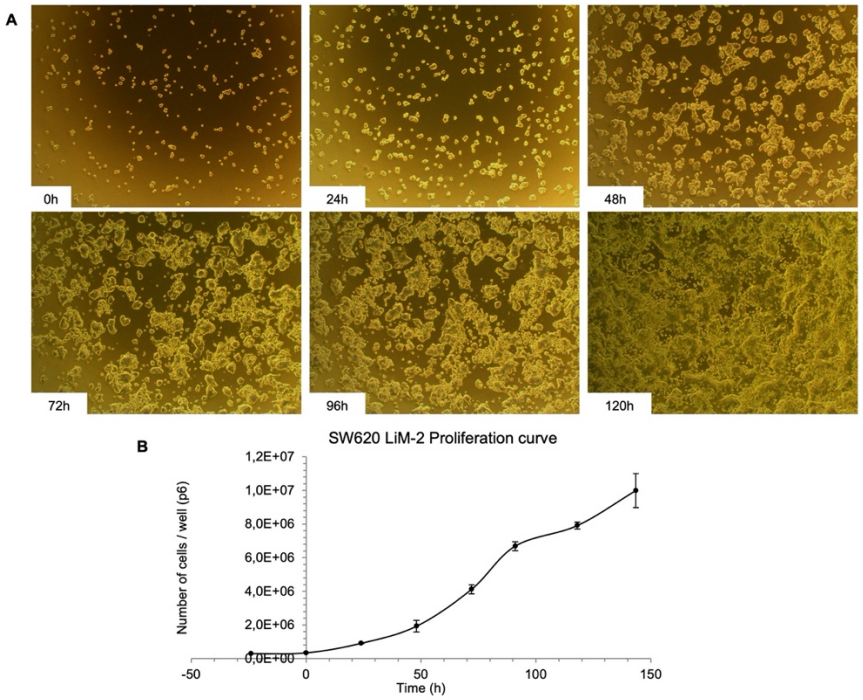

Figure A.I.7. Proliferation curve of LiM2 liver-derived colon metastatic cell line. A. Images from contrast-phase microscopy at 10X. **B.** Cell number measured by the automatic cell counter Scepter™ up to 144h, changing the medium (DMEM 25 mM Glc, 4 mM Gln, 5% FBS, and 1% S/P) every 24 hours.

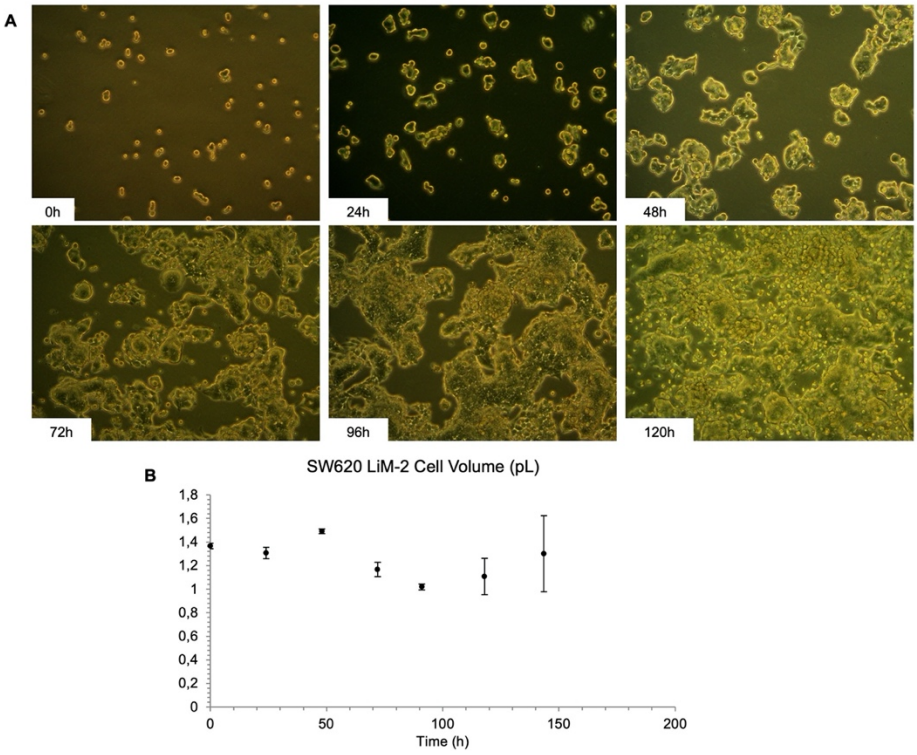

Figure A.I.8. Cell volume of LiM2 liver-derived colon metastatic cell line. A. Images from contrast-phase microscopy at 40X. **B.** Cell volume measured by the automatic cell counter Scepter™ at each point of the proliferation curve to 144h, changing the medium (DMEM 25 mM Glc, 4 mM Gln, 5% FBS, and 1% S/P) every 24 hours.

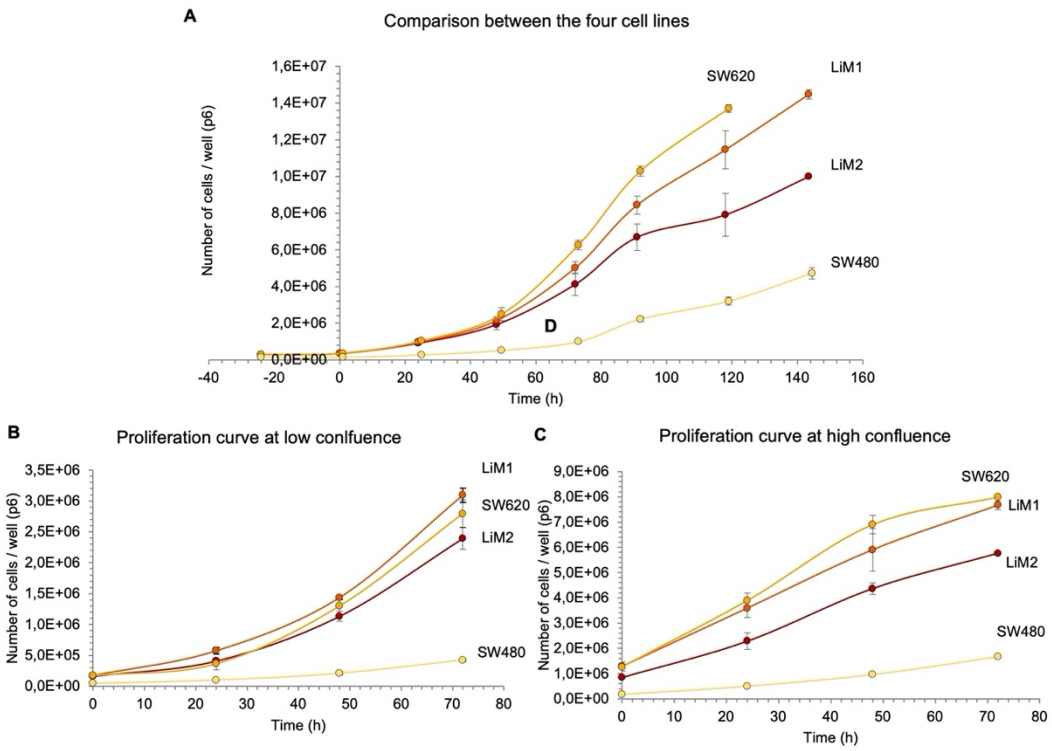

Figure A.I.9. Cell proliferation of the colon cell line from primary tumour SW480 and its metastatic derivatives SW620, LiM1, and LiM2. A. Cell curves measured by the automatic cell counter Scepter^{TM} up to 144h changing the medium (DMEM 25 mM Glc, 4 mM Gln, 5% FBS, and 1% S/P) every 24 hours. **B.** Proliferation curve up to 72h without changing the medium at low confluence. **C.** Proliferation curve up to 72h without changing the medium at high confluence.

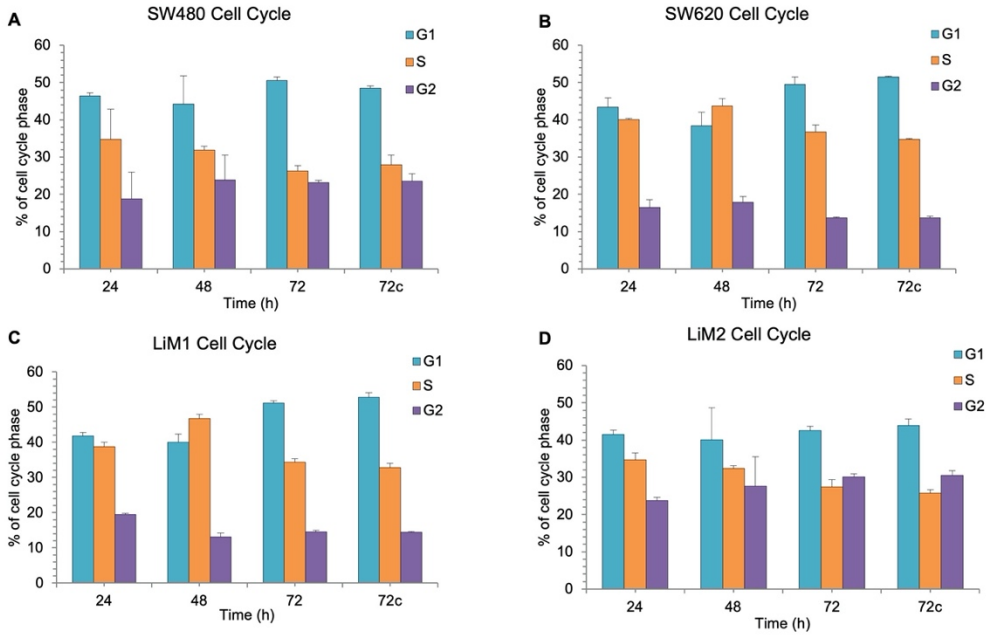

Figure A.I.10. Cell cycle analysis of proliferation SW480 (A), SW620 (B), LiM1 (C), and LiM2 (D) cells. Percentage of cell cycle phase measured by flow cytometre after 24, 48, 72 and 72c (changing the medium at 24h of incubation) (DMEM 25 mM Glc, 4 mM Gln, 5% FBS, and 1% S/P) at low confluence growth (panel B of Figure A.I.9).

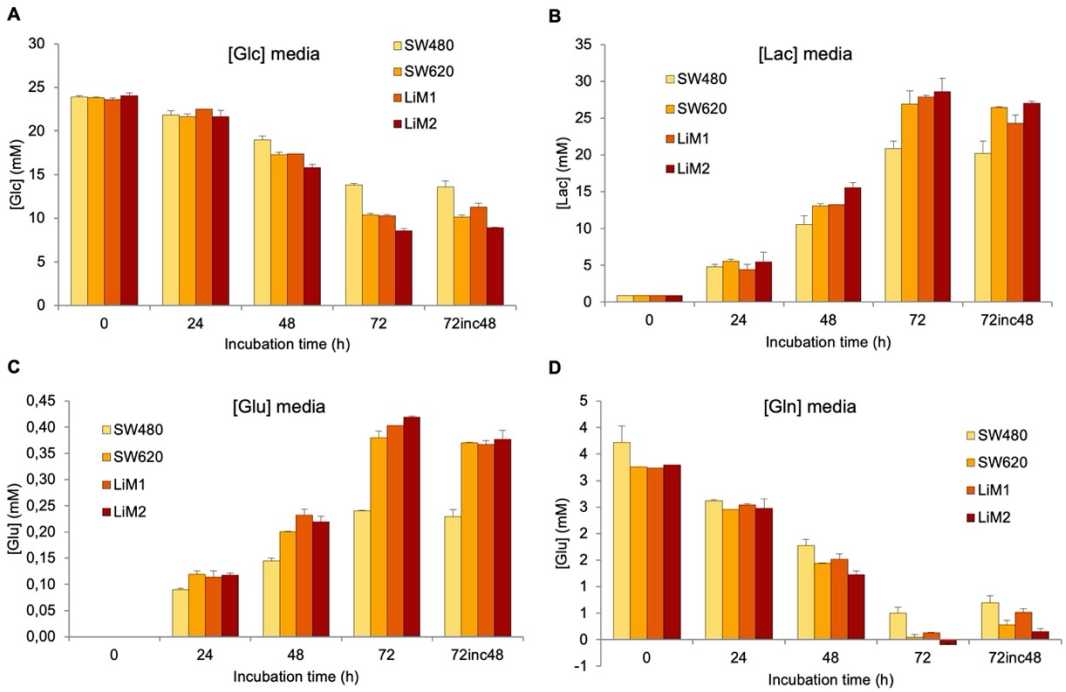

Figure A.I.11. Measurement of extracellular metabolites in proliferation SW480, SW620, LiM1, and LiM2. Concentration of glucose (A), lactate (B), glutamate (C) and glutamine (D) in the cell medium (DMEM 25 mM Glc, 4 mM Gln, 5% FBS, and 1% S/P) at time points 0h, 24h, 48h, 72h and incubation at 72h changing the medium at 24h at low confluence growth (panel B of Figure A.I.9).

SW480			Glucose Uptake			Lactate Secretion		
	Time (h)	Inc. (h)	*v*	Mean	SD	*v*	Mean	SD
ExpAI.1	24	24	-0,187	-0,302	0,162	x	x	x
			-0,416			x		
	48	24	-0,340	-0,403	0,089	0,751	0,905	0,218
			-0,466			1,059		
	72	24	-0,423	-0,399	0,035	x	0,837	x
			-0,374			0,837		
	96	24	-0,318	-0,318	0,000	0,496	0,534	0,054
			-0,318			0,572		
	120	24	-0,309	-0,327	0,025	0,504	0,471	0,048
			-0,345			0,437		
ExpAI.2	24	24	x	x	x	x	x	x
			x			x		
	48	48	-0,280	-0,280	x	x	x	x
			-0,712			x		
	72	72	-0,416	-0,353	0,089	x	x	x
			-0,290			x		
ExpAI.3	24	24	-0,411	-0,443	0,046	1,121	1,098	0,032
			-0,476			1,075		
	48	48	-0,366	-0,388	0,031	0,922	0,864	0,082
			-0,409			0,806		
ExpAI.4	48	48	-0,537	-0,519	0,016	1,013	1,006	0,028
			-0,514			0,975		
			-0,506			1,030		

Table A.I.1. Glucose uptake and lactate secretion of SW480 colon cell line from primary tumour. Glucose uptake and lactate secretion measured by spectrophotometry of various experiments at different incubation times, growing and confluence conditions. **ExpAI.1:** Complete growth curve up to 120 hours changing the medium every 24h. **ExpAI.2:** Growth curve up to 72h at high confluence without changing the medium. **ExpAI.3:** Growth curve up to 48h without changing the medium. **ExpAI.4:** Metabolite measurements at the optimised conditions. **Inc:** Incubation time from fresh medium. ***v*:** ($\mu mol \cdot h^{-1} \cdot \mu l$ (cell volume)$^{-1}$). **x:** Measurement not possible.

SW480			Glutamine Uptake			Glutamate Secretion		
	Time (h)	Inc. (h)	*v*	Mean	SD	*v*	Mean	SD
ExpAI.1	24	24	x	x	x	x	x	x
			x			x		
	48	24	-0,092	-0,104	0,018	0,0138	0,0142	0,0006
			-0,117			0,0147		
	72	24	-0,211	-0,212	0,001	0,0115	0,0115	0,0128
			-0,212			0,0296		
	96	24	-0,090	-0,092	0,003	0,0074	0,0073	0,0001
			-0,094			0,0073		
	120	24	-0,060	-0,061	0,002	0,0067	0,0068	0,0002
			-0,062			0,0070		
ExpAI.2	24	24	-0,048	-0,055	0,010	0,0062	0,0133	0,0101
			-0,062			0,0205		
	48	48	-0,142	-0,136	0,007	0,0132	0,0132	0,0000
			-0,131			0,0132		
	72	72	-0,140	-0,149	0,012	0,0136	0,0132	0,0006
			-0,158			0,0128		
ExpAI.3	24	24	-0,043	-0,053	0,015	0,0098	0,0091	0,0010
			-0,064			0,0083		
	48	48	-0,124	-0,117	0,009	0,0113	0,0106	0,0010
			-0,111			0,0099		
ExpAI.4	48	48	-0,217	-0,214	0,014	0,0244	0,0246	0,0001
			-0,199			0,0245		
			-0,226			0,0247		

Table A.I.2. Glutamine uptake and glutamate secretion of SW480 colon cell line from primary tumour. Glutamine uptake and glutamate secretion measured by spectrophotometry of various experiments at different incubation times, growing and confluence conditions. **ExpAI.1:** Complete growth curve up to 120 hours changing the medium every 24h. **ExpAI.2:** Growth curve up to 72h at high confluence without changing the medium. **ExpAI.3:** Growth curve up to 48h without changing the medium. **ExpAI.4:** Metabolite measurements at the optimised conditions. **Inc:** Incubation time from fresh medium. ***v*:** ($\mu mol \cdot h^{-1} \cdot \mu l$ (cell volume)$^{-1}$). **x:** Measurement not possible.

SW620			Glucose Uptake			Lactate Secretion		
	Time (h)	Inc. (h)	*v*	Mean	SD	*v*	Mean	SD
ExpAI.1	24	24	-0,236	-0,212	0,034	x	x	x
			-0,188			x		
	48	24	-0,271	-0,271	0,000	0,515	0,509	0,009
			-0,271			0,502		
	72	24	-0,221	-0,223	0,003	0,387	0,385	0,003
			-0,225			0,383		
	96	24	-0,168	-0,166	0,002	0,311	0,281	0,042
			-0,164			0,252		
	120	24	-0,130	-0,129	0,000	0,215	0,212	0,004
			-0,129			0,210		
ExpAI.2	24	24	-0,113	-0,129	0,022	x	x	x
			-0,145			x		
	48	48	-0,248	-0,254	0,008	x	x	x
			-0,259			x		
	72	72	-0,207	-0,181	0,036	x	x	x
			-0,155			x		
ExpAI.3	24	24	-0,299	-0,309	0,014	0,558	0,547	0,016
			-0,319			0,536		
	48	48	-0,309	-0,307	0,002	0,536	0,548	0,016
			-0,306			0,559		
ExpAI.4	48	48	-0,340	-0,353	0,013	0,566	0,586	0,017
			-0,366			0,596		
			-0,352			0,595		

Table A.I.3. Glucose uptake and lactate secretion of SW620 lymph node-derived colon metastatic cell line. Glucose uptake and lactate secretion measured by spectrophotometry of various experiments at different incubation times, growing and confluence conditions. **ExpAI.1:** Complete growth curve up to 120 hours changing the medium every 24h. **ExpAI.2:** Growth curve up to 72h at high confluence without changing the medium. **ExpAI.3:** Growth curve up to 48h without changing the medium. **ExpAI.4:** Metabolite measurements at the optimised conditions. **Inc:** Incubation time from fresh medium. ***v*:** ($\mu mol \cdot h^{-1} \cdot \mu l$ (cell volume)$^{-1}$). **x:** Measurement not possible.

SW620			Glutamine Uptake			Glutamate Secretion		
	Time (h)	Inc. (h)	*v*	Mean	SD	*v*	Mean	SD
ExpAI.1	24	24	x	x	x	x	x	x
			x			x		
	48	24	-0,048	-0,050	0,003	0,0057	0,0057	0,0001
			-0,052			0,0058		
	72	24	-0,038	-0,038	0,000	0,0045	0,0043	0,0003
			-0,038			0,0040		
	96	24	-0,027	-0,027	0,000	0,0036	0,0036	0,0000
			-0,027			0,0036		
	120	24	-0,019	-0,019	0,000	0,0029	0,0029	0,0000
			-0,019			0,0029		
ExpAI.2	24	24	-0,094	-0,099	0,007	0,0040	0,0057	0,0024
			-0,103			0,0074		
	48	48	-0,050	-0,065	0,021	0,0048	0,0053	0,0007
			-0,079			0,0058		
	72	72	-0,053	-0,053	0,001	0,0047	0,0046	0,0002
			-0,052			0,0045		
ExpAI.3	24	24	-0,060	-0,065	0,007	0,0081	0,0081	0,0001
			-0,070			0,0082		
	48	48	-0,054	-0,053	0,000	0,0073	0,0071	0,0002
			-0,053			0,0069		
ExpAI.4	48	48	-0,096	-0,102	0,005	0,0121	0,0125	0,0004
			-0,107			0,0125		
			-0,103			0,0129		

Table A.I.4. Glutamine uptake and glutamate secretion of SW620 lymph node-derived colon metastatic cell line. Glutamine uptake and glutamate secretion measured by spectrophotometry of various experiments at different incubation times, growing and confluence conditions. **ExpAI.1:** Complete growth curve up to 120 hours changing the medium every 24h. **ExpAI.2:** Growth curve up to 72h at high confluence without changing the medium. **ExpAI.3:** Growth curve up to 48h without changing the medium. **ExpAI.4:** Metabolite measurements at the optimised conditions. **Inc:** Incubation time from fresh medium. ***v*:** ($\mu mol \cdot h^{-1} \cdot \mu l$ (cell volume)$^{-1}$). **x:** Measurement not possible.

LiM1			Glucose Uptake			Lactate Secretion		
	Time (h)	Inc. (h)	*v*	Mean	SD	*v*	Mean	SD
ExpAI.1	24	24	-0,294	-0,260	0,048	x	x	x
			-0,226			x		
	48	24	-0,301	-0,311	0,015	0,575	0,575	0,001
			-0,322			0,574		
	72	24	-0,275	-0,271	0,006	0,399	0,411	0,017
			-0,267			0,424		
	96	24	-0,194	-0,195	0,001	0,352	0,333	0,026
			-0,196			0,315		
	120	24	-0,155	-0,156	0,002	0,257	0,259	0,003
			-0,157			0,261		
ExpAI.2	24	24	-0,271	-0,308	0,052	x	x	x
			-0,344			x		
	48	48	-0,311	-0,361	0,071	x	x	x
			-0,411			x		
	72	72	-0,215	-0,209	0,009	x	x	x
			-0,203			x		
ExpAI.3	24	24	-0,277	-0,279	0,003	0,547	0,545	0,002
			-0,280			0,543		
	48	48	-0,286	-0,288	0,003	0,498	0,493	0,007
			-0,290			0,488		
ExpAI.4	48	48	-0,354	-0,376	0,031	0,702	0,682	0,055
			-0,412			0,725		
			-0,362			0,620		

Table A.I.5. Glucose uptake and lactate secretion of LiM1 liver-derived colon metastatic cell line. Glucose uptake and lactate secretion measured by spectrophotometry of various experiments at different incubation times, growing and confluence conditions. **ExpAI.1:** Complete growth curve up to 120 hours changing the medium every 24h. **ExpAI.2:** Growth curve up to 72h at high confluence without changing the medium. **ExpAI.3:** Growth curve up to 48h without changing the medium. **ExpAI.4:** Metabolite measurements at the optimised conditions. **Inc:** Incubation time from fresh medium. ***v*:** ($\mu mol \cdot h^{-1} \cdot \mu l$ (cell volume)$^{-1}$). **x:** Measurement not possible.

LiM1			Glutamine Uptake			Glutamate Secretion		
	Time (h)	Inc. (h)	*v*	Mean	SD	*v*	Mean	SD
ExpAI.1	24	24	x	x	x	x	x	x
			x			x		
	48	24	-0,052	-0,053	0,001	0,0063	0,0064	0,0000
			-0,054			0,0064		
	72	24	-0,042	-0,033	0,013	0,0050	0,0053	0,0004
			-0,024			0,0056		
	96	24	-0,033	-0,033	0,000	0,0042	0,0042	0,0001
			-0,033			0,0041		
	120	24	-0,024	-0,024	0,000	0,0041	0,0040	0,0002
			-0,023			0,0038		
ExpAI.2	24	24	-0,095	-0,094	0,002	0,0073	0,0094	0,0029
			-0,093			0,0114		
	48	48	-0,077	-0,073	0,006	0,0065	0,0070	0,0006
			-0,069			0,0074		
	72	72	-0,052	-0,052	0,000	0,0066	0,0066	0,0001
			-0,052			0,0066		
ExpAI.3	24	24	-0,065	-0,065	0,000	0,0081	0,0083	0,0004
			-0,065			0,0086		
	48	48	-0,052	-0,050	0,003	0,0071	0,0069	0,0003
			-0,048			0,0067		
ExpAI.4	48	48	-0,101	-0,110	0,008	0,0141	0,0146	0,0005
			-0,114			0,0151		
			-0,116			0,0145		

Table A.I.6. Glutamine uptake and glutamate secretion of LiM1 liver-derived colon metastatic cell line. Glutamine uptake and glutamate secretion measured by spectrophotometry of various experiments at different incubation times, growing and confluence conditions. **ExpAI.1:** Complete growth curve up to 120 hours changing the medium every 24h. **ExpAI.2:** Growth curve up to 72h at high confluence without changing the medium. **ExpAI.3:** Growth curve up to 48h without changing the medium. **ExpAI.4:** Metabolite measurements at the optimised conditions. **Inc.:** Incubation time from fresh medium. ***v*:** ($\mu mol \cdot h^{-1} \cdot \mu l$ (cell volume)$^{-1}$). **x:** Measurement not possible.

LiM2			Glucose Uptake			Lactate Secretion		
	Time (h)	Inc. (h)	*v*	Mean	SD	*v*	Mean	SD
ExpAI.1	24	24	-0,387	**-0,398**	**0,016**	x	**x**	**x**
			-0,409			x		
	48	24	-0,418	**-0,431**	**0,019**	0,706	**0,742**	**0,052**
			-0,445			0,779		
	72	24	-0,352	**-0,358**	**0,008**	0,618	**0,657**	**0,056**
			-0,364			0,697		
	96	24	-0,243	**-0,246**	**0,003**	0,394	**0,404**	**0,014**
			-0,248			0,414		
	120	24	-0,207	**-0,205**	**0,003**	0,355	**0,352**	**0,005**
			-0,203			0,348		
ExpAI.2	24	24	-0,811	**-0,556**	**0,181**	x	**x**	**x**
			-0,556			x		
	48	48	-0,362	**-0,353**	**0,012**	x	**x**	**x**
			-0,345			x		
	72	72	-0,266	**-0,263**	**0,004**	x	**x**	**x**
			-0,260			x		
ExpAI.3	24	24	-0,561	**-0,539**	**0,031**	0,983	**0,973**	**0,014**
			-0,518			0,963		
	48	48	-0,361	**-0,399**	**0,054**	0,766	**0,743**	**0,032**
			-0,437			0,720		
ExpAI.4	48	48	-0,519	**-0,517**	**0,006**	0,943	**0,892**	**0,053**
			-0,520			0,837		
			-0,510			0,897		

Table A.I.7. Glucose uptake and lactate secretion of LiM2 liver-derived colon metastatic cell line. Glucose uptake and lactate secretion measured by spectrophotometry of various experiments at different incubation times, growing and confluence conditions. **ExpAI.1:** Complete growth curve up to 120 hours changing the medium every 24h. **ExpAI.2:** Growth curve up to 72h at high confluence without changing the medium. **ExpAI.3:** Growth curve up to 48h without changing the medium. **ExpAI.4:** Metabolite measurements at the optimised conditions. **Inc:** Incubation time from fresh medium. ***v*:** ($\mu mol \cdot h^{-1} \cdot \mu l$ (cell volume)$^{-1}$). **x:** Measurement not possible.

LiM2			Glutamine Uptake			Glutamate Secretion		
	Time (h)	Inc. (h)	*v*	Mean	SD	*v*	Mean	SD
ExpAI.1	24	24	x	x	x	x	x	x
			x			x		
	48	24	-0,071	-0,073	0,004	0,0100	0,0105	0,0007
			-0,076			0,0110		
	72	24	-0,056	-0,055	0,001	0,0071	0,0054	0,0024
			-0,054			0,0037		
	96	24	-0,042	-0,042	0,000	0,0058	0,0056	0,0003
			-0,042			0,0054		
	120	24	-0,032	-0,031	0,000	0,0048	0,0046	0,0002
			-0,031			0,0045		
ExpAI.2	24	24	-0,141	-0,141	0,000	0,0086	0,0102	0,0023
			-0,141			0,0118		
	48	48	-0,105	-0,103	0,003	0,0080	0,0080	0,0001
			-0,101			0,0081		
	72	72	-0,067	-0,069	0,002	0,0077	0,0084	0,0010
			-0,070			0,0091		
ExpAI.3	24	24	-0,106	-0,110	0,005	0,0141	0,0142	0,0001
			-0,114			0,0142		
	48	48	-0,072	-0,072	x	0,0100	0,0103	0,0005
			x			0,0106		
ExpAI.4	48	48	-0,161	-0,147	0,012	0,0217	0,0213	0,0004
			-0,138			0,0209		
			-0,142			0,0213		

Table A.I.8. Glutamine uptake and glutamate secretion of LiM2 liver-derived colon metastatic cell line. Glutamine uptake and glutamate secretion measured by spectrophotometry of various experiments at different incubation times, growing and confluence conditions. **ExpAI.1:** Complete growth curve up to 120 hours changing the medium every 24h. **ExpAI.2:** Growth curve up to 72h at high confluence without changing the medium. **ExpAI.3:** Growth curve up to 48h without changing the medium. **ExpAI.4:** Metabolite measurements at the optimised conditions. **Inc.:** Incubation time from fresh medium. ***v*:** ($\mu mol \cdot h^{-1} \cdot \mu l$ (cell volume)$^{-1}$). **x:** Measurement not possible.

10. Appendix II

10 APPENDIX II

Stable-isotope resolved metabolomics (SIRM) experiments of the central carbon metabolism using [1,2-^{13}C]-glucose and [U-^{13}C]-glutamine in NCM460, SW480, SW620, and LiM2 cells

The present appendix is a compilation of the SIRM experiments done *in vitro* for NCM460, SW480, SW620, and LiM2 cell lines using the tracers [1,2-^{13}C]-glucose and [U-^{13}C]-glutamine with incubations of 6 hours and 24 hours. Furthermore, also the SIRM experiments done *in vivo* from xenografts of SW480, SW620 and LiM2 after boluses [U-^{13}C]-glucose and [U-^{13}C]-glutamine. The results are presented and discussed in sections 5.1.2.2 and 5.1.2.5.

10.1 MATERIALS AND METHODS

Materials and methods of the present appendix are the ones described in the following sections: Stable isotope-resolved metabolomics (section 4.3.3) and stable isotope-resolved metabolomics *in vivo* (section 4.4.3).

10.2 RESULTS *IN VITRO*

The results presented here are the corrected isotopologue distribution from polar intracellular metabolites of *in vitro* cultured NCM460, SW480, SW620, and LiM2 cell lines after 6h incubation with [1,2-^{13}C]-glucose (Table A.II.1), 6h incubation with [U-^{13}C]-glutamine (Table A.II.4), 24h incubation with [1,2-^{13}C]-glucose (Table A.II.6) and 24h incubation with [U-^{13}C]-glutamine (Table A.II.11). Extracellular glucose was analysed for 6h and 24h incubation with [1,2-^{13}C]-glucose in order to discard any process of gluconeogenesis (Table A.II.2 and A.II.7). Furthermore, extracellular lactate was measured in all the cases in order to determine the flux of the glycolytic pathway (Table A.II.3, A.II.5, A.II.8, and A.II.12). Intracellular ribose was analysed in the 24h incubation with [1,2-^{13}C]-glucose in order to explore glucose incorporation into the pentose phosphate pathway (Table A.II.10). Finally, extracellular amino acids glutamate and glutamine were also analysed for 24h incubation with [1,2-^{13}C]-glucose (Table A.II.9).

[1,2-^{13}C]-glucose 6h incubation		NCM460		SW480		SW620		LiM2	
Polar intracellular metabolites		Mean	SD	Mean	SD	Mean	SD	Mean	SD
Ala-260 C1-C3	m0	0,8410	0,0029	0,8930	0,0022	0,8610	0,0008	0,8400	0,0022
	m1	0,0000	0,0007	0,0000	0,0011	0,0080	0,0006	0,0090	0,0011
	m2	0,1580	0,0022	0,1190	0,0007	0,1310	0,0002	0,1510	0,0010
	m3	0,0020	0,0001	0,0010	0,0008	0,0010	0,0006	0,0010	0,0003
Ala-232 C2-C3	m0	0,8830	0,0024	0,9310	0,0003	0,8650	0,0006	0,8450	0,0017
	m1	0,0000	0,0004	0,0000	0,0006	0,0070	0,0001	0,0030	0,0005
	m2	0,1500	0,0021	0,1130	0,0010	0,1290	0,0008	0,1520	0,0013
Asp-418 C1-C4	m0	0,9550	0,0033	1,0210	0,0015	0,9800	0,0050	0,9670	0,0040
	m1	0,0110	0,0019	0,0000	0,0011	0,0020	0,0032	0,0080	0,0024
	m2	0,0290	0,0009	0,0240	0,0006	0,0180	0,0022	0,0240	0,0017
	m3	0,0030	0,0004	0,0070	0,0004	0,0010	0,0003	0,0000	0,0002
	m4	0,0020	0,0013	0,0000	0,0002	0,0000	0,0001	0,0000	0,0001
Asp-390 C2-C4	m0	0,9490	0,0020	0,9610	0,0032	0,9750	0,0047	0,9660	0,0033
	m1	0,0300	0,0002	0,0220	0,0028	0,0140	0,0025	0,0180	0,0017
	m2	0,0200	0,0008	0,0160	0,0010	0,0120	0,0025	0,0160	0,0020
	m3	0,0010	0,0016	0,0010	0,0006	0,0000	0,0002	0,0000	0,0003
Cit-591	m0	0,8010	0,0032	0,8250	0,0050	0,8370	0,0011	0,8220	0,0053
	m1	0,0300	0,0036	0,0180	0,0063	0,0170	0,0012	0,0300	0,0031
	m2	0,1480	0,0047	0,1530	0,0076	0,1420	0,0024	0,1360	0,0021
	m3	0,0090	0,0006	0,0010	0,0031	0,0010	0,0004	0,0030	0,0016
	m4	0,0130	0,0033	0,0000	0,0038	0,0030	0,0004	0,0040	0,0016
	m5	0,0000	0,0012	0,0000	0,0012	0,0000	0,0008	0,0020	0,0017
	m6	0,0000	0,0009	0,0050	0,0022	0,0000	0,0004	0,0030	0,0030
Cys-406 C1-C3	m0	0,9690	0,0050	1,1270	0,0325	0,9610	0,0065	0,9410	0,0326
	m1	0,0000	0,0031	0,0000	0,0231	0,0000	0,0070	0,0300	0,0141
	m2	0,0000	0,0010	0,0000	0,0123	0,0010	0,0006	0,0080	0,0046
	m3	0,0370	0,0041	0,0000	0,0111	0,0500	0,0008	0,0110	0,0103
Cys-378 C2-C3	m0	0,9980	0,0037	0,9290	0,0552	1,0020	0,0053	0,9070	0,0457
	m1	0,0000	0,0037	0,1390	0,1224	0,0040	0,0082	0,0400	0,0252
	m2	0,0040	0,0017	0,0000	0,0534	0,0000	0,0052	0,0220	0,0101
Fum-287	m0	0,9690	0,0057	1,0730	0,0288	1,0210	0,0076	1,0000	0,0118
	m1	0,0090	0,0025	0,0000	0,0037	0,0050	0,0028	0,0030	0,0009
	m2	0,0250	0,0007	0,0000	0,0327	0,0000	0,0057	0,0000	0,0112
	m3	0,0000	0,0039	0,0020	0,0066	0,0000	0,0041	0,0010	0,0009
	m4	0,0020	0,0015	0,0030	0,0014	0,0000	0,0008	0,0000	0,0002
Glu-432 C1-C5	m0	0,9570	0,0017	1,0050	0,0161	0,9790	0,0034	1,0490	0,0118
	m1	0,0030	0,0022	0,0000	0,0017	0,0060	0,0006	0,0040	0,0014

	m2	0,0340	0,0011	0,0020	0,0173	0,0160	0,0027	0,0000	0,0116
	m3	0,0030	0,0001	0,0020	0,0009	0,0000	0,0006	0,0000	0,0002
	m4	0,0010	0,0001	0,0010	0,0004	0,0000	0,0001	0,0010	0,0008
	m5	0,0020	0,0017	0,0000	0,0001	0,0000	0,0001	0,0000	0,0002
Gly-246 C1-C2	m0	0,9910	0,0004	0,9900	0,0003	1,0000	0,0008	0,9990	0,0002
	m1	0,0090	0,0004	0,0110	0,0008	0,0010	0,0007	0,0020	0,0002
	m2	0,0000	0,0002	0,0000	0,0004	0,0000	0,0002	0,0000	0,0002
Gly-218 C2	m0	0,9900	0,0003	0,9930	0,0006	1,0010	0,0010	0,9980	0,0002
	m1	0,0100	0,0001	0,0080	0,0005	0,0000	0,0009	0,0020	0,0002
Lac-261	m0	0,8160	0,0030	0,8240	0,0053	0,8380	0,0103	0,8340	0,0005
	m1	0,0120	0,0007	0,0100	0,0002	0,0080	0,0003	0,0010	0,0002
	m2	0,1710	0,0032	0,1580	0,0028	0,1400	0,0069	0,1640	0,0004
	m3	0,0010	0,0001	0,0020	0,0002	0,0010	0,0002	0,0010	0,0001
Mal-419	m0	0,9570	0,0009	0,9570	0,0014	0,9730	0,0011	0,9750	0,0020
	m1	0,0120	0,0020	0,0120	0,0004	0,0060	0,0009	0,0070	0,0020
	m2	0,0270	0,0004	0,0310	0,0013	0,0210	0,0003	0,0180	0,0000
	m3	0,0020	0,0005	0,0010	0,0002	0,0000	0,0004	0,0010	0,0000
	m4	0,0020	0,0010	0,0000	0,0001	0,0000	0,0000	0,0000	0,0000
Met-320 C1-C5	m0	0,9980	0,0013	1,0000	0,0026	0,9990	0,0009	0,9680	0,0223
	m1	0,0010	0,0012	0,0000	0,0040	0,0010	0,0020	0,0050	0,0013
	m2	0,0000	0,0010	0,0040	0,0018	0,0010	0,0012	0,0050	0,0025
	m3	0,0020	0,0003	0,0000	0,0017	0,0000	0,0012	0,0050	0,0037
	m4	0,0010	0,0009	0,0030	0,0011	0,0000	0,0007	0,0020	0,0025
	m5	0,0000	0,0004	0,0000	0,0003	0,0000	0,0009	0,0100	0,0084
Met-292 C2-C5	m0	1,0070	0,0032	1,0260	0,0065	0,9970	0,0010	1,0070	0,0032
	m1	0,0000	0,0011	0,0000	0,0042	0,0000	0,0011	0,0000	0,0011
	m2	0,0000	0,0012	0,0000	0,0015	0,0020	0,0009	0,0000	0,0012
	m3	0,0000	0,0005	0,0000	0,0061	0,0010	0,0014	0,0000	0,0005
	m4	0,0000	0,0018	0,0000	0,0014	0,0020	0,0003	0,0000	0,0018
Pro-286 C1-C5	m0	0,9660	0,0062	0,8150	0,0794	0,6390	0,0276	0,9910	0,0009
	m1	0,0060	0,0010	0,0040	0,0015	0,0000	0,0003	0,0000	0,0008
	m2	0,0220	0,0005	0,0190	0,0046	0,0030	0,0004	0,0150	0,0010
	m3	0,0080	0,0051	0,1600	0,0972	0,3330	0,0265	0,0000	0,0002
	m4	0,0000	0,0005	0,0000	0,0151	0,0090	0,0011	0,0000	0,0000
	m5	0,0000	0,0002	0,0080	0,0023	0,0180	0,0011	0,0000	0,0000
Pro-257 C2-C5	m0	0,9700	0,0010	0,9650	0,0011	0,9780	0,0016	0,9820	0,0018
	m1	0,0080	0,0007	0,0100	0,0017	0,0040	0,0026	0,0030	0,0006
	m2	0,0200	0,0003	0,0240	0,0010	0,0190	0,0017	0,0150	0,0008
	m3	0,0010	0,0002	0,0010	0,0002	0,0000	0,0002	0,0000	0,0003
	m4	0,0010	0,0013	0,0000	0,0007	0,0000	0,0004	0,0000	0,0004
Pyr-174	m0	0,6960	0,1242	0,7790	0,0262	x	x	0,8050	0,0122
	m1	0,0300	0,0128	0,0110	0,0021	x	x	0,0090	0,0048

	m2	0,2000	0,0731	0,1390	0,0127	x	x	0,1850	0,0109
	m3	0,0700	0,0402	0,0660	0,0351	x	x	0,0020	0,0050
Ser-390 C1-C3	m0	0,9740	0,0019	0,9760	0,0015	1,0000	0,0050	0,9860	0,0040
	m1	0,0170	0,0014	0,0100	0,0011	0,0000	0,0032	0,0090	0,0024
	m2	0,0100	0,0005	0,0130	0,0006	0,0010	0,0022	0,0050	0,0017
	m3	0,0000	0,0001	0,0000	0,0004	0,0010	0,0003	0,0000	0,0002
Ser-362 C2-C3	m0	0,9770	0,0018	0,9740	0,0004	1,0000	0,0004	0,9900	0,0012
	m1	0,0150	0,0012	0,0140	0,0004	0,0000	0,0008	0,0070	0,0012
	m2	0,0090	0,0008	0,0140	0,0007	0,0010	0,0006	0,0040	0,0003
Succ-289	m0	x	x	0,7330	0,0904	0,9730	0,0027	0,9440	0,0022
	m1	x	x	0,1860	0,0886	0,0050	0,0023	0,0330	0,0024
	m2	x	x	0,0990	0,0023	0,0220	0,0009	0,0220	0,0003
	m3	x	x	0,0000	0,0052	0,0000	0,0005	0,0010	0,0001
	m4	x	x	0,0000	0,0009	0,0000	0,0001	0,0000	0,0000
αKG-345	m0	1,0020	0,0017	0,9850	0,0130	1,0080	0,0046	0,9970	0,0032
	m1	0,0000	0,0029	0,0170	0,0077	0,0000	0,0047	0,0040	0,0023
	m2	0,0000	0,0004	0,0000	0,0031	0,0020	0,0021	0,0000	0,0006
	m3	0,0010	0,0009	0,0020	0,0018	0,0000	0,0006	0,0000	0,0006
	m4	0,0000	0,0005	0,0000	0,0018	0,0000	0,0004	0,0000	0,0010
	m5	0,0000	0,0002	0,0000	0,0009	0,0000	0,0001	0,0010	0,0005

Table A.II.1. Glucose incorporation to polar intracellular metabolites in NCM460, SW480, SW620, and LiM2 cell lines. Corrected isotopologue distribution from [1,2-^{13}C]-glucose to polar intracellular metabolites after incubation of 6h.

[1,2-^{13}C]-glucose 6h incubation		**NCM460**		**SW480**		**SW620**		**LiM2**	
Extracellular glucose		**Mean**	**SD**	**Mean**	**SD**	**Mean**	**SD**	**Mean**	**SD**
Glc-328	m0	0,5397	0,0008	0,5388	0,0387	0,5373	0,0001	0,5389	0,0004
	m1	0,0054	0,0001	0,0053	0,0008	0,0052	0,0003	0,0056	0,0001
	m2	0,4451	0,0024	0,4461	0,0351	0,4485	0,0021	0,4450	0,0002
	m3	0,0018	0,0002	0,0016	0,0007	0,0016	0,0004	0,0017	0,0000
	m4	0,0075	0,0001	0,0076	0,0008	0,0076	0,0002	0,0076	0,0001
	m5	0,0002	0,0003	0,0000	0,0005	-0,0002	0,0003	0,0003	0,0000
	m6	0,0002	0,0002	0,0003	0,0003	0,0001	0,0002	0,0003	0,0000

Table A.II.2. Glucose incorporation to extracellular glucose in NCM460, SW480, SW620, and LiM2 cell lines. Corrected isotopologue distribution from [1,2-^{13}C]-glucose to extracellular glucose after incubation of 6h.

[1,2-^{13}C]-glucose 6h incubation		NCM460		SW480		SW620		LiM2	
Extracellular lactate		Mean	SD	Mean	SD	Mean	SD	Mean	SD
Lac-328	m0	0,8111	0,0031	0,8263	0,0108	0,8433	0,0078	0,8195	0,0068
	m1	0,0122	0,0005	0,0108	0,0011	0,0039	0,0014	0,0109	0,0022
	m2	0,1621	0,0027	0,1476	0,0012	0,1350	0,0095	0,1591	0,0006
	m3	0,0037	0,0010	0,0032	0,0015	0,0044	0,0009	0,0026	0,0013

Table A.II.3. Glucose incorporation to extracellular lactate in NCM460, SW480, SW620, and LiM2 cell lines. Corrected isotopologue distribution from [1,2-^{13}C]-glucose to extracellular lactate after incubation of 6h.

[U-^{13}C]-glutamine 6h incubation		NCM460		SW480		SW620		LiM2	
Polar intracellular metabolites		Mean	SD	Mean	SD	Mean	SD	Mean	SD
Ala-259 C1-C3	m0	0,9870	0,0026	0,9840	0,0009	0,9540	0,0003	0,9650	0,0021
	m1	0,0000	0,0002	0,0000	0,0011	0,0030	0,0007	0,0000	0,0007
	m2	0,0050	0,0028	0,0020	0,0004	0,0080	0,0020	0,0040	0,0005
	m3	0,0200	0,0005	0,0330	0,0003	0,0370	0,0016	0,0340	0,0015
Ala-232 C2-C3	m0	1,0260	0,0027	1,0220	0,0009	0,9550	0,0011	0,9660	0,0015
	m1	0,0000	0,0001	0,0000	0,0007	0,0040	0,0004	0,0000	0,0002
	m2	0,0150	0,0026	0,0220	0,0005	0,0410	0,0009	0,0360	0,0016
Asp-418 C1-C4	m0	0,5350	0,0023	0,5890	0,0023	0,5040	0,0088	0,5050	0,0036
	m1	0,0240	0,0010	0,0000	0,0005	0,0140	0,0016	0,0090	0,0021
	m2	0,0670	0,0007	0,0790	0,0001	0,0660	0,0011	0,0560	0,0003
	m3	0,1000	0,0013	0,0570	0,0002	0,0680	0,0006	0,0720	0,0009
	m4	0,3050	0,0026	0,3470	0,0030	0,3870	0,0075	0,3970	0,0032
Asp-390 C2-C4	m0	0,5120	0,0009	0,5010	0,0018	0,4930	0,0025	0,4900	0,0046
	m1	0,0550	0,0015	0,0620	0,0008	0,0390	0,0007	0,0340	0,0019
	m2	0,0870	0,0010	0,0700	0,0005	0,0650	0,0007	0,0650	0,0007
	m3	0,3520	0,0021	0,3730	0,0015	0,4070	0,0040	0,4160	0,0037
Cit-591	m0	0,5440	0,0045	0,5090	0,0066	0,4760	0,0048	0,4840	0,0039
	m1	0,0490	0,0043	0,0330	0,0004	0,0210	0,0018	0,0300	0,0040
	m2	0,0930	0,0036	0,0850	0,0081	0,0860	0,0004	0,0530	0,0050
	m3	0,0500	0,0010	0,0540	0,0035	0,0560	0,0011	0,0640	0,0025
	m4	0,1990	0,0036	0,2750	0,0028	0,3050	0,0066	0,2980	0,0085
	m5	0,0610	0,0053	0,0360	0,0037	0,0490	0,0026	0,0600	0,0077
	m6	0,0100	0,0013	0,0120	0,0010	0,0140	0,0005	0,0120	0,0028
Cys-406 C1-C3	m0	0,9720	0,0041	1,1550	0,0518	0,9520	0,0044	0,9230	0,0869
	m1	0,0000	0,0043	0,0000	0,0732	0,0050	0,0079	0,0350	0,0300
	m2	0,0010	0,0007	0,0350	0,0371	0,0010	0,0024	0,0000	0,0020
	m3	0,0320	0,0032	0,0000	0,0104	0,0480	0,0026	0,0380	0,0536
Cys-378 C2-C3	m0	1,0000	0,0048	0,8260	0,0950	0,9990	0,0057	0,9010	0,0768
	m1	0,0020	0,0033	0,2950	0,1149	0,0070	0,0065	0,0380	0,0205
	m2	0,0000	0,0023	0,0000	0,0152	0,0000	0,0010	0,0160	0,0226
Fum-287	m0	0,5390	0,0020	0,5630	0,0175	0,5000	0,0087	0,4980	0,0012
	m1	0,0330	0,0012	0,0290	0,0016	0,0330	0,0050	0,0210	0,0006
	m2	0,0570	0,0009	0,0290	0,0180	0,0410	0,0094	0,0460	0,0018

	m3	0,0990	0,0002	0,0320	0,0040	0,0660	0,0035	0,0730	0,0016
	m4	0,2990	0,0015	0,3810	0,0066	0,3940	0,0035	0,3980	0,0020
Glu-432 C1-C5	m0	0,5210	0,0023	0,5260	0,0053	0,5010	0,0045	0,5480	0,0200
	m1	0,0100	0,0005	0,0000	0,0006	0,0100	0,0002	0,0050	0,0003
	m2	0,0160	0,0007	0,0000	0,0094	0,0000	0,0062	0,0000	0,0142
	m3	0,0690	0,0005	0,0950	0,0019	0,0680	0,0011	0,0330	0,0184
	m4	0,0150	0,0001	0,0160	0,0004	0,0160	0,0003	0,0150	0,0020
	m5	0,4090	0,0037	0,4080	0,0042	0,4520	0,0084	0,5250	0,0162
Gly-246 C1-C2	m0	1,0020	0,0006	1,0050	0,0007	1,0010	0,0012	1,0010	0,0011
	m1	0,0000	0,0006	0,0000	0,0008	0,0000	0,0015	0,0000	0,0005
	m2	0,0000	0,0002	0,0000	0,0003	0,0000	0,0005	0,0000	0,0007
Gly-218 C2	m0	1,0020	0,0011	1,0030	0,0002	0,9990	0,0009	1,0010	0,0008
	m1	0,0000	0,0008	0,0000	0,0003	0,0010	0,0012	0,0000	0,0004
Lac-261	m0	0,9610	0,0061	0,9590	0,0016	0,9660	0,0115	0,9930	0,0008
	m1	0,0000	0,0005	0,0010	0,0005	0,0000	0,0008	0,0000	0,0002
	m2	0,0080	0,0021	0,0070	0,0005	0,0110	0,0047	0,0020	0,0001
	m3	0,0320	0,0043	0,0310	0,0019	0,0080	0,0010	0,0140	0,0009
Mal-419	m0	0,5270	0,0028	0,5100	0,0006	0,5100	0,0033	0,5040	0,0030
	m1	0,0270	0,0003	0,0290	0,0009	0,0140	0,0017	0,0120	0,0010
	m2	0,0610	0,0009	0,0900	0,0006	0,0620	0,0005	0,0550	0,0010
	m3	0,1060	0,0008	0,0550	0,0007	0,0660	0,0001	0,0730	0,0010
	m4	0,3110	0,0009	0,3560	0,0013	0,3880	0,0018	0,3970	0,0030
Met-320 C1-C5	m0	0,9980	0,0009	1,0020	0,0021	1,0020	0,0026	0,9120	0,1014
	m1	0,0000	0,0020	0,0000	0,0039	0,0000	0,0038	0,0090	0,0075
	m2	0,0000	0,0024	0,0010	0,0043	0,0000	0,0003	0,0040	0,0059
	m3	0,0010	0,0005	0,0000	0,0013	0,0010	0,0014	0,0160	0,0197
	m4	0,0050	0,0044	0,0030	0,0009	0,0000	0,0005	0,0040	0,0065
	m5	0,0000	0,0010	0,0000	0,0002	0,0000	0,0002	0,0380	0,0435
Met-292 C2-C5	m0	1,0080	0,0030	1,0250	0,0019	1,0030	0,0045	1,0080	0,0030
	m1	0,0000	0,0008	0,0000	0,0015	0,0000	0,0021	0,0000	0,0008
	m2	0,0000	0,0015	0,0000	0,0016	0,0000	0,0025	0,0000	0,0015
	m3	0,0000	0,0006	0,0000	0,0035	0,0020	0,0005	0,0000	0,0006
	m4	0,0000	0,0012	0,0000	0,0005	0,0010	0,0004	0,0000	0,0012
Pro-286 C1-C5	m0	0,5680	0,0071	0,5400	0,0283	0,6070	0,0126	0,6420	0,0117
	m1	0,0150	0,0008	0,0170	0,0006	0,0040	0,0004	0,0040	0,0017
	m2	0,0150	0,0007	0,0110	0,0022	0,0040	0,0007	0,0080	0,0001
	m3	0,0550	0,0050	0,1430	0,0373	0,1220	0,0204	0,0030	0,0001
	m4	0,0000	0,0055	0,0000	0,0066	0,0180	0,0005	0,0000	0,0002
	m5	0,3800	0,0032	0,3100	0,0039	0,2530	0,0092	0,3820	0,0105

Pro-257 C2-C5	m0	0,5670	0,0012	0,5890	0,0008	0,5380	0,0047	0,5620	0,0079
	m1	0,0140	0,0004	0,0180	0,0002	0,0080	0,0008	0,0040	0,0038
	m2	0,0550	0,0005	0,0740	0,0010	0,0630	0,0002	0,0510	0,0006
	m3	0,0120	0,0000	0,0110	0,0005	0,0120	0,0008	0,0120	0,0003
	m4	0,3750	0,0009	0,3340	0,0012	0,4040	0,0033	0,3990	0,0042
Pyr-174	m0	0,8620	0,0096	0,8600	0,0229	x	x	0,9600	0,0021
	m1	0,0120	0,0011	0,0150	0,0007	x	x	0,0030	0,0031
	m2	0,0140	0,0064	0,0020	0,0041	x	x	0,0090	0,0042
	m3	0,1150	0,0061	0,1200	0,0234	x	x	0,0310	0,0010
Ser-390 C1-C3	m0	1,0000	0,0006	0,9990	0,0023	1,0050	0,0088	0,9950	0,0036
	m1	0,0010	0,0009	0,0020	0,0005	0,0000	0,0016	0,0050	0,0021
	m2	0,0000	0,0007	0,0000	0,0001	0,0000	0,0011	0,0010	0,0003
	m3	0,0000	0,0002	0,0010	0,0002	0,0010	0,0006	0,0000	0,0009
Ser-362 C2-C3	m0	1,0000	0,0007	0,9960	0,0002	1,0010	0,0015	0,9970	0,0015
	m1	0,0010	0,0005	0,0040	0,0003	0,0000	0,0013	0,0020	0,0017
	m2	0,0000	0,0004	0,0000	0,0006	0,0000	0,0004	0,0010	0,0002
Succ-289	m0	x	x	0,1120	0,0163	0,4470	0,0172	0,4650	0,0039
	m1	x	x	0,0530	0,0021	0,0140	0,0009	0,0280	0,0047
	m2	x	x	0,7140	0,0225	0,1770	0,0442	0,0560	0,0005
	m3	x	x	0,0000	0,0051	0,0000	0,0012	0,0140	0,0004
	m4	x	x	0,2440	0,0144	0,3880	0,0279	0,4670	0,0027
αKG-345	m0	1,0030	0,0019	1,0060	0,0051	1,0060	0,0044	0,8820	0,1015
	m1	0,0000	0,0011	0,0000	0,0069	0,0000	0,0036	0,0710	0,0631
	m2	0,0030	0,0021	0,0000	0,0011	0,0010	0,0003	0,0240	0,0258
	m3	0,0000	0,0008	0,0030	0,0030	0,0000	0,0014	0,0040	0,0027
	m4	0,0000	0,0001	0,0000	0,0012	0,0000	0,0003	0,0030	0,0023
	m5	0,0020	0,0009	0,0000	0,0005	0,0000	0,0001	0,0180	0,0086

Table A.II.4. Glutamine incorporation to polar intracellular metabolites in NCM460, SW480, SW620, and LiM2 cell lines. Corrected isotopologue distribution from [U-^{13}C]-glutamine to polar intracellular metabolites after incubation of 6h.

[U-^{13}C]-glutamine 6h incubation		NCM460		SW480		SW620		LiM2	
Extracellular lactate		Mean	SD	Mean	SD	Mean	SD	Mean	SD
Lac-328	m0	0,9568	0,0211	0,9439	0,0205	0,9849	0,0139	0,9777	0,0053
	m1	0,0037	0,0025	0,0066	0,0035	0,0000	0,0017	0,0032	0,0028
	m2	0,0099	0,0075	0,0089	0,0029	0,0069	0,0051	0,0033	0,0015
	m3	0,0177	0,0025	0,0223	0,0103	0,0077	0,0017	0,0090	0,0010

Table A.II.5. Glutamine incorporation to extracellular lactate in NCM460, SW480, SW620, and LiM2 cell lines. Corrected isotopologue distribution from [U-^{13}C]-glutamine extracellular lactate after incubation of 6h.

[1,2-^{13}C]-glucose 24h incubation		NCM460		SW480		SW620		LiM2	
Polar intracellular metabolites		Mean	SD	Mean	SD	Mean	SD	Mean	SD
Ala-259 C1-C3	m0	0,8040	0,0001	0,8270	0,0008	0,7950	0,0003	0,7910	0,0011
	m1	0,0050	0,0002	0,0000	0,0002	0,0150	0,0000	0,0110	0,0006
	m2	0,1890	0,0003	0,1710	0,0006	0,1890	0,0000	0,1970	0,0005
	m3	0,0030	0,0002	0,0030	0,0002	0,0020	0,0001	0,0020	0,0001
Ala-232 C2-C3	m0	0,8470	0,0011	0,8690	0,0011	0,7910	0,0080	0,7940	0,0009
	m1	0,0000	0,0003	0,0000	0,0002	0,0180	0,0044	0,0100	0,0006
	m2	0,1810	0,0007	0,1630	0,0009	0,1920	0,0041	0,1970	0,0004
Asp-418 C1-C4	m0	0,8540	0,0062	0,9630	0,0047	0,9320	0,0030	0,9250	0,0065
	m1	0,0520	0,0029	0,0000	0,0023	0,0160	0,0017	0,0200	0,0029
	m2	0,0810	0,0028	0,0560	0,0024	0,0480	0,0017	0,0520	0,0036
	m3	0,0120	0,0007	0,0120	0,0001	0,0030	0,0004	0,0030	0,0001
	m4	0,0020	0,0001	0,0010	0,0001	0,0010	0,0001	0,0000	0,0000
Asp-390 C2-C4	m0	0,8630	0,0065	0,8990	0,0019	0,9320	0,0040	0,9270	0,0048
	m1	0,0820	0,0044	0,0600	0,0010	0,0380	0,0026	0,0410	0,0021
	m2	0,0520	0,0025	0,0400	0,0008	0,0290	0,0020	0,0310	0,0024
	m3	0,0040	0,0003	0,0020	0,0004	0,0010	0,0004	0,0010	0,0004
Cit-591	m0	0,6700	0,0040	0,7340	0,0022	0,7470	0,0027	0,7410	0,0013
	m1	0,0700	0,0014	0,0490	0,0006	0,0320	0,0010	0,0410	0,0006
	m2	0,2100	0,0015	0,1930	0,0007	0,2020	0,0021	0,1980	0,0013
	m3	0,0250	0,0014	0,0130	0,0012	0,0090	0,0004	0,0080	0,0018
	m4	0,0210	0,0004	0,0100	0,0008	0,0100	0,0006	0,0100	0,0001
	m5	0,0030	0,0007	0,0000	0,0002	0,0000	0,0001	0,0010	0,0001
	m6	0,0010	0,0003	0,0010	0,0007	0,0000	0,0000	0,0000	0,0002
Cys-406 C1-C3	m0	0,9580	0,0102	1,0770	0,0153	0,9300	0,0455	1,0150	0,0073
	m1	0,0000	0,0015	0,0000	0,0171	0,0010	0,0049	0,0070	0,0011
	m2	0,0000	0,0019	0,0000	0,0011	0,0060	0,0020	0,0000	0,0006
	m3	0,0540	0,0103	0,0000	0,0057	0,0720	0,0486	0,0000	0,0067
Cys-378 C2-C3	m0	1,0000	0,0024	0,8710	0,0584	1,0020	0,0026	1,0040	0,0035
	m1	0,0000	0,0032	0,2280	0,1090	0,0000	0,0019	0,0030	0,0025
	m2	0,0060	0,0012	0,0000	0,0553	0,0000	0,0015	0,0000	0,0013
Fum-287	m0	0,8700	0,0090	0,9030	0,0029	0,9290	0,0040	0,9270	0,0041
	m1	0,0510	0,0030	0,0360	0,0016	0,0230	0,0001	0,0200	0,0014
	m2	0,0740	0,0017	0,0600	0,0012	0,0440	0,0038	0,0510	0,0026
	m3	0,0030	0,0047	0,0000	0,0014	0,0040	0,0012	0,0020	0,0003
	m4	0,0010	0,0001	0,0000	0,0005	0,0000	0,0007	0,0000	0,0001
Glu-432 C1-C5	m0	0,8380	0,0076	0,9080	0,0025	0,9320	0,0024	0,9570	0,0051
	m1	0,0400	0,0034	0,0090	0,0006	0,0140	0,0019	0,0210	0,0013

	m2	0,1010	0,0034	0,0730	0,0018	0,0510	0,0015	0,0180	0,0057
	m3	0,0140	0,0005	0,0070	0,0003	0,0010	0,0004	0,0020	0,0003
	m4	0,0070	0,0003	0,0030	0,0001	0,0010	0,0001	0,0020	0,0000
	m5	0,0010	0,0001	0,0000	0,0001	0,0000	0,0000	0,0000	0,0000
Gly-246 C1-C2	m0	0,9660	0,0014	0,9580	0,0008	0,9880	0,0012	0,9900	0,0005
	m1	0,0330	0,0012	0,0430	0,0008	0,0120	0,0012	0,0100	0,0004
	m2	0,0000	0,0002	0,0000	0,0001	0,0000	0,0000	0,0000	0,0001
Gly-218 C2	m0	0,9680	0,0020	0,9620	0,0007	0,9900	0,0014	0,9910	0,0005
	m1	0,0340	0,0017	0,0410	0,0007	0,0110	0,0012	0,0100	0,0004
Lac-261	m0	0,7910	0,0021	0,8060	0,0027	0,7940	0,0011	0,7940	0,0009
	m1	0,0170	0,0009	0,0170	0,0004	0,0140	0,0008	0,0080	0,0003
	m2	0,1910	0,0013	0,1760	0,0025	0,1910	0,0006	0,1980	0,0008
	m3	0,0020	0,0002	0,0020	0,0003	0,0010	0,0002	0,0010	0,0001
Mal-419	m0	0,8600	0,0052	0,8960	0,0016	0,9310	0,0031	0,9290	0,0030
	m1	0,0520	0,0023	0,0350	0,0009	0,0180	0,0017	0,0210	0,0010
	m2	0,0760	0,0029	0,0650	0,0007	0,0480	0,0013	0,0480	0,0010
	m3	0,0100	0,0001	0,0050	0,0006	0,0020	0,0002	0,0030	0,0000
	m4	0,0020	0,0001	0,0000	0,0001	0,0010	0,0001	0,0000	0,0000
Met-320 C1-C5	m0	0,9890	0,0008	0,9830	0,0018	0,9820	0,0023	0,9820	0,0012
	m1	0,0040	0,0005	0,0070	0,0010	0,0090	0,0010	0,0060	0,0001
	m2	0,0050	0,0005	0,0040	0,0004	0,0090	0,0007	0,0100	0,0004
	m3	0,0020	0,0004	0,0010	0,0002	0,0000	0,0003	0,0010	0,0003
	m4	0,0000	0,0014	0,0080	0,0010	0,0000	0,0010	0,0000	0,0003
	m5	0,0000	0,0003	0,0000	0,0007	0,0000	0,0002	0,0010	0,0006
Met-292 C2-C5	m0	0,9960	0,0019	1,0050	0,0017	0,9900	0,0013	0,9960	0,0019
	m1	0,0000	0,0007	0,0000	0,0003	0,0020	0,0020	0,0000	0,0007
	m2	0,0050	0,0008	0,0020	0,0016	0,0060	0,0019	0,0050	0,0008
	m3	0,0000	0,0002	0,0000	0,0003	0,0010	0,0001	0,0000	0,0002
	m4	0,0000	0,0008	0,0000	0,0002	0,0010	0,0008	0,0000	0,0008
Pro-286 C1-C5	m0	0,8900	0,0031	0,8930	0,0238	1,0520	0,1758	0,9630	0,0016
	m1	0,0330	0,0012	0,0200	0,0011	0,0070	0,0018	0,0060	0,0011
	m2	0,0770	0,0013	0,0520	0,0019	0,0350	0,0105	0,0420	0,0009
	m3	0,0050	0,0045	0,0470	0,0308	0,0000	0,1727	0,0000	0,0003
	m4	0,0000	0,0027	0,0000	0,0063	0,0030	0,0075	0,0000	0,0000
	m5	0,0000	0,0001	0,0030	0,0021	0,0120	0,0094	0,0010	0,0000
Pro-257 C2-C5	m0	0,8850	0,0032	0,9220	0,0006	0,9400	0,0009	0,9470	0,0015
	m1	0,0410	0,0016	0,0260	0,0005	0,0150	0,0004	0,0120	0,0011
	m2	0,0640	0,0013	0,0490	0,0004	0,0430	0,0006	0,0390	0,0006
	m3	0,0090	0,0002	0,0030	0,0005	0,0020	0,0000	0,0020	0,0003
	m4	0,0010	0,0000	0,0000	0,0003	0,0000	0,0001	0,0000	0,0001
Pyr-174	m0	0,7900	0,0033	0,8080	0,0030	x	x	0,7850	0,0057
	m1	0,0240	0,0020	0,0220	0,0005	x	x	0,0110	0,0016

	m2	0,1830	0,0049	0,1620	0,0034	x	x	0,2050	0,0026
	m3	0,0030	0,0003	0,0070	0,0045	x	x	0,0000	0,0019
Ser-390 C1-C3	m0	0,9050	0,0006	0,8760	0,0047	0,9690	0,0030	0,9580	0,0065
	m1	0,0800	0,0005	0,0950	0,0023	0,0250	0,0017	0,0330	0,0029
	m2	0,0160	0,0002	0,0310	0,0024	0,0050	0,0017	0,0090	0,0036
	m3	0,0000	0,0001	0,0000	0,0001	0,0010	0,0004	0,0010	0,0001
Ser-362 C2-C3	m0	0,9090	0,0019	0,8780	0,0022	0,9700	0,0005	0,9610	0,0008
	m1	0,0780	0,0020	0,0960	0,0023	0,0230	0,0009	0,0310	0,0004
	m2	0,0160	0,0003	0,0310	0,0004	0,0070	0,0009	0,0100	0,0007
Succ-289	m0	x	x	0,9780	0,0222	0,9230	0,0021	0,9210	0,0034
	m1	x	x	0,0000	0,0044	0,0220	0,0025	0,0220	0,0041
	m2	x	x	0,0300	0,0305	0,0510	0,0015	0,0530	0,0008
	m3	x	x	0,0000	0,0042	0,0030	0,0002	0,0030	0,0003
	m4	x	x	0,0000	0,0002	0,0010	0,0003	0,0010	0,0001
αKG-345	m0	1,0020	0,0010	0,9980	0,0029	1,0070	0,0015	0,9970	0,0014
	m1	0,0010	0,0017	0,0070	0,0026	0,0000	0,0019	0,0050	0,0014
	m2	0,0000	0,0020	0,0000	0,0006	0,0030	0,0016	0,0000	0,0004
	m3	0,0010	0,0005	0,0020	0,0007	0,0000	0,0003	0,0000	0,0003
	m4	0,0000	0,0000	0,0000	0,0002	0,0000	0,0003	0,0000	0,0001
	m5	0,0000	0,0001	0,0000	0,0002	0,0000	0,0000	0,0000	0,0002

Table A.II.6. Glucose incorporation to polar intracellular metabolites in NCM460, SW480, SW620, and LiM2 cell lines. Corrected isotopologue distribution from [1,2-^{13}C]-glucose to polar intracellular metabolites after incubation of 24h.

[1,2-^{13}C]-glucose 24h incubation		**NCM460**		**SW480**		**SW620**		**LiM2**	
Extracellular glucose		**Mean**	**SD**	**Mean**	**SD**	**Mean**	**SD**	**Mean**	**SD**
Glc-328	m0	0,5399	0,0008	0,5389	0,0387	0,5401	0,0001	0,5377	0,0004
	m1	0,0057	0,0001	0,0060	0,0008	0,0054	0,0003	0,0056	0,0001
	m2	0,4430	0,0024	0,4440	0,0351	0,4438	0,0021	0,4420	0,0002
	m3	0,0022	0,0002	0,0020	0,0007	0,0019	0,0004	0,0028	0,0000
	m4	0,0079	0,0001	0,0078	0,0008	0,0077	0,0002	0,0080	0,0001
	m5	0,0003	0,0003	0,0005	0,0005	0,0003	0,0003	0,0014	0,0000
	m6	0,0004	0,0002	0,0004	0,0003	0,0003	0,0002	0,0008	0,0000

Table A.II.7. Glucose incorporation to extracellular glucose in NCM460, SW480, SW620, and LiM2 cell lines. Corrected isotopologue distribution from [1,2-^{13}C]-glucose to extracellular glucose after incubation of 24h.

[1,2-^{13}C]-glucose 24h incubation		NCM460		SW480		SW620		LiM2	
Extracellular lactate		Mean	SD	Mean	SD	Mean	SD	Mean	SD
Lac-328	m0	0,7936	0,0038	0,8026	0,0031	0,8014	0,0034	0,7870	0,0045
	m1	0,0162	0,0002	0,0171	0,0004	0,0057	0,0003	0,0128	0,0003
	m2	0,1836	0,0021	0,1755	0,0009	0,1859	0,0033	0,1946	0,0006
	m3	0,0027	0,0006	0,0023	0,0006	0,0018	0,0013	0,0016	0,0006

Table A.II.8. Glucose incorporation to extracellular lactate in NCM460, SW480, SW620, and LiM2 cell lines. Corrected isotopologue distribution from [1,2-^{13}C]-glucose to extracellular lactate after incubation of 24h.

[1,2-^{13}C]-glucose 24h incubation		NCM460		SW480		SW620		LiM2	
Extracellular amino acids		Mean	SD	Mean	SD	Mean	SD	Mean	SD
Glu-228 C1-C5	m0	0,9721	0,0073	0,9214	0,0722	0,9770	0,0068	0,9880	0,0103
	m1	0,0000	0,0031	0,0056	0,0226	0,0009	0,0139	0,0000	0,0078
	m2	0,0325	0,0094	0,0381	0,0061	0,0171	0,0105	0,0246	0,0072
	m3	0,0036	0,0004	0,0168	0,0236	0,0000	0,0036	0,0000	0,0046
	m4	0,0010	0,0029	0,0160	0,0232	0,0034	0,0057	0,0024	0,0019
	m5	0,0013	0,0008	0,0011	0,0028	0,0008	0,0024	0,0000	0,0007
Gln-228 C1-C5	m0	1,0039	0,0033	1,0018	0,0041	1,0129	0,0081	1,0080	0,0021
	m1	0,0000	0,0018	0,0000	0,0036	0,0000	0,0085	0,0000	0,0033
	m2	0,0084	0,0016	0,0115	0,0003	0,0035	0,0004	0,0081	0,0008
	m3	0,0006	0,0005	0,0016	0,0007	0,0005	0,0004	0,0005	0,0006
	m4	0,0007	0,0003	0,0004	0,0001	0,0001	0,0001	0,0005	0,0001
	m5	0,0019	0,0028	0,0023	0,0004	0,0020	0,0012	0,0000	0,0007

Table A.II.9. Glucose incorporation to extracellular amino acids glutamate and glutamine in NCM460, SW480, SW620, and LiM2 cell lines. Corrected isotopologue distribution from [1,2-^{13}C]-glucose to extracellular amino acids glutamate and glutamine after incubation of 24h.

[1,2-^{13}C]-glucose 24h incubation		NCM460		SW480		SW620		LiM2	
Extracellular ribose		Mean	SD	Mean	SD	Mean	SD	Mean	SD
Ribose-257	m0	0,8311	0,0073	0,7682	0,0062	0,6942	0,0018	0,7020	0,0020
	m1	0,0845	0,0054	0,1289	0,0069	0,1582	0,0007	0,1608	0,0023
	m2	0,0567	0,0053	0,0683	0,0037	0,0992	0,0013	0,0886	0,0025
	m3	0,0170	0,0037	0,0186	0,0016	0,0324	0,0038	0,0347	0,0014
	m4	0,0094	0,0025	0,0088	0,0036	0,0143	0,0012	0,0123	0,0009
	m5	0,0004	0,0003	0,0033	0,0055	0,0004	0,0003	0,0005	0,0002

Table A.II.10. Glucose incorporation to intracellular ribose in NCM460, SW480, SW620, and LiM2 cell lines. Corrected isotopologue distribution from [1,2-^{13}C]-glucose to intracellular ribose after incubation of 24h.

[U-^{13}C]-glutamine 24h incubation		NCM460		SW480		SW620		LiM2	
Polar intracellular metabolites		Mean	SD	Mean	SD	Mean	SD	Mean	SD
Ala-259 C1-C3	m0	0,9850	0,0005	0,9780	0,0009	0,9680	0,0005	0,9780	0,0001
	m1	0,0000	0,0003	0,0000	0,0003	0,0050	0,0007	0,0010	0,0003
	m2	0,0030	0,0002	0,0030	0,0002	0,0050	0,0001	0,0030	0,0000
	m3	0,0210	0,0001	0,0320	0,0004	0,0240	0,0003	0,0200	0,0002
Ala-232 C2-C3	m0	1,0230	0,0000	1,0150	0,0004	0,9680	0,0006	0,9770	0,0008
	m1	0,0000	0,0001	0,0000	0,0001	0,0070	0,0007	0,0030	0,0007
	m2	0,0140	0,0001	0,0220	0,0003	0,0250	0,0003	0,0210	0,0001
Asp-418 C1-C4	m0	0,5710	0,0033	0,5890	0,0028	0,5010	0,0024	0,4980	0,0029
	m1	0,0730	0,0006	0,0000	0,0005	0,0360	0,0007	0,0330	0,0033
	m2	0,1080	0,0008	0,1090	0,0005	0,1030	0,0003	0,1020	0,0027
	m3	0,0490	0,0012	0,0460	0,0004	0,0490	0,0002	0,0520	0,0005
	m4	0,2210	0,0025	0,2920	0,0018	0,3460	0,0020	0,3490	0,0024
Asp-390 C2-C4	m0	0,5610	0,0039	0,5150	0,0018	0,4920	0,0016	0,4890	0,0007
	m1	0,1150	0,0008	0,1000	0,0007	0,0750	0,0007	0,0750	0,0028
	m2	0,0830	0,0019	0,0790	0,0004	0,0750	0,0004	0,0780	0,0009
	m3	0,2460	0,0020	0,3090	0,0018	0,3620	0,0010	0,3600	0,0026
Cit-591	m0	0,5470	0,0064	0,4970	0,0023	0,4190	0,0505	0,4780	0,0015
	m1	0,0930	0,0015	0,0660	0,0015	0,0510	0,0080	0,0490	0,0022
	m2	0,1200	0,0011	0,1130	0,0009	0,1170	0,0069	0,0970	0,0004
	m3	0,0390	0,0008	0,0460	0,0007	0,0630	0,0140	0,0480	0,0001
	m4	0,1740	0,0049	0,2600	0,0004	0,2660	0,0373	0,2990	0,0063
	m5	0,0240	0,0015	0,0130	0,0010	0,0450	0,0030	0,0260	0,0027
	m6	0,0060	0,0005	0,0110	0,0009	0,0180	0,0105	0,0090	0,0010
Cys-406 C1-C3	m0	0,9590	0,0065	1,0170	0,0087	0,9680	0,0057	0,9960	0,0051
	m1	0,0000	0,0025	0,0000	0,0098	0,0090	0,0037	0,0260	0,0006
	m2	0,0000	0,0004	0,0070	0,0062	0,0030	0,0012	0,0000	0,0023
	m3	0,0520	0,0069	0,0000	0,0005	0,0260	0,0071	0,0000	0,0027
Cys-378 C2-C3	m0	0,9990	0,0017	0,7780	0,0081	1,0080	0,0028	0,9890	0,0005
	m1	0,0000	0,0017	0,3790	0,0146	0,0000	0,0049	0,0100	0,0004
	m2	0,0020	0,0003	0,0000	0,0036	0,0000	0,0025	0,0000	0,0025
Fum-287	m0	0,5560	0,0057	0,5030	0,0020	0,4760	0,0020	0,4800	0,0019
	m1	0,0820	0,0016	0,0690	0,0005	0,0540	0,0034	0,0470	0,0015
	m2	0,1000	0,0012	0,1130	0,0003	0,0980	0,0008	0,1010	0,0025
	m3	0,0510	0,0024	0,0390	0,0004	0,0490	0,0007	0,0510	0,0003
	m4	0,2320	0,0026	0,3030	0,0032	0,3540	0,0022	0,3520	0,0021
Glu-432 C1-C5	m0	0,5440	0,0027	0,5150	0,0004	0,5120	0,0080	0,5120	0,0017
	m1	0,0540	0,0010	0,0210	0,0007	0,0250	0,0005	0,0240	0,0009

	m2	0,0420	0,0005	0,0310	0,0006	0,0170	0,0033	0,0000	0,0076
	m3	0,1130	0,0014	0,1230	0,0013	0,1030	0,0010	0,1060	0,0012
	m4	0,0110	0,0002	0,0140	0,0000	0,0130	0,0006	0,0150	0,0002
	m5	0,2630	0,0048	0,3290	0,0029	0,3690	0,0038	0,4140	0,0084
Gly-246 C1-C2	m0	1,0010	0,0008	1,0020	0,0007	0,9990	0,0003	1,0010	0,0007
	m1	0,0000	0,0007	0,0000	0,0006	0,0010	0,0004	0,0000	0,0009
	m2	0,0000	0,0003	0,0000	0,0001	0,0010	0,0001	0,0000	0,0002
Gly-218 C2	m0	1,0000	0,0002	1,0030	0,0002	0,9990	0,0006	1,0010	0,0003
	m1	0,0000	0,0003	0,0000	0,0002	0,0010	0,0006	0,0000	0,0002
Lac-261	m0	0,9680	0,0017	0,9670	0,0027	0,9670	0,0153	0,9860	0,0010
	m1	0,0040	0,0006	0,0040	0,0011	0,0160	0,0135	0,0000	0,0006
	m2	0,0060	0,0002	0,0050	0,0004	0,0050	0,0029	0,0020	0,0002
	m3	0,0240	0,0009	0,0240	0,0013	0,0130	0,0026	0,0140	0,0003
Mal-419	m0	0,5570	0,0020	0,5140	0,0018	0,4990	0,0039	0,5040	0,0040
	m1	0,0770	0,0014	0,0590	0,0006	0,0390	0,0002	0,0370	0,0020
	m2	0,1060	0,0010	0,1210	0,0006	0,1000	0,0005	0,1020	0,0020
	m3	0,0540	0,0006	0,0420	0,0005	0,0480	0,0009	0,0500	0,0000
	m4	0,2300	0,0004	0,2970	0,0031	0,3510	0,0041	0,3440	0,0010
Met-320 C1-C5	m0	0,9970	0,0010	0,9960	0,0017	0,9950	0,0041	0,9920	0,0028
	m1	0,0030	0,0014	0,0030	0,0009	0,0050	0,0017	0,0010	0,0008
	m2	0,0000	0,0009	0,0000	0,0013	0,0000	0,0003	0,0020	0,0003
	m3	0,0010	0,0004	0,0000	0,0001	0,0000	0,0007	0,0010	0,0004
	m4	0,0000	0,0007	0,0040	0,0022	0,0000	0,0023	0,0000	0,0002
	m5	0,0010	0,0013	0,0000	0,0006	0,0000	0,0003	0,0030	0,0008
Met-292 C2-C5	m0	1,0040	0,0006	1,0060	0,0017	1,0010	0,0019	1,0040	0,0006
	m1	0,0000	0,0005	0,0000	0,0007	0,0000	0,0020	0,0000	0,0005
	m2	0,0000	0,0001	0,0000	0,0008	0,0000	0,0003	0,0000	0,0001
	m3	0,0000	0,0000	0,0000	0,0009	0,0000	0,0002	0,0000	0,0000
	m4	0,0000	0,0002	0,0000	0,0012	0,0010	0,0002	0,0000	0,0002
Pro-286 C1-C5	m0	0,5560	0,0014	0,5410	0,0033	0,8940	0,0687	0,5850	0,0153
	m1	0,0490	0,0001	0,0300	0,0014	0,0250	0,0034	0,0160	0,0003
	m2	0,0360	0,0003	0,0240	0,0004	0,0240	0,0033	0,0200	0,0002
	m3	0,0950	0,0016	0,1270	0,0060	0,0000	0,1051	0,0310	0,0164
	m4	0,0010	0,0023	0,0000	0,0081	0,1300	0,1314	0,1830	0,1632
	m5	0,2820	0,0010	0,3040	0,0037	0,0950	0,1165	0,1900	0,1604
Pro-257 C2-C5	m0	0,5640	0,0005	0,5520	0,0020	0,5170	0,0022	0,5340	0,0087
	m1	0,0580	0,0007	0,0440	0,0006	0,0290	0,0002	0,0260	0,0019
	m2	0,1050	0,0007	0,1070	0,0006	0,1010	0,0007	0,0900	0,0021
	m3	0,0110	0,0001	0,0110	0,0004	0,0120	0,0002	0,0110	0,0001
	m4	0,2800	0,0007	0,3070	0,0009	0,3650	0,0023	0,3650	0,0053
Pyr-174	m0	0,9270	0,0022	0,8900	0,0022	x	x	0,8650	0,1061
	m1	0,0170	0,0012	0,0230	0,0011	x	x	0,0330	0,0312

	m2	0,0120	0,0008	0,0160	0,0003	x	x	0,0190	0,0136
	m3	0,0450	0,0013	0,0730	0,0015	x	x	0,0420	0,0188
Ser-390 C1-C3	m0	0,9980	0,0004	0,9990	0,0028	1,0050	0,0024	0,9960	0,0029
	m1	0,0020	0,0006	0,0010	0,0005	0,0000	0,0007	0,0050	0,0033
	m2	0,0000	0,0001	0,0010	0,0005	0,0000	0,0003	0,0000	0,0027
	m3	0,0000	0,0004	0,0000	0,0004	0,0010	0,0002	0,0000	0,0005
Ser-362 C2-C3	m0	0,9990	0,0019	0,9960	0,0011	1,0040	0,0009	0,9990	0,0005
	m1	0,0020	0,0016	0,0040	0,0003	0,0000	0,0010	0,0000	0,0003
	m2	0,0000	0,0008	0,0010	0,0014	0,0000	0,0006	0,0020	0,0002
Succ-289	m0	x	x	0,1360	0,0103	0,4360	0,0428	0,4680	0,0008
	m1	x	x	0,0000	0,0157	0,0280	0,0043	0,0270	0,0024
	m2	x	x	0,8900	0,0096	0,2200	0,1186	0,1050	0,0025
	m3	x	x	0,0000	0,0027	0,0000	0,0031	0,0130	0,0005
	m4	x	x	0,1170	0,0068	0,3400	0,0732	0,4140	0,0001
αKG-346	m0	1,0000	0,0010	1,0010	0,0009	1,0080	0,0022	0,9870	0,0001
	m1	0,0000	0,0023	0,0040	0,0011	0,0000	0,0051	0,0090	0,0003
	m2	0,0000	0,0006	0,0000	0,0013	0,0040	0,0028	0,0000	0,0008
	m3	0,0010	0,0007	0,0030	0,0003	0,0000	0,0010	0,0000	0,0002
	m4	0,0000	0,0003	0,0000	0,0003	0,0000	0,0002	0,0000	0,0001
	m5	0,0020	0,0002	0,0000	0,0002	0,0010	0,0003	0,0050	0,0008

Table A.II.11. Glutamine incorporation to polar intracellular metabolites in NCM460, SW480, SW620, and LiM2 cell lines. Corrected isotopologue distribution from [U-^{13}C]-glutamine to polar intracellular metabolites after incubation of 24h.

[U-^{13}C]-glutamine 24h incubation		**NCM460**		**SW480**		**SW620**		**LiM2**	
Extracellular lactate		**Mean**	**SD**	**Mean**	**SD**	**Mean**	**SD**	**Mean**	**SD**
Lac-328	m0	0,9700	0,0053	0,9691	0,0037	0,9904	0,0020	0,9862	0,0014
	m1	0,0038	0,0006	0,0038	0,0007	0,0000	0,0003	0,0023	0,0006
	m2	0,0057	0,0022	0,0061	0,0004	0,0033	0,0006	0,0016	0,0011
	m3	0,0189	0,0007	0,0181	0,0006	0,0106	0,0005	0,0111	0,0002

Table A.II.12. Glutamine incorporation to polar extracellular lactate in NCM460, SW480, SW620, and LiM2 cell lines. Corrected isotopologue distribution from [U-^{13}C]-glutamine to extracellular lactate after incubation of 24h.

10.3 RESULTS *IN VIVO*

The results presented here are the corrected isotopologue distributions from polar intracellular metabolites after 15 minutes bolus of [1,2-^{13}C]-glucose (Table A.I.13) or two 15 minutes boluses of [U-^{13}C]-glutamine (Table A.I.14) to immunocompromised NOD/SCID mice waring xenografts of SW480, SW620, and LiM2 cell lines.

[U-^{13}C]-glucose bolus		SW480		SW620		LiM2	
Polar intracellular metabolites		Mean	SD	Mean	SD	Mean	SD
Asp-418 C1-C4	m0	0,92760	0,01210	0,95739	0,00719	0,95090	0,00439
	m1	0,02581	0,00406	0,01344	0,00285	0,01676	0,00100
	m2	0,04096	0,00688	0,02446	0,00402	0,02642	0,00299
	m3	0,00536	0,00235	0,00453	0,00088	0,00586	0,00087
	m4	0,00067	0,00043	0,00049	0,00019	0,00038	0,00017
Cit-591	m0	0,88271	0,02366	0,93342	0,00627	0,93132	0,00694
	m1	0,03212	0,00812	0,01273	0,00393	0,01178	0,00171
	m2	0,07475	0,01375	0,04897	0,00362	0,05082	0,00577
	m3	0,00695	0,00230	0,00336	0,00078	0,00434	0,00033
	m4	0,00296	0,00091	0,00143	0,00024	0,00143	0,00052
	m5	0,00053	0,00037	0,00005	0,00017	0,00032	0,00024
	m6	0,00007	0,00011	0,00006	0,00012	0,00007	0,00004
Fum-287	m0	0,93911	0,01129	0,95490	0,01010	0,95571	0,00183
	m1	0,02015	0,00369	0,01827	0,00961	0,01354	0,00178
	m2	0,03424	0,00630	0,02358	0,00137	0,02440	0,00059
	m3	0,00608	0,00199	0,00504	0,00304	0,00572	0,00066
	m4	0,00062	0,00059	0,00000	0,00226	0,00072	0,00037
Glu-432 C1-C5	m0	0,92053	0,00880	0,95355	0,00439	0,94124	0,00456
	m1	0,01461	0,00705	0,00404	0,00247	0,01215	0,00237
	m2	0,06056	0,00968	0,03931	0,00509	0,04457	0,00396
	m3	0,00248	0,00103	0,00209	0,00069	0,00115	0,00117
	m4	0,00157	0,00087	0,00109	0,00023	0,00062	0,00019
	m5	0,00043	0,00043	0,00000	0,00053	0,00029	0,00028
Lac-261	m0	0,83617	0,02594	0,91765	0,01400	0,90403	0,00756
	m1	0,01776	0,00232	0,00960	0,00255	0,00939	0,00554
	m2	0,02177	0,00205	0,01330	0,00090	0,01445	0,00157
	m3	0,13328	0,02750	0,06374	0,01356	0,07728	0,00434
Mal-419	m0	0,93912	0,01428	0,96121	0,00733	0,95871	0,00309
	m1	0,01487	0,00504	0,00794	0,00361	0,00720	0,00248
	m2	0,03886	0,00760	0,02586	0,00438	0,02766	0,00116
	m3	0,00668	0,00246	0,00500	0,00100	0,00618	0,00081

	m4	0,00102	0,00039	0,00038	0,00040	0,00064	0,00026
Succ-289	m0	0,93687	0,01852	0,96372	0,01202	0,95727	0,00457
	m1	0,01429	0,00544	0,00423	0,00609	0,00636	0,00216
	m2	0,04379	0,01166	0,02975	0,00590	0,03349	0,00260
	m3	0,00436	0,00159	0,00198	0,00067	0,00262	0,00019
	m4	0,00081	0,00034	0,00050	0,00051	0,00032	0,00016
αKG-345	m0	0,92373	0,01790	0,94501	0,00115	0,94204	0,00879
	m1	0,01255	0,00465	0,00784	0,00184	0,00945	0,00374
	m2	0,05809	0,01201	0,04373	0,00224	0,04437	0,00758
	m3	0,00307	0,00086	0,00172	0,00389	0,00146	0,00174
	m4	0,00199	0,00086	0,00067	0,00164	0,00202	0,00081
	m5	0,00061	0,00108	0,00037	0,00065	0,00082	0,00045

Table A.II.13. Glucose incorporation to polar intracellular metabolites in SW480, SW620, and LiM2 xenografts. Corrected isotopologue distribution from [U-^{13}C]-glucose to polar intracellular metabolites after a bolus of 15 minutes.

[U-^{13}C]-glutamine bolus		SW480		SW620		LiM2	
Polar intracellular metabolites		**Mean**	**SD**	**Mean**	**SD**	**Mean**	**SD**
Asp-418 C1-C4	m0	0,8510	0,0048	0,8516	0,0222	0,8224	0,0231
	m1	0,0284	0,0025	0,0204	0,0046	0,0247	0,0022
	m2	0,0441	0,0028	0,0366	0,0076	0,0438	0,0053
	m3	0,0095	0,0007	0,0125	0,0010	0,0140	0,0017
	m4	0,0745	0,0017	0,0880	0,0121	0,1057	0,0165
Cit-591	m0	0,8632	0,0140	0,8931	0,0195	0,8758	0,0204
	m1	0,0303	0,0027	0,0192	0,0053	0,0219	0,0045
	m2	0,0364	0,0033	0,0302	0,0045	0,0361	0,0042
	m3	0,0156	0,0034	0,0118	0,0019	0,0128	0,0026
	m4	0,0351	0,0039	0,0340	0,0077	0,0421	0,0077
	m5	0,0187	0,0035	0,0112	0,0016	0,0105	0,0024
	m6	0,0019	0,0007	0,0014	0,0005	0,0018	0,0008
Fum-287	m0	0,8617	0,0019	0,8568	0,0119	0,8538	0,0264
	m1	0,0254	0,0020	0,0212	0,0032	0,0203	0,0046
	m2	0,0388	0,0016	0,0334	0,0044	0,0354	0,0079
	m3	0,0093	0,0005	0,0130	0,0011	0,0128	0,0010
	m4	0,0691	0,0016	0,0806	0,0066	0,0831	0,0163
Glu-432 C1-C5	m0	0,8363	0,0092	0,8268	0,0125	0,8080	0,0251
	m1	0,0183	0,0088	0,0142	0,0046	0,0168	0,0046
	m2	0,0222	0,0036	0,0190	0,0055	0,0211	0,0035
	m3	0,0382	0,0048	0,0352	0,0065	0,0466	0,0069
	m4	0,0043	0,0002	0,0055	0,0008	0,0056	0,0009
	m5	0,0888	0,0049	0,1111	0,0185	0,1145	0,0121
Lac-261	m0	0,9541	0,0066	0,9679	0,0123	0,9622	0,0128
	m1	0,0168	0,0033	0,0099	0,0077	0,0134	0,0077
	m2	0,0151	0,0014	0,0117	0,0030	0,0125	0,0030
	m3	0,0152	0,0024	0,0115	0,0022	0,0130	0,0033
Mal-419	m0	0,8560	0,0075	0,8565	0,0144	0,8372	0,0259
	m1	0,0198	0,0011	0,0155	0,0043	0,0183	0,0033
	m2	0,0424	0,0008	0,0373	0,0057	0,0431	0,0064
	m3	0,0123	0,0024	0,0137	0,0004	0,0141	0,0024
	m4	0,0780	0,0064	0,0865	0,0078	0,0978	0,0170
Succ-289	m0	0,8639	0,0168	0,8659	0,0091	0,8550	0,0323
	m1	0,0179	0,0033	0,0125	0,0027	0,0144	0,0041
	m2	0,0423	0,0032	0,0384	0,0075	0,0456	0,0105
	m3	0,0061	0,0005	0,0057	0,0010	0,0055	0,0010
	m4	0,0749	0,0117	0,0830	0,0077	0,0855	0,0188

αKG-345	m0	0,8488	0,0121	0,8359	0,0110	0,8138	0,0263
	m1	0,0125	0,0049	0,0152	0,0027	0,0213	0,0079
	m2	0,0251	0,0091	0,0214	0,0045	0,0242	0,0010
	m3	0,0328	0,0015	0,0328	0,0074	0,0427	0,0071
	m4	0,0022	0,0026	0,0035	0,0013	0,0044	0,0016
	m5	0,0840	0,0104	0,0971	0,0056	0,1001	0,0133

Table A.II.14. Glutamine incorporation to polar intracellular metabolites in SW480, SW620, and LiM2 xenografts. Corrected isotopologue distribution from [U-^{13}C]-glutamine to polar intracellular metabolites after two boluses of 15 minutes each.

11. Appendix III

11 APPENDIX III

Mitochondrial function experiments in Seahorse Analyser for the primary (SW480) and metastatic (SW620 and LiM2) colon cancer cell lines.

The experiments that are shown in the present appendix and discussed in section 5.1.2.2. were performed by Xavier Hernández-Alias under the supervision of Dr Fionnuala Morrish and Dr David Hockenbery at the Fred Hutchinson Cancer Research Center in Seattle.

11.1 MATERIALS AND METHODS

Oxygen consumption rates were measured using a Seahorse XF24 Flux Analyzer (Seahorse Bioscience, USA). Cells were seeded at 7.5 x 10^4 cells/well density for SW480 and 10^5 cell/well density for SW620 and LiM2 in 24-well plate pre-coated with collagen (Advanced Biomatrix). Plating technique involved 100 µL seeding of cell suspension and 100 µL extra addition of medium 3 hours later once cells had attached to the surface. After overnight growth, the medium was replaced with Seahorse medium (buffer-free DMEM supplemented with glucose, glutamine, and antibiotics). The plates were equilibrated in a 37ºC-incubator without CO_2 for 60 minutes. The cartridge with the sensors was hydrated with calibration solution (Seahorse Bioscience, USA) overnight at 37ºC and loaded into the Seahorse Analyser at least 30 minutes before starting the experiment to calibrate the sensors.

For the Mito-Stress Assay, under baseline conditions (12.5 mM glucose, 4 mM glutamine, 1% streptomycin and penicillin) injections of 2.5 µM oligomycin (ATP synthetase inhibitor), 500 nM FCCP (Carbonyl cyanide-4-(trifluoromethoxy)phenylhydrazone, uncoupling agent), and 2 µM rotenone (inhibitor of complex I) together with 2 µM antimycin A (inhibitor of complex III) were made in order to calculate de different respiratory parameters (basal respiration, ATP production, proton leak, maximal respiration, spare capacity, and non-mitochondrial respiration).

For glucose, glutamine, and fatty acids Mito-Fuel Assay, baseline conditions were used (12.5 mM glucose, 4 mM glutamine, and 1% streptomycin and penicillin). The capacity, dependency and flexibility for each substrate were assessed with the convenient injections of 2 µM UK5099 (inhibitor of pyruvate carrier), 3 µM BPTES (inhibitor of glutaminase), and 4 µM etomoxir (inhibitor of CPT1A).

11.2 RESULTS

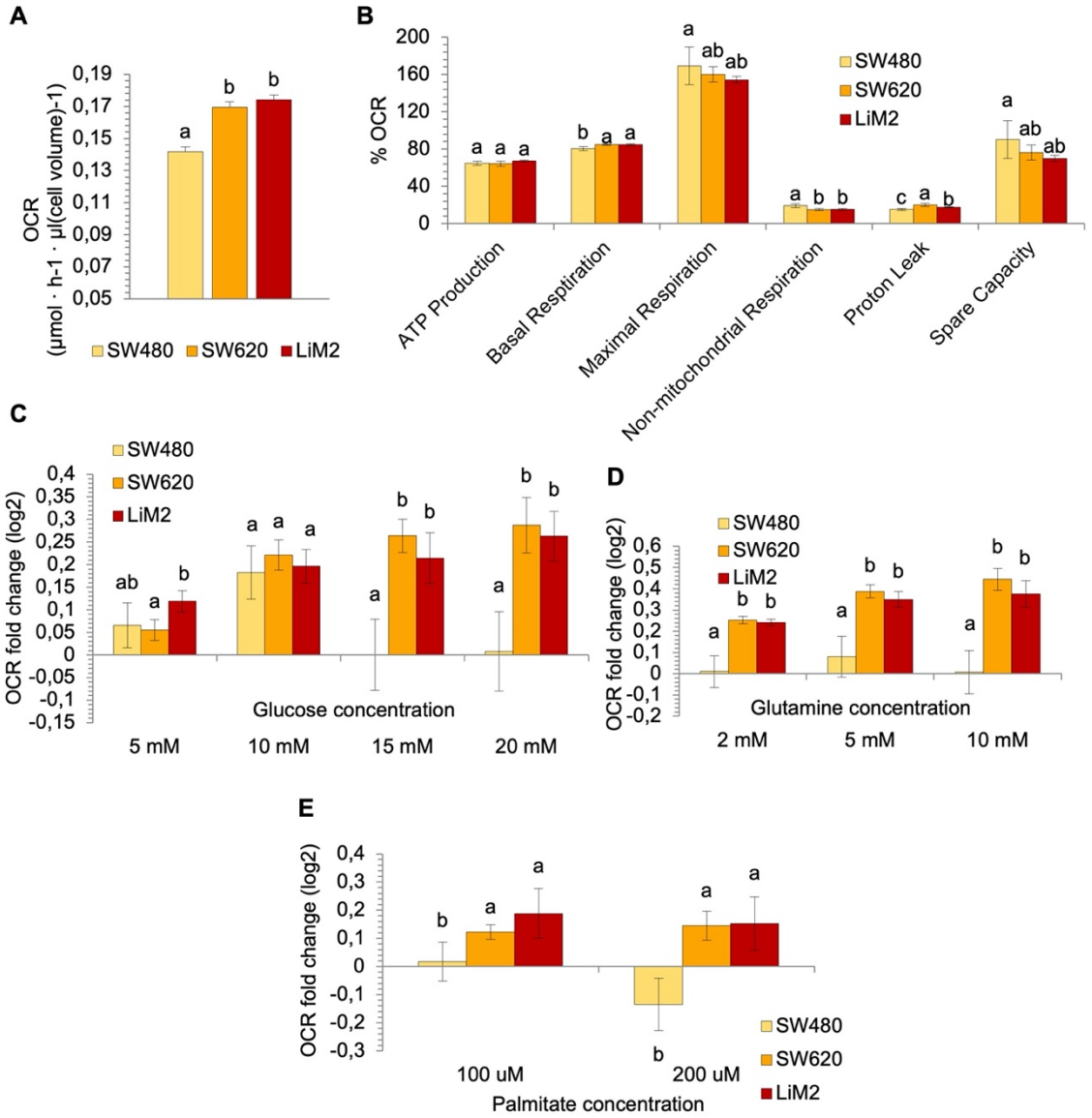

Figure A.III.1. Mitochondrial function and titrations in primary (SW480) and metastatic (SW620 and LiM2) colon cancer cell lines. A. Oxygen consumption rate (OCR) values normalised by cell volume at a baseline condition of 12.5 mM Gln and 4 mM Gln. **B.** Mito Stress assay under a baseline of 12.5 mM Glc and 4 mM Gln. All parameters were assessed with the convenient injections of 2.5 µM oligomycin, 500 µM FCCP, 2 µM rotenone and 2 µM antimycin A. **C.** OCR after glucose titration under a baseline of 3 mM Glc and 4 mM of Gln. 5, 10, 15, and 20 mM are the final concentration of glucose in the well. **D.** OCR after glutamine titration under a baseline of 3 mM Glc. 2, 5, and 10 mM are the final concentration of glutamine in the well. **E.** OCR after palmitate titration under a baseline of 3 mM Glc. 100 and 200 µM are the final concentrations of palmitate in well. A one-way ANOVA and Scheffe's test for multiple comparisons was performed for the factor "cell line". Groups with different letter show significant difference with α=0.05.

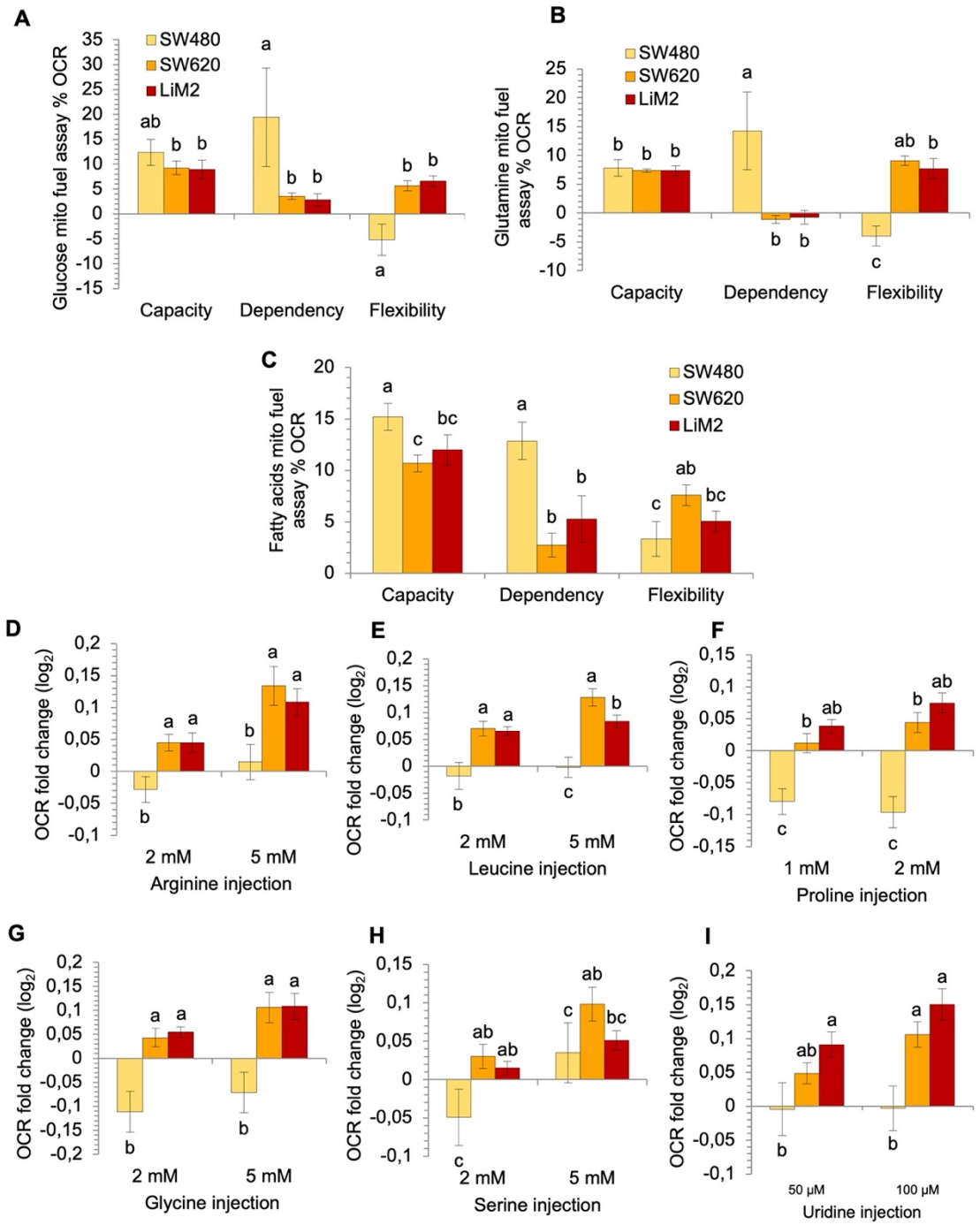

Figure A.III.2. Mito fuel assays and alterative substrates respiration assays in primary (SW480) and metastatic (SW620 and LiM2) colon cancer cell lines. A. – C. Mito fuel assay for glucose (A), glutamine (B), and fatty acids (C) for each cell line. Percentage of oxygen consumption rate (OCR) with respect to basal OCR in Figure 2L. All parameters were assessed with the convenient injections of 2 µM UK5099, 3 µM BPTES, and 4 µM etomoxir. **D. – I.** OCR measured after injections of alternative substrates (arginine, leucine, proline, glycine, serine, and uridine) under a baseline of 12,5 mM Glc and 4 mM of Gln. Concentrations shown in the graphics are the final concentrations of each substrate in well. A one-way ANOVA and Scheffe's test for multiple comparisons was performed for the factor "cell line". Groups with different letter show significant difference with α=0.05.

12. Appendix IV

12 APPENDIX IV

Biocrates experiments for the healthy colon cell line (NCM460), primary (SW480), and metastatic (SW620, LiM1, and LiM2) colon cancer cell lines.

The Biocrates Absolute IDQ™ p180 kit allows determining the concentration in cell pellet or media of 40 acylcarnitines, 21 amino acids, 19 biogenic amines, 90 glycerophospholipids, 15 sphingolipids, and hexose sugars. The analysis was done for cell pellet to determine the intracellular concentration of these metabolites, and cell media at the initial and final incubation time to determine the uptake and secretion rates of amino acids and biogenic amines. The cell lines NCM460, SW480, SW620, LiM1 and LiM2 were included in the analysis, that is presented and discussed in sections 5.1.2.4 and 5.2.2.1.

12.1 MATERIALS AND METHODS

For the detailed experimental procedure see Targeted metabolomics, section 4.3.2.

12.2 RESULTS

Complete intracellular concentrations are shown in Table A.IV.1 and Figures A.IV.1 and 2. Uptake and secretion rates of amino acids and biogenic amines are shown in Table A.IV.2 and Figures A.IV.3 and A.IV.4.

Concentration nmol/mg protein						
Compound	**Type**	**NCM460**	**SW480**	**SW620**	**LiM1**	**LiM2**
C0	acylcarnitines	23,2614	32,0213	9,3535	1,3183	1,2974
C10	acylcarnitines	0,0337	0,1151	0,0750	0,0595	0,0521
C10:1	acylcarnitines	0,0130	0,0443	0,0533	0,0519	0,0379
C10:2	acylcarnitines	0,0080	0,0142	0,0256	0,0311	0,0195
C12	acylcarnitines	0,0712	0,3784	0,1628	0,1444	0,1214
C12-DC	acylcarnitines	0,0293	0,0620	0,0924	0,0841	0,0610
C12:1	acylcarnitines	0,0215	0,0816	0,0738	0,0669	0,0574
C14	acylcarnitines	0,2874	1,4289	0,3448	0,4033	0,4072
C14:1	acylcarnitines	0,0205	0,1089	0,0452	0,0405	0,0488
C14:1-OH	acylcarnitines	0,0331	0,1426	0,0421	0,0437	0,0429
C14:2	acylcarnitines	0,0029	0,0073	0,0079	0,0073	0,0057
C14:2-OH	acylcarnitines	0,0032	0,0111	0,0095	0,0084	0,0091
C16	acylcarnitines	1,7864	5,1784	2,2864	3,0787	3,0812
C16-OH	acylcarnitines	0,0478	0,0279	0,0323	0,0445	0,0359
C16:1	acylcarnitines	0,1108	0,3325	0,2082	0,1731	0,1701
C16:1-OH	acylcarnitines	0,0833	0,1299	0,0689	0,0811	0,0770
C16:2	acylcarnitines	0,0039	0,0103	0,0128	0,0117	0,0096
C16:2-OH	acylcarnitines	0,0154	0,0358	0,0291	0,0268	0,0235
C18	acylcarnitines	0,7616	0,6342	0,4615	0,6906	0,5751
C18:1	acylcarnitines	0,3051	0,9415	0,6994	0,6816	0,6597
C18:1-OH	acylcarnitines	0,0237	0,0283	0,0383	0,0326	0,0315
C18:2	acylcarnitines	0,0103	0,0326	0,0257	0,0203	0,0191
C2	acylcarnitines	4,9801	4,8454	1,5510	1,7441	1,1920
C3	acylcarnitines	0,4962	2,5809	0,3574	0,3958	0,2543
C3-DC (C4-OH)	acylcarnitines	0,4618	0,0553	0,0561	0,0663	0,0625
C5-OH (C3-DC-M)	acylcarnitines	0,1116	0,1470	0,0667	0,0609	0,0596
C3-OH	acylcarnitines	0,0056	0,0110	0,0228	0,0196	0,0173
C3:1	acylcarnitines	0,0081	0,0103	0,0201	0,0150	0,0139
C4	acylcarnitines	1,4017	3,5004	2,4316	2,2625	2,4704
C4:1	acylcarnitines	0,0111	0,0151	0,0288	0,0262	0,0189
C6 (C4:1-DC)	acylcarnitines	0,3723	0,4168	0,2884	0,2562	0,2224
C5	acylcarnitines	0,7102	3,2065	0,3112	0,3000	0,2835
C5-DC (C6-OH)	acylcarnitines	0,0492	0,0395	0,0447	0,0463	0,0394
C5-M-DC	acylcarnitines	0,0126	0,0170	0,0286	0,0266	0,0194
C5:1	acylcarnitines	0,0766	0,0924	0,0594	0,0550	0,0401
C5:1-DC	acylcarnitines	0,0247	0,0300	0,0262	0,0236	0,0173
C6:1	acylcarnitines	0,0189	0,0120	0,0158	0,0149	0,0111
C7-DC	acylcarnitines	0,0145	0,0135	0,0222	0,0226	0,0215
C8	acylcarnitines	0,0695	0,1830	0,0708	0,0640	0,0570
C9	acylcarnitines	0,0076	0,0165	0,0181	0,0143	0,0110
Ala	aminoacids	1336,2252	328,6488	335,8434	352,2846	390,6651
Arg	aminoacids	104,4575	23,5214	17,5298	18,9598	23,6319
Asn	aminoacids	240,5019	51,2045	35,9232	39,6529	36,1069

Asp	aminoacids	298,4471	910,8430	334,5631	275,9288	314,1614
Cit	aminoacids	2,2254	0,9880	1,5378	1,4839	1,6079
Gln	aminoacids	450,2810	836,3922	1319,4368	1447,9542	1331,0095
Glu	aminoacids	926,5458	1056,1821	1532,4229	1638,1445	1542,9009
Gly	aminoacids	993,9697	474,4597	785,1579	836,9695	673,0435
His	aminoacids	158,9013	59,1430	43,3057	49,0117	52,5305
Ile	aminoacids	140,9863	188,5599	141,4411	157,5655	175,9853
Leu	aminoacids	186,7095	207,6185	126,4884	162,7010	181,1913
Lys	aminoacids	55,4818	52,0285	31,9871	38,3652	46,7492
Met	aminoacids	67,7317	45,0018	31,3814	39,1580	44,3646
Orn	aminoacids	6,9750	8,9064	8,3327	9,1190	7,6247
Phe	aminoacids	122,4274	114,1255	68,8154	88,0637	83,2654
Pro	aminoacids	0,0000	345,3450	536,6945	582,1699	483,3711
Ser	aminoacids	417,7172	136,8973	146,9510	171,1658	165,4044
Thr	aminoacids	502,6847	265,3426	365,5929	394,5484	393,9656
Trp	aminoacids	23,9645	28,3631	13,6309	18,2971	15,7087
Tyr	aminoacids	214,9651	114,3821	68,1487	84,8138	81,7405
Val	aminoacids	164,0929	208,3894	152,3183	175,5670	180,5134
Ac-Orn	biogenic amines	1,0459	0,8516	0,9478	1,0593	0,8476
ADMA	biogenic amines	0,4553	0,3187	0,4875	0,5089	0,4691
alpha-AAA	biogenic amines	1,7187	1,8074	1,8222	2,1363	1,5023
c4-OH-Pro	biogenic amines	0,2394	0,0000	0,0000	0,0000	0,0000
Carnosine	biogenic amines	0,7165	1,3049	0,1923	0,2217	0,1841
Creatinine	biogenic amines	5,4559	8,3620	1,2650	1,4991	3,0474
DOPA	biogenic amines	0,0000	0,0000	0,0000	0,0000	0,0000
Dopamine	biogenic amines	0,0000	0,0258	0,0000	0,0000	0,0000
Histamine	biogenic amines	0,0332	0,0528	0,0469	0,1323	0,0000
Kynurenine	biogenic amines	0,3956	0,0000	0,0000	0,0000	0,0000
Met-SO	biogenic amines	5,9472	1,1648	1,1134	1,4180	1,1884
Nitro-Tyr	biogenic amines	0,0000	0,0000	0,0000	0,0000	0,0000
PEA	biogenic amines	0,0000	0,0000	0,0000	0,0000	0,0000
Putrescine	biogenic amines	14,1081	0,0000	0,0000	0,0000	0,0000
SDMA	biogenic amines	0,1264	0,5119	0,3862	0,4509	0,3313
Serotonin	biogenic amines	0,0683	0,1404	0,1284	0,2224	0,1723
Spermidine	biogenic amines	6,1995	33,0934	30,8965	36,3800	26,2207
Spermine	biogenic amines	8,6892	8,8814	5,0237	6,4652	8,0830
t4-OH-Pro	biogenic amines	6,7294	3,0575	5,5272	6,1279	5,4407
Taurine	biogenic amines	0,0000	0,0000	0,0000	0,0000	0,0000
total DMA	biogenic amines	0,2746	0,1980	0,1520	0,2246	0,3199
lysoPC a C14:0	glycero-P-lipids	1,3156	2,4872	3,8159	4,3082	3,1391
lysoPC a C16:0	glycero-P-lipids	2,3910	3,2541	1,8676	2,5350	2,0976
lysoPC a C16:1	glycero-P-lipids	0,9414	1,4716	1,1298	1,2175	1,0488
lysoPC a C17:0	glycero-P-lipids	0,1753	0,3655	0,1718	0,2273	0,2221
lysoPC a C18:0	glycero-P-lipids	1,4259	1,9760	0,9580	1,4611	1,2891
lysoPC a C18:1	glycero-P-lipids	2,3319	4,9469	2,8129	3,6714	3,3503

lysoPC a C18:2	glycero-P-lipids	0,2103	0,4000	0,2513	0,2922	0,2928
lysoPC a C20:3	glycero-P-lipids	0,1032	0,2757	0,2087	0,2835	0,1879
lysoPC a C20:4	glycero-P-lipids	0,1745	0,6405	0,8658	0,9216	0,6548
lysoPC a C24:0	glycero-P-lipids	0,1918	0,7393	0,4404	0,5819	0,4450
lysoPC a C26:0	glycero-P-lipids	0,5909	2,7498	1,2566	1,6733	1,1726
lysoPC a C26:1	glycero-P-lipids	0,1840	0,5935	0,2801	0,4670	0,3015
lysoPC a C28:0	glycero-P-lipids	1,1344	2,9225	2,8014	3,8337	2,9643
lysoPC a C28:1	glycero-P-lipids	1,7686	1,5683	1,2912	1,4860	1,1944
PC aa C24:0	glycero-P-lipids	0,1245	0,2874	0,2202	0,2635	0,1894
PC aa C26:0	glycero-P-lipids	0,6105	2,2938	1,1759	1,4486	1,0925
PC aa C28:1	glycero-P-lipids	1,0714	1,9483	1,8561	1,7857	1,2600
PC aa C30:0	glycero-P-lipids	5,4359	19,2762	27,2068	24,3509	24,3988
PC aa C30:2	glycero-P-lipids	0,3277	0,4919	0,8104	0,7105	0,7939
PC aa C32:0	glycero-P-lipids	3,0212	19,3453	25,1317	22,7275	16,7514
PC aa C32:1	glycero-P-lipids	40,5719	115,3806	139,4923	99,7764	87,3986
PC aa C32:2	glycero-P-lipids	7,0902	7,2545	10,6983	6,7683	8,6670
PC aa C32:3	glycero-P-lipids	0,2706	0,3296	0,6364	0,4508	0,4771
PC aa C34:1	glycero-P-lipids	56,7219	290,8698	389,6562	332,1717	279,6755
PC aa C34:2	glycero-P-lipids	39,1933	81,5264	104,2157	71,3045	77,9304
PC aa C34:3	glycero-P-lipids	2,6194	4,3941	5,9486	4,0585	4,1878
PC aa C34:4	glycero-P-lipids	0,4609	0,7876	1,0064	0,8891	0,8521
PC aa C36:0	glycero-P-lipids	0,6066	4,1730	9,5800	9,2783	8,0844
PC aa C36:1	glycero-P-lipids	15,5197	43,1123	46,5743	50,6999	44,7189
PC aa C36:2	glycero-P-lipids	39,3114	144,3985	185,6055	151,1007	121,6297
PC aa C36:3	glycero-P-lipids	7,6023	23,0761	25,7081	20,3549	17,9167
PC aa C36:4	glycero-P-lipids	3,7499	13,5417	18,5605	12,9872	11,3618
PC aa C36:5	glycero-P-lipids	1,9695	5,1749	6,6634	4,9076	5,0036
PC aa C36:6	glycero-P-lipids	0,4018	0,8498	1,1874	0,9541	0,9104
PC aa C38:0	glycero-P-lipids	0,4766	6,3356	16,0243	15,3598	11,0705
PC aa C38:1	glycero-P-lipids	0,3770	1,5131	2,4094	2,5600	1,3183
PC aa C38:3	glycero-P-lipids	1,3905	6,8814	8,7384	7,8298	6,2199
PC aa C38:4	glycero-P-lipids	2,7613	8,8435	10,3063	8,2294	7,0210
PC aa C38:5	glycero-P-lipids	3,8090	16,5816	19,8287	15,6096	13,9109
PC aa C38:6	glycero-P-lipids	3,1355	11,4690	12,6811	11,0890	10,2693
PC aa C40:1	glycero-P-lipids	0,1257	0,6121	0,7516	0,7455	0,5477
PC aa C40:2	glycero-P-lipids	0,1335	1,6374	1,4756	1,3487	1,1216
PC aa C40:3	glycero-P-lipids	0,1103	1,1054	0,8785	0,9878	0,8157
PC aa C40:4	glycero-P-lipids	0,1402	1,1400	1,4756	1,4860	1,1070
PC aa C40:5	glycero-P-lipids	0,4490	3,1160	3,8274	3,5215	2,4763
PC aa C40:6	glycero-P-lipids	1,6820	7,2545	7,1591	6,6309	5,6081
PC aa C42:0	glycero-P-lipids	0,0280	0,1327	0,1821	0,1511	0,0896
PC aa C42:1	glycero-P-lipids	0,0713	0,2895	0,3343	0,2647	0,2170
PC aa C42:2	glycero-P-lipids	0,0709	0,6695	0,7540	0,6444	0,6227
PC aa C42:4	glycero-P-lipids	0,0213	0,1948	0,2064	0,2223	0,1544
PC aa C42:5	glycero-P-lipids	0,0662	0,3724	0,5487	0,5145	0,4435

PC aa C42:6	glycero-P-lipids	0,1032	0,5479	0,7597	0,7255	0,5987
PC ae C30:0	glycero-P-lipids	1,9222	12,0908	13,7187	15,4847	13,7653
PC ae C30:1	glycero-P-lipids	1,5835	3,5305	6,2714	6,7308	5,9431
PC ae C30:2	glycero-P-lipids	0,3978	0,2860	0,4957	0,4096	0,3154
PC ae C32:1	glycero-P-lipids	10,7535	62,6648	55,5664	50,6999	38,9652
PC ae C32:2	glycero-P-lipids	2,2413	7,2545	11,6436	10,6769	9,6867
PC ae C34:0	glycero-P-lipids	1,0123	9,1890	7,2513	7,2054	5,4770
PC ae C34:1	glycero-P-lipids	13,9047	107,7807	83,0037	82,0439	66,0588
PC ae C34:2	glycero-P-lipids	7,4448	36,9633	37,9281	33,9664	31,9733
PC ae C34:3	glycero-P-lipids	1,0754	3,5651	4,3808	3,9211	3,5032
PC ae C36:0	glycero-P-lipids	0,7799	1,7894	1,4756	1,6109	1,4931
PC ae C36:1	glycero-P-lipids	4,7268	30,0542	24,3247	23,9763	15,8774
PC ae C36:2	glycero-P-lipids	7,2084	35,7887	31,8181	29,7206	23,3791
PC ae C36:3	glycero-P-lipids	1,6623	13,0580	11,5283	12,0756	9,8323
PC ae C36:4	glycero-P-lipids	1,5717	22,5925	30,5500	30,7196	27,0207
PC ae C36:5	glycero-P-lipids	1,2959	10,2944	16,4855	15,7344	13,5468
PC ae C38:0	glycero-P-lipids	1,1069	1,7963	1,8561	1,8357	1,7043
PC ae C38:1	glycero-P-lipids	0,6302	2,9363	1,9368	1,6983	1,3765
PC ae C38:2	glycero-P-lipids	1,1187	9,1890	10,2141	9,1035	7,9387
PC ae C38:3	glycero-P-lipids	0,5239	4,1040	3,8274	3,8087	3,6270
PC ae C38:4	glycero-P-lipids	0,8154	9,1199	11,9894	15,3598	11,2890
PC ae C38:5	glycero-P-lipids	1,1187	23,2143	37,1211	38,3371	33,3571
PC ae C38:6	glycero-P-lipids	1,1975	21,6943	37,5822	37,5878	33,7213
PC ae C40:1	glycero-P-lipids	0,4569	1,3265	1,1217	0,7642	0,6679
PC ae C40:2	glycero-P-lipids	0,2375	1,2920	0,9672	0,9004	0,7939
PC ae C40:3	glycero-P-lipids	0,1564	0,8153	0,7032	0,6631	0,5572
PC ae C40:4	glycero-P-lipids	0,1946	1,5476	2,1443	2,1354	1,9592
PC ae C40:5	glycero-P-lipids	0,2647	4,2836	6,9631	7,2928	6,0378
PC ae C40:6	glycero-P-lipids	0,5003	7,7381	14,7562	16,6086	13,3283
PC ae C42:0	glycero-P-lipids	0,2304	0,7531	1,2220	1,1539	0,6788
PC ae C42:1	glycero-P-lipids	0,1134	0,4228	0,3874	0,3771	0,2666
PC ae C42:2	glycero-P-lipids	0,2572	0,8498	0,7505	0,5757	0,4603
PC ae C42:3	glycero-P-lipids	0,2107	0,7531	0,5764	0,4271	0,3853
PC ae C42:4	glycero-P-lipids	0,1001	0,4056	0,3389	0,2910	0,2862
PC ae C42:5	glycero-P-lipids	0,1867	0,8636	0,9396	0,9178	0,7647
PC ae C44:3	glycero-P-lipids	0,0516	0,2163	0,2375	0,2060	0,1646
PC ae C44:4	glycero-P-lipids	0,0800	0,3303	0,2755	0,2423	0,1690
PC ae C44:5	glycero-P-lipids	0,0788	0,2999	0,2548	0,2298	0,1697
PC ae C44:6	glycero-P-lipids	0,0319	0,2135	0,2167	0,2085	0,1391
SM (OH) C14:1	sphingolipids	1,0517	2,1349	1,7062	1,7982	1,2818
SM (OH) C16:1	sphingolipids	0,2714	0,8360	0,5845	0,5644	0,0000
SM (OH) C22:1	sphingolipids	0,1249	0,1423	0,3804	0,5145	0,3940
SM (OH) C22:2	sphingolipids	0,0902	0,9396	1,6716	1,3986	0,7429
SM (OH) C24:1	sphingolipids	0,0390	0,0491	0,2283	0,1499	0,0670
SM C16:0	sphingolipids	19,4588	38,0687	54,2982	58,5671	38,3825

SM C16:1	sphingolipids	2,1862	5,3752	3,9311	4,3457	3,3430
SM C18:0	sphingolipids	0,7642	1,4923	2,0866	1,8357	0,7429
SM C18:1	sphingolipids	0,1237	0,7945	0,3816	0,3659	0,3430
SM C20:2	sphingolipids	0,0087	0,0290	0,0115	0,0587	0,0918
SM C22:3	sphingolipids	0,0000	0,0000	0,0000	0,0100	0,0000
SM C24:0	sphingolipids	1,7332	14,3708	16,1396	21,1041	15,8774
SM C24:1	sphingolipids	1,1463	5,7345	16,2549	18,3569	12,0901
SM C26:0	sphingolipids	0,0217	0,0000	0,0000	0,0462	0,0269
SM C26:1	sphingolipids	0,0284	0,0000	0,1810	0,0512	0,0910
H1	sugars	34,3483	49,3304	60,8694	36,3391	23,2335

Table A.IV.1. Intracellular concentration of acylcarnitines, amino acids, biogenic amines, glycerophospholipids, and sphingolipids in NCM460, SW480, SW620, LiM1, and LiM2 cell lines. The intracellular content of these metabolites was obtained by the Absolute IDQ p180 kit (Biocrates Life Sciences AG) after 24 hours of incubation with DMEM 12.5 mM Glc and 4 mM Gln, 5% FBS, and 1% S/P.

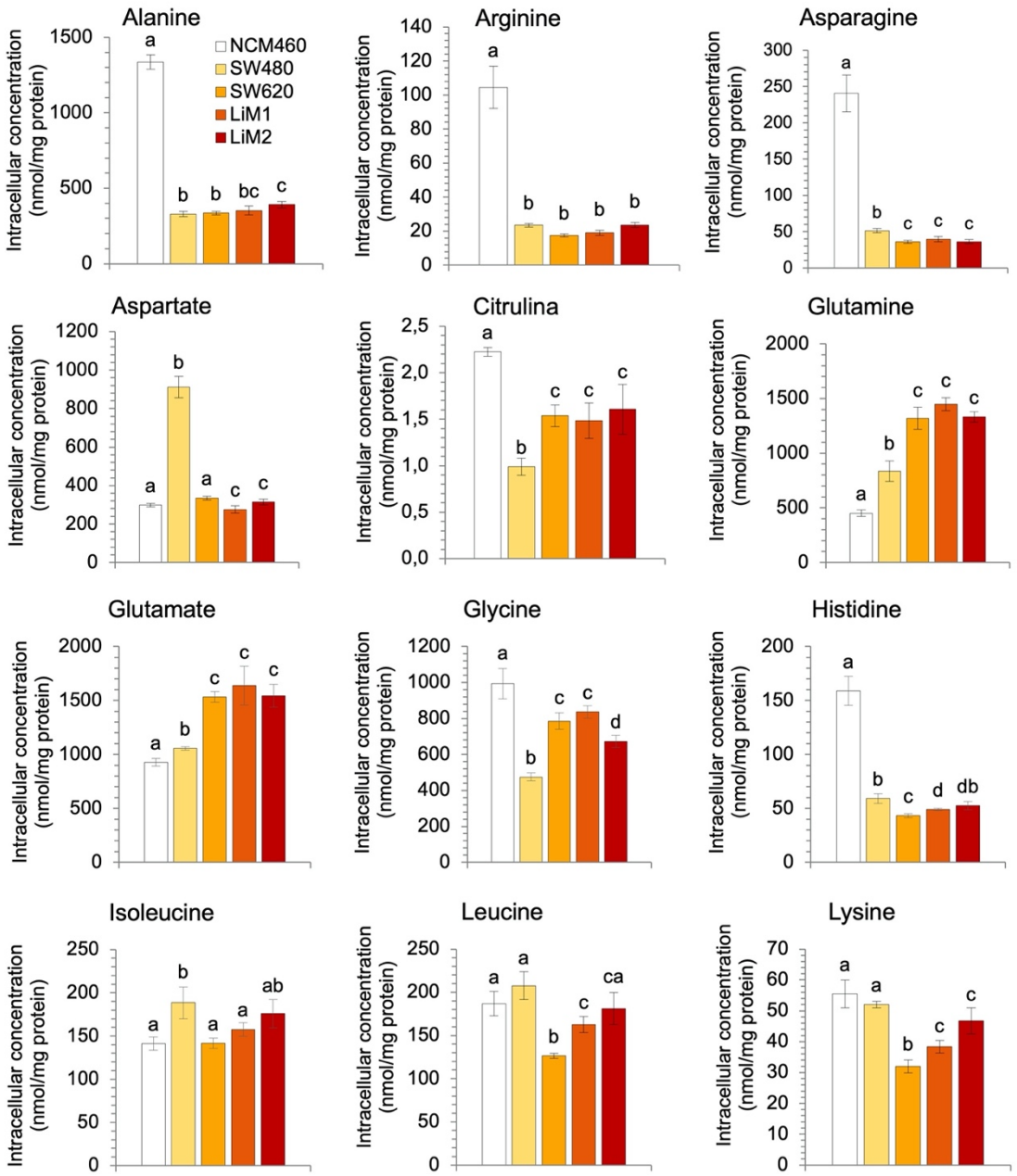

Figure A.IV.1. Amino acid intracellular concentration of NCM460, SW480, SW620, LiM1, and LiM2 cell lines. Intracellular content of amino acids obtained by the Absolute IDQ p180 kit (Biocrates Life Sciences AG) after 24 hours of incubation with DMEM 12.5 mM Glc and 4 mM Gln, 5% FBS, and 1% S/P. [a,b,c,d] In all cases, a one-way ANOVA and Scheffe's test for multiple comparisons was performed for the factor "cell line". Groups with different letter show significant differences with α=0.05.

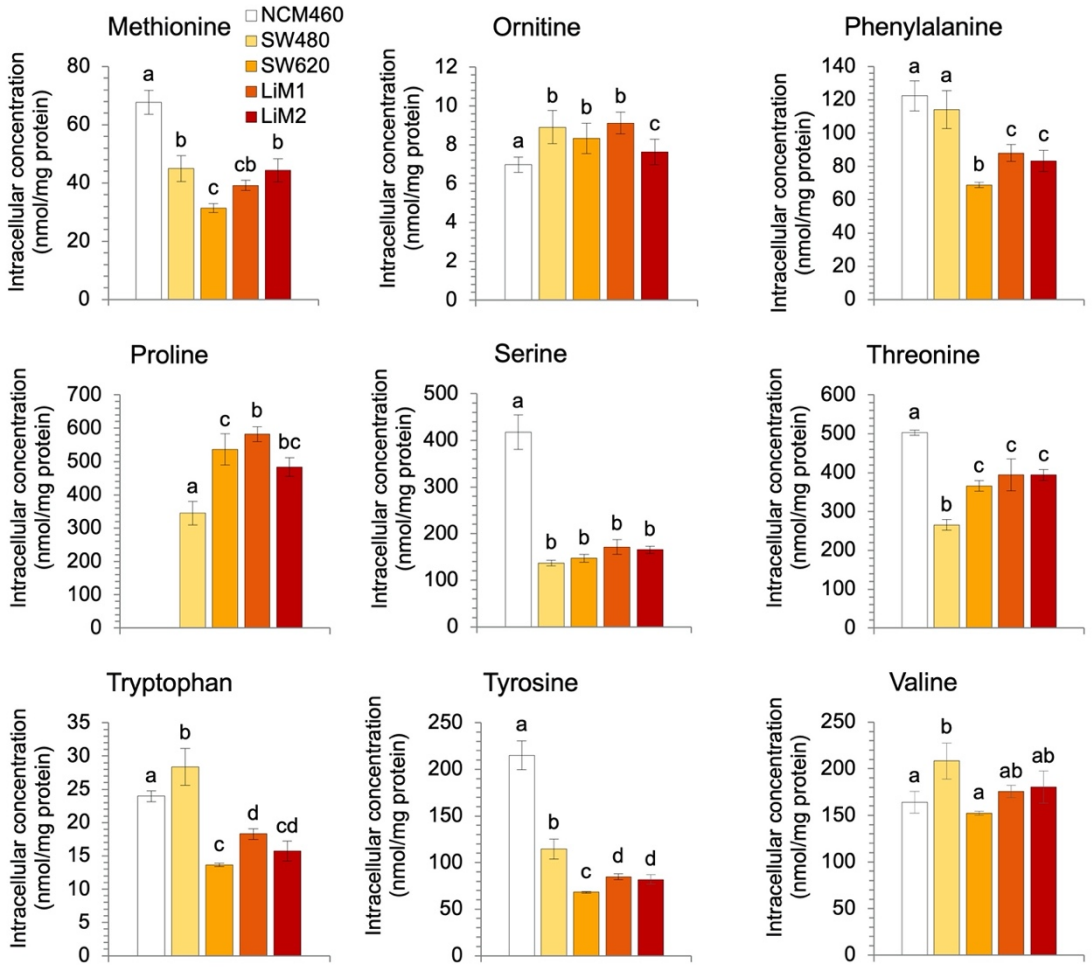

Figure A.IV.2. Amino acid intracellular concentration of NCM460, SW480, SW620, LiM1, and LiM2 cell lines. Intracellular content of amino acids obtained by the Absolute IDQ p180 kit (Biocrates Life Sciences AG) after 24 hours of incubation with DMEM 12.5 mM Glc and 4 mM Gln, 5% FBS, and 1% S/P. [a,b,c,d] In all cases, a one-way ANOVA and Scheffe's test for multiple comparisons was performed for the factor "cell line". Groups with different letter show significant differences with α=0.05.

v (nmol / (10 ^{6} · cell volume · h))						
Compound	**Type**	**NCM460**	**SW480**	**SW620**	**LiM1**	**LiM2**
Ala	aminoacids	44,7488	29,2320	23,6578	32,2353	36,8024
Arg	aminoacids	-0,8799	9,6612	-4,0322	-5,3484	-5,6475
Asn	aminoacids	3,0187	4,6879	0,4745	0,5947	0,6239
Asp	aminoacids	0,7557	2,0817	0,4603	0,6314	0,8173
Cit	aminoacids	0,1725	-0,0554	0,0208	0,0143	-0,0302
Gln	aminoacids	-156,2310	-100,6322	-82,5711	-88,2237	-114,2604
Glu	aminoacids	16,6293	15,3443	8,4084	8,3622	9,8946
Gly	aminoacids	10,2153	12,2838	6,2773	6,0354	9,3582
His	aminoacids	-0,9835	-2,5416	-0,0303	-0,9930	-1,6167
Ile	aminoacids	2,2425	-5,0386	-0,0849	-3,8401	-7,2982
Leu	aminoacids	1,7272	-5,5537	-2,5341	-7,0174	-9,5175
Lys	aminoacids	10,7123	5,9123	-0,0652	-0,5608	-3,9931
Met	aminoacids	-1,3356	-1,5457	0,5104	-0,9851	-1,9516
Orn	aminoacids	2,4621	5,0740	1,6690	1,9047	1,9289
Phe	aminoacids	0,7066	2,1920	0,7948	1,2090	-3,0990
Pro	aminoacids	8,4955	4,5841	4,7951	6,6599	7,6792
Ser	aminoacids	1,9785	-10,1576	-14,7027	-15,5823	-19,2719
Thr	aminoacids	13,6420	-5,5713	1,6088	-1,5717	-1,6916
Trp	aminoacids	0,8296	2,5491	-0,0850	-0,0818	-1,3756
Tyr	aminoacids	2,3023	6,7695	1,4327	-1,5135	-0,6986
Val	aminoacids	10,4680	9,7455	2,8664	-2,8387	-6,0404
Ac-Orn	biogenic amines	0,0375	0,0317	0,0110	0,0086	0,0056
alpha-AAA	biogenic amines	0,0401	0,0641	-0,0006	-0,0081	-0,0373
Carnosine	biogenic amines	-0,0037	0,0010	0,0066	0,0083	0,0082
Creatinine	biogenic amines	0,1590	-0,1233	0,1786	0,0392	0,0448
DOPA	biogenic amines	0,0047	-0,0380	0,0030	-0,0144	-0,0083
Kynurenine	biogenic amines	0,9881	0,0238	0,0108	-0,0011	-0,0088
Met-SO	biogenic amines	-0,7316	-0,8123	-0,1899	-0,2887	-0,2784
Putrescine	biogenic amines	0,0001	0,0032	0,0083	0,0132	0,0112
Spermidine	biogenic amines	-0,0015	-0,0021	-0,0004	0,0002	0,0022
t4-OH-Pro	biogenic amines	0,1702	0,1375	0,0618	0,0404	0,0569
Taurine	biogenic amines	-0,5192	-0,7738	-0,2179	-0,1974	-0,2400
total DMA	biogenic amines	0,0243	0,0272	0,0092	0,0194	0,0243

Table A.IV.2. Uptake and secretion rates of amino acids and biogenic amines sphingolipids in NCM460, SW480, SW620, LiM1, and LiM2 cell lines. The uptake and secretion rates of these metabolites were obtained by measuring the culture medium by the Absolute IDQ p180 kit (Biocrates Life Sciences AG) before and after 24 hours of incubation with DMEM 12.5 mM Glc and 4 mM Gln, 5% FBS, and 1% S/P. Calculations were done according to section 4.3.1.

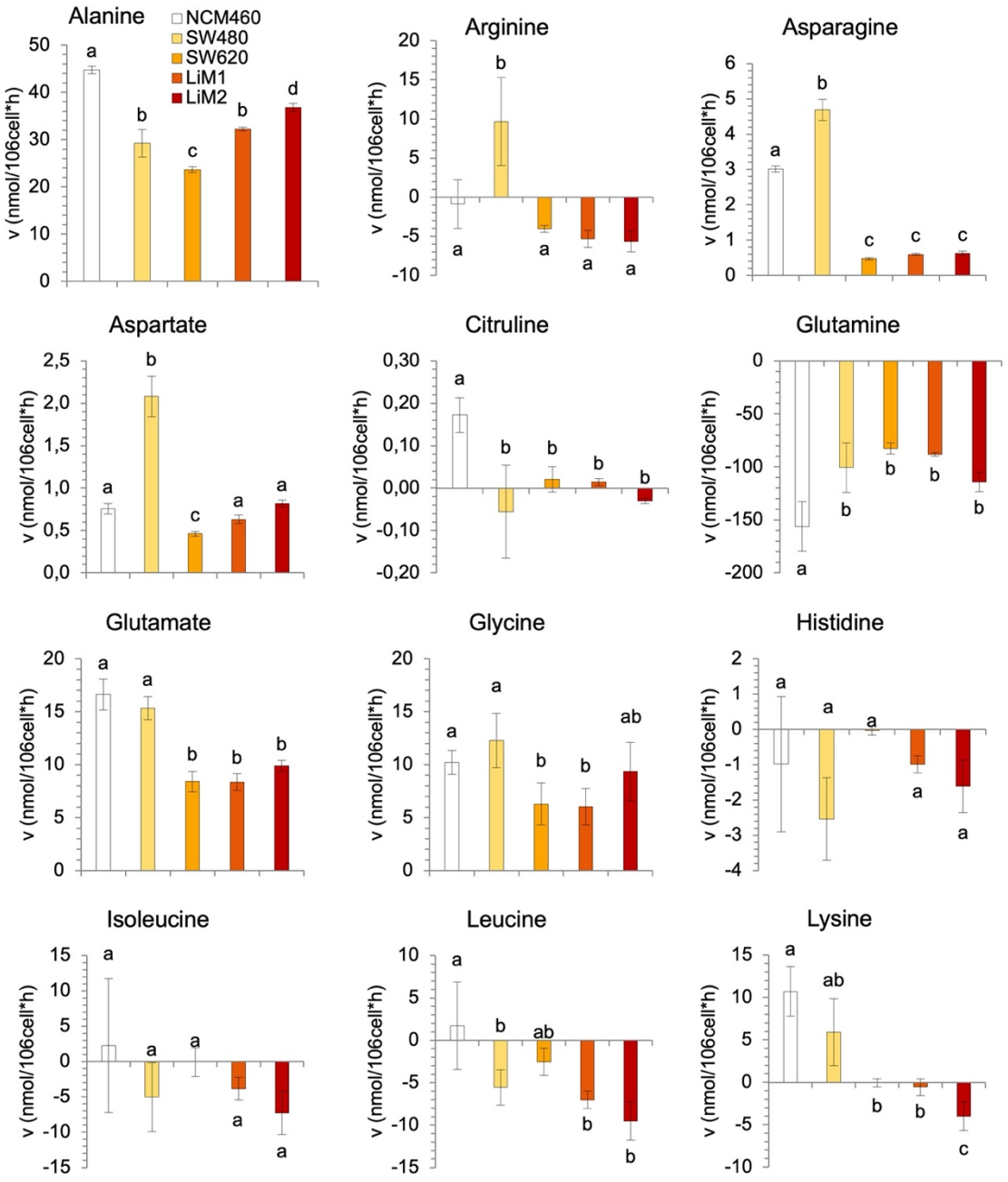

Figure A.IV.3. Amino acid uptake and secretion rates of NCM460, SW480, SW620, LiM1, and LiM2 cell lines. Amino acid uptake and secretion rates obtained by measuring the culture medium by the Absolute IDQ p180 kit (Biocrates Life Sciences AG) before and after 24 hours of incubation with DMEM 12.5 mM Glc, 4 mM Gln, 5% FBS, and 1% S/P. [a,b,c] In all cases, a one-way ANOVA and Scheffe's test for multiple comparisons was performed for the factor "cell line". Groups with different letter show significant differences with α=0.05.

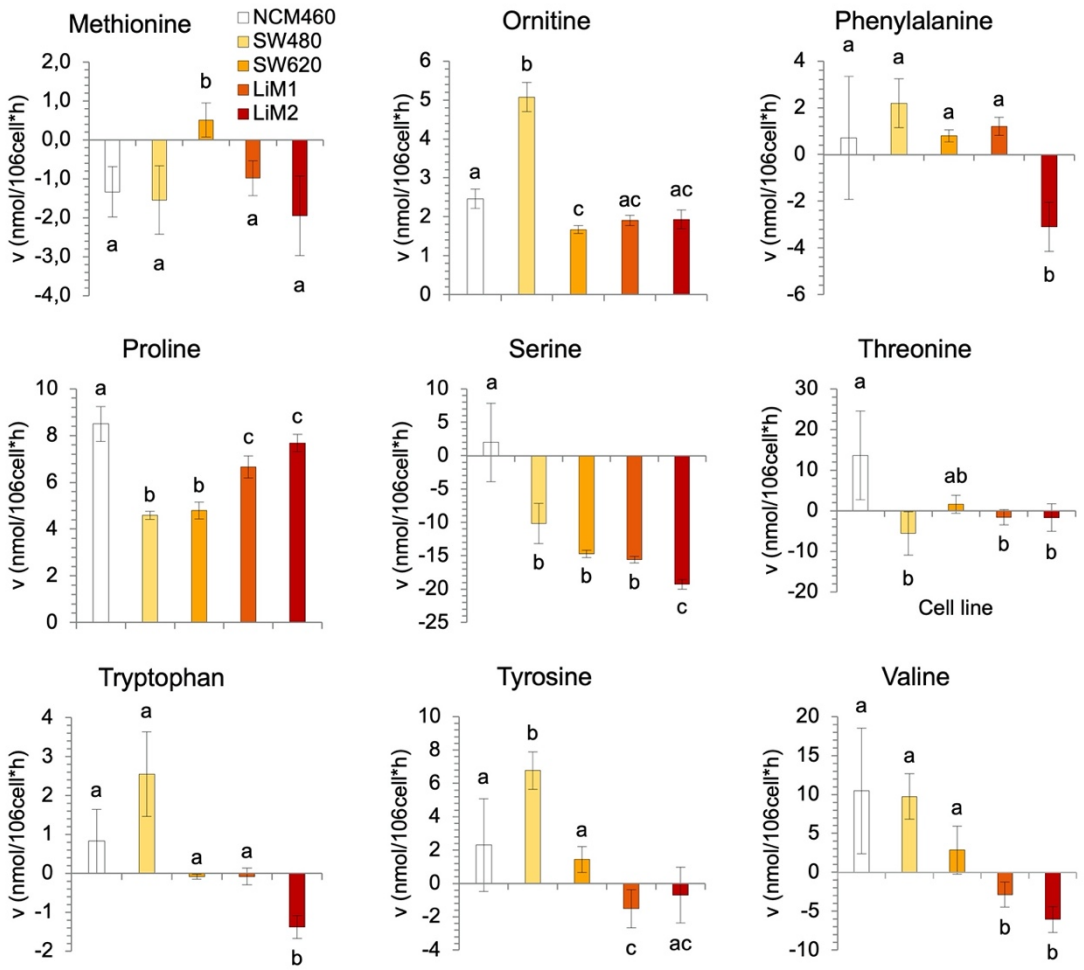

Figure A.IV.3. Amino acid uptake and secretion rates of NCM460, SW480, SW620, LiM1, and LiM2 cell lines. Amino acid uptake and secretion rates obtained by measuring the culture medium by the Absolute IDQ p180 kit (Biocrates Life Sciences AG) before and after 24 hours of incubation with DMEM 12.5 mM Glc, 4 mM Gln, 5% FBS, and 1% S/P. [a,b,c] In all cases, a one-way ANOVA and Scheffe's test for multiple comparisons was performed for the factor "cell line". Groups with different letter show significant differences with α=0.05.

13. Appendix V

13 APPENDIX V

Computational analysis of SW480, SW620, and LiM2 specific metabolic flux maps and metabolic targets through multi-omics data integration

The analysis described in this appendix was done by Dr Carles Foguet and supervised by Dr Pedro de Atauri, from the computational team of the research group. They used the experimental data exposed in this thesis on the metabolic characterisation of SW480, SW620 and LiM2 cell lines.

13.1 MATERIALS AND METHODS

13.1.1 TRANSCRIPTOMICS

Transcriptomics data were obtained from the gene expression omnibus repository (Barrett et al., 2013). For the cancer models (i.e., SW480, SW620, and LiM2), data was taken from GSE1323 (SW480-SW620) (Provenzani et al., 2006) and GSE33350 (SW620-LIM1-LIM2) (Urosevic et al., 2014). Because both sets shared the SW620 cell line, the batch effect was corrected using the sva package for "R" (Leek et al., 2012).

Transcriptomics were mapped to reactions using the gene protein reaction rules (GPR) defined in Recon 2.2 (Swainston et al., 2016). In detail, first OR operators were replaced by "MAX()" operators and AND operators by "MIN()" in the GPR expressions. Then, GPR expressions for each reaction were evaluated, replacing gene IDs by their respective transcript abundances. Under such a system, a reaction catalysed by multiple isoenzymes will be mapped to the maximum gene expression values of all isoenzymes, while reactions catalysed by protein complexes will be mapped to the minimum transcript abundance of the complex's components.

13.1.2 INTEGRATING EXTRACELLULAR FLUX MEASUREMENTS

Measures of extracellular metabolite concentrations (measured either through spectrophotometric methods or targeted metabolomics) were used to compute the rate of metabolite uptake or secretion normalised by cellular volume using the following the calculations explained in section 4.3.1 (equation 1).

13.1.3 INTEGRATING OCR MEASUREMENTS, MITO STRESS AND MITO FUEL ASSAYS

For the SW620, SW480, and LiM2 cell lines, Seahorse measurements were integrated to constraint the oxidative metabolism. Firstly, OCR measurements were used to constrain the rate of oxygen consumption in the cell line-specific models. Next, the percentage of OCR associated

with ATP synthase, measured in the Mito Stress Assay, was used to constrain the flux through ATP synthase. Finally, from the Mito Fuel Assay, the dependency and capacity for fatty acid oxidation were used to define the lower and upper bound, respectively, for the transport of palmitate into the mitochondria.

13.1.4 INTEGRATING INTRACELLULAR AMINO ACID AND BIOGENIC AMINES MEASUREMENTS

Metabolomics measured in the cellular pellet can be integrated with the proliferation rate to account for the dilution associated with proliferation. In the framework of constraint-based modelling, this can be represented by adding a sink reaction to measured metabolites that represents the requirements of metabolite synthesis to maintain the concentrations of such metabolite in steady state (Reimers and Reimers, 2016).

$$v_{M_{sink}} = [M] \cdot p \cdot \mu$$

Equation 2

Where:

$[M]$ is the concentration of metabolite M (µmol/mg prot)

p is the protein per cellular volume (mg prot/µl cell volume)

μ: is the proliferation rate in h^{-1}

$v_{M_{sink}}$ is the estimated flux through the sink reaction

To account for uncertainty, the 99.5% confidence intervals for $v_{M_{sink}}$ were added as flux boundaries in the model.

13.1.5 USING LIPIDOMIC MEASUREMENTS TO PERSONALISE THE BIOMASS FUNCTION

Across the analysed conditions, the most abundant phospholipids were the phosphatidylcholines (PC aa) PC aa C34:1, PC aa C34:2, PC aa C36:1 and PC aa C36:2 (Table A.V.1). Such species represent isomeric phosphatidylcholines C x:y where x is the total carbon number of both chains and y is the total number of unsaturations. The relative abundance of such species in each cell line was used to customise the biomass function in each cell line-specific model.

Due to the large number of potential fatty acid chain combinations, Recon 2.2 (Swainston et al., 2016) does not simulate individual phospholipid species. Instead, it simulates the fatty acid chains in phospholipids through an artificial “Rtotalcoa” metabolite that is synthesised from a combination of acyls-CoA with stoichiometric coefficients representing the relative abundance of each fatty acid chain in phospholipids.

Isobaric species	Most probable acyl chains	SW480 (nmol/mg prot)	SW620 (nmol/mg prot)	LiM2 (nmol/mg prot)
PC aa C34:1	C16:0 + C18:1	207.886	345.588	293.647
PC aa C34:2	C16:1 + C18:1	56.178	90.967	79.069
PC aa C36:1	C:18 + C18:1	30.288	44.433	40.421
PC aa C36:2	C18:1 + C18:1	97.877	168.484	145.409

Table A.V.1. Levels of the most abundant phosphatidylcholines (PC AA) and the most probable acyl chain for each of the most abundant phosphatidylcholines. PC AA were obtained by measuring the intracellular content by an Absolute IDQ p180 kit (Biocrates Life Sciences AG) after incubation with DMEM 12.5 mM Glc and 4 mM Gln, 5% FBS, and 1% S/P, normalised by protein content for each cell line SW480, SW620 and LiM2.

The most abundant fatty acids in mammals are reported to be oleic (C18:1), palmitate (C16:0), stearic acid (18:0) and palmitoleic (16:1), in that order(Sheikh et al., 2005) (Table A.V.1). Hence, we assumed that the side chains of the phosphatidylcholines primarily consisted of such fatty acids and their relative abundance was used as coefficients for "Rtotalcoa" synthesis (Table A.V.2).

Acyl chain	SW480	SW620	LiM2
C16:0	30.5%	30.3%	29.9%
C16:1	14.3%	13.8%	13.6%
C18:0	3.0%	2.9%	3.1%
C18:1	52.2%	53.0%	53.4%

Table A.V.2. Predicted relative abundance of each acyl chain in each cell line. These abundances were inferred from the relative abundance of phosphatidylcholines (Table A.V.1) and used to define the acyl-CoA requirements for biomass synthesis in each cell line SW480, SW620, and LiM2.

It is worth noting, that even if other combinations of acyl-CoA can give rise to the measured isobaric phosphatidylcholines, the metabolic cost (i.e., NADPH, ATP, and Acetyl-CoA) of producing any given phosphatidylcholine will depend primarily on the total length of the fatty acid chains and the number of unsaturations. Hence, the assumption that oleic, palmitate, stearic acid, and palmitoleic, are the components of "Rtotalcoa" it is a valid approximation.

13.1.6 INTEGRATING GROWTH RATES

The proliferation rates for each cell line were integrated to reflect the different proliferation rates of the cell lines of study. First maximum biomass production in SW620($v_{biomass}^{SW620}$) was computed using FBA(Orth et al., 2010). Then the biomass production of the remaining cell lines was set as follows:

$$v_{biomass}^{cell\ line} = v_{biomass}^{SW620} \cdot \frac{\mu^{cell\ line}}{\mu^{SW620}}$$

Equation 3

$v_{biomass}^{cell\ line}$ is then set as the upper bound for the biomass reaction allowing the models to accurately reflect the different growth rates of the different cell lines.

13.1.7 ^{13}C MFA AND GSMM INTEGRATION

The central metabolism flux maps consistent with the measured ^{13}C propagation and the measured rates of uptake and secretion for glucose, lactate, and amino acids, as well as data on mitochondrial respiration, were computed in the framework of ^{13}C MFA (Antoniewicz, 2018).

^{13}C MFA was performed in a metabolic network of central carbon metabolism built from Recon 2.2 (Swainston et al., 2016). The network comprised 347 reactions including, glycolysis, TCA cycle, pentose phosphate pathway, energy and redox metabolism and the main pathways of amino acid metabolism and biomass components synthesis.

Using INCA (isotopomer network compartmental analysis) (Young, 2014), 95% confidence intervals for flux values were computed for all reactions in the network. Such confidence intervals were added as flux boundaries in the cell line-specific GSMMs. While most reactions could be directly mapped, some reactions that were defined as single reactions in the ^{13}C MFA network were defined as multiple reactions in Recon 2.2 (e.g., a reaction that can occur in multiple compartments or a reaction that can take either NAD or NAPD as a cofactor). In such instances, the ^{13}C MFA confidence intervals were used to constraint the summation of the flux through the equivalent reactions in Recon 2.2.

13.1.8 MINIMAL CUT SET ANALYSIS

From the project DRIVE database, the list of essential metabolic genes in SW480 and SW620 was obtained (McDonald et al., 2017a). A gene was considered essential if it's Redundant siRNA Activity (RSA) (König et al., 2007) score was equal or lower than -2. Conversely, a gene was defined as dispensable (i.e., not essential) if it had an RSA score larger or equal than -1.

Minimal cut set (MCS) analysis (Apaolaza et al., 2017, 2019) was performed to identify the MCSs containing the essential genes identified in Project DRIVE. MCS are minimal sets of genes or reactions whose simultaneous removal directly blocks a metabolic task, biomass production in this case. MCS analysis was run in Recon 2.2 (Swainston et al., 2016) assuming an extracellular metabolite availability in the media defined based on the composition of DMEM. Furthermore, blocked reactions were removed and reactions that could only be part of linear pathways were grouped. MCS analysis was set to seek 8 MCS containing each Project DRIVE essential gene and all reactions were evaluated as possible gene set candidates. As reported by Apaolaza *et a*l. (Apaolaza et al., 2017), in some instances, the MCS algorithm can fail to reach

optimality and provide a gene set, that although it contains MCS, is not minimal. When this occurred, we used FASTL (Pratapa et al., 2015) to identify the MCS within the returned set.

It can be assumed that if a gene metabolic function is essential in a given cell line, then this gene will be part of an MCS where the other MCS members have low activity. To integrate this information for SW480 and SW620, the following workflow was used for each cell line:

- *Rank essential genes based on their RSA score (low to high)*
- *For each essential gene in the ranked list:*
    - *Rank each MCS containing the gene of interest based on the total gene expression evidence of the reactions in the set, excluding reactions associated with the gene of interest. This is achieved by mapping transcriptomics to reactions using the GPR rules defined in Recon 2.2 and adding the gene expression value associated with each reaction. MCS with more than 8 reactions, not counting reactions associated with the gene of interest, are excluded.*
    - *For each MCS in the ranked list:*
        - *Implement the MCS. Force the reactions in the set to be inactive, excluding the reactions associated with the essential gene. Following the definition of MCS, the gene of interest is now an essential gene.*
        - *Use flux variability analysis* (Gudmundsson and Thiele, 2010) *to evaluate if the MCS is consistent with:*
            - *Intracellular metabolomics (all detected metabolites can be produced).*
            - *All measured rates of uptake and secretion and OCR measurements.*
            - *^{13}C MFA flux intervals.*
        - *Systematically simulate the effect of gene the KO for all metabolic genes defined as dispensable in Project DRIVE using FBA. Compute the number of false positives (dispensable genes in Project DRIVE that are predicted as essential by the model).*
        - *If implementing the MCS a) increases the number of false positives or b) is inconsistent with metabolomics, flux measurements or ^{13}C MFA:*
            - *Revert the MCS implementation.*
            - *Continue with the next MCS in the ranked list.*
        - *Else:*
            - *Continue to the next essential gene.*

For LiM2, we implemented the MCSs 1) shared between SW480 and SW620, and 2) the MCSs in SW620 where none of the genes associated with the reactions in the MCS was significantly overexpressed in LiM2.

In total, 8 ,7 and 6 MCSs were implemented into SW480, SW620 and LiM2, respectively.

13.1.9 GENE INACTIVATION MODERATED BY METABOLISM, AND EXPRESSION (GIMME)

GIMME (Becker and Palsson, 2008; Schmidt et al., 2013) was used to integrate transcriptomics together with the aforementioned data sets (e.g., extracellular fluxes, metabolomics, ^{13}C MFA, MCS) to build cell line-specific genome-scale flux maps. GIMME optimises biomass production and then performs a second optimisation where fluxes through reactions are minimised with a weight that is a function of the gene expression value mapped to each reaction. In our analysis, the minimisation weight (w_i) of each reaction was defined as follows:

$$w_i = 1 + \max(Th - ge_i, 0)$$

Equation 4

where,

ge_i is the gene expression value mapped to reaction *i following the* GPR rules defined in Recon2.

Th is the maximum gene expression value for metabolic genes.

For each cell line, GIMME was run in a condition-specific GSMM obtained by implementing MCS, the personalised biomass function, metabolomics, respiration parameters, rates of metabolite uptake and secretion, ^{13}C MFA in Recon2 as detailed in the previous sections. From the optimal GIMME solution, any inactive reaction with a mapped gene expression value under the 25th percentile of metabolic genes expression was removed. This allows pruning reactions analysed by lowly expressed enzymes from the network. Next, Following the GIM3E approach (Schmidt et al., 2013), each flux was maximised and minimised to identify the ranges of feasible fluxes within the optimal GIMME solution with a tolerance of 99.9%. This space of solution represents the space of most likely flux distributions in the conditions of study.

Finally, GIMME was also run with 90% tolerance in a model integrating cell line-specific MCS and biomass function but no other cell lines-specific measurements such as ^{13}C MFA or metabolomics. Rather than representing the flux map under the conditions of study, the purpose of this model is to represent the metabolic potential of each cell line. Thus, in such model, the flux boundaries for each reaction are modified to always include 0 (i.e., no reaction is forced to be active). These models, that we termed “base model”, serve as a framework to simulate gene KO with MOMA (Segrè et al., 2002).

13.1.10 FLUX SAMPLING AND REFERENCE FLUX DISTRIBUTION SELECTION

From the GIMME, a space of solutions was identified for each cell line. However, such space was still relatively wide and a strategy to select the most representative and accurate flux distributions from such space was applied. For the SW480, SW620, LiM2 the following approach was used to select the most representative flux distributions:

1. Compute 1000 flux samples from within the GIMME solution space. Flux samples were computed using the Artificially Centered hit-and-run (ACHR) algorithm implemented into COBRApy (Ebrahim et al., 2013; Heirendt et al., 2019). ACHR was run with a thinning factor of 10000. The thinning factor defines the number of iterations between each returned sample and a large thinning factor reduces the correlation between samples resulting in a more representative set of samples.
2. Using each flux sample as a wild type flux distribution, systematically simulate the KO with MOMA(Segrè et al., 2002) of all metabolic genes analysed in Project DRIVE. Such simulations were run in the cell line-specific base model.
3. Use the following equation to give a discrepancy score to each flux sample based on how well they encapsulate gene essentiality/dispensability data (equation 5):

$$S_j = \sum_{i \in DRIVE} max(2 + RSA_i, 0) \cdot \left(1 - \frac{BiomassKO_i}{Biomass_{WT}}\right)$$

Equation 5

Where:

S_j is the discrepancy score for flux sample *j*

RSA_i is the RSA score for gene *i* (RSA scores have negative values and more negative values indicate more dependency on a gene's function). For LiM2, the DRIVE RSA measurements for SW620 were used as it was the most closely related cell line.

$BiomassKO_i$ is the flux through the biomass reaction when the KO of gene *i* is simulated with MOMA (Segrè et al., 2002) using flux sample *j* as input.

$Biomass_{WT}$ is the flux through the biomass reaction in the wild type (no reaction inactivated).

4. Select the top 100 flux samples with the least discrepancy score. The average of such flux samples will be used as reference flux distribution for the cell line of study.

Such an approach primarily serves to reduce the number of false positives (i.e., genes predicted as essential by the model and described as dispensable in DRIVE) that might emerge from unrepresentative flux distributions.

13.1.11 IDENTIFYING PUTATIVE METABOLIC TARGETS

To identify metabolic targets against colon cancer, gene KOs were systematically simulated for metabolic genes, single or in pairs. The reactions to be blocked by each gene KO(s) were determined by combining gene expression data with the GPR rules of Recon 2.2. A reaction was considered to be inactive if when a gene was inactivated (i.e., its expression set to 0), the mapped gene expression value decreased at least 16^{th} fold. Then the effect of reaction KOs was simulated using the reference flux distribution computed for each cell line as input for running MOMA (Segrè et al., 2002) in the framework of cell line specific base models.

Single gene KOs were systematically performed for all cell lines under study. Conversely, for synthetic lethal (SL) pairs, due to the larger number of combinations to test (175000>), all potential SL pairs were only evaluated in SW620. The SL gene combinations that resulted in a biomass production below 15% of wild type in SW620 and displayed synergy were evaluated on the remaining cell lines. A gene pair was considered to have synergy if the fraction of biomass production under the double KO was less than the product of the fraction of biomass production under the individual KOs. A gene or gene pair was considered a selective target if it reduced the biomass production to 10% or less of the wild type in both SW620 and LiM2

Some of the identified targets where potentially inherent vulnerabilities to all human metabolic networks (as opposed to only cancer-specific metabolic networks). Bearing this in mind, all single and SL gene combinations were simulated on a Recon2 network unconstrained by condition-specific data (e.g. transcriptomics, metabolomics, gene dependency, etc) and those targets that prevented the synthesis of biomass components in this generic network were filtered out. The whole workflow is summarised in Figure A.V.1.

13.2 RESULTS

The metabolic flux analysis result for the three cell lines SW480, SW620, and LiM2 is shown in Table A.V.3 and a specification of each reaction in Table A.V.4. Only the reactions that were significant between one or two of the three cell lines are shown, all the other reactions of the model are considered to be equal among the three cell lines. Figure A.V.2 shows some of the relevant flux predictions for the model and discussed in section 5.2.1.1. Finally, the results of the individual targets and target pairs predictions from the GSMM are shown in Table A.V.5.

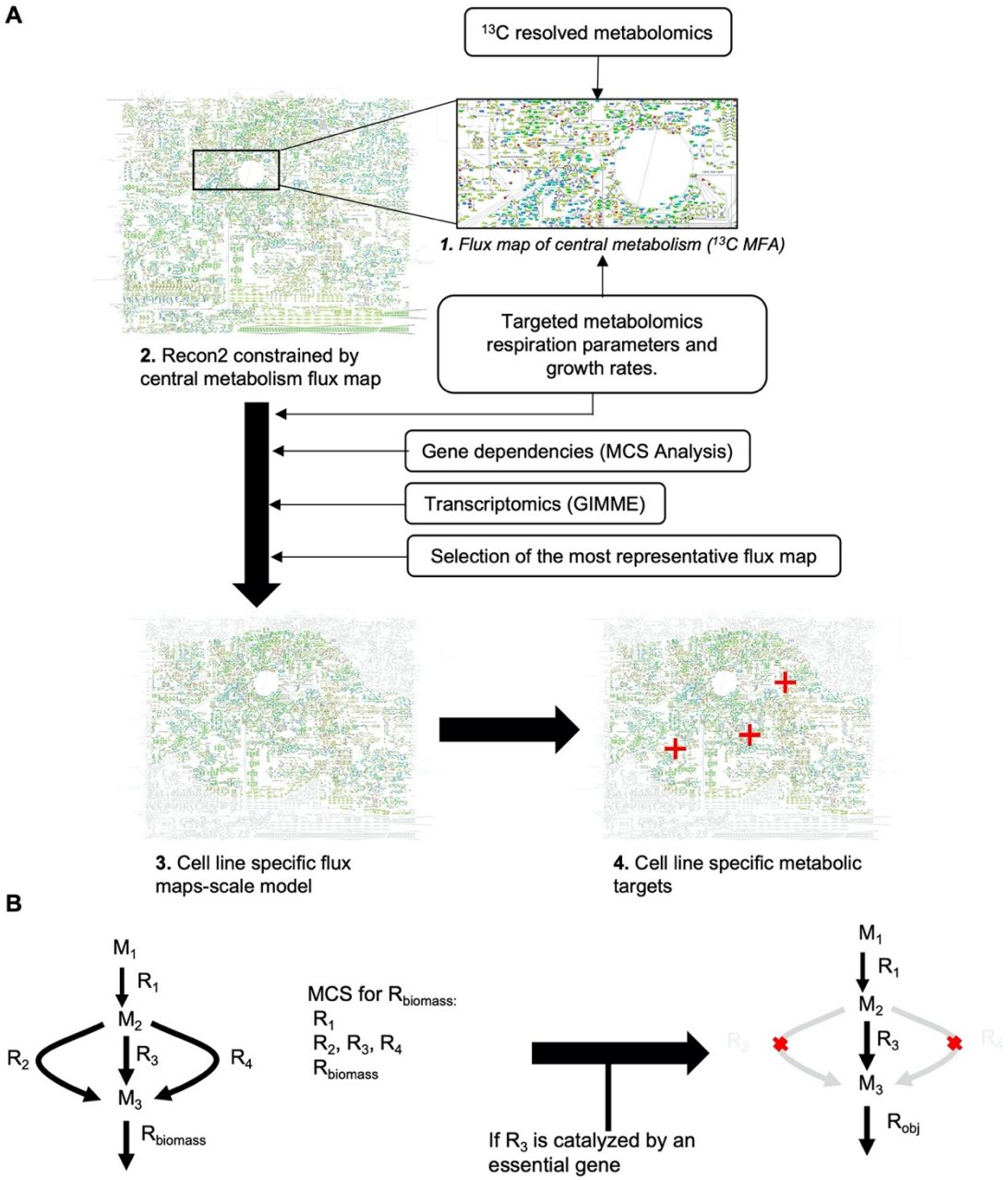

Figure A.V.1 Computational inference of cell line-specific metabolic flux maps and metabolic targets through multi-omics data integration. A. Graphical representation of the multi-omics integration workflow. First, a central carbon metabolism flux map is estimated using ^{13}C MFA, next the flux map is used to constrain Recon2, then several layers of omics data are used to estimate the cell line-specific flux maps which can be used to identify metabolic vulnerabilities d to selectively target specific populations. **B.** Integrating known gene dependencies using MCS analysis. Reactions catalysed by genes described as essential can be assumed to be part of a MCS where the other reactions are already inactive. In this example, because R_3 is catalysed by a gene described as essential, R_2 and R_4 can be assumed to be inactive.

	SW480		SW620		LiM2	
Reaction ID	**MFA Min**	**MFA Max**	**MFA Min**	**MFA Max**	**MFA Min**	**MFA Max**
ACITL	0,039	0,0017	0,0596	0,0851	0,0552	0,0852
ACONTm_group_ICDHxm	0,0326	0,0565	0,0209	0,0306	0,0164	0,0251
ALATA_L_reverse	0,0152	0,0171	0,0288	0,0324	0,0296	0,0313
ASPGLUm	0	-0,0289	0	0,0709	0	0,1104
CDS	3,52E-04	0,0017	5,99E-04	5,99E-04	5,55E-04	5,55E-04
CEPTC_group_CHLPCTD_CHOLK	0,0017	-0,039	0,0028	0,0028	0,0026	0,0026
CTPS2	3,44E-04	0,1462	5,87E-04	5,87E-04	5,43E-04	5,43E-04
CYOR_u10m	0,2711	0,0029	0,3473	0,3667	0,3053	0,356
CYTK1	0,002	5,21E-04	0,0034	0,0034	0,0032	0,0032
DESAT16_2	5,21E-04	0,0018	8,88E-04	8,88E-04	8,22E-04	8,22E-04
ENO_group_PGM	0,6029	0,1043	0,6751	0,7167	0,6648	0,684
FAS100COA_group_FAS120COA_FAS140COA_FAS160COA_et_al	0,0043	0,0019	0,0065	0,0097	0,006	0,0098
FDH	4,00E-07	0,0021	4,00E-07	0,0159	0,0052	0,0106
FTHFL_reverse	0	0,0472	0	0,0159	0,0052	0,0106
G3PD1	-0,002	0,0122	-0,0034	-0,0034	-0,0031	-0,0031
GAPD_group_PGK	0,6115	0,0059	0,6775	0,7186	0,666	0,6851
H2CO3D_reverse	0	0,325	0	43,9937	0	43,9987
LDH_L_reverse	0,5677	0,002	0,6001	0,6356	0,5814	0,6176
NADH2_u10m	0,1763	0,0016	0,2318	0,2762	0,2082	0,2693
NADPHtru	0,0016	0,0016	0,0027	0,0027	0,0025	0,0025
NDPK1	7,31E-04	-0,0818	0,0012	0,0516	0,0012	0,0485
P5CRxm_group_r0911	0,0054	0,0054	0,0093	0,0109	0,0093	0,0103
PCm	6,98E-04	0,0714	0	0,0021	0	0,0025
PDHm	0,0638	0,046	0,0788	0,096	0,0722	0,0854
PFK	0,307	0,013	0,3377	1,3489	0,3302	1,3426
PRPPS	0,0016	0,0014	0,0028	0,0032	NaN	0,0029
PYK	0,6036	0,0751	0,6751	0,7505	0,6652	0,7243
TPI	0,305	3,24E-04	0,3344	0,3579	0,327	0,3403
ala_L_et_reverse	0,0129	-0,0247	0,0232	0,0263	0,0239	0,0256
arg_L_et	-0,0267	0,0016	-0,0035	0,0052	0,0011	0,0054
cit_et_reverse	0	44,2035	0	0,0122	0	0,0127
co2_et_reverse	0,2285	0,325	0,24	44,2522	0,2159	44,2409
glc_D_et	0,3102	0,1075	0,3488	0,3689	0,3439	0,3525
gln_L_et	NaN	0,0147	0,0958	0,1069	0,0846	0,0974
gly_et	-0,0013	44	-0,0096	0,0051	-0,0047	-6,26E-04
hco3_et	0,0392	0,003	0,0167	44	0,0019	0,8026
lac_L_et_reverse	0,5677	0,0056	0,6001	0,6356	0,5814	0,6176
lys_L_et	0,0042	0,005	0,0072	0,0072	0,0066	0,0066
o2_et	0,1431	0,0035	0,1804	0,1896	0,1678	0,1838
orn_et_reverse	0,0026	0,0081	0,0014	0,0021	9,52E-04	0,0017

pro_L_et_reverse	0,0025	0,0013	0,0043	0,0059	0,0047	0,0057

Table A.V.3. Metabolic flux analysis (MFA) results for SW480, SW620, and LiM2. List of reactions from MFA results (minimum and maximum value) that are significantly different between SW480, SW620 or LiM2. Table A.V.4 show details of each reaction ID.

Reaction ID	Reaction name	Reaction
ACITL	ATP-Citrate lyase	atp.c + cit.c -> adp.c + oaa.c + accoa.c
ACONTm_group_ICDHxm	GroupAconitate hydratase;Isocitrate dehydrogenase (NAD+);	nad.m + cit.m <-> co2.m + nadh.m + akg.m
ALATA_L_reverse	L-alanine transaminase	glu_L.c + pyr.c -> akg.c + ala_L.c
ASPGLUm	aspartate-glutamate mitochondrial shuttle	asp_L.m + glu_L.c -> asp_L.c + glu_L.m
CDS	phosphatidate cytidylyltransferase	pa_hs.c + ctp.c -> cdpdag_hs.c
CEPTC_group_CHLPCTD_CHOLK	Groupcholine phosphotransferase;choline phosphate cytididyltransferase;Choline kinase;	chol.c + dag_hs.c + atp.c + ctp.c -> pchol_hs.c + adp.c + cmp.c
CTPS2	CTP synthase (glutamine)	utp.c + gln_L.c + atp.c -> glu_L.c + adp.c + ctp.c
CYOR_u10m	ubiquinol-6 cytochrome c reductase, Complex III	4*h.m + 2*ficytC.m + q10h2.m -> 2*focytC.m + q10.m + 4*h.c
CYTK1	cytidylate kinase (CMP)	cmp.c + atp.c -> cdp.c + adp.c
DESAT16_2	palmitoyl-CoA desaturase (n-C16:0CoA -> n-C16:1CoA)	o2.c + pmtcoa.c + nadh.c -> hdcoa.c + nad.c
ENO_group_PGM	Groupenolase;phospho glycerate mutase;	3pg.c <-> pep.c
FAS100COA_group_FAS120COA_FAS140COA_FAS160COA_et_al	Groupfatty acyl-CoA synthase (n-C10:0CoA);fatty-acyl-CoA synthase (n-C12:0CoA); fatty-acyl-CoA synthase (n-C14:0CoA);fatty-acyl-CoA synthase (n-C16:0CoA); fatty acyl-CoA synthase (n-C8:0CoA), lumped reaction;	malcoa.c + malcoa.c + malcoa.c + malcoa.c + malcoa.c + malcoa.c + malcoa.c + accoa.c + 14*nadph.c -> 14*nadp.c + pmtcoa.c
FDH	formate dehydrogenase	for.c + nad.c -> co2.c + nadh.c
FTHFL_reverse	Formate-tetrahydrofolate ligase	10fthf.c + adp.c -> for.c + thf.c + atp.c
G3PD1	glycerol-3-phosphate dehydrogenase (NAD)	glyc3p.c + nad.c <-> dhap.c + nadh.c

GAPD_group_PGK	Groupglyceraldehyde-3-phosphate dehydrogenase;phosphoglycerate kinase;	nad.c + g3p.c + adp.c <-> 3pg.c + atp.c + nadh.c
H2CO3D_reverse	carboxylic acid dissociation	hco3.c -> co2.c
LDH_L_reverse	L-lactate dehydrogenase	nadh.c + pyr.c -> lac_L.c + nad.c
NADH2_u10m	NADH dehydrogenase, mitochondrial	nadh.m + q10.m + 4*h.m -> nad.m + q10h2.m + 4*h.c
NADPHtru	NADPH transporter, endoplasmic reticulum	nadph.c -> nadph.r
NDPK1	nucleoside-diphosphate kinase (ATP:GDP)	atp.c + gdp.c -> gtp.c + adp.c
P5CRxm_group_r0911	Grouppyrroline-5-carboxylate reductase (m);Facilitated diffusion;	nadh.m + glu_L.c + 1pyr5c.m -> glu_L.m + nad.m + pro_L.c
PCm	pyruvate carboxylase	atp.m + pyr.m + hco3.m -> adp.m + oaa.m
PDHm	pyruvate dehydrogenase	nad.m + pyr.m -> accoa.m + nadh.m + co2.m
PFK	phosphofructokinase	atp.c + f6p.c -> fdp.c + adp.c
PRPPS	phosphoribosylpyrophosphate synthetase	atp.c + r5p.c -> art_ribose.c + amp.c + prpp.c
PYK	pyruvate kinase	pep.c + adp.c -> pyr.c + atp.c
TPI	triose-phosphate isomerase	dhap.c <-> g3p.c
ala_L_et_reverse	ala_L transport	ala_L.c -> ala_L.e
arg_L_et	arg_L transport	arg_L.e <-> arg_L.c
cit_et_reverse	cit transport	cit.c -> cit.e
co2_et_reverse	co2 transport	co2.c -> co2.e
glc_D_et	glc_D transport	glc_D.e -> glc_D.c
gln_L_et	gln_L transport	gln_L.e -> gln_L.c
gly_et	gly transport	gly.e <-> gly.c
hco3_et	hco3 transport	hco3.e -> hco3.c
lac_L_et_reverse	lac_L transport	lac_L.c -> lac_L.e
lys_L_et	lys_L transport	lys_L.e -> lys_L.c
o2_et	o2 transport	o2.e -> o2.c
orn_et_reverse	orn transport	orn.c -> orn.e
pro_L_et_reverse	pro_L transport	pro_L.c -> pro_L.e

Table A.V.4. Reactions from Table A.V.3. Correspondence between each reaction ID from Table A.V.3 with the reaction name and reaction components.

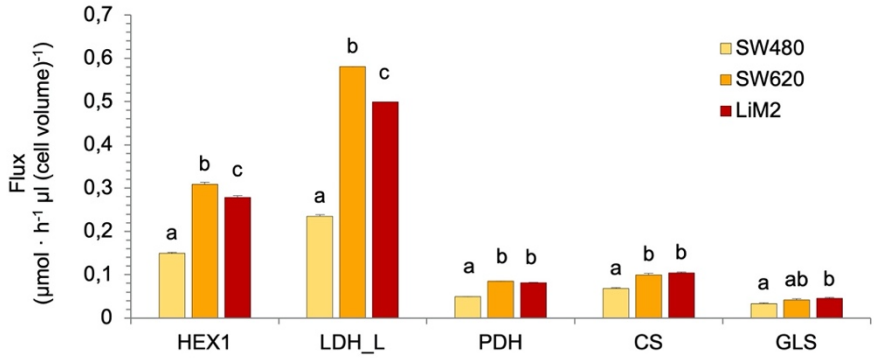

Figure A.V.2. Selected predicted fluxes by the GSMM model. HEX1: Hexokinase; LDH-L: Lactate dehydrogenase; PDH: pyruvate dehydrogenase; CS: Citrate synthase; and GLS: Glutaminase. [a,b,c] denote cell lines with an overlap of the sampled flux values for a given reaction.

Gene symbols		The predicted fraction of growth compared to wild type		
		SW480	SW620	LiM2
Single Targets	***MTHFD1***	100.0%	0.0%	0.0%
	GSR	99.0%	0.0%	0.0%
	SCD	25.4%	0.0%	0.0%
	DLD	5.5%	0.0%	3.5%
	PKM	2.3%	0.0%	0.0%
	PRODH	0.0%	0.0%	0.0%
	GAPDH	0.0%	0.0%	0.0%
	GPT	0.0%	0.0%	0.0%
	RRM1	0.0%	0.0%	0.0%
	GUK1	0.0%	0.0%	0.0%
Target pairs	***SLC7A9, SLC3A2***	86%	0%	0%
	SLC3A1, SLC3A2	86%	0%	0%
	SLC7A9, SLC7A11	85%	0%	0%
	SLC7A11, SLC3A1	85%	0%	0%
	ETFA, GPI	49%	10%	9%
	ETFB, GPI	49%	10%	9%
	AGXT, GPI	49%	9%	8%
	GPI, GRHPR	49%	9%	8%
	CTH, GPI	42%	4%	7%
	DLST, GPI	40%	5%	7%
	GPI, OGDH	40%	5%	7%
	GPI, SUCLG1	35%	1%	1%
	G6PD, GPI	24%	2%	2%
	PGLS, GPI	24%	2%	2%
	FH, GPI	19%	2%	7%
	PPA2, GPI	18%	0%	0%
	GPI, PGD	16%	0%	0%
	GPI, SDHD	14%	0%	0%
	GPI, SDHC	14%	0%	0%
	GPI, SDHA	14%	0%	0%
	GPI, SDHB	14%	0%	0%
	GPI, UQCRH	12%	0%	0%
	UQCRQ, GPI	12%	0%	0%
	GPI, UQCRFS1	12%	0%	0%
	UQCR11, GPI	12%	0%	0%
	GPI, UQCR10	12%	0%	0%

	GPI, MT-CYB	12%	0%	0%
	CYC1, GPI	12%	0%	0%
	GPI, UQCRC1	12%	0%	0%
	GPI, UQCRB	12%	0%	0%
	GPI, UQCRC2	12%	0%	0%
	FH, PDHB	6%	8%	9%
	DLAT, FH	6%	8%	9%
	FH, ATP5J	0%	0%	0%
	MT-CO1, SDHA	0%	4%	0%
	COX4I1, SDHA	0%	4%	0%
	CYC1, ACOX1	0%	0%	0%
	SDHD, COX5A	0%	4%	0%
	NSF, SDHD	0%	0%	0%
	COX4I1, SDHD	0%	4%	0%
	COX7B2, SDHA	0%	4%	0%
	COX4I1, SDHC	0%	4%	0%
	COX7B, SDHC	0%	4%	0%
	ATP5B, SDHA	0%	0%	0%
	SDHC, COX4I2	0%	4%	0%
	COX6B2, SDHD	0%	4%	0%
	COX8A, ACOX1	0%	0%	0%
	ATP5C1, SDHA	0%	0%	0%
	GPI, SORD	0%	0%	0%
	MT-CYB, ACOX1	0%	0%	0%
	COX7B, GPI	0%	0%	0%
	MT-CO2, ACOX1	0%	0%	0%
	COX5B, SDHD	0%	4%	0%
	ATP5H, SDHC	0%	0%	0%
	COX7C, ACOX1	0%	0%	0%
	UQCRQ, ACOX1	0%	0%	0%
	ACOX1, UQCRH	0%	0%	0%
	GPI, COX8C	0%	0%	0%
	ATP5H, GPI	0%	0%	0%
	GPI, ATP5C1	0%	0%	0%
	ATP5L, SDHA	0%	0%	0%
	GPI, ATP5F1	0%	0%	0%
	COX7B, ACOX1	0%	0%	0%
	ATP5D, SDHB	0%	0%	0%
	GPI, ATP5D	0%	0%	0%

	SDHC, COX5A	0%	4%	0%
	ATP5E, SDHC	0%	0%	0%
	COX7A2, GPI	0%	0%	0%
	COX7B2, ACOX1	0%	0%	0%
	SDHA, ATP5J2	0%	0%	0%
	COX7A2, SDHB	0%	4%	0%
	COX7C, SDHC	0%	4%	0%
	COX6B1, SDHD	0%	4%	0%
	COX6B1, SDHB	0%	4%	0%
	COX6B2, SDHC	0%	4%	0%
	GPI, COX5A	0%	0%	0%
	COX7A2, ACOX1	0%	0%	0%
	GPI, ATP5A1	0%	0%	0%
	MT-CO2, SDHD	0%	4%	0%
	ATP5I, SDHC	0%	0%	0%
	GPI, MT-CO2	0%	0%	0%
	COX7A1, SDHD	0%	4%	0%
	FH, ATP5D	0%	0%	0%
	FH, ATP5C1	0%	0%	0%
	COX5B, SDHC	0%	4%	0%
	GPI, ATP5J	0%	0%	0%
	ACOX1, UQCRB	0%	0%	0%
	COX7B2, SDHD	0%	4%	0%
	COX6C, SDHB	0%	4%	0%
	SDHD, COX7A2L	0%	4%	0%
	SDHC, ATP5J2	0%	0%	0%
	ACOX1, UQCRC1	0%	0%	0%
	ATP5L, SDHB	0%	0%	0%
	ACOX1, UQCRC2	0%	0%	0%
	ATP5J, SDHC	0%	0%	0%
	ATP5E, SDHA	0%	0%	0%
	COX7A2, SDHC	0%	4%	0%
	COX6A1, SDHC	0%	4%	0%
	COX7C, SDHD	0%	4%	0%
	ATP5D, SDHD	0%	0%	0%
	COX6A1, GPI	0%	0%	0%
	COX7B, SDHA	0%	4%	0%
	COX6A2, GPI	0%	0%	0%
	ATP5A1, SDHD	0%	0%	0%

	GPI, NSF	0%	0%	0%
	ACOX1, COX7A2L	0%	0%	0%
	UQCR11, ACOX1	0%	0%	0%
	COX6A1, ACOX1	0%	0%	0%
	SDHB, COX4I2	0%	4%	0%
	COX8C, SDHC	0%	4%	0%
	ATP5H, SDHA	0%	0%	0%
	COX7A1, SDHC	0%	4%	0%
	ATP5I, SDHA	0%	0%	0%
	MT-CO2, SDHB	0%	4%	0%
	SDHC, COX7A2L	0%	4%	0%
	FH, ATP5I	0%	0%	0%
	COX7A1, GPI	0%	0%	0%
	ATP5D, SDHA	0%	0%	0%
	FH, ATP5F1	0%	0%	0%
	COX7B2, SDHB	0%	4%	0%
	MT-CO3, SDHC	0%	4%	0%
	ATP5F1, SDHC	0%	0%	0%
	COX6A1, SDHA	0%	4%	0%
	COX6C, GPI	0%	0%	0%
	COX6C, ACOX1	0%	0%	0%
	NSF, SDHC	0%	0%	0%
	ATP5J, SDHA	0%	0%	0%
	COX8A, GPI	0%	0%	0%
	COX6A2, SDHC	0%	4%	0%
	ATP5F1, SDHA	0%	0%	0%
	COX6B1, SDHA	0%	4%	0%
	MT-CO1, SDHD	0%	4%	0%
	ATP5A1, SDHB	0%	0%	0%
	COX5B, GPI	0%	0%	0%
	MT-CO1, SDHB	0%	4%	0%
	ATP5C1, SDHD	0%	0%	0%
	FH, ATP5E	0%	0%	0%
	MT-CO2, SDHA	0%	4%	0%
	SDHA, COX5A	0%	4%	0%
	COX7A2, SDHD	0%	4%	0%
	COX8C, ACOX1	0%	0%	0%
	MT-CO3, SDHA	0%	4%	0%
	GPI, ATP5B	0%	0%	0%

	GPI, COX7A2L	0%	0%	0%
	NSF, SDHA	0%	0%	0%
	ATP5L, FH	0%	0%	0%
	MT-CO3, ACOX1	0%	0%	0%
	COX4I1, ACOX1	0%	0%	0%
	ATP5C1, SDHC	0%	0%	0%
	SDHA, COX7A2L	0%	4%	0%
	COX7B, SDHD	0%	4%	0%
	COX8A, SDHC	0%	4%	0%
	SDHD, ATP5J2	0%	0%	0%
	COX7A1, ACOX1	0%	0%	0%
	COX6B2, SDHA	0%	4%	0%
	COX7C, GPI	0%	0%	0%
	COX8C, SDHA	0%	4%	0%
	FH, ATP5B	0%	0%	0%
	ATP5H, SDHD	0%	0%	0%
	GPI, COX4I2	0%	0%	0%
	ATP5L, SDHD	0%	0%	0%
	ATP5H, SDHB	0%	0%	0%
	COX6C, SDHD	0%	4%	0%
	ACOX1, COX4I2	0%	0%	0%
	GPI, ATP5E	0%	0%	0%
	COX6A1, SDHD	0%	4%	0%
	COX6B2, ACOX1	0%	0%	0%
	ACOX1, COX5A	0%	0%	0%
	ATP5D, SDHC	0%	0%	0%
	GPI, ATP5J2	0%	0%	0%
	COX6B1, ACOX1	0%	0%	0%
	SDHB, COX7A2L	0%	4%	0%
	ATP5E, SDHB	0%	0%	0%
	COX7B, SDHB	0%	4%	0%
	COX7C, SDHB	0%	4%	0%
	COX6B1, SDHC	0%	4%	0%
	COX6A2, SDHA	0%	4%	0%
	ATP5B, SDHC	0%	0%	0%
	FH, ATP5J2	0%	0%	0%
	COX7A1, SDHA	0%	4%	0%
	ATP5I, SDHB	0%	0%	0%
	MT-CO2, SDHC	0%	4%	0%
	GPI, MT-CO1	0%	0%	0%

	FH, ATP5A1	0%	0%	0%
	COX5B, SDHB	0%	4%	0%
	GPI, ATP5I	0%	0%	0%
	ACOX1, UQCRFS1	0%	0%	0%
	COX7A2, SDHA	0%	4%	0%
	COX4I1, GPI	0%	0%	0%
	COX6C, SDHC	0%	4%	0%
	ATP5H, FH	0%	0%	0%
	SDHD, COX4I2	0%	4%	0%
	MT-CO3, SDHD	0%	4%	0%
	ATP5F1, SDHD	0%	0%	0%
	ATP5L, SDHC	0%	0%	0%
	SDHB, COX5A	0%	4%	0%
	ATP5J, SDHB	0%	0%	0%
	FH, NSF	0%	0%	0%
	COX6A1, SDHB	0%	4%	0%
	ATP5B, SDHD	0%	0%	0%
	UQCR10, ACOX1	0%	0%	0%
	COX5B, SDHA	0%	4%	0%
	ATP5A1, SDHA	0%	0%	0%
	COX8A, SDHA	0%	4%	0%
	COX5B, ACOX1	0%	0%	0%
	COX8C, SDHD	0%	4%	0%
	COX8C, SDHB	0%	4%	0%
	COX6A2, ACOX1	0%	0%	0%
	SDHB, ATP5J2	0%	0%	0%
	COX7A1, SDHB	0%	4%	0%
	COX6B2, SDHB	0%	4%	0%
	ATP5I, SDHD	0%	0%	0%
	ATP5C1, SDHB	0%	0%	0%
	COX6C, SDHA	0%	4%	0%
	COX7B2, SDHC	0%	4%	0%
	COX7B2, GPI	0%	0%	0%
	MT-CO3, SDHB	0%	4%	0%
	NSF, SDHB	0%	0%	0%
	COX4I1, SDHB	0%	4%	0%
	ATP5F1, SDHB	0%	0%	0%
	ATP5L, GPI	0%	0%	0%
	ATP5J, SDHD	0%	0%	0%
	COX7C, SDHA	0%	4%	0%

	ATP5E, SDHD	0%	0%	0%
	SDHA, COX4I2	0%	4%	0%
	COX6B1, GPI	0%	0%	0%
	COX6A2, SDHD	0%	4%	0%
	COX6A2, SDHB	0%	4%	0%
	ATP5B, SDHB	0%	0%	0%
	MT-CO1, SDHC	0%	4%	0%
	COX8A, SDHB	0%	4%	0%
	COX8A, SDHD	0%	4%	0%
	ATP5A1, SDHC	0%	0%	0%
	COX6B2, GPI	0%	0%	0%
	MT-CO1, ACOX1	0%	0%	0%
	GPI, MT-CO3	0%	0%	0%

Table A.V.5 Putative metabolic targets. List of the individual or targets pairs identified in the GSMM model that can preferentially impair SW620 and LiM2 proliferation or also SW480 proliferation.

14. Appendix VI

14 APPENDIX VI

Research articles published during the realisation of the thesis

The main results of the present theses thesis have been compiled in an article and recently submitted in Nature Metabolism:

Authors: Tarragó-Celada, Josep; Foguet, Carles; Tarrado-Casatellarnau, Míriam; Marin, Silvia; Hernández-Alias, Xavier; Perarnau, Jordi; Morrish, Fionnuala; Hockenbery, David; Gomis, Roger R; Ruppin, Eytan; Yuneva, Mariia; de Atauri, Pedro; Cascante, Marta.
Title: *Cysteine and folate metabolism are targetable vulnerabilities of metastatic colorectal cancer.*
Abstract: With most cancer-related deaths resulting from metastasis, the development of new therapeutic approaches against metastatic colorectal cancer (mCRC) are essential to increasing patient survival. The metabolic adaptations that support mCRC remain undefined and their elucidation is crucial to identify potential therapeutic targets. Here, we employed a strategy for the rational identification of targetable metabolic vulnerabilities. This strategy involved a thorough metabolic characterisation of the same patient-derived cell lines from a primary colon adenocarcinoma (SW480), its lymph node metastasis (SW620) and a liver metastatic derivative (SW620-LiM2). Using a novel multi-omics integration workflow, we build cell line-specific genome-scale metabolic models to identify metastatic cell-specific metabolic vulnerabilities. We discovered that metastatic cell lines are selectively vulnerable to the inhibition of cystine import and folate metabolism, and we identified the system xCT and MTHFD1 genes as potential therapeutic targets, both individually and combined, for combating mCRC.

Furthermore, during the realisation of the thesis, two original articles, two review articles, and one book chapter have been published, directly or indirectly related to the thesis.

Original articles:

Authors: Tarrado-Castellarnau, Míriam; **Tarragó-Celada, Josep***; de Atauri, Pedro*; Perarnau, Jordi; Yuneva, Mariia; Thompson, Timothy M; Cascante, Marta. (*: equal contribution).
Title: *De novo MYC addiction as an adaptative response of cancer cells to CDK4/6 inhibition.*
Publication details: Molecular Systems Biology, 13:940. August 2017.
DOI: 10.15252/msb.20167321.
Abstract: Cyclin-dependent kinases (CDK) are rational cancer therapeutic targets fraught with the development of acquired resistance by tumor cells. Through metabolic and transcriptomic analyses, we show that the inhibition of CDK4/6 leads to a metabolic reprogramming associated with gene networks orchestrated by the MYC transcription factor. Upon inhibition of CDK4/6, an accumulation of MYC protein ensues which explains an increased glutamine metabolism, activation of the mTOR pathway and blunting of HIF-1α-mediated responses to hypoxia. These MYC-driven adaptations to CDK4/6 inhibition render cancer cells highly sensitive to inhibitors of MYC, glutaminase or mTOR and to hypoxia, demonstrating that metabolic adaptations to antiproliferative drugs unveil new vulnerabilities that can be exploited to overcome acquired drug tolerance and resistance by cancer cells.

Authors: Tarrado-Castellarnau, Míriam; Cortés, Roldán; Zanuy, Miriam.; **Tarragó-Celada, Josep**; Polat, Ibrahim H.; Hill, Richard; Fan, Teresa. W. M.; Link, Wolfgang; Cascante, Marta.
Title: *Methylseleninic acid promotes antitumour effects via nuclear FOXO3a translocation through Akt inhibition.*
Publication details: Pharmacological Research 102:218-234. December 2015.
DOI: 10.1016/j.phrs.2015.09.009.
Abstract: Selenium supplement has been shown in clinical trials to reduce the risk of different cancers including lung carcinoma. Previous studies reported that the antiproliferative and pro-apoptotic activities of methylseleninic acid (MSA) in cancer cells could be mediated by inhibition of the PI3K pathway. A better understanding of the downstream cellular targets of MSA will provide information on its mechanism of action and will help to optimize its use in combination therapies with PI3K inhibitors. For this study, the effects of MSA on viability, cell cycle, metabolism, apoptosis, protein and mRNA expression, and reactive oxygen species production were analysed in A549 cells. FOXO3a subcellular localization was examined in A549 cells and in stably transfected human osteosarcoma U2foxRELOC cells. Our results demonstrate that MSA induces FOXO3a nuclear translocation in A549 cells and in U2OS cells that stably express GFP-FOXO3a. Interestingly, sodium selenite, another selenium compound, did not induce any significant effects on FOXO3a translocation despite inducing apoptosis. Single strand break of DNA, disruption of tumour cell metabolic adaptations, decrease in ROS production, and cell cycle arrest in G1 accompanied by induction of apoptosis are late events occurring after 24h of MSA treatment in A549 cells. Our findings suggest that FOXO3a is a relevant mediator of the antiproliferative effects of MSA. This new evidence on the mechanistic action of MSA can open new avenues in exploiting its antitumour properties and in the optimal design of novel combination therapies. We present MSA as a promising chemotherapeutic agent with synergistic antiproliferative effects with cisplatin.

Review articles:

Authors: Tarragó-Celada, Josep*; Balcells, Cristina*; Foguet, Carles*; De Atauri, Pedro; Marin, Silvia; Cascante, Marta. (*: equal contribution)
Title: *Tracing metabolic fluxes using mass spectrometry: Stable isotope-resolved metabolomics in Health and disease*.
Publication details: TrAC Trends in Analytical Chemistry, Volume 120, 115371. November 2019.
DOI: 10.1016/j.trac.2018.12.025.
Abstract: Tracing metabolic fluxes, defined as the reaction and transport rates in living cells, is essential to characterize metabolic phenotypes. One of the most informative methods to predict fluxes is stable isotope-resolved metabolomics (SIRM). In SIRM, a biological system is fed with substrates labeled with stable heavy isotopes. This isotopic label propagates along metabolic pathways and is incorporated into metabolites. After incubation, metabolites are extracted, and the incorporation of the isotopic label is quantified with isotope-sensitive analytical techniques, either mass spectrometry (MS) or nuclear magnetic resonance (NMR). Here we review the most suitable and widely-used MS platforms and methodologies for SIRM. We also provide an overview of state of the art in the analysis of SIRM data to trace metabolic fluxes, covering both local flux predictions and network-wide flux analysis. Finally, we highlight the role of SIRM in shaping our current understanding of metabolism in both health and pathological conditions.

Authors: Tarragó-Celada, Josep*; Martín-Bernabé, Alfonso*; Balcells, Cristina*; Foguet, Carles*; Bourgoin-voillard, Sandrine; Seve, Michel; Cascante, Marta. (*: equal contribution).
Title: *The importance of post-translational modifications in Systems biology approaches to identify therapeutic targets in cancer metabolism*.
Publication details: Current Opinion in Systems Biology, 3:161-169. June 2017.
DOI: 10.1016/j.coisb.2017.05.011.
Abstract: Cancer metabolism is reprogrammed to fulfill the needs of proliferation and migration, which is accomplished through different levels of regulation. In recent years, new advances in protein post-translational modifications (PTMs) research have revealed a complex layer of regulatory mechanisms through which PTMs control cell signaling and metabolic pathways, contributing to the diverse metabolic phenotypes found in cancer. Despite the efficacy of current modeling approaches to study cancer metabolism they still lack the capacity to integrate PTMs in their predictions. Here we will review the importance of PTMs in cancer metabolic reprogramming and suggest ways in which computational predictions could be enhanced through the integration of PTMs.

Book chapter:

Authors: Selivanov, Vitaly A; Marin, Silvia; **Tarragó-Celada, Josep**; Lane, Andrew N; Higashi, Richard M; Fan, Teresa W-M; de Atauri, Pedro; Cascante, Marta.
Title: *Software supporting a workflow of quantitative dynamic flux maps estimation in central metabolism from SIRM experimental data*.
Publication details: Methods in Molecular Biology 2088:271-298. 2020.
DOI: 10.1007/978-1-0916-0159-4_12.
Abstract: Stable isotope-resolved metabolomics (SIRM), based on the analysis of biological samples from living cells incubated with artificial isotope enriched substrates, enables mapping the rates of biochemical reactions (metabolic fluxes). We developed software supporting a workflow of analysis of SIRM data obtained with mass spectrometry (MS). The evaluation of fluxes starting from raw MS recordings requires at least three steps of computer support: first, extraction of mass spectra of metabolites of interest, then correction of the spectra for natural isotope abundance, and finally, evaluation of fluxes by simulation of the corrected spectra using a corresponding mathematical model. A kinetic model based on ordinary differential equations (ODEs) for isotopomers of metabolites of the corresponding biochemical network supports the final part of the analysis, which provides a dynamic flux map.